

**Searches For The Exclusive Neutral Higgs and the
Charged Higgs Bosons with the ATLAS Detector
at the LHC**

by
LAST FEREMENGA

Presented to the Faculty of the Graduate School of
The University of Texas at Arlington in Partial Fulfillment
of the Requirements
for the Degree of

DOCTOR OF PHILOSOPHY

THE UNIVERSITY OF TEXAS AT ARLINGTON
December 2016

ABSTRACT

Searches For The Exclusive Neutral Higgs and the Charged Higgs Bosons with the ATLAS Detector at the LHC

LAST FEREMENGA, Ph.D.

The University of Texas at Arlington, 2016

Supervising Professor: Jaehoon Yu

In this thesis, searches for the exclusive Standard Model (SM) and charged hMSSM Higgs bosons are performed. While observations of the SM Higgs boson in 2012 by ATLAS and CMS collaborations were ground-breaking, several of the SM Higgs boson properties such as its coupling strengths and branching ratios of its decays still carry large systematic uncertainties. Higgs boson candidates from exclusive production could lower these systematic uncertainties due to their cleaner production environment, improving knowledge of the SM Higgs boson sector. Since the charged Higgs boson is not included in the SM, its evidence would clearly indicate physics beyond the SM which could address the hierarchy problem. Since no signal is observed for either of these bosons, limits to their production cross sections are set. A 95% confidence-level upper limit on the total production cross-section for exclusive Higgs boson is set to 1.2 pb. Limits on the total production cross section of the charged Higgs boson times its branching ratio to $\tau\nu$ are set between 1.9 pb and 15 fb, for charged Higgs boson masses ranging from 200 to 2000 GeV.

Contents

ABSTRACT	ii
Chapter	Page

1.	Introduction	1
2.	Theoretical Framework	4
2.1	The Standard Model	4
2.1.1	Overview of the Standard Model	4
2.1.2	Building the Standard Model	7
2.1.3	The Higgs Boson	14
2.2	Exclusive Particle Interactions	16
2.2.1	Overview of exclusivity or diffraction	16
2.2.2	Production of the exclusive Higgs boson	18
2.3	Minimal Supersymmetric Standard Model	20
2.3.1	Two-Higgs-Doublet Model	20
2.3.2	The charged Higgs boson	22
3.	Experimental Setup	25
3.1	The Large Hadron Collider	25
3.2	The ATLAS Detector	28
3.2.1	The Inner Detector	29
3.2.2	Calorimeters	33
3.2.3	The Muon Spectrometer	36
3.2.4	The Trigger and Data Acquisition System	39
4.	ATLAS Simulation Chain	60
4.1	Event Generation	60
4.1.1	Parton Shower Development	63
4.1.2	Hadronization	64
4.1.3	Underlying Event and Pileup	65
4.1.4	Monte Carlo Generators	65
4.2	Detector Simulation and Data Management	67
5.	Physics Objects	68
5.1	Tracks	68
5.1.1	Inner Detector Tracks	68
5.1.2	Muon Spectrometer Tracks	69
5.2	Electrons	71
5.2.1	Reconstruction and Identification	71
5.2.2	Measurement of efficiencies, corrections and uncertainties	74
5.3	Muons	78
5.3.1	Reconstruction and Identification	78
5.3.2	Measurement of efficiencies, corrections and uncertainties	79
5.4	Jets	82
5.4.1	The anti- k_T clustering scheme	83
5.4.2	Performance and Calibration	84
5.4.3	B-Tagging	90
5.5	Taus	94
5.5.1	Reconstruction and Identification	94

5.6	Missing Energy	97
5.6.1	Run I Reconstruction	98
5.6.2	Run II Reconstruction	100
6.	Charged Higgs Search	102
6.1	Data and Simulation	102
6.2	Object Selection	105
6.3	Event Selection	106
6.3.1	Trigger Efficiency	109
6.4	Background Modelling	111
6.4.1	Lepton to τ	112
6.4.2	$j \rightarrow \tau$ backgrounds	113
6.4.3	True $\tau_{\text{had-vis}}$ backgrounds	117
6.5	Systematic Uncertainties and Statistical Methods	119
6.5.1	Systematic Uncertainties	119
6.5.2	Statistical Methods	125
6.6	Results	127
6.6.1	Expected and Observed Event Yields	127
6.6.2	Statistical Analysis	129
7.	Exclusive Higgs Search	134
7.1	Data and Simulation	134
7.2	Object Selection	136
7.3	Event Selection	138
7.3.1	Exclusivity Selection	142
7.3.2	Performance and calibration of exclusivity	143
7.4	Modelling of background processes	152
7.4.1	Exclusive backgrounds	152
7.4.2	Inclusive backgrounds	153
7.5	Validation of background modelling	157
7.5.1	Exclusive W^+W^-	157
7.5.2	Inclusive $Z \rightarrow \tau\tau$	158
7.6	Systematic Uncertainties and Statistical analysis	159
7.7	Results	160
7.7.1	Expected and observed event yields	160
7.7.2	Statistical Analysis	162
8.	Conclusion	164
	Bibliography	165

List of Figures

2.1	Feynman diagram of a quark-gluon vertex	8
2.2	Feynman diagrams of gluon-gluon vertices	9
2.3	Feynman diagrams of left handed fermion- W^\pm vertices	11
2.4	Feynman diagrams of fermion- Z/γ vertices	12
2.5	Feynman diagrams showing self gauge interactions in the electroweak theory	13
2.6	Feynman diagrams showing SM neutral Higgs boson vertices with Z and W^\pm	15
2.7	Feynman diagrams showing SM neutral Higgs boson vertices with photons and gluons	15
2.8	Feynman diagrams showing SM neutral Higgs boson production modes in pp collisions. Taken from Ref [18]	16
2.9	Plots showing distributions of expected cross sections for SM Higgs boson production modes in pp collisions, and branching ratios for its decay modes, plotted against the Higgs mass. Taken from Ref [19]	17
2.10	Diagrams showing exclusive processes through photon exchanges, producing a pair of W^\pm bosons	18
2.11	Feynman diagram showing the production of the exclusive Higgs boson	19
2.12	Feynman diagrams showing tree level charged Higgs vertices	23
2.13	Feynman diagrams showing charged Higgs production	23
2.14	Plots of the charged Higgs production cross section against $\tan\beta$ at $\sqrt{s} = 13$ TeV collision energy, for $m_{H^+} = 200$ GeV	24
2.15	Charged Higgs decay branching ratios in the hMSSM scenario, where $m_h^{\text{mod}+}$ alludes to the fact that h is the observed SM Higgs. Left shows $\tan\beta = 10$ and right shows $\tan\beta = 50$	24
3.1	The accelerator complex for the LHC. Apart from accelerating protons, the LHC is also used to accelerate and collide heavy ions. Arrows represent the particles' pathway from production to collision, with a key at the bottom left indicating the type of particle	27
3.2	Peak luminosity from the LHC during Run I and Run II	29
3.3	The coordinate system used by the ATLAS experiment to describe the ATLAS detector	30
3.4	A cutaway view of the ATLAS Inner Detector	31

3.5	A cutaway view of the ATLAS Pixel Detector, which is the innermost sub-detector of the Inner Detector	32
3.6	A schematic diagram of the ATLAS SCT	32
3.7	A cutaway view of the ATLAS calorimeter system	36
3.8	A photograph of a Tile Calorimeter module	37
3.9	The ATLAS magnetic system. The red toroid encapsulate the muon spectrometer sub-detectors, while the solenoid encapsulates the inner detector, which was discussed in Section 3.2.1	38
3.10	A cut-out of a Monitored Drift Tube chamber showing multi-layers of MDTs and the supporting beam structures	39
3.11	A cutaway view of the ATLAS Muon Spectrometer and its sub-detectors	40
3.12	Schematic diagram of showing cell segmentation in the EM Cal, across multiple layers	41
3.13	Illustration of the search algorithm for electrons and photons in the EM Cal	42
3.14	Distributions of variables used to separate electrons and π^0 s. [Top Left] ρ_{layer} for Layer 1 and Layer 2. [Top Right] ρ_{comp} for Layer 1 and Layer 2. [Middle Left] $R_\eta^{(1)}$ for π^0 s and electrons across several energies. [Middle Right] $R_\eta^{(1)}$ for 20 GeV electrons and π^0 s. [Bottom Left] $R_\eta^{(1)}$ with vertex smearing on. [Bottom Right] $R_\eta^{(1)}$ with vertex smearing turned on and η scanned across a 0.025 range	45
3.15	A schematic of the Run I ATLAS TDAQ. Data flow is depicted by black arrows and message flow by red. The L2 and the EF run separate sets of algorithms on the data. Applications running in this system are configured under segments that make up a partition	47
3.16	A flow-chart showing data flow in a partition at ANL’s test bed	48
3.17	A flow-chart showing Configuration 1 of the partition. This configuration was used to determine the optimal values of the parameters in Table 3.3 by producing the plots in Figures 3.18, 3.19 and 3.20	51
3.18	Plot showing the number of Cores maxes the rate at 25. The number of cores available on ustb13, ustb21 and ustb12 sums up to 20. An additional data point would show that the Number of Cores maxes at 20	52
3.19	Plot showing the processing time less than 3 ms is not physical. Above that, it makes sense that the rate would decrease	52
3.20	Plot showing the number of threads assigned to the HLTSV	53
3.21	Flow chart showing configuration for running the partition without the RoIB. The HLTSVApplication host generates random numbers in place of data. The HLTSVApplication was (25,5,4). The DCMs and the HLTSVApplication were run on the test bed’s most powerful PCs. 68 kHz was achieved by this configuration	53

3.22	Flow chart showing Configuration 2 . The only difference between this configuration and the one on the left is that there is an additional DCM node (ustb4). The rate was boosted to 107 kHz by adding this node. The HTTSV can therefore achieve 100 kHz if it runs on a capable PC .	54
3.23	Plot showing rate variation with the number of threads. At 7 number of threads the rate is highest and the most stable. The error bars show the instability	55
3.24	Illustrations of 3 variations of Configuration 2	57
3.25	Configuration 3: The RoIB is added and real data fragments are read. The rate maxes at 55 kHz with 1 RoIB input (see Table 3.4)	58
3.26	Plots showing rate variations under several configurations. Each plot shows rates recorded independently but under Configuration 3. Differences between versions A and B are extensively discussed in the text. These large variations are still not understood, but they are only observed when the HTSVApplication is running of 32-bit PCs. Their averages are entered in Table 3.4	59
4.1	Parton distribution functions obtained from the MSTW group. This image was obtained from Ref. [71]	61
4.2	Feynman diagram for the exclusive Higgs boson production	63
4.3	An illustration of the parton shower development, hadronization and hadron decays. Taken from Ref [75]	66
5.1	Illustration of perigee parameters. The most common of these are d_0 and z_0 . The perigee may be defined relative to either the beam-line or the interaction point. The analysis in Chapter 7 utilizes this choice. Illustration taken from Ref [96]	70
5.2	Illustration of track fitting in the MS. A track fit to an MDT can be any of 4 cases: track path coincides with drift circle (on track), is smaller than drift circle (out of time), is larger than drift circle (δ -electron), and no drift circle (hole). Track quality is evaluated by the multiplicity of these cases.	71
5.3	Plots of electron identification efficiencies during Run 1, binned in E_T , and η . Taken from Ref [101]	76
5.4	Plots of electron reconstruction efficiencies during Run 1, binned in E_T , and η . Taken from Ref [101]	77
5.5	Plots of the invariant mass of the ee system in $J/\psi \rightarrow e^+e^-$ and $Z \rightarrow ee$ events in data, calibrated and uncalibrated Monte Carlo simulation. Taken from Ref [102]	78
5.6	Plots of the muon identification efficiencies, binned in p_T . $Z \rightarrow \mu\mu$ events were used for high p_T muons while $J/\psi \rightarrow \mu^+\mu^-$ events were used for low p_T muons	80

5.7	Plots showing comparisons of $m_{\mu\mu}$ distributions for muons from $J/\psi \rightarrow \mu^+\mu^-$ events in data, MC in which muon p_T is corrected and MC in which p_T is not corrected	82
5.8	Plots showing the pileup density ρ , the pileup contribution to jet p_T , at several number of vertices N_{PV} for jets reconstructed from LCW topological clusters	86
5.9	Plots showing the jet energy response for simulated LCW jets reconstructed with the anti-kt algorithm at $R= 0.4$ is plotted against p_T^{true} and $ \eta_{det} $. Taken from Ref [109]	87
5.10	Plots showing the JVF distributions for pileup jets and jets from the primary vertex (hard-scatter), evaluated for the primary vertex. Taken from Ref [112]	88
5.11	Plots showing distributions of variables used to correct for JVF's dependence on the number of reconstructed vertices, and hence number of pileup tracks, in an event. The distributions from pileup and hard-scatter jets are overlayed. The simulated jets are reconstructed with the LCW scale and the jet energy scale is applied. Taken from Ref [112]	89
5.12	Plots showing the fake rate from pileup jets versus efficiency hard scatter jets for JVF, corrJVF, R_{p_T} , and JVT. JVT uses a kNN model in corrJVF- R_{p_T} space where 100 neighbors determine whether a jet is from pileup or from hard scatter. Taken from Ref [112]	90
5.13	Plots showing the MV2c10 BDT output, taken from Ref [115]	92
5.14	Plots showing the b -jet efficiency and c -jet rejection parametrized with jet p_T , for the MV2c10 (2016 config) and the MV2c20 (2015 config) algorithms, at a 77% b -jet selection efficiency working point. Taken from Ref [115]	93
5.15	Plots showing distributions of E_T^{miss} in data, compared to predictions from Monte Carlo distributions, taken from Ref [117]	99
5.16	Plots showing distributions of E_T^{miss} in data, compared to predictions from Monte Carlo distributions, taken from Ref [118]	101
6.1	Leading order Feynman diagrams for the charged Higgs boson production	103
6.2	Leading order Feynman diagrams for $t\bar{t}$ production at the LHC. Taken from Ref [129]	104
6.3	Leading order Feynman diagrams for single top quark production at the LHC. Taken from Ref [129]	104
6.4	Plots of the efficiencies of several E_T^{miss} -based triggers, obtained from simulation of signal with $m_{H^+} = 200$ GeV	109
6.5	$N-1$ distributions after the full selection criteria have been applied. The black vertical line marks the point at which the variable being plotted is cut on	110

6.6	E_T^{miss} and m_T distributions in the control region used to measure trigger efficiencies. Since trigger thresholds studied were at minimum $E_T^{\text{miss}} = 70$, disagreements in the low E_T^{miss} and low m_T regions did not have significant impact on measurements	111
6.7	Plots showing trigger efficiency fits	112
6.8	Plot showing the probability of an electron to fake a $\tau_{\text{had-vis}}$, parametrized in η	113
6.9	Plots showing the comparison of estimations using direct MC versus the FF method	115
6.10	Plots showing m_T distributions in the multi-jet and the $W + \text{jets}$ control regions	116
6.11	Plots showing the measured FF parametrized in $\tau_{\text{had-vis}} p_T$	116
6.12	FF closure plots in the multi-jet measurement control region	117
6.13	FF closure plots in the $W + \text{jets}$ control region	118
6.14	FF closure plots in the $t\bar{t}$ control region	118
6.15	Plots showing kinematic distributions in the $t\bar{t}$ control region	120
6.16	Plots showing kinematic distributions in the $W + \text{jets}$ control region . .	121
6.17	Plots showing m_T distributions with variation in jet BDT score selection criteria	123
6.18	p_b illustration from a distribution of $f(q b)$ and an observed q_{obs} in data	127
6.19	Plots showing the m_T and E_T^{miss} distributions in the signal region	128
6.20	Plots showing distributions of $\tau_{\text{had-vis}} p_T$, number of reconstructed jets, number of b-tagged jets and the angular separation between the $\tau_{\text{had-vis}}$ and E_T^{miss} , in the signal region	129
6.21	Plots showing distributions of $\tau_{\text{had-vis}} \eta$ and ϕ in the signal region	130
6.22	Plots of the expected and observed limits on $\mu = \sigma_{H^+}^{Obs}$, without including systematic uncertainties in the background and signal predictions	132
6.23	Plots of the expected and observed limits on $\mu = \sigma_{H^+}^{Obs}$. Systematic uncertainties were included in the background and signal predictions . .	133
7.1	Leading order Feynman diagram for the exclusive Higgs production	135
7.2	Plots showing the expected signal and background distributions after pre-selection	139
7.3	Plots showing the preliminary expected m_T distributions in the signal region, minus the m_T selection	141
7.4	Plots showing the number of tracks matched to the electron (left) and the muon (right) tracks	143
7.5	Illustration of the geometry of the exclusivity selection criteria	143
7.6	Plot of the efficiency of the exclusivity selection, extracted from the exclusive Higgs boson signal simulation, is plotted against the average number of interactions per beam crossing μ	144

7.7	The rejection of $Z \rightarrow \mu\mu$ between data and simulation. Simulated samples are normalized to the data. Circles are before Δz_0^{iso} was applied, and squares are after Δz_0^{iso} was applied	145
7.8	Plots showing the exclusive (1.0 mm) di-muon $p_T^{\mu\mu}$ distributions predicted and observed. The highest bin includes overflow. No scale factors are applied to elastic or SD or DD predictions	148
7.9	Plots of acoplanarity distributions for elastic, SD, DD and Drell-Yan each normalized to the data	148
7.10	Plots of dimuon acoplanarity distributions after applying the exclusivity selection and requiring $p_T^{\mu\mu} < 3$ GeV. The expected Drell-Yan shape and the elastic and combined SD and DD (Dissociative) shapes normalized from the fit are stacked. This fit determines the factor f_{EL}	149
7.11	Plots of absolute Δz_0 of the extra track to the lepton vertex in the region defined by acoplanarity < 0.0015 . The exclusivity requirement was changed to select exactly one extra track within 3 mm. The exclusive predictions are scaled by a factor of 0.70	150
7.12	Plots of the dilepton invariant mass distribution for muon candidates (left) and electron candidates (right). The elastic yield is scaled by $f_{\text{EL}} = 0.76$ and the SD distribution is scaled to bring the sum of the elastic and SD contributions to the HERWIG++ prediction for the elastic process multiplied by the f_γ factor in the mass region above 160 GeV. The last bin includes overflow	152
7.13	Plots showing $m_{e\mu}$, $\Delta\phi_{e\mu}$, m_T and $p_T^{e\mu}$ distributions in an inclusive W^+W^- -rich region	154
7.14	Plots showing $m_{e\mu}$, $\Delta\phi_{e\mu}$, m_T and $p_T^{e\mu}$ distributions in the inclusive W^+W^- -rich region	156
7.15	Plots showing $m_{e\mu}$, $\Delta\phi_{e\mu}$, m_T and $p_T^{e\mu}$ distributions in the exclusive W^+W^- validation region	158
7.16	Plots showing $m_{e\mu}$, $\Delta\phi_{e\mu}$, m_T and $p_T^{e\mu}$ distributions in the $Z \rightarrow \tau\tau$ validation region	160
7.17	Plots showing $m_{e\mu}$, $\Delta\phi_{e\mu}$, m_T and $p_T^{e\mu}$ distributions in the signal region, minus the selection criteria for the variable being plotted	162

List of Tables

2.1	A list of fermions and their properties.	5
-----	--	---

2.2	List of bosons. ‘Multiplicity’ column is the number of types that a boson appears as. A gluon appears in 8 forms of different color-anticolor combinations. The gluon is the only boson that has a color charge.	6
3.1	Values of some of LHC parameters during Run I (2010→2012) and Run II (2015→16). The design values are also listed.	27
3.2	Linux run PCs on the ANL Test Bed. They have diversely varying CPU strength and hardware structure, so some custom-made cards can only be installed on specific computers. <i>HT</i> stands for hyperthreading. The cores are the total number of cores in all the physical CPUs. FILAR and TILAR cards transmit data fragments from the RoIB to the HLTSV. The QUEST cards supplies data fragments to the RoIB. Although ustb1, ustb3 and ustb10 are the most powerful, none can host any custom cards because they have a very thin structure.	49
3.3	Parameters that have the most impact on the HLTSV rate in a partition.	50
3.4	Summary of HLTSV rates for all tested configurations in all releases of the tdaq software. The <i>v</i> next to a rate indicates that the rate recorded is an average over multiple rates because of the large rate variations. Version A and B of software differ over the number of buffers available to the FILAR card; 100 for A and 16 for B. For tdaq 05-02-00 the buffer size is 1. There is a general increase in the rate from tdaq 05-02-00 to tdaq 05-03-00.	56
3.5	Summary of HLTSV rates with the RoIB in all releases of the tdaq software using the TILAR card. The configuration is similar to Configuration 3, but with HLTSVApplication running on ustb11. The large variations in rates were still observed so there was nothing wrong with the FILAR card.	56
3.6	Summary of HLTSV rates with the RoIB in version B of tdaq 05-03-00 using the FILAR card. The configuration is similar to Configuration 3, but with HLTSVApplication running on ustb11. The average rates observed are larger than those observed with a TILAR card as shown in Table 3.5.	56
5.1	Selection criteria for tracks from the Inner Detector that are matched to τ -jet candidates.	95
6.1	Selection criteria for physics objects.	106
6.2	Signal region definition. Additionally, measures were taken to ensure that events originated from inelastic pp collisions and no jets originated from unwanted experimental effects.	107
6.3	Experimental systematic uncertainties.	122
6.4	Theoretical systematic uncertainties on the signal acceptance (in %) due to the QCD scale. The factorization scales are varied by a factor of 2 for up and down variations.	124

6.5	Theoretical systematic uncertainty on the signal acceptance due to choice of parton shower and underlying event tune.	124
6.6	Expected event yields in the signal region, compared to observed event yields from data.	128
6.7	Description of each of the nuisance parameters, along with the samples they were applied to. If the same nuisance parameter was applied to different backgrounds, all correlations were kept. A ‘✓’ indicates that the systematic uncertainty was considered and included in the fit. A ‘✗’ indicates that the systematic uncertainty was considered but not included in the fit, otherwise the given systematic uncertainty is not applied to the given background.	131
6.8	Impact of various sources of uncertainty on the expected 95% CL exclusion limit.	133
7.1	Electron isolation criteria.	137
7.2	Muon isolation criteria.	138
7.3	Event selection criteria.	141
7.4	Measured $f_{n_{trk}}^{sim}$ values for several different Monte Carlo generators, under different exclusivity settings. Exclusivity window sizes other than 1 mm were used to study the impact of systematic variations on the results. . .	146
7.5	Ratio of the exclusivity selection efficiency in Drell-Yan $\mu^+\mu^-$ production as a function of dimuon mass of different generators to SHERPA. Only statistical uncertainties are shown. The statistical uncertainty from SHERPA is included and contributes 2.9%, 0.8%, 0.7% and 5.7% in the four mass regions.	147
7.6	Summary of background yields in the control region used to correct POWHEG+PYTHIA8’s prediction of inclusive W^+W^- processes.	154
7.7	Selection criteria for the region used to study inclusive W^+W^- events.	155
7.8	Event yields in the inclusive W^+W^- -rich region.	156
7.9	$Z \rightarrow \tau\tau$ validation region definition.	159
7.10	Most important sources of systematic uncertainties and their contribution to the event yields. The largest ones come from estimates of background. Dashed lines imply that the source was not directly applicable to that particular process.	160
7.11	List of all systematic uncertainties associated with the reconstruction of physics objects. Chapter 5 discusses methods with which these uncertainties were calculated. The individual uncertainties were assumed to be uncorrelated so they were added in quadrature.	161

7.12	Summary of signal and background yields at different stages of the Higgs boson event selection. Only major background sources are listed explicitly. All the other background sources are summed up in the ‘Other’ category. For the background, the uncertainties are only shown for the yields after exclusivity selection, where they are relevant for the measurement. They include the systematic and statistical components, added in quadrature.	162
7.13	Upper limits on σ_H [pb] at 95% CL. The $\pm 1\sigma$ and $\pm 2\sigma$ uncertainties quoted here are on the expected upper limit.	163

Chapter 1

Introduction

Driven by the curiosity to understand the universe and the desire to manipulate matter in our universe to make lives better for the whole humanity, scientists have been trying to understand matter's fundamental building blocks and the interactions between them for over a millennium. While studies of components of the universe can be traced back to the ancient Greek society,¹ the introduction of the Quantum Theory in the early 1900s, when the atom was thought to be the fundamental building block of matter, was revolutionary. Scattering experiments by Ernest Rutherford, Hans Geiger and Ernest Marsden showed that atoms have a positive nucleus, debunking the theory that the atom was fundamental. The first of many proposals on the Quantum Theory were put forward by Max Planck and Albert Einstein, suggesting that radiation may be quantized. Arthur Compton's scattering experiments confirmed these proposals when he discovered X-rays in 1923.

This pattern of seemingly radical theoretical proposals followed by a series of experimental verifications was to be repeated over several decades, discovering more particles as candidates for fundamental building blocks of matter and forming a new branch of physics – Particle Physics. This culminated to the Standard Model (SM) [1, 2], a model that classifies fundamental particles into bosons and fermions.

While the SM summarizes the well known fundamental particles and their forces, it has also been used to predict existence of other particles. Its most recent successful prediction is the existence of the Higgs boson, which was discovered in 2012 from data collected from proton-proton scattering experiments at the Large Hadron Collider [3] (LHC).

As with most models, the SM has its failures. One of the most prominent is its inability to solve the *hierarchy problem*. Simply stated, the hierarchy problem encapsulates the uneasiness with which most scientists take the fact that the strength of the weak force is 10^{24} times that of the gravitational force. In the SM, this problem appears in the form of the unexpectedly small size of the Higgs field strength. One proposed solution is to fine-tune parameters of the SM to moderate this field strength. Done by itself, a fine-tuning of 1 part in 10^{30} on SM parameters is required. Such level of fine-tuning seems a bit contrived. Supersymmetric theories attempt to reduce

¹Thales of Miletus (500-547 B.C) postulated that water is the basic substance of the Earth.

this level of fine-tuning by postulating additional particles with quantum numbers supersymmetric to particles in the SM. With these supersymmetric particles, the level of fine-tuning is reduced to 1 part in 100. So far none of these supersymmetric particles have been observed in scattering experiments.

Several Minimal Supersymmetric extensions to the Standard Model (MSSM) include these supersymmetric particles. In these extensions, the SM Higgs boson is a member of a family comprising five physical Higgs bosons. No evidence has been observed for the existence of any of these Higgs bosons. Part of this thesis discusses work done towards a search for one of these Higgs bosons using data collected by scattering protons at the LHC.

This thesis is divided into two parts. First, a search for the charged Higgs boson (H^\pm), a member of the MSSM Higgs sector, is described. Second, a search for a particular production mode for the SM Higgs boson, called diffraction, is discussed. A brief introduction to diffraction is presented in the next few paragraphs, and its link to *exclusive* processes is explained. Detailed discussions of exclusive processes and the theoretical framework underlying MSSM are presented in Chapter 2. The experimental setup, simulations, and reconstruction of physics objects are presented in Chapters 3, 4, and 5. Chapters 6 and 7 discuss searches for the MSSM H^\pm and the exclusive SM Higgs bosons, respectively.

The units used in this thesis, while conventional in the particle physics community, may seem unusual. Here, natural units are used, where quantities are measured in terms of physical constants such as the speed of light c and the Planck constant \hbar . To achieve this, c and \hbar are normalized such that $c = \hbar = 1$. In this system, Einstein's famous energy-mass relation becomes $E = m$. So, energy has the same units as mass – electron-volts (eV). This formalism significantly simplifies algebraic equations. In scattering experiments the likelihood of an event happening is quantified by the event's cross section, denoted by σ . Cross sections, being a measure of area, are quantified in units of *barns*.

As already alluded to earlier, both the SM Higgs boson and the MSSM H^\pm are expected to be produced at high energies. For the work presented in this thesis, protons were scattered at the LHC at very high energies to provide such an environment. While scattering experiments have been conducted since the early 1900s, the LHC provides scattering energies at unprecedented scales. For example, in 2015 and 2016, protons were accelerated to 6.5 TeV before being scattered against protons of the same energy moving in the opposite direction. In experiments of this kind, the scattering energy of concern is that which is measured in the rest frame, where the total momentum is zero. For beams with momenta \vec{p}_1 and \vec{p}_2 the square of the center of mass energy, s , is defined as

$$s = (p_1 + p_2)^2 = (E_1 + E_2, \vec{p}_1 + \vec{p}_2)^2 \quad (1.1)$$

where p_i are relativistic 4-momenta defined as $p_i = (E_i, \vec{p}_i)$. In the LHC case $\vec{p}_1 = -\vec{p}_2$ and $E_1 = E_2$, simplifying Equation 1.1 to $s = 4E_1^2$. For $E_1 = 6.5$ TeV the center of mass energy is 13 TeV.

The advantage of scattering two beams with opposing and equal momenta over scattering a high energy beam with a fixed target can be made obvious by further examining Equation 1.1. Suppose the fixed target is a proton, with rest mass m_p . Suppose also that the high energy beam is made up of protons of the same rest mass. The square of the center of mass energy for this system becomes

$$s = (E_1 + m_p, \vec{p}_1 + \vec{0})^2 = E_1^2 + m_p^2 + 2E_1 m_p - |\vec{p}_1|^2 = 2m_p^2 + 2E_1 m_p. \quad (1.2)$$

For $E_1 = 6.5$ TeV the center of mass energy is obviously less than in the former case. What is more interesting is that for $E_1 = 13$ TeV, and $m_p = 0.938$ GeV the center of mass energy is lower than 0.2 TeV. So, to reach $\sqrt{s} = 13$ TeV, a fixed target proton experiment needs a proton beam of about 90 000 TeV!

A search for an exclusively produced SM Higgs boson is motivated chiefly by the need to perform precision measurements on the Higgs boson in an environment with as little background contamination as possible. In diffractive processes protons may be elastically scattered, emerging from the collision intact. While in some cases one or both protons may disintegrate, the remnants from the disintegration fall in a region outside the detector phase space. In both cases, the diffractively produced Higgs boson is in principle isolated from activity other than that from its production. Such a *clean* mode of production is necessary in order to minimize systematic uncertainties when measuring the Higgs mass, spin or coupling strengths to other particles. Part of this thesis sets limits to the production cross section of the exclusive SM Higgs boson using data collected LHC collisions in 2012.

Chapter 2

Theoretical Framework

A theoretical framework for elementary particles is introduced and discussed in detail in this chapter, in the form of the Standard Model (SM). Fundamental particles that the SM predicts are presented, along with their quantum numbers and other properties. SM is formally constructed from concepts borrowed from relativistic and quantum theories. Motivation for the existence of a neutral Higgs boson is introduced from spontaneous symmetry breaking. Supersymmetry is presented as a possible solution to one of the hierarchy problem. Through this lens, a family of Higgs bosons is presented in the Two-Higgs Doublet Model (2HDM), an extension of the Standard Model; the charged Higgs boson (H^\pm) is presented as a member of this family. Finally, diffractive production¹ of the neutral SM Higgs is explored in the context of proton-proton scattering experiments.

2.1 The Standard Model

2.1.1 Overview of the Standard Model

Elementary particles in the SM are classified into *fermions* and *bosons*. Fermions are grouped into leptons and quarks, all of which are spin-1/2. All elementary bosons are spin-1, except for the Higgs boson which is spin-0. The bosons mediate interaction between the fermions by transmitting and conserving quantum numbers. Each quark and lepton has an antiparticle, which has the same mass as the original particle but different quantum numbers.

Leptons and quarks are each grouped into 3 generations, totalling 6 fermion generations. Leptons (or quarks) in a generation have the same quantum numbers as the other generations, but different masses. The lightest lepton generation is made of the *electron* (e) and its neutrino (ν_e). The heaviest lepton generation comprises the *tau* (τ) and its neutrino (ν_τ), the τ lepton being heavier than the e by 3 orders of magnitude. The lightest quark generation is made of the *up* (u) and *down* (d) quarks while the heaviest is made up of the *top* (t) and *bottom* (b) quarks – the t is about 90000 times heavier than the u . In the SM neutrinos are assumed to be massless but

¹Diffractive production is also referred to as exclusive production in this thesis.

recent experimental observations of their oscillation have confirmed that they have non-zero mass [4]. These observations have set an upper bound of 2 eV on the masses of each of the neutrinos. Table 2.1 lists the properties of these neutrinos and other fermions.

	Generation	Name	Symbol	Electric Charge	Mass
Leptons	First	Electron	e	-1	0.5 MeV
		Electron Neutrino	ν_e	0	< 2 eV
	Second	Muon	μ	-1	105.7 MeV
		Muon Neutrino	ν_μ	0	< 2 eV
	Third	Tau	τ	-1	1.8 GeV
		Tau Neutrino	ν_τ	0	< 2 eV
Quarks	First	Up	u	+2/3	2.3 MeV
		Down	d	-1/3	4.8 MeV
	Second	Charm	c	+2/3	1.3 GeV
		Strange	s	-1/3	95 MeV
	Third	Top	t	+2/3	173.5 GeV
		Bottom	b	-1/3	4.65 GeV

Table 2.1. A list of fermions and their properties.

There are 4 types of interactions in nature, mediated by 4 types of forces. All of them are included in the SM except for the gravitational force. The strength of the gravitational force is proportional to the product of the masses of the interacting particles. At the scale of elementary particle masses, the strength of gravity can be assumed to be negligible compared to the strength of any of the other three types of interactions. The W^+ boson mediates the *weak* force, and the W^- is its antiparticle. These bosons are massive and carry a positive and negative electric charge respectively. The Z also mediates the weak force. It is massive and carries no electric charge. The *photon* (γ) mediates the *electromagnetic* force, and it is its own antiparticle. It is massless and carries no electric charge. The Z , W^\pm and γ bosons can interact with each other. The electromagnetic and weak forces are therefore combined into the *electro-weak* force. There are 8 *gluons* (g) that mediate the *strong* force. Each is massless and carries two units of the *color* charge – one is positive and

the other is negative. A unit color charge can be either blue, red or green. Since the gluons can exchange color, they can also interact among themselves.

The *Higgs* boson is a quantum of the Higgs field, which is due to the Higgs mechanism. The Higgs field gives masses to the massive bosons described in the preceding paragraph, and all the fermions. The Higgs boson is spin-0, and does not carry any electric charge.

Table 2.2 lists all the bosons described above and their properties.

Interaction Type	Symbol	Multiplicity	Electric Charge	Mass
Weak	W^\pm	2	± 1	91.2 GeV
	Z	1	0	80.4 GeV
Electromagnetic	γ	1	0	0
Strong	g	8	0	0
Mass	H	1	0	125.4 GeV

Table 2.2. List of bosons. ‘Multiplicity’ column is the number of types that a boson appears as. A gluon appears in 8 forms of different color-anticolor combinations. The gluon is the only boson that has a color charge.

The SM has successfully predicted many particles. Most recently, the Higgs boson was discovered by scattering experiments at the Large Hadron Collider using the ATLAS and CMS detectors [5], after it was added to the SM over 50 years ago. In 1983, evidence for W^\pm and Z bosons was observed using data from the UA1 [6] and UA2 experiments [7]. Gluons were discovered by the TASSO [8] and PETRA [9] collaborations in 1979. While the top quark was discovered rather late, in 1995 at Fermilab [10] near Chicago, the charm and bottom quarks were indirectly discovered in the 1970s.

Some of the SM’s shortfalls have already been hinted in the preceding paragraphs. One of the most glaring shortfall is that the SM does not include the gravitational force. It also predicts neutrinos to be massless, while several experiments have placed lower limits on their masses. The hierarchy problem, which motivates some of the work done for this thesis, has also not been fixed by the SM. Stated simply, it is unsettling that the weak force is 10^{24} times as heavy as the gravitational force. This discrepancy has undesired effects on the size of the Higgs field strength. This thesis sheds more light on the possibility of super-symmetry as a solution to this problem.

2.1.2 Building the Standard Model

In natural units,² the SM represents fermions and bosons by fields ψ that are functions of space-time $x = (t, \vec{x})$. These fields' kinetic and potential energies are in turn represented by a Lagrangian that operates on them – the Lagrangian is made up of kinetic and potential terms. Transformation of fields is governed by symmetries. The Lagrangian is required to be invariant upon several symmetry transformations.

Probabilities of particle interactions have been shown to diverge in some limiting cases of energy and distance [11]. This undesirable behavior is kept in check by renormalizing the model at meaningful energy and distance scales [12]. After renormalization schemes have been applied the SM Lagrangian can be separated into a component responsible for the strong and electroweak interactions. Here, the electromagnetic and weak interactions have been combined into the electroweak interaction (EWK); reasons will become clearer as the SM takes shape. Since the strong interaction is facilitated by color exchanges, its component is called the *Quantum Chromodynamics (QCD)* term. Overall, the SM Lagrangian can be written compactly as

$$\mathcal{L}_{SM} = \mathcal{L}^{QCD} + \mathcal{L}^{EWK}. \quad (2.1)$$

2.1.2.1 Quantum Chromodynamics (QCD)

As mentioned before, quarks and gluons carry a charge called color. This charge can take either of 3 states: red, green or blue. Conservation of this charge dictates the behavior of quarks and gluons. $SU(3)_C$, the multiplicative group of all unitary transformations in the color space, is the simplest group that represents rotations. \mathcal{L}^{QCD} is required to be invariant under $SU(3)_C$ symmetry transformations. The generators of the group are the 8 3×3 hermitian matrices denoted by $\lambda_a/2$. For quarks represented by the scalar fields $\psi(x)$ the Lagrangian

$$\mathcal{L}_q = i\bar{\psi}(x)\gamma^\mu D_\mu\psi(x), \quad (2.2)$$

where the γ^μ are the Dirac γ -matrices, is invariant under local $SU(3)$ transformations. Here, $D_\mu \equiv \partial_\mu + ig_s A_\mu^a \lambda_a/2$ where g_s is the strong coupling constant³ that is usually written as $\sqrt{4\pi\alpha_s}$ and $A_\mu = A_\mu^a \lambda_a/2$, a gauge field invariant under $SU(3)$ rotations. The gauge field A_μ^a represents a gluon with a color combination a , so terms in the Lagrangian with both A_μ^a and $\psi(x)$ represent interaction between gluons and quarks; the accompanying factors represent the coupling strength of such an interaction. For example, the interaction term in Equation 2.2 can be expanded into

$$\mathcal{L}_{int} = -\sqrt{4\pi\alpha_s} \left(\bar{\psi}_j(x) A_\mu^a \frac{\lambda_a^{ji}}{2} \gamma^\mu \psi_j(x) \right) \quad (2.3)$$

²Natural units dictate that $c = \hbar = 1$. See Chapter 1

³Not purely constant, as will be shown soon.

where α_s has replaced g_s and the $\frac{\lambda_a^{ji}}{2}$ term ensures that the quark changes color from i to j after the interaction with a gluon. Figure 2.1 illustrates this interaction term as a quark-gluon *vertex*, where q represents the quark flavor.

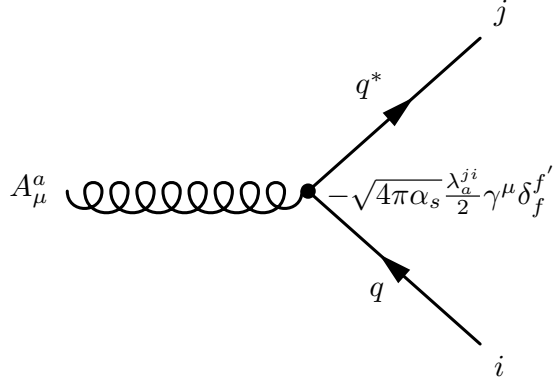


Figure 2.1. Feynman diagram of a quark-gluon vertex.

To include the propagation of gluons in space-time in the model a term \mathcal{L}_g is added using the field strength tensor $F_a^{\mu\nu} = \partial^\mu A_a^\nu - \partial^\nu A_a^\mu - \sqrt{4\pi\alpha_s} f^{abc} A_b^\mu A_c^\nu$. Here, f^{abc} are the structure constants for the $SU(3)$ group.⁴ A more compact definition of the gluon propagation term is

$$\mathcal{L}_g = -\frac{1}{4} F^{\mu\nu a} F_{\mu\nu a}. \quad (2.4)$$

This term includes terms of orders two, three and four in A_μ^a . Terms of order two are kinetic terms representing propagation of gluons in space and time. Terms of orders three and four represent gluon self interaction. Figures 2.2(a) and 2.2(b) illustrate these interactions as gluon vertices.

The coupling strength α_s is dependent on the energy scale μ_R^2 at which the theory is renormalized. Normally, a cutoff energy (Λ_{QCD}) above which the theory becomes non-perturbative is imposed as well. The dependence is described by

$$\alpha_s(\mu_R^2) = \frac{4\pi}{\beta_0 \log\left(\frac{\mu_R^2}{\Lambda_{QCD}}\right)} \text{ where } \beta_0 = \frac{33 - 2n_f}{3}, \quad (2.5)$$

Here, n_f is the number of quark/gluon types taking part in the interaction. For $n_f < 16$, $\alpha_s \xrightarrow{\text{large } \mu_R^2} 0$ and $\alpha_s \xrightarrow{\text{small } \mu_R^2} \infty$. This implies that at large enough energies quarks and gluons can move freely. At these energies summation of diagrams such

⁴These encode the commutation relations between the $\lambda_a/2$ matrices.

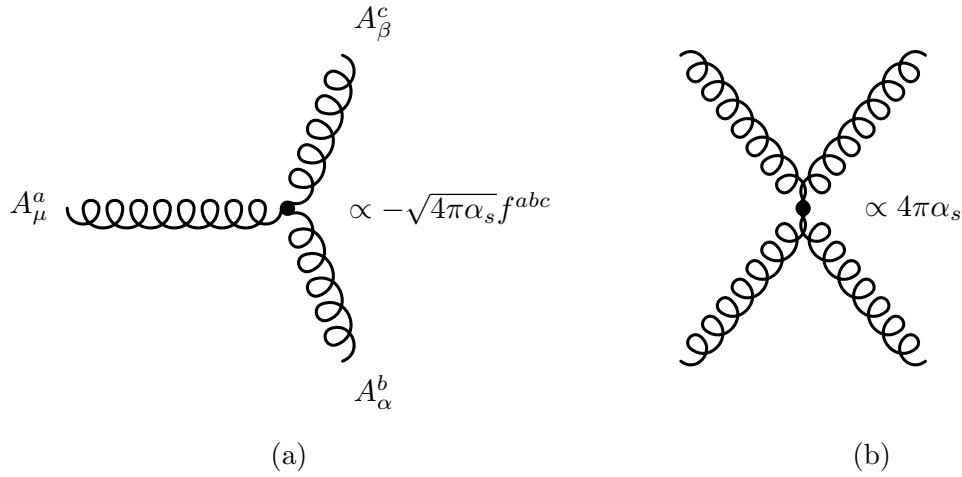


Figure 2.2. Feynman diagrams of gluon-gluon vertices.

as those in Figure 2.2(b) can be done perturbatively, ignoring higher order diagrams. At low energies quarks and gluons are strongly coupled together and cannot move freely. In this scenario, perturbation theory is not applicable. This is why QCD is best studied at high energy colliders where approximations of these energy scales can be reached. The phenomena at these two limiting cases are known as *asymptotic freedom* and *confinement* respectively. Their practical treatment will be revisited in later chapters.

2.1.2.2 Electroweak Theory

Fermions that interact through the electroweak force are grouped into left- and right-handed, depending on their chirality. Chirality is an intrinsic property of fermions, and it is an eigenvalue of the Weyl operator γ_5 [13] on the fermion fields. Left handed fermions are represented by field doublets $\psi_1(x) = \begin{pmatrix} q \\ q' \end{pmatrix}_L$ or $(\begin{pmatrix} \nu_l \\ l \end{pmatrix})_L$ where q, q' are the up and down type quarks respectively, and l, ν_l are leptons. Right-handed fermions are singlets $\psi_2(x) = q_R$ or ν_{lR} , and $\psi_3(x) = q'_R$ or l_R . So, overall, all the fermions are represented as

$$\psi(x) = \sum_{j=1}^3 \psi_j(x). \quad (2.6)$$

$SU(2)$ is the simplest group that accommodates doublets so it is used to partly describe $\psi_1(x)$ transformations. Generators in this group are the weak isospin operators $\hat{I} = i\sigma_j/2$, where the σ_j are the Pauli matrices with $j \in [1, 3]$. $SU(2)_L$ is therefore a multiplicative group of all unitary rotations in the isospin space. $U(1)$, a group of rotations in the complex space, is sufficient to describe singlet transformations so it

is used to describe all components of ψ . Generators of this group are the complex numbers iY_j , where Y is the hypercharge and $j \in [1, 3]$. $U(1)_Y$ is therefore a group of rotations in the complex hypercharge space. The free⁵ Lagrangian

$$\mathcal{L}_{\text{free}} = \sum_{j=1}^3 i\bar{\psi}_j(x)\gamma^\mu D_\mu \psi_j(x) \quad (2.7)$$

is required to be invariant under local $SU(2)_L \times U(1)_Y$ transformations. The scalar fields for the fermions are required to transform as

$$\begin{aligned} \psi_1(x) &\rightarrow \psi'_1(x) = \exp(iY_1\beta(x)) \exp(i\sigma_1\alpha(x)/2) \psi_1(x) \\ \psi_2(x) &\rightarrow \psi'_2(x) = \exp(iY_2\beta(x)) \psi_2(x) \\ \psi_3(x) &\rightarrow \psi'_3(x) = \exp(iY_3\beta(x)) \psi_3(x) \end{aligned} \quad (2.8)$$

with $SU(2)_L$ imposed only on the doublets. The derivatives D_μ transform as

$$\begin{aligned} D_\mu \psi_1(x) &= [\partial_\mu - ig\widetilde{W}_\mu(x) - ig'y_1B_\mu(x)]\psi_1(x), \\ D_\mu \psi_2(x) &= [\partial_\mu - ig'y_2B_\mu(x)]\psi_2(x), \\ D_\mu \psi_3(x) &= [\partial_\mu - ig'y_3B_\mu(x)]\psi_3(x), \end{aligned} \quad (2.9)$$

with $\widetilde{W}_\mu(x) = \sigma_i W_\mu^i(x)/2$ is an $SU(2)$ matrix field. Transformations of the gauge fields B_μ, \widetilde{W}_μ are fixed for $D_\mu(x)\psi_j(x)$ to transform exactly like the $\psi_j(x)$. The g and g' parameters are the coupling constants corresponding to the $SU(2)$ and $U(1)$ groups respectively.

Kinetic terms of the gauge fields are built from the gauge field tensors $B_{\mu\nu}, \widetilde{W}_{\mu\nu}$ defined as

$$\begin{aligned} B_{\mu\nu} &= \partial_\mu B_\nu - \partial_\nu B_\mu, \\ \widetilde{W}_{\mu\nu} &= \frac{\sigma_i}{2} [\partial W_\nu^i - \partial_\nu W_\mu^i + g\epsilon^{ijk}W_\mu^j W_\nu^k] \end{aligned} \quad (2.10)$$

to get

$$\mathcal{L}_{kin} = -\frac{1}{4}B_{\mu\nu}B^{\mu\nu} - \frac{1}{4}W_{\mu\nu}^i W_i^{\mu\nu}. \quad (2.11)$$

Because the $W_{\mu\nu}^i$ term contains a quadratic piece, \mathcal{L}_{kin} gives rise to cubic and quartic gauge self interactions whose coupling strengths are governed by g . The full free Lagrangian is obtained by adding the \mathcal{L}_{kin} term to Equation 2.7 to get

⁵The term ‘free’ is meant to describe a simple case where the fermions are not subject to any type of potential. Introduction of a potential to the Lagrangian leads to other interesting features.

$$\mathcal{L}_{free} = \sum_{j=1}^3 i\bar{\psi}_j(x)\gamma^\mu D_\mu\psi_j(x) - \frac{1}{4}B_{\mu\nu}B^{\mu\nu} - \frac{1}{4}W_{\mu\nu}^i W_i^{\mu\nu} = (D_\mu\psi)^\dagger D^\mu\psi. \quad (2.12)$$

A mass term \mathcal{L}_{mass} is not added because it destroys the gauge symmetries. Interaction terms included in Equation 2.12 can be expanded into

$$\mathcal{L}_{int} = g\bar{\psi}_1(x)\gamma^\mu \widetilde{W}_\mu \psi_1 + g' B_\mu \sum_{j=1}^3 Y_j \bar{\psi}_j \gamma^\mu \psi_j \quad (2.13)$$

where the term with \widetilde{W}_μ can in turn be expanded into

$$\widetilde{W}_\mu = \frac{\sigma^i}{2} W_\mu^i = \frac{1}{\sqrt{2}} \begin{pmatrix} \sqrt{2}W_\mu^3 & W_\mu^\dagger \\ W_\mu & -\sqrt{2}W_\mu^3 \end{pmatrix} \quad (2.14)$$

The term containing \widetilde{W}_μ gives rise to fermion interactions with a gauge boson $W_\mu = (W_\mu^1 + iW_\mu^2)/\sqrt{2}$ and its conjugate W_μ^\dagger . These are identified as the W^+, W^- bosons. To first order the Lagrangian component for the interaction of left-handed leptons l, ν_l and quarks q, q' with the W^\pm bosons can be expanded into

$$\mathcal{L}_{W_{bosons}} = \frac{g}{2\sqrt{2}} W_\mu^\dagger \left(q\gamma^\mu(1-\gamma^5)q' + \bar{\nu}_l\gamma^\mu(1-\gamma^5)l \right) \quad (2.15)$$

leading to vertices shown in Figure 2.3.

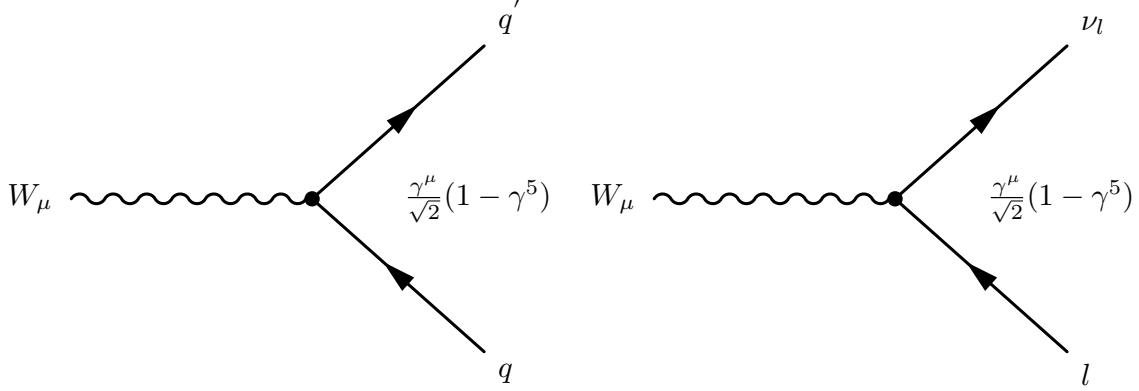


Figure 2.3. Feynman diagrams of left handed fermion- W^\pm vertices.

Linear combinations of W_μ^3 and B_μ form the Z^0 and the γ bosons, represented by Z_μ and A_μ respectively. They are also included in Equation 2.13 and generalized as

$$\begin{pmatrix} A_\mu \\ Z_\mu \end{pmatrix} = \begin{pmatrix} \cos \theta_W & \sin \theta_W \\ -\sin \theta_W & \cos \theta_W \end{pmatrix} \begin{pmatrix} B_\mu \\ W_\mu^3 \end{pmatrix} \quad (2.16)$$

Given that the electromagnetic charge operator is Q , that the electromagnetic charge is e and $T_3 = \sigma_3/2$, the A_μ definition is fixed by

$$g \sin \theta_W = g' \cos \theta_W = e \text{ and } Y = Q - T_3. \quad (2.17)$$

The first equation links the $SU(2)_L, U(1)_Y$ coupling constants to the electromagnetic coupling constant. The second equation fixes the fermion hypercharge, electromagnetic charge, and isospin quantum numbers. Figure 2.4 illustrate the γ, Z^0 interactions with fermions, where Q_f indicates electromagnetic charge operation on a fermion of flavor f .

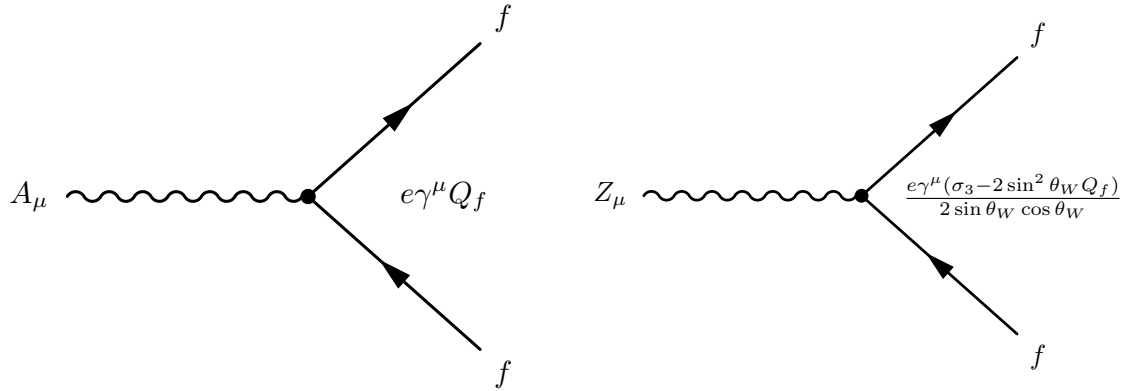


Figure 2.4. Feynman diagrams of fermion- Z/γ vertices.

Equation 2.11 also generates gauge self-interactions, shown in Figure 2.5.

2.1.2.3 Spontaneous Symmetry Breaking (SSB) and the Higgs Mechanism

As discussed earlier, the W^\pm and Z gauge bosons are massive, but the theory built so far describes them as massless. The starting point for giving mass to these gauge bosons is to explore the effects of introducing an $SU(2)_L$ doublet of scalar fields $\phi(x) = \begin{pmatrix} \phi^+ \\ \phi^0 \end{pmatrix}$, where the ϕ^0 is the ground state, and a potential $V = -(\mu^2 \phi^\dagger \phi + h(\phi^\dagger \phi)^2)$. The minimum of this potential is taken as the ground state of the system. This vacuum has to be unique. This is because all the other states are computed as perturbations from the vacuum. The parameters μ, h are free and their boundary conditions can also be explored. $h < 0$ represents an unphysical potential. $h > 0$ and $\mu^2 > 0$ has a trivial minimum at $\phi = 0$. Interesting conditions are when $h > 0$ and

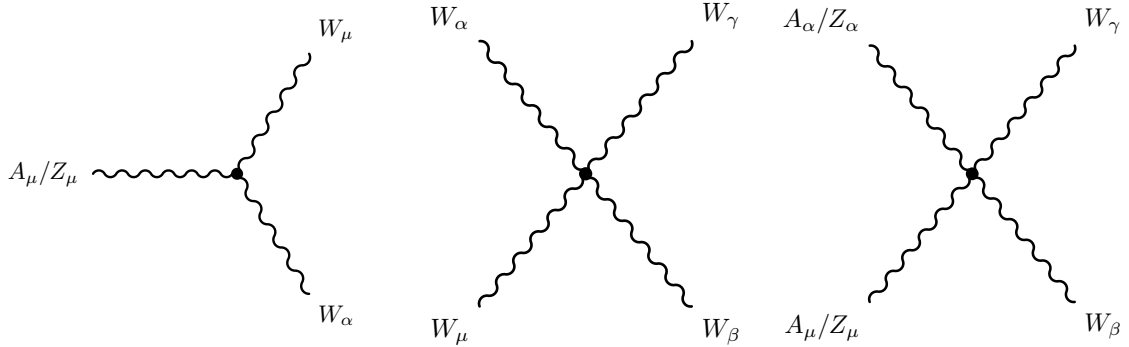


Figure 2.5. Feynman diagrams showing self gauge interactions in the electroweak theory.

$\mu^2 < 0$. When V is added to Equation 2.12, the not-so-free Lagrangian, still invariant under $SU(2)_L \times U(1)_Y$ transformations, becomes

$$\mathcal{L} = \mathcal{L}_{\text{free}} + V, \text{ where } h > 0, \mu^2 < 0. \quad (2.18)$$

V , with the free parameters restricted to conditions quoted in Equation 2.18 has a ground state ϕ^0 with $|\langle 0 | \phi^0 | 0 \rangle| = \sqrt{\frac{-\mu^2}{2h}} \equiv \frac{v}{\sqrt{2}}$. There is an infinite number of such degenerate states, each invariant under $U(1)$ rotations but no longer invariant under $SU(2)_L \times U(1)_Y$. When one of these is chosen, the system is said to have acquired a vacuum expectation value (VEV). Here, the symmetry group that any of the ground states is invariant under, is denoted by $U(1)_Q$ to indicate that its generator Q is different from the original hypercharge and isospin generators Y, I . The Q represents electromagnetic charge and it is defined as $I_3 + Y/2$. Since the ground state is invariant under a symmetry different from \mathcal{L} 's symmetry, $SU(2)_L \times U(1)_Y$ is said to be *spontaneously broken* to $U(1)_Q$. More specifically, 3 $SU(2)_L \times U(1)_Y$ generators are broken and one $U(1)_Q$ generator is unbroken. This mechanism is called *spontaneous symmetry breaking (SSB)*. The Goldstone Theorem [14] states that for every generator broken during SSB, the theory must contain a massless boson – a Goldstone boson. For the SM Lagrangian, three Goldstone bosons are expected to appear after SSB.

To generalize SSB the scalar doublet fields introduced above can be generalized as

$$\phi(x) = \exp\left(i\frac{\sigma_j}{2}\theta^j(x)\right) \frac{1}{\sqrt{2}} \begin{pmatrix} 0 \\ v + H(x) \end{pmatrix} \quad (2.19)$$

where the Goldstone bosons are represented by $\theta^j(x)$. The $H(x)$ is a real scalar field. The $\theta^j(x)$ fields can be eliminated from the Lagrangian by choosing an appro-

priate orientation in the ground state since the fields are still invariant under $U(1)$ rotations. The kinetic piece of Equation 2.18 becomes

$$(D_\mu \phi)^\dagger D^\mu \phi \text{ with } D_\mu \equiv \partial_\mu - \frac{ig'}{2} Y B_\mu - ig I_i W_\mu^i \quad (2.20)$$

where W_μ^i for $i \in [1, 3]$ are associated with eliminating the 3 Goldstone bosons through appropriate orientation adjustments and B_μ is associated with the unbroken $U(1)$ symmetry. Expanding this term shows that

$$\begin{aligned} W_\mu^\pm &= \frac{W_\mu^1 \mp i W_\mu^2}{\sqrt{2}} \text{ gain masses } M_{W^\pm}^2 = \frac{1}{4} g^2 v^2, \\ M_Z^2 &= \frac{M_W^2}{\cos^2 \theta_W} \text{ and } M_\gamma = 0. \end{aligned} \quad (2.21)$$

SSB has effectively introduced masses to the massive gauge bosons and no mass to γ owing to the unbroken $U(1)_Q$ symmetry. The most precise measurement of M_{W^\pm} to date was performed using data collected by the CDF II detector: 80.385 ± 0.016 GeV [15]. Similarly, the most precise measurement of M_Z is a combination result from LEP experiments: 91.1876 ± 0.0021 GeV [16]. Expanding the kinetic energy term shows that a new particle, a neutral Higgs boson corresponding to the field H , with mass $\sqrt{2\hbar v}$ is introduced. The mechanism with which the gauge bosons gain mass and a neutral Higgs boson appears is called the *Higgs Mechanism*.

2.1.3 The Higgs Boson

The mass of the Higgs boson was a free parameter in the Standard Model until July 2012, when it was measured to be 125.09 ± 0.24 GeV [17] from data collected by LHC experiments. While several of its interaction modes have already been observed, the SM predicts that it couples to gauge bosons, at tree level or through a loop, and to fermions.

Figure 2.6 shows the allowed Higgs vertices and their coupling strengths. For interactions with massive gauge bosons the coupling strengths are proportional to the square of the gauge boson mass. For interactions with fermions the coupling strengths are proportional to the fermion mass m_f . The coupling strengths with fermions are called Yukawa couplings. Through SSB, fermions gain mass from interacting with the Higgs field.

From the discussion in the preceding section, it is clear that the Higgs field does not interact with massless bosons. The Higgs boson however, couples indirectly to the massless bosons – γ and gluon. Figure 2.7 shows some of the one loop Feynman diagrams through which the Higgs boson interacts with photons and gluons.

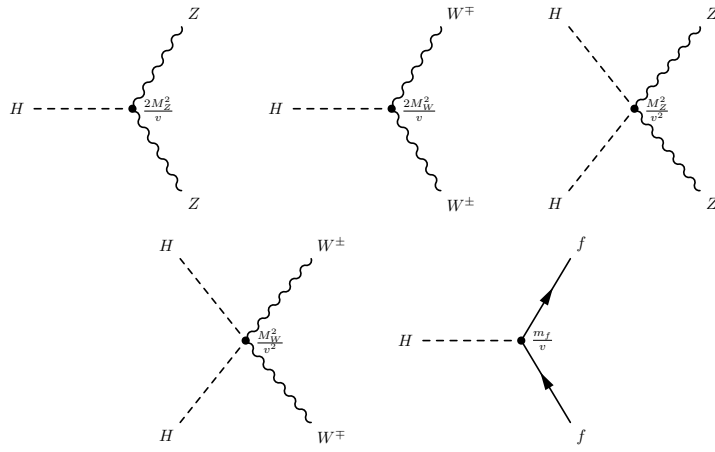


Figure 2.6. Feynman diagrams showing SM neutral Higgs boson vertices with Z and W^\pm .

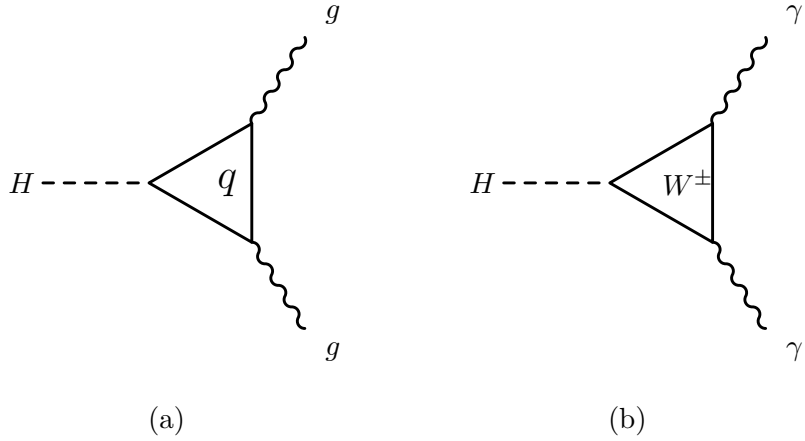


Figure 2.7. Feynman diagrams showing SM neutral Higgs boson vertices with photons and gluons.

2.1.3.1 Production and decay of the Higgs boson in pp collisions

During a pp collisions the Higgs boson may be produced from gluon and quark interactions, through any of the vertices described above. The main production modes, where V represents a W^\pm or a Z , are

1. gluon fusion (ggF) : $gg \rightarrow H$; an inversion of the diagram in Figure 2.7(a);
2. vector boson fusion (VBF) : $q\bar{q} \rightarrow VVq\bar{q} \rightarrow Hq\bar{q}$;
3. associated production with a vector boson : $q\bar{q} \rightarrow VH$.
4. and associated production with top : $gg, q\bar{q} \rightarrow t\bar{t}H$;

The diagrams for these production modes are shown in Figure 2.8. Figure 2.9(a) shows distributions of cross sections for all the production modes, when the protons

are collided at an energy of 8 TeV, versus the mass of the Higgs boson. For a 125 GeV Higgs boson, the ggF production mode significantly dominates, followed by VBF. Other production modes have significantly lower cross sections.

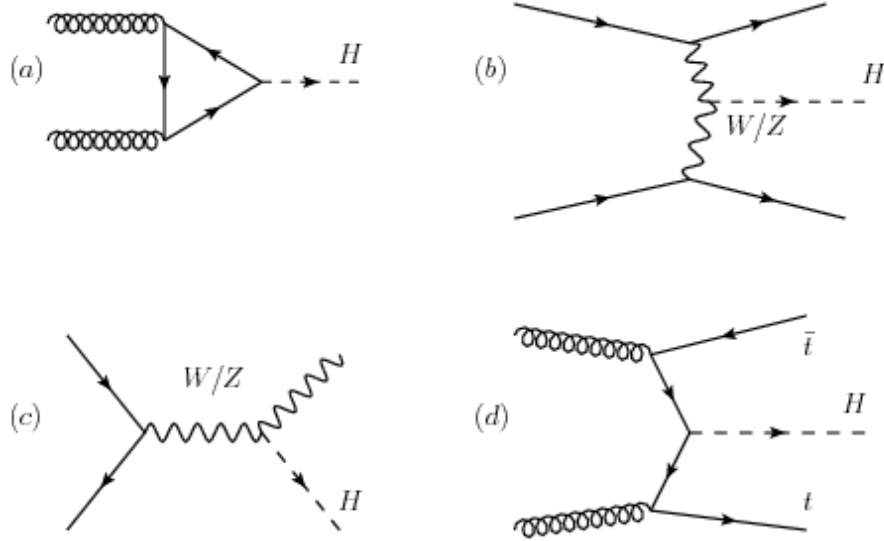


Figure 2.8. Feynman diagrams showing SM neutral Higgs boson production modes in pp collisions. Taken from Ref [18].

The Higgs boson can decay through any of the vertices discussed already. Figure 2.9(b) shows distributions of the branching fractions for these decay modes, plotted against the Higgs boson mass. At 125 GeV, the most dominant decay mode is $b\bar{b}$, followed by WW . Although $b\bar{b}$ is dominant, most experiments search for the Higgs boson through the WW decay mode because the former suffers from significantly larger backgrounds than the latter. As a matter of fact, the analysis presented in this text searches for evidence of the Higgs boson through the WW decay channel. This discussion will be revisited in Chapter 7.

2.2 Exclusive Particle Interactions

2.2.1 Overview of exclusivity or diffraction

pp collisions can be grouped into two categories: *elastic* and *inelastic*. During elastic collisions the two protons scatter and emerge out of the collision intact. During inelastic collisions either one or both protons may dissociate after collision. Remnants of dissociation eventually fragment and hadronize, as discussed in detail in Section 4.1.

Diffraction is a term widely used in optical experiments, where a beam of light is separated into its multiple components by frequency or wavelength. It is important

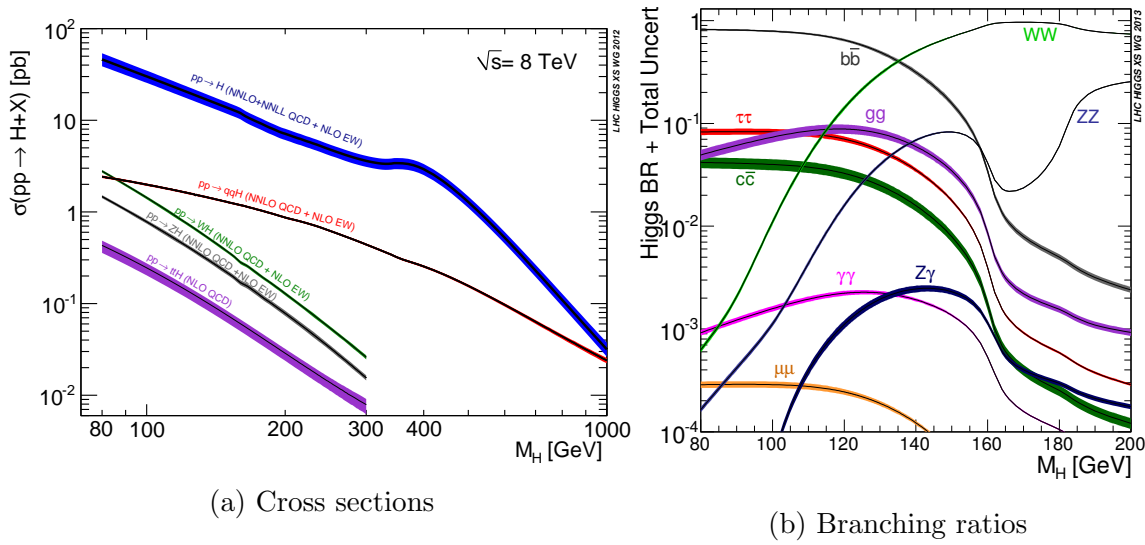


Figure 2.9. Plots showing distributions of expected cross sections for SM Higgs boson production modes in pp collisions, and branching ratios for its decay modes, plotted against the Higgs mass. Taken from Ref [19].

to note that in that usage the sum of the components is exactly the same as the original beam of light. In pp collisions, the term diffraction is used to refer to cases where no quantum numbers from the two protons are exchanged during the collision, such that the outgoing particles are just components of the incoming protons. More precisely, a virtual particle is exchanged during the pp collision. Elastic processes are trivially diffractive. Inelastic processes may or may not be diffractive.

Although the pp collision may be at high energy, the actual momentum exchanged during the scattering in diffractive processes is by comparison small. In that sense, diffractive processes fall in the ‘soft’ energy regime where perturbative QCD does not apply. The Regge Theory [20] was the first attempt at modelling this phenomenon.⁶ Here, the amplitude of the diffractive scattering is given by the sum of all possible virtual exchange particles. The most dominant of these virtual particles in this theory is known as the *Pomeron*. Several models have since substituted this pomeron with other options. One such model is discussed in Section 2.2.2.

Inelastic diffractive processes in which one of the protons dissociates is known as Single Dissociation (SD). Inelastic diffractive processes in which both protons dissociate is known as Double Dissociation (DD). In this text, elastic, SD and DD processes are collectively referred to as *exclusive*. The motivation behind this nomenclature will become clear in Section 2.2.2.

During an exclusive pp collision photons may be exchanged. This exchange does not change the original quantum numbers of the colliding protons. With large enough

⁶It is important to note that this theory has since been replaced by QCD.

momentum, the photons may interact to form a pair of W^\pm ($pp(\gamma\gamma) \rightarrow ppWW$) bosons through one of the vertices shown in Figure 2.5. Such a quartic gauge coupling is interesting. Efforts have been made to measure its cross section. This process may be elastic, SD or DD. Figure 2.10 illustrates these possibilities, where X represents the remnants of proton dissociation.

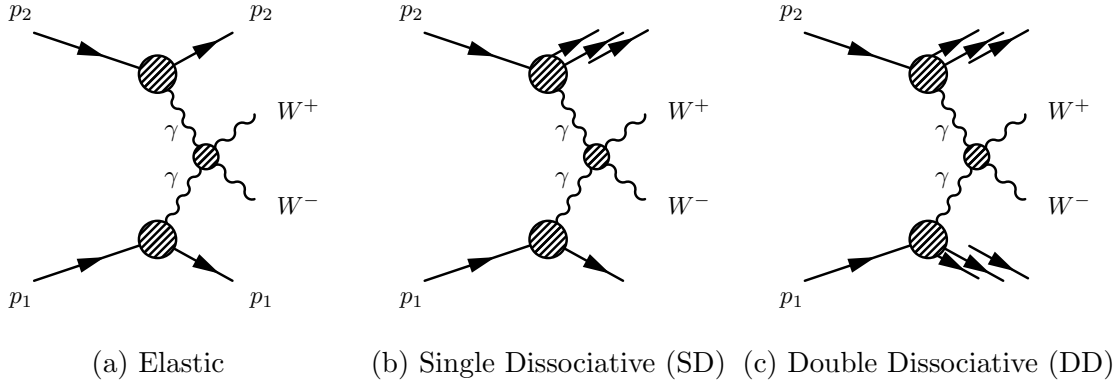


Figure 2.10. Diagrams showing exclusive processes through photon exchanges, producing a pair of W^\pm bosons.

The cross section for the $pp(\gamma\gamma) \rightarrow ppWW$ process shown in Figure 2.10 is calculated using the equivalent photon approximation (EPA) [21, 22]. In EPA the photons are described by equivalent photon distributions $f(x)$. $f(x)$ is the probability of a photon that carries a fraction of proton energy x to be emitted by the proton during the pp collision. The cross section $\sigma_{pp(\gamma\gamma) \rightarrow ppWW}^{\text{EPA}}$ is then

$$\sigma_{pp(\gamma\gamma) \rightarrow ppWW}^{\text{EPA}} = \iint f(x_1)f(x_2)\sigma_{\gamma\gamma \rightarrow WW}(m_{\gamma\gamma}^2)dx_1dx_2 \quad (2.22)$$

where $m_{\gamma\gamma}$ is the center of mass energy of the two-photon system. This formulation has been used in several experiments to describe exclusive dilepton⁷ results [23–26].

2.2.2 Production of the exclusive Higgs boson

With enough shared momentum during a diffractive pp collision, a 125 GeV Standard Model Higgs boson (see Section 2.1.3) can be created through an exchange of either photons or gluons. From the production cross sections shown in Figure 2.9(a) the exchange of gluons is much more preferable than the exchange of photons. The interaction between the Higgs boson and the gluons is done through a top quark loop. Since exchange of gluons would alter the quantum numbers of the initial and final

⁷Replace the W^\pm -pair with leptons in Figure 2.10.

state protons, another gluon is exchanged during the collision to neutralize the overall color. The Feynman diagram in Fig. 2.11 illustrates this process.

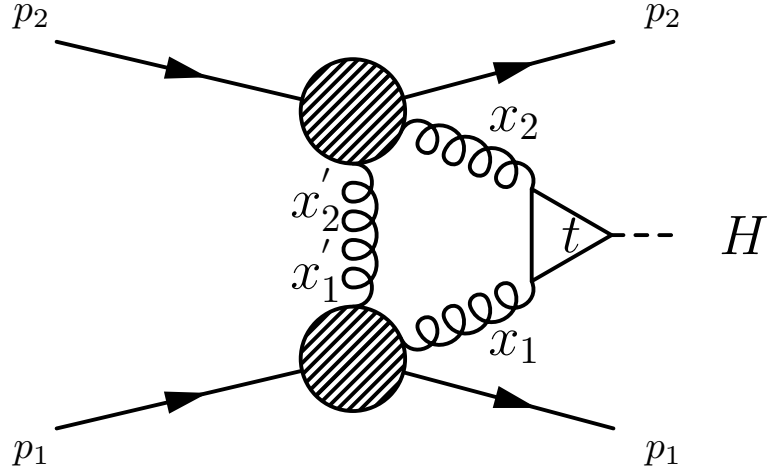


Figure 2.11. Feynman diagram showing the production of the exclusive Higgs boson.

The Khoze-Martin-Ryskin (KMR) model [27] calculates the cross section for this process, and formulates it as

$$\sigma_{pp(gg) \rightarrow ppH} \propto \hat{\sigma}(gg \rightarrow H) \left(\int \frac{dQ_t^2}{Q_t^4} f_g(x_1, x_1', Q_t^2) f_g(x_2, x_2', Q_t^2) \right)^2. \quad (2.23)$$

Here, $\hat{\sigma}(gg \rightarrow H)$ is the cross-section for the gluon fusion process that produces the Higgs boson. This quantity can be read directly from Figure 2.9(a). The functions f_g [28] are the generalized gluon densities for the finite proton size, that take into account the impact parameter. The variables x_1 and x_2 are the fractions of the momenta carried by the gluons that contribute to the production of the Higgs boson, with respect to the momenta of the protons p_1 and p_2 . The variables x_1' and x_2' are the fractions of the momentum carried by the exchanged third gluon with respect to the momenta of the protons p_1 and p_2 as shown in Fig. 2.11. These gluon densities are integrated over the exchanged (third) gluon transverse momentum Q_t .

For a 125 GeV Standard Model Higgs boson in all decay modes, a total production cross-section of 3 fb is predicted when the protons collide at center-of-mass energy 8 TeV. The decay modes for the exclusive Higgs boson are the same as those discussed in Section 2.1.3.1, and the branching ratios are identical to those shown in Figure 2.9(b). The analysis discussed in Chapter 7 conducts a search for events in

which an exclusive Higgs boson is created in pp collision at a center-of-mass energy of 8 TeV.

2.3 Minimal Supersymmetric Standard Model

The hierarchy problem alluded to in Chapter 1 induces a discrepancy in the predicted and observed Higgs boson masses. To match the observed Higgs mass, the SM has to be fine-tuned by subtracting semi-divergent terms from the Lagrangian. To reduce this fine-tuning, the Minimal Supersymmetric Standard Model (MSSM) [29] postulates that for each particle predicted by the SM there exists a super-partner with different quantum numbers. Adding such particles does reduce the level of fine-tuning required on the SM and moderates corrections to the Higgs mass. In this framework, the Higgs boson becomes a member of a family of Higgs bosons, and is referred to as h .⁸ In this specification, MSSM is referred to as hMSSM [30]. In addition to h , hMSSM predicts 4 more Higgs bosons: two charged H^\pm , one CP-even H , and one CP-odd A .

2.3.1 Two-Higgs-Doublet Model

One of the models that predict a family of Higgs bosons is the Two-Higgs-Doublet Model (2HDM) [31]. The phenomenology of this model is categorized into two classes: type-I and type-II. The type-II model corresponds to the hMSSM. MSSM is built on two Higgs doublet fields

$$\begin{aligned} \phi_1 &= \begin{pmatrix} \phi_1^+ \\ \phi_1^0 \end{pmatrix} \text{ with VEV } \langle \phi_1 \rangle = \frac{v_1}{\sqrt{2}}, \text{ and,} \\ \phi_2 &= \begin{pmatrix} \phi_2^+ \\ \phi_2^0 \end{pmatrix} \text{ with VEV } \langle \phi_2 \rangle = \frac{v_2 e^{i\theta}}{\sqrt{2}}. \end{aligned} \quad (2.24)$$

In type-I 2HDM all fermions couple to one of the Higgs doublets, while in type-II up-type quarks couple to a different doublet from down-type quarks. Following the strategy used to construct SSB in the preceding section, the doublet fields can be generalized as

$$\begin{aligned} \phi_1 &= \begin{pmatrix} \phi_1^+ \\ \frac{h_1 + v_1 + ig_1}{\sqrt{2}} \end{pmatrix}, \\ \phi_2 &= \begin{pmatrix} \phi_2^+ \\ \frac{h_2 + v_2 e^{i\theta} + ig_2}{\sqrt{2}} \end{pmatrix}. \end{aligned} \quad (2.25)$$

The total Lagrangian for the system is $\mathcal{L} = \mathcal{L}_{kin} + \mathcal{L}_{pot} + \mathcal{L}_{Yukawa}$, which is a sum of kinetic, potential and Yukawa terms. \mathcal{L} is required to conserve both charge

⁸In preceding sections h was represented by H . Apologies for the expected confusion.

and charge-parity (CP) symmetries, just like the Lagrangian in the SM. The potential term, $\mathcal{L}_{pot} = \langle \phi^\dagger | V | \phi \rangle$ is built by

$$V = -\mu_1^2 \hat{A} - \mu_2^2 \hat{B} + h_1 \hat{A}^2 + h_2 \hat{B}^2 + h_3 (\hat{C}^2 + \hat{D}^2) + h_5 \hat{A} \hat{B} \quad (2.26)$$

where

$$\hat{A} \equiv \phi_1^\dagger \phi_1, \hat{B} \equiv \phi_2^\dagger \phi_2, \hat{C} \equiv \Re(\phi_1^\dagger \phi_2), \hat{D} \equiv \Im(\phi_1^\dagger \phi_2).$$

This potential is designed to conserve both charge and parity symmetries as well. The μ_i, h_i are free terms that eventually define the Higgs masses. From these parameters the Higgs bosons H, h, A and (H^\pm) emerge. The studies presented in this text are concerned only with H^\pm . Present discussion is therefore limited to H^\pm . Moreover, since the 2HDM Lagrangian is invariant under charge transformations, H^\pm is referred to as H^\pm , ignoring charge.

In this setup both doublets can have real vacuum expectation values (VEVs). The ratio of these VEVs is known as $\tan \beta$. The entire parameter space of this Higgs sector is defined by $\tan \beta$ and the mass of H^\pm , m_{H^\pm} .

The minimum conditions on V give rise to the following solutions

$$\begin{aligned} v_1^2 &= \frac{h_1 - h_2 \pm Z_1}{2(h_1 - h_+)(h_2 - h_+)} \\ v_2^2 &= \frac{h_2 - h_1 \pm Z_2}{2(h_1 - h_+)(h_2 - h_+)} \\ Z_1 &= \sqrt{(h_1 - h_2)^2 - 4(h_1 - h_+)(h_2 - h_+) \left[(h_+ v^2 - \mu_1^2)(h_+ v^2 - \mu_2^2) - \frac{\mu_3^4}{4} \right]} \quad (2.27) \\ Z_2 &= \sqrt{(h_1 - h_2)^2 - 4(h_2 - h_+)(h_1 - h_+) \left[(h_+ v^2 - \mu_2^2)(h_+ v^2 - \mu_1^2) - \frac{\mu_3^4}{4} \right]} \end{aligned}$$

giving rise to the following higgs masses

$$\begin{aligned} m_{H^\pm}^2 &= -h_3(v_1^2 + v_2^2) + \mu_3^2 \frac{v_1^2 + v_2^2}{v_1 v_2} \\ m_{A^0}^2 &= \frac{1}{2} \mu_3^2 \frac{v_1^2 + v_2^2}{v_1 v_2} \quad (2.28) \end{aligned}$$

and

$$\begin{aligned} m_{H^0, h^0}^2 &= h_1 v_1^2 + h_2 v_2^2 + \frac{1}{4} \mu_3^4 (\tan \beta + \cot \beta) \\ &\pm \sqrt{\left[h_1 v_1^2 - h_2 v_2^2 + \frac{1}{4} \mu_3^4 (\tan \beta - \cot \beta) \right]^2 + \left(2v_1 v_2 h_+ - \frac{1}{2} \mu_3^2 \right)^2}. \quad (2.29) \end{aligned}$$

Expanding the potential term of the Lagrangian reveals that H^+ can interact with other Higgs bosons in the sector, with a coupling strength dependent on the VEVs of the doublets, which is $\tan \beta$.

The kinetic term of the Lagrangian is

$$\mathcal{L}_{kin} = (D_\mu \phi_1)^\dagger (D_\mu \phi_1) + (D_\mu \phi_2)^\dagger (D_\mu \phi_2) \quad (2.30)$$

where $D_\mu = \partial_\mu + g L_i W_\mu^i + g' L_4 B_\mu$. The i index runs from 1 to 3. L_i and L_4 are 4×4 matrices. Expanding this term reveals that the charged Higgs boson can also interact with gauge bosons, with vertices such as ZH^+H^- .

Interaction of 2HDM Higgs bosons with fermions is governed by the Yukawa term in the Lagrangian

$$-\mathcal{L}_{Yukawa} = \eta_{ij}^D \bar{Q}_{iL} \phi_1 D_{jR} + \varepsilon_{ij}^U \bar{Q}_{iL} i\sigma_2 \phi_2 U_{jR} + \text{leptonic sector} + \dots \quad (2.31)$$

$\eta_{ij}^0, \varepsilon_{ij}^0$ are non-diagonal 3×3 matrices and i, j denote quark family indices. \bar{Q}_{iL} denote the quark weak isospin left-handed doublets. D_{jR}, U_{jR} denote the up-type and down-type weak isospin right-handed singlets respectively. The leptonic sector is similar to the quark sector. One Higgs doublet couples to the up-type fermions (ϕ_2) and the other couples to the down-type fermions.

2.3.2 The charged Higgs boson

Unlike the Standard Model Higgs boson mass, the charged Higgs boson mass is a free parameter in the 2HDM. As already mentioned, $\tan \beta$ is also a free parameter. Analyses presented in this text scan through the mass of the charged Higgs boson. Expanding Equation 2.31 reveals that couplings to fermions, $g_{H^+}(ud)$, are dependent on $\tan \beta$:

$$g_{H^+}(ud) = m_d \tan \beta (1 + \gamma_5) + m_u \cot \beta (1 - \gamma_5) \quad (2.32)$$

Figure 2.12 shows the allowed vertices between H^+ and fermions, as well as with the SM Higgs boson h .

2.3.2.1 Production & decay in pp collisions

Production of the charged Higgs boson from pp collisions depends on its mass, m_{H^+} . For m_{H^+} less than the mass of the t quark, m_t , the dominant mode of production is through the $t \rightarrow bH^+$ process. For m_{H^+} greater than m_t production of the charged Higgs in association with a top quark is dominant. Figure 2.13 shows such tree-level diagrams. The most dominant process for t production is $gg \rightarrow t\bar{t}$ (known as $t\bar{t}$);

For $m_{H^+} < m_t$ the charged Higgs is produced when one of the t decays to a bottom quark. Clearly $t\bar{t}$ events constitute a major background to the charged Higgs

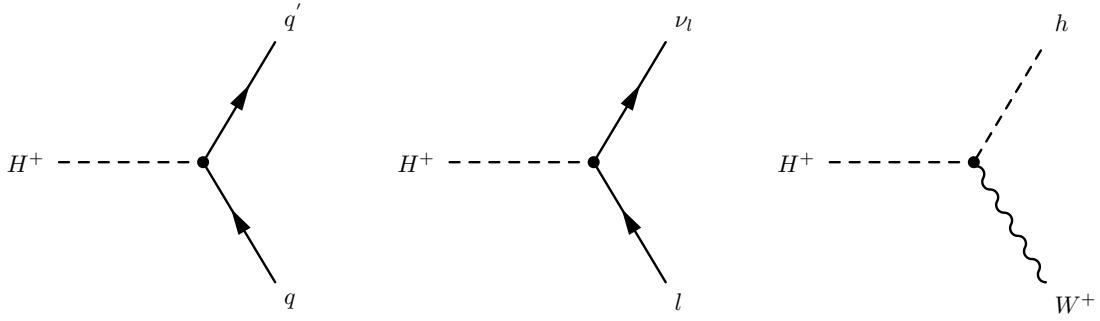


Figure 2.12. Feynman diagrams showing tree level charged Higgs vertices.

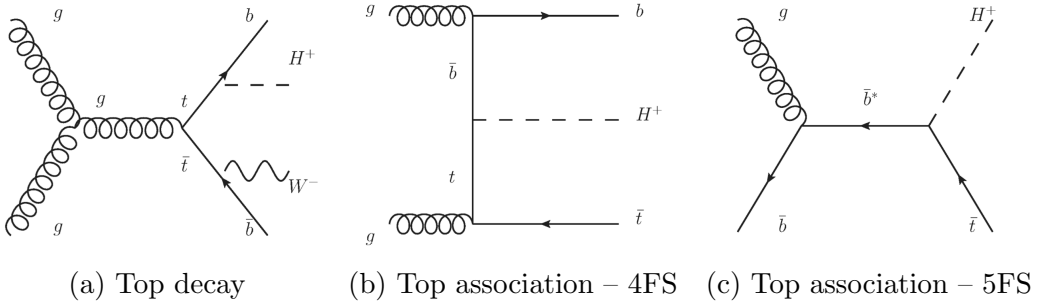


Figure 2.13. Feynman diagrams showing charged Higgs production.

when conducting a search. When calculating amplitudes for these production vertices, the quark family is assumed to contain just 4 flavors of quarks (u, d, c, s). The b quark is included in the models only when it is necessary. For $m_{H^+} > m_t$ production can be through $gb \rightarrow tH^+$. Since the b is included in this process, the scheme is known as the 5-flavor scheme. A 4-flavor scheme is $gg \rightarrow tbH^+$. Using m_t as a boundary, charged Higgs bosons with mass less than 165 GeV are referred to as *light*; those with mass greater than 200 GeV are *heavy*, otherwise they are *intermediate*.

Figure 2.14 shows the total production cross section for a charged Higgs with $m_{H^+} = 200$ GeV plotted against $\tan \beta$, produced at pp collision center-of-mass energy of $\sqrt{s} = 13$ TeV.

The H^+ can decay through any of the vertices in Figure 2.12. Modes with interactions between H^+ and other Higgs bosons in the Higgs sector are very low, so they are ignored. Figure 2.15 shows branching fractions for the significant decay modes for H^+ in the MSSM as a function of m_{H^+} . The $m_h^{\text{mod+}}$ alludes to the fact that h is taken with a mass of 125 GeV, so the branching ratios correspond to an hMSSM scenario at $\tan \beta = 10$ and 50. At both $\tan \beta = 10$ and 50 the dominant decay mode is $t\bar{b}$ for $m_{H^+} > 200$ GeV. This is followed by the $\tau\nu_\tau$ mode, which is in fact more dominant at low m_{H^+} . Due to its low expected background, with at least 10% branching ratio the $\tau\nu_\tau$ mode is more attractive than the $t\bar{b}$ mode due to copious background contamination in the latter. The analysis presented in this text

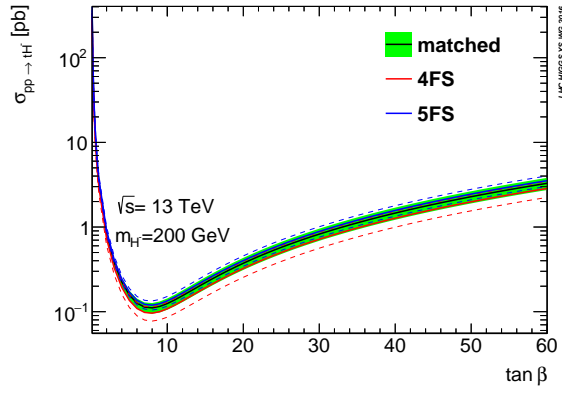


Figure 2.14. Plots of the charged Higgs production cross section against $\tan \beta$ at $\sqrt{s} = 13$ TeV collision energy, for $m_{H^+} = 200$ GeV.

searches for evidence of H^+ through the $\tau\nu_\tau$ mode. This discussion will be revisited in Chapter 6.

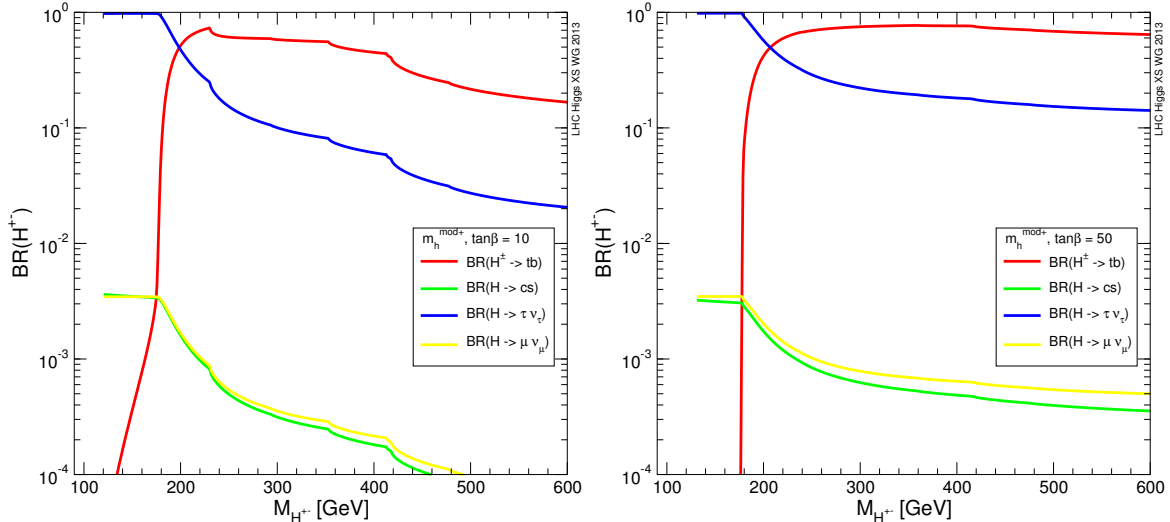


Figure 2.15. Charged Higgs decay branching ratios in the hMSSM scenario, where $m_h^{\text{mod}+}$ alludes to the fact that h is the observed SM Higgs. Left shows $\tan \beta = 10$ and right shows $\tan \beta = 50$.

Chapter 3

Experimental Setup

This chapter introduces the Large Hadron Collider and the ATLAS detector. The Large Hadron Collider is discussed in Section 3.1, and the ATLAS detector is presented in Section 3.2.

3.1 The Large Hadron Collider

The Large Hadron Collider (LHC) [3] is a 27 km-long underground synchrotron designed to accelerate and collide protons. For this reason, it is also referred to as an *accelerator*. It is located in a tunnel on the border of France and Switzerland, in which the Large Electron-Positron (LEP) collider [32] once sat. Designed to accelerate beams of protons to a maximum energy of 7 TeV and to collide them at a total center-of-mass collision energy (\sqrt{s}) of 14 TeV, it is the largest accelerator ever built and collides the most energetic sub-atomic particles to date.

The fundamental principles on which an accelerator operates are complex. Reference [33] provides a detailed introduction to such principles. For a synchrotron built in a tunnel such as the LHC, particles are constrained in the circular path by dipole magnetic fields pointed in and out of the ground. Deviations in the directions parallel to the dipole magnetic fields are controlled by quadrupole magnetic fields. In other words, a series of dipole magnets is used to control circular motion, and a series of quadrupole magnets is used to focus the particles in a narrow aperture. Acceleration of particles is handled by electric fields pointing in the same direction as the particles' direction. In a circular arrangement such as in a synchrotron, these fields cannot be produced by a direct current voltage because the particles will get no overall acceleration over one cycle. Rather, an alternating voltage is used so that while the particles are accelerated at selected points in the circle, they do not decelerate at other points in the circle. These alternating fields are provided by radio-frequency (RF) cavities, whose frequency must always be an integer multiple of the particle revolution frequency. This arrangement causes particles of similar energies to group together, forming bunches of particles rather than a homogenous beam of particles.

The LHC is part of a series of connected particle accelerators that make up the *accelerator complex*, shown by the schematic in Figure 3.1. First, hydrogen atoms are

stripped of their electrons by an electric field in the Linear Accelerator 2 (Linac2) [34]. The resultant protons are accelerated by alternating electric fields due to an RF cavity arrangement in the Linac2. This splits the beam into multiple bunches of protons that eventually emerge from the other end of the Linac2 at 50 MeV into the Proton Synchrotron Booster (PSB) [34]. The PSB uses superconducting dipole and quadrupole magnets to direct the proton bunches in a circular path and focus the beam into an aperture respectively. It also uses an RF cavity arrangement to accelerate the protons and split the beam even further.

Protons emerge from the PSB at 1.4 GeV into the Proton Synchrotron (PS) [34]. The PS is slightly larger than the PSB but the magnet and RF cavity arrangement is similar. The beam is fed into the Super Proton Synchrotron (SPS) [34]. The SPS further splits the proton beam, accelerates the protons to 450 GeV and injects them into the LHC, which finally ramps their energy to 7 TeV. During Run I, the LHC ramped protons to 4 TeV and during Run II it ramped them to 6.5 TeV.¹

The LHC achieves this acceleration through the use of higher-frequency RF cavities. The protons are also kept in the circular tunnel and focused by stronger dipole and quadrupole superconducting magnets respectively. More specifically dipole superconducting magnets, with a current of 11850 A, provides a 8.33 T peak magnetic field. Superconducting quadrupole magnets, with a current of 11870 A, provide a 6.85 T peak magnetic field. 400 MHz RF cavities are used for acceleration, with a total voltage of 16 MV. This setup produces a beam, which is made up of 2808 bunches of length 7.55 cm, of radius 16.7 μm upon collision. With this nominal setup, on average there are 1.15×10^{11} protons in each bunch. During Run I each beam comprised 1374 bunches, and the number of protons in each bunch ranged between $1.6 \rightarrow 1.7 \times 10^{11}$. During Run II each beam comprised 2076 bunches, and the number of protons in each bunch was about 1.18×10^{11} . The number of collisions during each bunch crossing is known as *in-time pileup*, while the number of overlapping collisions from separate bunch crossings is known as *out-of-time pileup*. During Run I and Run II pileup of 40 was observed; the design pileup is 20. Table 3.1 summarizes these parameters.

Red arrows in Figure 3.1 illustrate the proton beam passage through this accelerator complex.

In addition to accelerating protons, the LHC is also accelerates heavy ions. Passage of such ions is illustrated by arrows in Figure 3.1 as well, as defined in the key. Collisions in the LHC are done at 4 points, at which high resolution detectors are built: ATLAS [35] on which the work for this thesis was done, CMS [36], LHCb [37] and ALICE [38].

A major LHC goal is to produce rare physics processes in abundance through proton-proton (pp) collisions. The number of events per second $N_{process}$ during which such rare process are produced is proportional to the cross-section $\sigma_{process}$ of the process in question:

¹Run I and Run II are defined in the Introduction

Parameter	Run I Value	Run II Value	Design Value
Beam Energy [TeV]	4	6.5	7
Bunch spacing [ns]	50	25	25
Protons per bunch	1.7×10^{11}	1.18×10^{11}	1.15×10^{11}
Collisions per bunch crossing	40	40	20

Table 3.1. Values of some of LHC parameters during Run I (2010→2012) and Run II (2015→16). The design values are also listed.

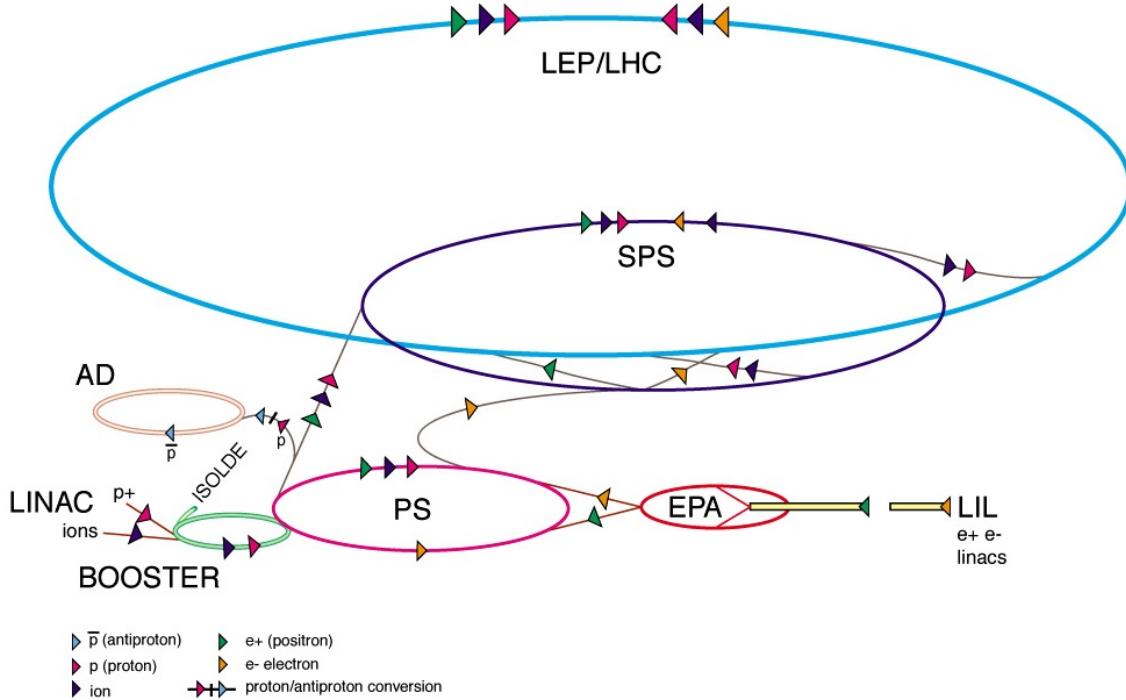


Figure 3.1. The accelerator complex for the LHC. Apart from accelerating protons, the LHC is also used to accelerate and collide heavy ions. Arrows represent the particles' pathway from production to collision, with a key at the bottom left indicating the type of particle.

$$N_{process} = L\sigma_{process} \quad (3.1)$$

where L is a property called *luminosity*. The integral of luminosity over a time of LHC operation T is usually quoted:

$$\mathcal{L} = \int_0^T L dt. \quad (3.2)$$

From Equation 3.1 $N_{process}$ is optimized by either increasing L , $\sigma_{process}$, or both. $\sigma_{process}$ is directly proportional to \sqrt{s} , which is in turn directly proportional to beam energies. To increase $\sigma_{process}$, two options are available:

1. the superconducting dipole magnets used to control the beam's circular path could be upgraded while keeping the circular path constant;
2. or the radius of the LHC could be increased.

Superconductivity in general is a very active area of modern research and the LHC has exploited the most current results. The second option is under serious consideration [39] for future generation colliders. A more feasible strategy to optimize $N_{process}$ would be to optimize L whose parameters are shown in Equation 3.3, rather than $\sigma_{process}$.

$$L \propto \frac{N_b^2 n_b f_{rev} \gamma_r}{4\pi \epsilon_n \beta^*} \quad (3.3)$$

N_b is the number of protons in a bunch, n_b is the number of bunches in a beam, f_{rev} is the beam revolution frequency, γ_r is the relativistic gamma factor at the collision point, ϵ_n is the normalized transverse beam emittance and β^* is the beta function at the collision point. Beam emittance is a measure of the beam size in angular and position phase space. At the LHC it is measured in $\mu\text{m rad}$ and it is not always constant during beam acceleration. In contrast, the normalized beam emittance, ϵ_n , is always constant and therefore more useful in optimizing L . β^* is the width of the beam divided by its emittance. So for low β^* and ϵ_n the chance of protons colliding increases, in turn increasing L .

As the proton beam traverses the collider ring, it forms a current and hence a magnetic field around itself. Upon bunch collision, the colliding protons may be deflected by fields induced by the magnetic fields due to each beam. The beam crossing angle is designed to be kept at $285 \mu\text{rad}$ to tune the protons against these deflections. A larger crossing angle would lead to emittance growth and beam instabilities.

During Run I, the LHC reached $L = 7.7 \times 10^{33} \text{ cm}^{-2}\text{s}^{-1}$. During Run II, reached $L = 1.2 \times 10^{34} \text{ cm}^{-2}\text{s}^{-1}$. Figure 3.2 shows distributions of the peak luminosity during Run II (2016 data-taking period) and during Run I. At the end of Run I the LHC delivered 20.3 fb^{-1} of data and by July 2016 during Run II

3.2 The ATLAS Detector

ATLAS [42] is a multipurpose cylindrical detector built around one of the LHC collision points; this particular collision point is referred to as Point 1 (P1) in this thesis. The ATLAS detector comprises a group of pixel detectors and drift-tubes for tracking, calorimeters for energy measurements, and the muon spectrometer dedicated to muon tracking. The coordinate system used to describe this composite arrangement of sub-detectors is a right-handed one with the origin at the nominal interaction point (IP) in the center of the detector and the z -axis along the beam direction. The x -

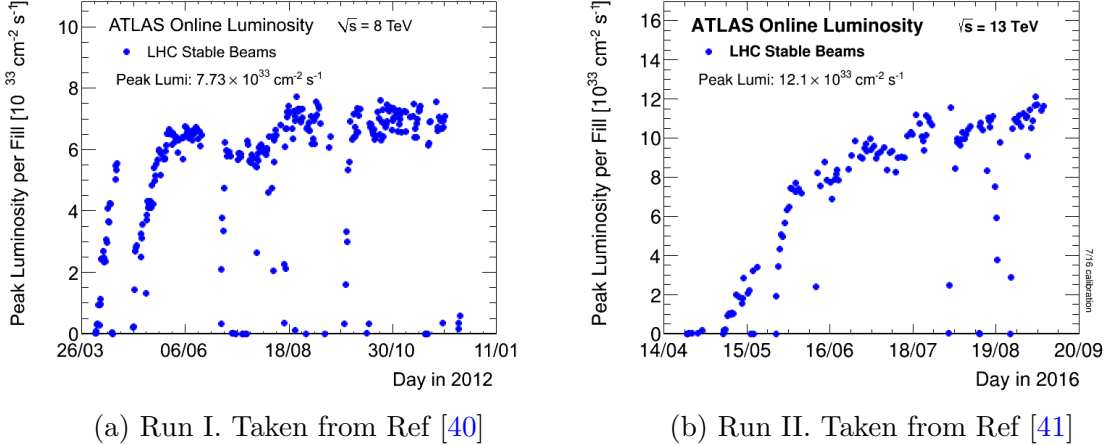


Figure 3.2. Peak luminosity from the LHC during Run I and Run II.

axis points from the IP to the center of the LHC ring and the y -axis points upward. Cylindrical coordinates (r, ϕ) are used in the transverse (x, y) plane, ϕ being the azimuthal angle around the z -axis. The pseudorapidity is defined in terms of the polar angle θ as $\eta = -\ln \tan(\theta/2)$. The angular distance ΔR in the η - ϕ space is defined as $\Delta R = \sqrt{(\Delta\eta)^2 + (\Delta\phi)^2}$. Figure 3.3 illustrates this arrangement.

3.2.1 The Inner Detector

The Inner Detector [43] (ID) is the innermost detector in ATLAS. Its two main goals are to track charged particles, some of which are short-lived, and to determine their transverse momenta, p_T . The first goal is achieved by reconstructing data from three sub-detectors that track the path of any charged ionizing particle. The second goal is achieved by bending the charged particle paths in a 2 T magnetic field due to a superconducting solenoid that surrounds the three aforementioned sub-detectors. In this setup, the ID is therefore incapable of determining the p_T of chargeless particles such as photons. The two innermost sub-detectors are the Pixel Detector [44] and the Semiconductor Tracker [45] (SCT), which both rely on semiconductor technology. The outermost sub-detector is the Transition Radiation Tracker [46] (TRT) and it relies on drift tube technology. The 3 sub-detectors are arranged in concentric cylinders around the IP. These cylinders are called *barrel* components of the sub-detectors. There are also *forward* or *end-cap* components dedicated high- η particle tracking. All-in-all the entire ID structure, including the 2 T solenoid, sits in a 115 cm radius cylindrical cavity with a 7 m total length in the z direction. The ID components are shown in Figure 3.4.

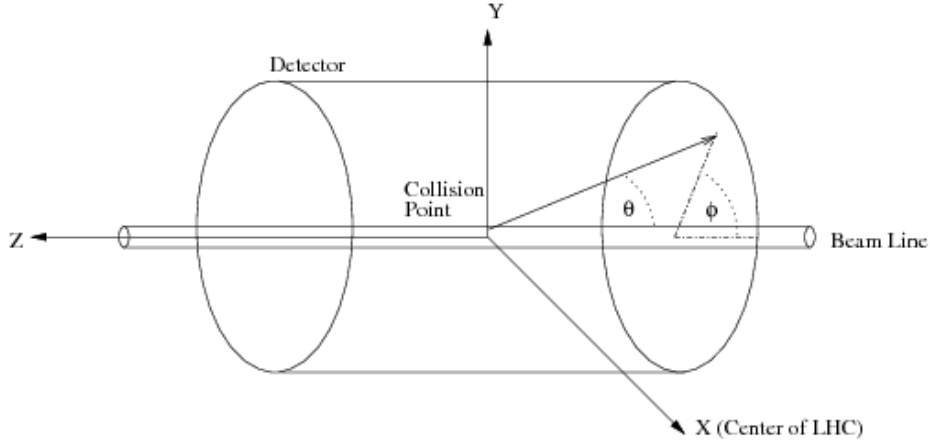


Figure 3.3. The coordinate system used by the ATLAS experiment to describe the ATLAS detector.

3.2.1.1 Semiconductor Technology

Semiconductor technology is widely used in modern image capturing devices. A case in point is a digital camera sensor, which comprises millions of modular sensors. A sensor of this kind is normally made up of a *depletion zone* and an electronics readout system. A depletion zone is a connective region between two very differently charged regions of a semiconductor when a charge equilibrium is achieved; one region is doped with impurities such that there are more free electrons than there are positive ions, while the other region is doped such that the opposite is true. The connection between these two regions is known as a *negative-positive (np) junction* because of the polar opposite charge populations in the two regions. As the free electrons near the np junction on the n-side drift towards the positive ions on the p-side, the region around the junction eventually achieves charge equilibrium. When this happens the region is known as the depletion zone, and the number of free electrons in the semiconductor is minimized. The depletion zone is therefore a good candidate region for detecting ionizing particles.

In a modern camera sensor, a photon with energy of a few eV deposits all its energy in the depletion zone. A bunch of these deposits can knock off enough electrons to form a signal, which is amplified and digitized by the electronics readout system of the sensor. Contrastingly, in high energy experiments particles with energy of several GeV pass through the depletion zone, ionizing the material and leaving a trail of electrons that could be collected as signal. Because of this, pixels are used for tracking rather than for energy measurement.

The ATLAS Pixel Detector is a good example of a semiconductor detector in high energy physics. As the sub-detector closest to the IP, it is designed to withstand intense radiation and yet provide high resolution precision tracking capabilities. Dur-

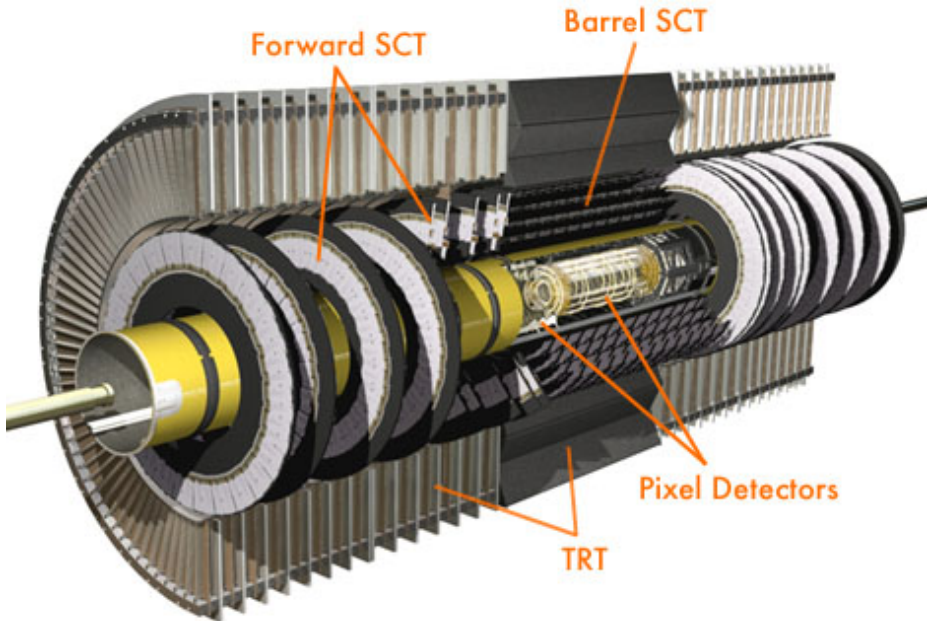


Figure 3.4. A cutaway view of the ATLAS Inner Detector.

ing Run I it was segmented into 3 barrel layers and 3 end-cap layers, mounted on circular wheels. Expecting higher particle rates in Run II, an additional layer called the Insertable B-Layer [47] (IBL) was added to become the innermost layer in the barrel. The building block in all these layers is the module, which is a group of 46080 pixels sensors. Each pixel in the IBL is $50 \times 250 \mu\text{m}^2$ and $50 \times 400 \mu\text{m}^2$ everywhere else, in $\phi \times z$ in the barrel and $\phi \times r$ in the end-caps. The cylindrical arrangement of the modules ensures that the interaction point is covered by as much area as possible. This arrangement achieves a spatial resolution of $8 \times 40 \mu\text{m}^2$ in the IBL and $10 \times 115 \mu\text{m}$ everywhere else. With 1456 barrel modules and 288 disk modules, excluding the IBL, the Pixel Detector covers $|\eta| < 2.5$ and $5 < r < 12 \text{ cm}$. The cut-out view of the Pixel Detector in Figure 3.5 shows layer segmentation in both the barrel and end-caps.

The SCT, which is a cylindrical sub-detector that sits immediately outside the Pixel Detector, is another example of a semiconductor detector in ATLAS. Covering $30 < r < 52 \text{ cm}$, a region expected to receive lower particle rates than that covered by the Pixel Detector, the SCT affords to use slightly less expensive sensors. The sensors in this case are silicon microstrips which are larger than the pixels used in the Pixel Detector. Read-out electronics are located on one end of each strip, covering only one spatial dimension. To access the second spatial dimension, another microstrip is placed at a slight angle to the original strip. The result of this rather forced arrangement is that modules in the SCT are different from those in the Pixel Detector. Four strips are laid on top of a baseboard used for support. Another set of four

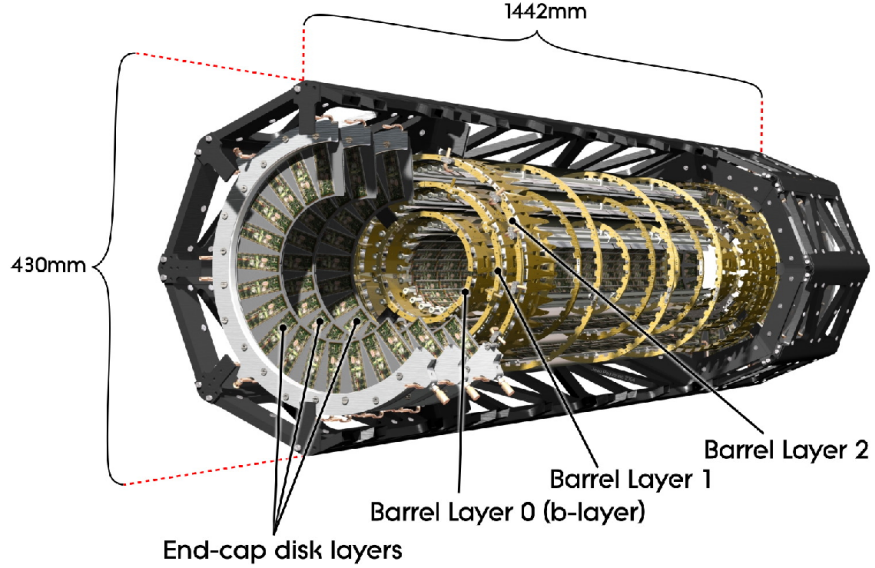


Figure 3.5. A cutaway view of the ATLAS Pixel Detector, which is the innermost sub-detector of the Inner Detector.

perpendicular strips are further laid at the bottom of the same baseboard. The crossing between the top and bottom strips covers $16 \times 500 \mu\text{m}^2$ rectangles. This arrangement achieves a spatial resolution of $17 \times 580 \mu\text{m}^2$. While the barrel component of the SCT is made up of 4 layers, the endcap region is covered by 9 annular disks on each side, as shown in Figure 3.6. The module arrangement is the same in both regions, covering $|\eta| < 2.5$.

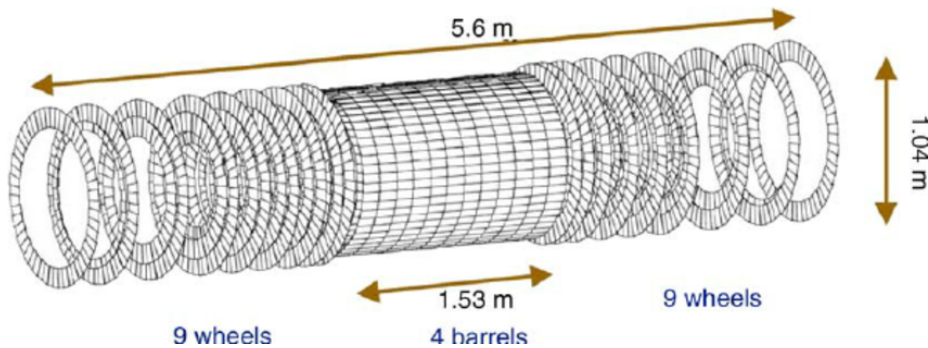


Figure 3.6. A schematic diagram of the ATLAS SCT.

3.2.1.2 Drift Tube Technology

Drift tube technology is a relatively older technique for detecting ionizing particles through a gaseous medium. A more complete discussion of this and other related technologies is reserved for Section 3.2.3. In a nutshell however, a drift tube is a gas-filled cylindrical hollow tube with a thin anode wire on the center and cathode walls. As an ionizing particle passes through the gas it liberates electrons from atoms, leaving behind positive ions. The electrons drift towards the positive wire at a much greater speed than the positive ions do towards the tube walls. The electrons are collected and converted to signal.

The basic sensor for the TRT is a 144 cm long drift tube whose walls are made of Kapton, a polyimide well known for its stability over a wide range of temperatures, and are kept at negative potential. A 30 μm in diameter gold-plated tungsten wire goes through its center and is kept at positive potential. The gas in the tube is a mixture of 90% Xe, 27% CO₂ and 3% O₂. The O₂ is added to increase electron drift velocity towards the tungsten wire and improve the time resolution. The TRT barrel region is made up of three identical layers, where each layer is a module. Each layer is made up of 32 drift tubes, which are laid parallel to z . The three layers cover a range in $56 < r < 107$ cm, and $|z| < 72$ cm. This corresponds to and coverage of $|\eta| < 0.7$. The endcap region comprises 18 layers on each side, making up 224 tubes on each side, and covering $83 < |z| < 340$ cm. This corresponds to $0.7 < |\eta| < 2.5$. The overall resolution achieved with this arrangement is approximately 130 μm .

3.2.2 Calorimeters

Calorimeters are detectors in particle and nuclear physics that measure the energy of particles by inevitably absorbing all of the particle's energy and converting it into heat. This absorption can be through scintillation, ionization or cherenkov radiation, among several other options through which the candidate particle can interact with matter. Scintillation and ionization are most commonly used to detect high energy particles.

For scintillation the candidate particle excites electrons that are subsequently de-excited, emitting photons which are multiplied and turned into signal. Detectors in which the electrons are excited from molecules are known as organic scintillators, while those in which the electrons are excited from atoms are called inorganic scintillators. Inorganic scintillators tend to have a higher photon yield than organic scintillators so they are widely used in high energy experiments. Organic scintillators are therefore outside the scope of this thesis. For inorganic scintillators, the atomic medium is a high density crystal of low cost material. Electrons in the valence state are excited by the ionizing particle to a conduction state, leaving a hole in the valence state. Upon de-excitation, a photon is emitted and is turned into signal. To minimize the de-excitation response time impurities whose energy levels lie between the valence band and the conduction band are added to the material. This offers the excited electrons

a faster de-excitation option, drastically improving the detector time resolution. For ionization detectors on the other hand, electrons on average rarely get de-excited from the conduction state. Rather, they are collected and the resultant current is turned into signal.

In the ionization case, excited electrons are in general so energetic that they further interact with matter, producing secondary and tertiary particles that in turn produce other particles of lower energy. This creates a particle shower whose shape can be studied to reconstruct the original particle energy. The primary interaction of electrons and matter at high energy is primarily through deflection by atomic nuclei, emitting photons which in turn decay into an positron-electron (e^+e^-) pair. The e^+e^- pair in turn interacts similarly, producing even more e^+e^- pairs until their energies are below an energy where the main form of dissipation is ionization and excitation rather than the creation of other particles. A particle shower initiated by leptons and photons through electromagnetic processes is known as an electromagnetic (EM) shower, and the medium of the calorimeter in which it develops is known as an absorber. The EM shower depth is characterized by a property of the absorber called radiation length X_0 , which is the length on which an electron of energy E loses its energy to E/e . Its transverse spread is in turn determined by multiple scattering of electrons and positrons away from the shower axis.

Particle showers can also be initiated by hadrons through strong interactions with the absorber, producing a hadronic shower that is relatively more complex than an EM shower. For high energy hadrons, energetic secondary particles (at GeV scale, and with usually high p_T) are produced from partonic interactions and the subsequent hadronization. The secondary particles could be charged hadrons such as pions, Kaons and protons, or neutral hadrons such as neutrons and neutral pions (π^0). π^0 s immediately decay to a pair of photons, each of which subsequently initiates an EM shower within the parent hadronic shower. As a result, a third of a hadronic shower is electromagnetic. All the other hadrons re-interact with the absorber just like the primary hadron, until a critical energy is reached. The primary hadron can also initiate nuclear excitations and nuclear spallations that result in low energy secondary particles. These usually have energies below the critical energy and rarely contribute to shower development. In contrast to em showers, hadronic shower depths are characterized by the nuclear interaction length λ_I , defined as the average length in the material traveled by a hadronic particle before inelastically interacting with another nucleus. Just like X_0 , λ_I is a property of the absorber. Because of the relatively large p_T that the secondary particles have, hadronic showers are in general wider than EM showers.

To measure the energy of the primary particle, calorimeters are designed to contain the entire shower. Because of the clear differences between EM and hadronic showers, EM calorimeters are dedicated to containing EM showers while hadronic calorimeters are dedicated to containing hadronic showers. Both calorimeters could be *homogenous* or *sampling*. For the former, the shower is contained in a homogenous

material that acts as both an absorber and an active medium where the shower is detected. The latter is made up of alternating layers of an absorber and active materials. One advantage that a sampling calorimeter has over a homogenous calorimeter is that the absorber and active materials can be optimized separately, allowing construction of a more compact calorimeter. The absorber could be made of a very dense material such as Fe, Pb or U, while the active material could be made of liquid Ar or Si detectors. Since only a part of the shower is detected, the energy resolution in a sampling calorimeter is usually lower than in a homogenous calorimeter.

The ATLAS calorimeter system [48] is made up of a dedicated set of sampling calorimeters that cover up to $|\eta| < 4.9$. These calorimeters are can be grouped into the Liquid Ar Calorimeter [49] (LAr) and the Tile Calorimeter [50], where the Tile Calorimeter is designed to contain hadronic particle showers and the LAr Calorimeter has dedicated components for both hadronic and EM particle showers.

3.2.2.1 Liquid Argon Calorimeter

As show in Figure 3.7 the LAr Cal is made up of the Electromagnetic Calorimeter (EM Cal), the hadronic end-cap (HEC) and the forward calorimeter (FCAL). For most of the LAr the absorber material is Pb, held in place by a thin layer of stainless steel and molded into an accordion shape. In parts of the FCAL and the HEC Pb is replaced by Cu and W as the absorber material to accommodate higher particle rates. The active material in all components is liquid Ar, filled in between Pb, Cu or W to a 2 mm width. Electrode boards that are molded into accordion shapes are placed inside the liquid Ar to collect electrons from the particle showers. These electrons are amplified and constitute signal.

The barrel component of the EM Cal is made up of two half wheels that are each made up of 1024 absorber sheets. It covers up to $|\eta| < 1.475$ and $r < 22X_0$. A 1 cm thick liquid Ar region with electrodes perpendicular to the beam axis is at the innermost surface of the barrel EM Cal to act as a presampler. A cell is defined in η by etching the electrode boards and in ϕ by grouping 4 electrode boards. Overall, the EM Cal end-caps cover $1.375 < |\eta| < 3.2$. Each end-cap is made up of to concentric wheels. The inner wheel has 256 absorbers and the outer wheel has 768 absorbers. The presampler for this region is similar to the barrel region except that it is 5 mm thick. The copper absorbers in the HEC are 25 mm thick, interleaved with 7.4 mm thick liquid Ar. The FCal on the other hand is made of 3 levels. The first level is of Cu absorbers and the other two levels are made of W absorbers. All the other components in the FCal are the same as in the EM Cal.

3.2.2.2 Tile Calorimeter

The largest calorimeter in ATLAS is the Tile Cal, shown in Figure 3.7, covering up to $|\eta| < 1.7$. It is placed just outside the LAr Calorimeter, with an inner radius of 2.28 m and an outer radius of 4.25 m. It is split into a barrel region and an two *extended*

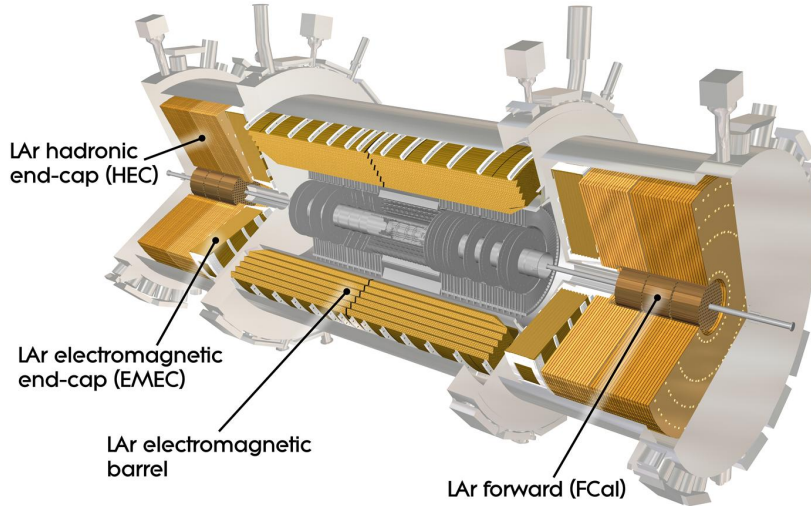


Figure 3.7. A cutaway view of the ATLAS calorimeter system.

regions that align with the Lar end-caps. The barrel and extended components each comprise 64 modules. Each module is made up of 5 mm thick Fe absorbers interleaved with 3 mm scintillating tiles. This structure makes a wedge shaped module that has a width $\Delta\phi = 0.1$. A picture of one such module is shown in Figure 3.8. Readout fibres are placed at the edges of each scintillating tile to collecting photons as signal. These fibres are then grouped at the edge of each module and connected to a photomultiplier, which multiplies the collected photons to make a detectable signal. The fibres are visible at the bottom of the picture in Figure 3.8.

3.2.3 The Muon Spectrometer

The Muon Spectrometer [51] is a composite detector designed to track muons with high precision and measure their p_T . These two goals are achieved by a set of sub-detectors encapsulated in a toroidal magnetic field supplied by superconducting toroids. Figure 3.9 shows the toroidal arrangement of the superconducting coils. Each coil is $5 \times 26 \text{ m}^2$ in area, providing a magnetic field strength ranging from 0.5 to 2 T.

All the sub-detectors in the muon spectrometer rely on ionizable gases. Their construction could be classified into drift chambers, multiwire proportional chambers (MWPCs) and resistive plate chambers (RPCs). In general the construction of each chamber is such that ionizable gas is enclosed in gas-tight structure made of a cathode and an anode, the arrangement of which supplies a near-constant electric field to the gas. As the muon ionizes the gas, the resultant electrons drift towards the anode and

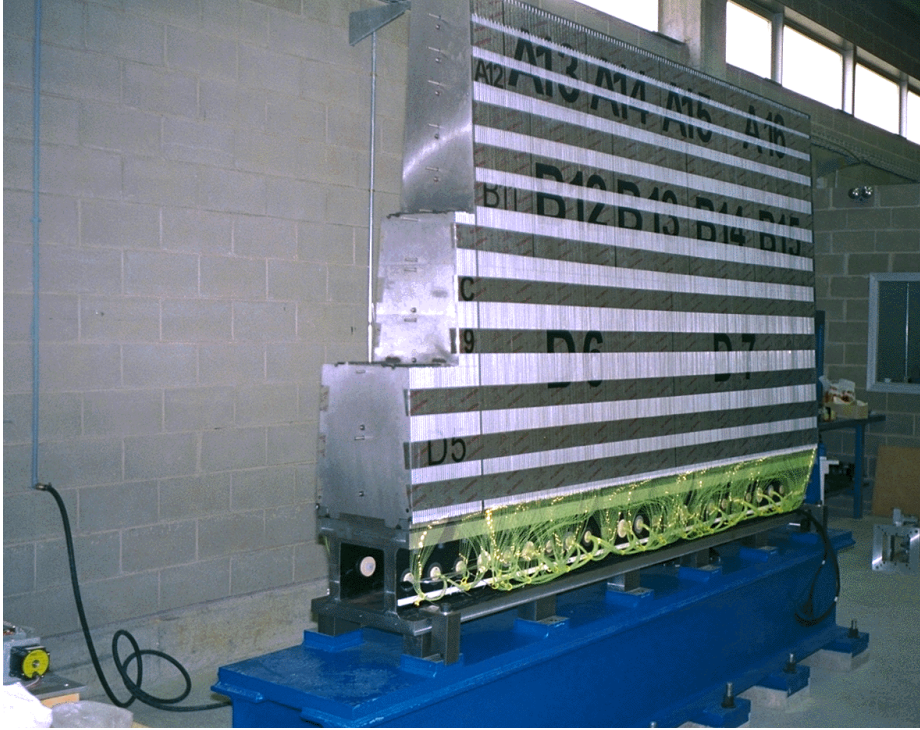


Figure 3.8. A photograph of a Tile Calorimeter module.

the positive ions towards the cathode, albeit at a much slower rate. The electrons create an avalanche near the anode. This avalanche in turn creates a pulse of current that is recorded as signal. On average the pulse width of the signal corresponds to the electron drift time. Because the electric field is near-constant, the drift velocity is well known. The pulse width and the electric field are therefore used to precisely locate the original position of the muon in the chamber. In a drift chamber (or drift tube) the cathode is the cylindrical casing and the anode is a thin wire at the center. As for the multiwire chamber the cathodes are parallel planar walls while the anodes are multiple thin wires at the center of the cathode structure. The multiple wire arrangement enables the MWPC to handle higher muon rates than the drift tube. In a resistive plate chamber parallel planar plates of high resistivity act as the cathode and anode, with gas in the middle. Electric charges collected in the anode causes the electric field in the gas to momentarily drop, temporarily disabling the chamber; high resistivity minimizes the charge dissipation time, and consequently optimizes the chamber resolution. To put this into perspective, a $10^{12} \Omega \text{ cm}$ anode has a 10 m s charge dissipation time.

Just like the arrangement of sub-detectors in the calorimeter, here a distinction is placed between barrel and end-cap sub-detectors. The strengths in each of them is always a trade-off between the measurement speed, spatial resolution and the ability to operate at high noise rates. Since there is more noise at high pseudorapidity,

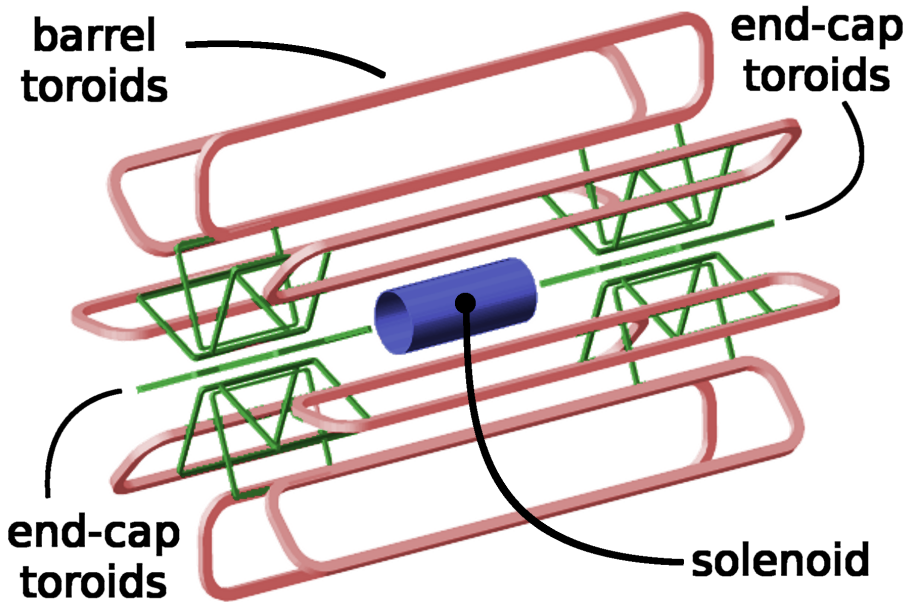


Figure 3.9. The ATLAS magnetic system. The red toroid encapsulate the muon spectrometer sub-detectors, while the solenoid encapsulates the inner detector, which was discussed in Section 3.2.1.

MWPCs are generally placed in the endcaps while drift tubes are placed in the barrel. A further distinction is placed between precision sub-detectors and fast-measurement detectors, which are used for triggering for events that include a muon.

RPCs are placed in the barrel component of the muon spectrometer specifically for triggering events with muons [52]. The resistive plates are 2 mm thick and are made of bakelite, whose resistivity ranges between $10^9 \Omega \text{ cm}$ and $10^{12} \Omega \text{ cm}$. The chambers have a 2 mm spacing that is enabled by insulating spacers, and are filled with 94.7% of $\text{C}_2\text{H}_2\text{F}_4$ as the ionizable gas. The resistive plates are coated on the outside by graphite, which is of significantly lower resistivity. This arrangement helps in distributing the high voltage on the bakelite plates. Readout strips are placed immediately outside the graphite coating.

Thin Gap Chambers [53] (TGC) are placed in the end-caps for triggering events with muons of relatively lower p_T . A TGC is a multiwire chamber with graphite plates and 50 μm gold-plated tungsten wires with a 1.8 mm spacing. A mixture of 45% n-Pentane and 55% CO_2 is filled in an air-tight 2.8 mm thick space between the graphite plates. This arrangement gives signal rise times below 5 ns, which is a very convenient time-frame for triggering events at the LHC.

Monitored Drift Tube [54] (MDT) chambers are used for precision measurements in the barrel and end-cap region. Each tube length ranges from 0.9 m to 6.2 m, with a constant diameter of 3 cm. The casing is a 400 μm thick aluminum alloy and the anode wire is a 50 μm W-Re wire, while the gas is a mixture of 93% Ar and 3%

CO_2 . Each tube offers a spatial resolution of about $100\ \mu\text{m}$. An MDT chamber has two multilayers of tubes. A multilayer is made up of 3 to 4 layers of tubes supported by a beam structure shown in Figure 3.10. The alignment of these tubes is constantly monitored by x-ray beams to make sure that the tubes are not sagged.

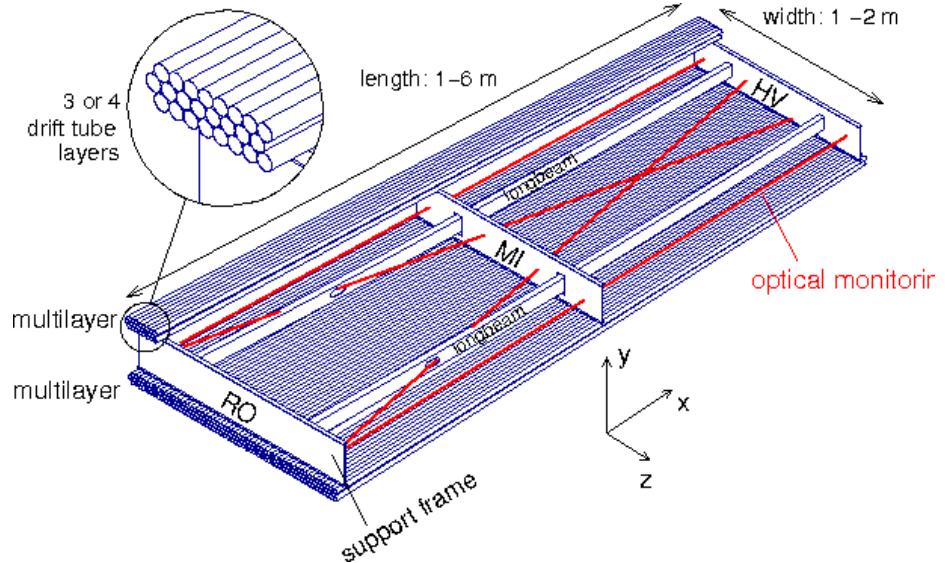


Figure 3.10. A cut-out of a Monitored Drift Tube chamber showing multi-layers of MDTs and the supporting beam structures.

Cathode Strip Chambers [55] (CSCs) are MWPCs that are placed in the end-caps for precision measurements because they have higher precision than MDTs and can handle the higher rates at high pseudorapidity. The plates are graphite and the wires are tungsten. The wire separation is $2.54\ \text{mm}$ and the readout strips are $5.08\ \text{mm}$ wide. The gas mixture used is 20% Ar and 20% CO_2 . The CSCs are segmented in ϕ on two wheels of eight chambers in the end-cap region, offering for layers of CSCs that a muon object has to traverse past. This arrangement give a $60\ \mu\text{m}$ resolution on muon track position.

Figure 3.11 shows the full muon spectrometer and all the sub-detectors.

3.2.4 The Trigger and Data Acquisition System

During stable LHC runs in Run I and Run II proton bunches collided at 40 MHz; the current ATLAS data storage system however can only record events at about 200 Hz. The ATLAS Trigger [56] is responsible for selecting potentially interesting collisions and discarding the rest, reducing the 40 MHz to about 100 Hz. This reduction was achieved in 3 and 2 levels during Run I and Run II respectively.

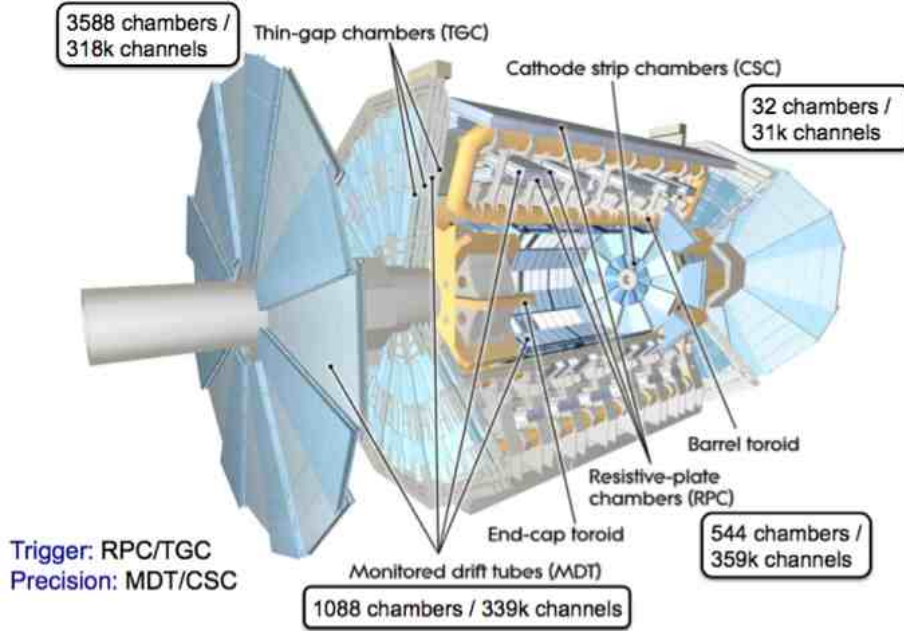


Figure 3.11. A cutaway view of the ATLAS Muon Spectrometer and its sub-detectors.

3.2.4.1 Level 1

Level 1 Trigger [57] (L1) during Run II is almost identical to that used in Run I. In Run I it reduced the 40 MHz rate to about 65 kHz while in Run II it reduced it to 100 kHz. The decision to accept or reject a bunch crossing is based on the multiplicity of physics objects ($e, \gamma, \mu, \tau, E_T^{\text{miss}}$ and jets) from that crossing with energies that pass any of the energy thresholds in a pre-defined set. The definitions of these physics objects is discussed in more detail in Chapter 5. To keep up with the 40 MHz bunch crossing rate, the maximum time to make the decision (latency) is kept 2.5 μm . Signals from the EM and the hadronic calorimeters are used to construct e, γ, τ and jet candidates based on shower shape properties while patterns of hits from the muon spectrometer chambers are used to construct μ candidates and their p_T . All these physics objects are assigned to a Bunch-Crossing Identification (BCID), which tags them to a specific proton bunch crossing. After all known physics objects are identified, E_T^{miss} is constructed as the remainder that enables the system to conserve transverse momentum.

To keep up with the 2.5 μm latency, L1 has no access to full calorimeter granularity. Rather, it uses groups of cells called Trigger Towers (TTs) of size $\eta \times \phi = 0.1 \times 0.1$. As described in Section 3.2.2 and as shown in Figure 3.12 the EM Cal comprises four layers of varying segmentation in r . The number of cells that make up a TT is therefore dependent on the EM Cal layer. In Layer 2 one TT comprises 4×4 cells while in Layer 3 it comprises 2×4 cells in $\eta \times \phi$. Since Layer 2 has the largest radiation length

and contains most of the energy deposit, the feature extraction algorithm uses it as seed in searching for physics objects. The e/γ algorithm first runs a sliding window to find a local maximum that comprises 2×2 TTs in $\eta \times \phi$. These 2×2 tower regions shown in green in Figure 3.13 are called *clusters*. The algorithm then computes the horizontal and vertical sums of energy in this local maximum and labels the highest as the candidate energy for the cluster. The neighboring towers that surround the cluster make up the Isolation Ring (IR), which is used to distinguish between shower profiles from different particles. The τ algorithm is similar to the e/γ algorithm except that it allows showers to penetrate into the hadronic calorimeter because τ s can decay to collimated clusters of hadrons. Showers detected in the hadronic calorimeter are labeled as jets. Since τ objects also leave showers in this region of the calorimeter, they are a special kind of jets that satisfy extra isolation requirements. Regardless, there is a dedicated algorithm for searching for jets. The procedure is similar to the e/γ algorithm, but it instead uses 4×4 TT windows called *jet elements* (groups of TTs 0.2×0.2 in $\eta \times \phi$).

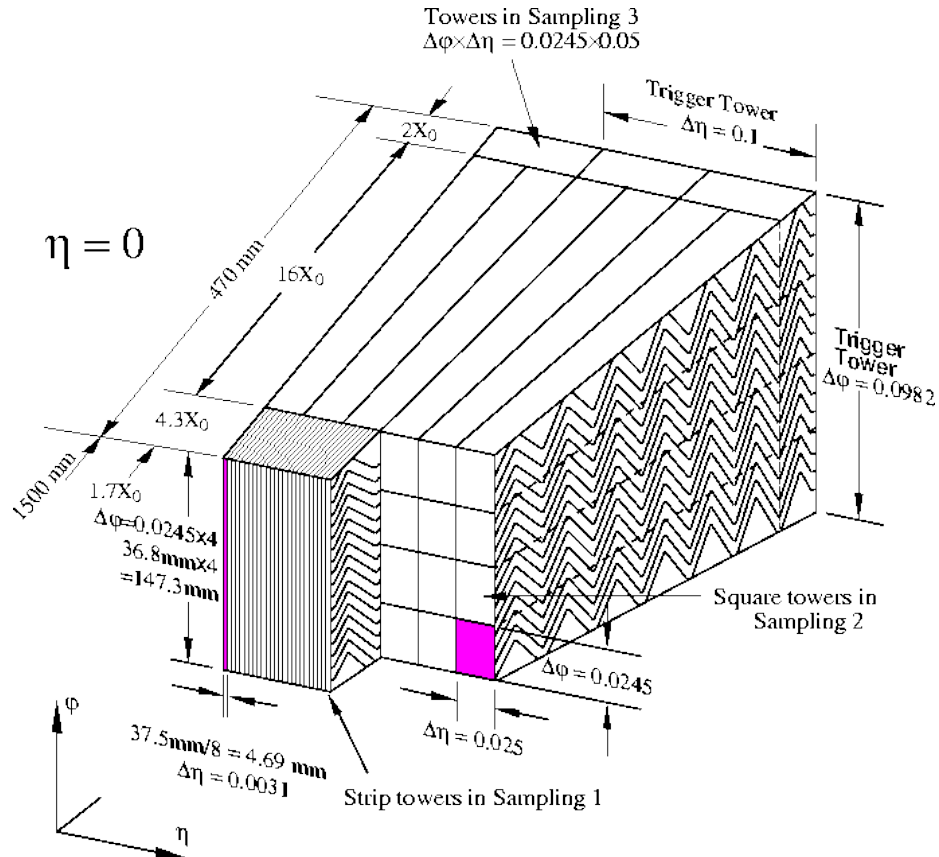


Figure 3.12. Schematic diagram of showing cell segmentation in the EM Cal, across multiple layers.

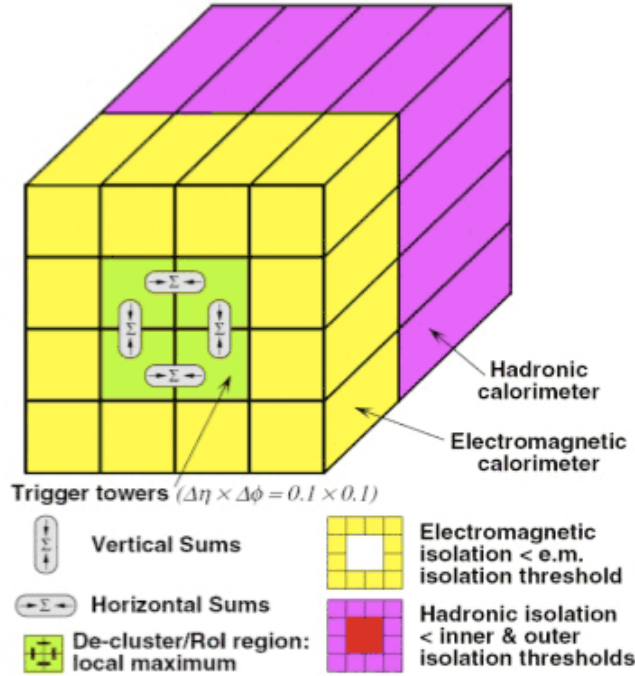


Figure 3.13. Illustration of the search algorithm for electrons and photons in the EM Cal.

With a 1.5 ns time resolution, [RPCs](#) and [TGCs](#) in the Muon Spectrometer offer muon hits in all three dimensions in the barrel and end-cap regions respectively. The goal of the muon trigger is to identify muons originating from the interaction point. As discussed in Section 3.2.3 [RPCs](#) are arranged in three layers. Just like in the calorimeters the second [RPC](#) layer is used as seed in identifying a muon track. In this case a [TT](#) is of size $\Delta\phi \times \Delta\eta = 0.2 \times 0.2$. If a hit is found in the second layer, a *coincidence window* in relation with the hit is defined in the first and third layers based on the line connecting the hit and the interaction point. Hits are then searched in the coincidence window in the first and third layer. If more than one hit is found in the first and third layers, multiple hit combinations are combined in parallel and one with the highest acceptance probability of p_T greater than a given threshold is picked. A similar algorithm is employed in the end-caps where TGCs handle the relatively higher muon rates.

For events that pass [L1](#) coordinates of the detector where physics objects that triggered [L1](#), their p_T and the [BCID](#) are saved in buffers and handed over to upper levels of the trigger. This information is called a Region of Interest (RoI).

3.2.4.2 Example Shower Profile Classification

As discussed above, algorithms used at [L1](#) are designed to distinguish between hadronic showers and EM showers. The EM showers in most cases are initiated by electrons and photons (e/γ). Due to the limited calorimeter granularity available at [L1](#), it is difficult to distinguish some hadronic showers from e/γ showers. A case in point is a π^0 versus an electron. With a lifetime of about 8×10^{-17} s the π^0 immediately decays to a pair of photons when it interacts with the calorimeter absorber material. These two photons each initiate an EM shower that is hardly distinguishable using the [L1](#) algorithms in the preceding section.

The strategy used to distinguish between π^0 and electron showers relies heavily on resolving the two photon showers contained within the π^0 shower. Simulation studies have shown that [TTs](#) are too coarse to resolve these two photon showers, so such a strategy is employed at Level 2 (see Section 3.2.4.3). As the instantaneous luminosity of the LHC is expected to more than double by 2022, the trigger is expected to handle more input data. One way to ensure that trigger rates are kept constant is to upgrade [L1](#) such that it becomes capable of performing some of the tasks that would otherwise be left for [L2](#). One of such tasks is the classification of π^0/e showers.

An improvement in granularity from [TTs](#) at [L1](#) was explored as a potential setup to separate π^0 showers from electron showers. This upgrade would constitute upgrading from [TTs](#) to *supercells*, where a supercell is a group of calorimeter cells that span a 0.025×0.1 region in η, ϕ . More precisely, 1 supercell corresponds to 1 cell in the EM Cal presampler, 8 in Layer 1 and 4 in Layer 2. In Layer 3 the cell granularity in η is coarser than a single supercell, so no segmentation is required. The objective of this study was to determine the feasibility of rejecting more than 50% π^0 showers while retaining at least 95% of electron showers using supercell granularity. This amounts to deriving variables that quantify shower shapes in the lateral and longitudinal planes and distinguishing between shapes due to π^0 to those due to electrons.

The procedure for obtaining simulation data samples is the following : Single, isolated electrons or π^0 's were generated with a predefined energy and direction in (η, ϕ) in the EM Cal. For simplicity the chosen direction ($\eta = 0.4125, \phi = 0.1125$) is the center of a cell. Geant4 [58] was used to simulate the EM Cal. The output of this simulation was digitized and subsequently reconstructed. Separate samples were also made in which electrons and π^0 's were generated over a range in η covering the width of a cell in Layer 2 ($\Delta\eta = 0.025$), which is also the width of a supercell. These samples are referred to as *scanned η* samples. Contrastingly, samples generated in the standard manner are called *fixed η* samples. By default, simulated particles were generated from the interaction point. A simplistic model of the generation point be described by a δ -function at $z = 0$ while a more realistic one with a Gaussian distribution with RMS ≈ 5 cm. Smearing the interaction point with a known RMS is referred to in this thesis as *vertex smearing*.

Figure 3.14 shows a comparison of electron and π^0 showers using several variables that exploit the difference in their longitudinal and lateral profiles. For longitudinal comparisons the fraction of energy deposited in a layer and cluster cl is used. It is quantified by ρ_{layer} where

$$\rho_{layer} = \frac{\sum_{c \in cl, c \in layer} (E_c)}{E_{cl}}. \quad (3.4)$$

ρ_{layer} can be used to classify electrons and π^0 s of low p_T but it loses its robustness for those of high p_T . The same can be said of $\rho_{comp} = \frac{\rho_1}{\rho_2}$, which is a comparison between ρ_{layer} from Layer 1 and Layer 2. To study lateral profiles the ratio of the energy deposited in the supercell with the highest energy deposited (colloquially referred to as the *hottest* supercell), to the sum of that energy and the energy deposited in the two neighboring supercells in η is used. This ratio is quantified as

$$R_\eta^{(1)} = \frac{E_0}{E_{+1} + E_0 + E_{-1}}, \quad (3.5)$$

where E_0 is the energy deposited in the hottest supercell, E_1 in the supercell to the right of the hottest supercell and E_{-1} to the left of the hottest supercell. $R_\eta^{(1)}$ performs superbly for low p_T electrons and π^0 s. For high p_T it becomes less robust but can still classify electrons and π^0 s with high accuracy. Figure 3.14 shows that for 20 GeV π^0 s and electrons more than 50% π^0 s are rejected while less than 5% electrons are accepted. In the more realistic case where vertex smearing is turned on and the η position is scanned however, $R_\eta^{(1)}$ loses its robustness.

These results show that even with supercell granularity at L1, separation between electrons and π^0 s is not a trivial subject. More studies on this subject will have to be done during the long LHC shutdown that starts in 2018 to meet the higher trigger rates that ATLAS has to face afterwards.

3.2.4.3 High Level Trigger and Data Acquisition

The High Level Trigger [59] (HLT) is responsible for reducing the rate from 100 kHz to about 100 Hz. During Run I it comprised two separate levels : Level 2 [60] (L2) that reduced the rate to 1 kHz and the Event Filter [61] (EF) that reduced it to 100 Hz. During Run II a lot of components in L2 were combined with the EF. Data management is handled by a separate system called Data Acquisition [62] (DAQ). So combined, the HLT and DAQ are referred to as TDAQ.

To minimize latency, input to the HLT is a set of RoIs from L1 whose associated data is just a few percentage of the raw data. The rest of the raw data are kept in buffers known as Readout Buffers (ROBs) and are extracted upon request using the Readout System (ROS) by the Data Collection Manager (DCM). For L2, RoIs are assembled by a Region Of Interest Builder (RoIB) and passed over to a farm of Linux PCs. Here five L2 Supervisors (L2SVs) schedule and assign events to nodes on the

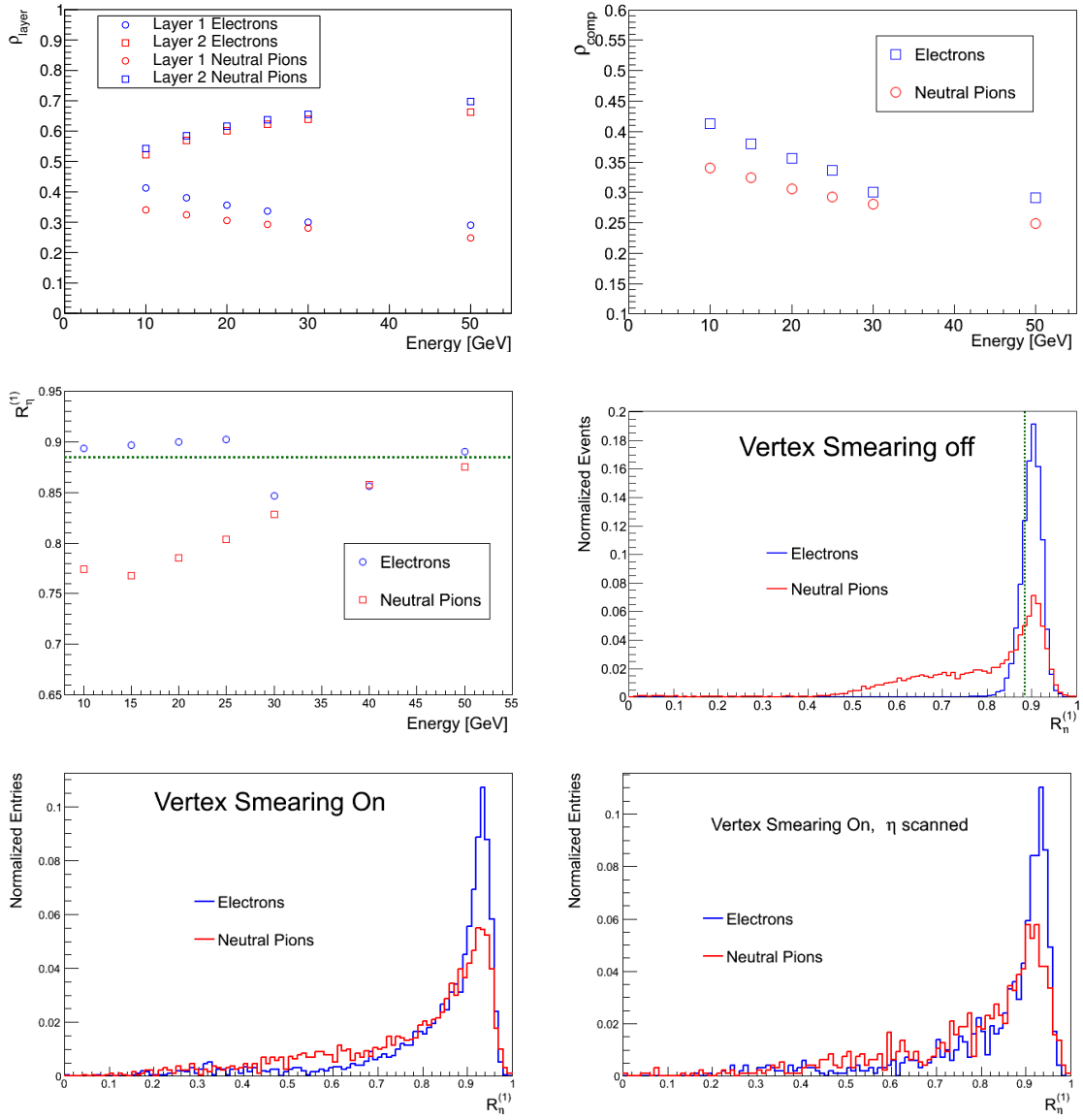


Figure 3.14. Distributions of variables used to separate electrons and π^0 s. [Top Left] ρ_{layer} for Layer 1 and Layer 2. [Top Right] ρ_{comp} for Layer 1 and Layer 2. [Middle Left] $R_{\eta}^{(1)}$ for π^0 s and electrons across several energies. [Middle Right] $R_{\eta}^{(1)}$ for 20 GeV electrons and π^0 s. [Bottom Left] $R_{\eta}^{(1)}$ with vertex smearing on. [Bottom Right] $R_{\eta}^{(1)}$ with vertex smearing turned on and η scanned across a 0.025 range.

Linux farm. L2 Processing Units (L2PUs) run event selection algorithms on the **RoI** while taking advantage of the full calorimeter granularity and requesting more data from **ROBs** when necessary. These selection algorithms take a wholistic approach by making decisions based on **RoIs** from a combination of detector components. For

example, information from both the [ID](#) and the Muon Spectrometer is used to identify muons and their p_T . Ultimately, [L2PUs](#) report their decisions back to [L2SVs](#), which pass the decisions and logs to L2 Result Handlers (L2RH).

During Run I, upon [L2](#) acceptance event raw data was passed to a separate farm of Linux PCs that ran [EF](#) off-line event selection algorithms. These algorithms were similar to [L2](#) algorithms but included the latest calibrations and alignment information. During Run II a series of upgrades were executed that merged [L2](#) and [EF](#) Linux PC farms, where each [HLT](#) node accepts the [RoIs](#) through the [RoIB](#), makes a decision, builds the event and executes the [EF](#) algorithms. In this setup new but fewer components are introduced: the High Level Trigger Supervisor (HLTSV), the High Level Trigger Processing Unit (HLTPU), and the [DCM](#). A component of the HLTSV replaces the [L2SV](#). Only one [HLTSV](#) is needed to handle a pair of inputs, compared with 5 [L2SVs](#) in Run I. Additionally, the [HLTSV](#) is responsible for grouping decisions from the [HLTPUs](#) and sending them to [ROS](#) PCs to either clear or keep event fragments. The [HLTPUs](#) assume the role similar to [L2PUs](#) and the Event Filter Processing Units ([EFPUs](#)). Each [HLTPU](#) is accompanied by a couple of [DCMs](#), which serve as media for collecting fragments from the [HLTSV](#).

A schematic of the Run I setup is shown in Figure 3.15. In this setup all components are run by applications on several PCs. The applications are configured and controlled by a common software framework [63] referred to in this thesis at in the format *tdaq 05-xx-yy*, where *xx* and *yy* are release tags. The structure and settings of the system is specified in a set of XML files, which form a configuration database. Application configurations are grouped into *segments* that make up a *partition* when grouped together. The main configuration used at Point 1 is called the [ATLAS partition](#). It is possible to create individual partitions parallel to the [ATLAS](#) partition for testing purposes, where network connections are handled by a common partition called the *initial* partition.

There are three main reasons the Run II trigger performs more efficiently than the Run I trigger. First, the [L2](#) and the [EF](#) share a large fraction of code. Merging these two components reduces code duplication and optimizes resource usage. Second, [RoI](#) data are retrieved twice Run I while in Run II data are retrieved once. Third, the whole Run II system has fewer components and is therefore easier to configure and optimize. Section 3.2.4.4 discusses a study that was influential testing the feasibility of merging [L2](#) with [EF](#) to form the [HLT](#).

3.2.4.4 Feasibility studies on HLT upgrade – RoIB Evaluation Tests

Argonne National Laboratory [64] (ANL) hosts a farm of 13 Linux PCs that is a prototype of the farm at Point 1. This section discusses tests done on the RoIB using the [ANL](#) test stand. The goal was to determine if there is a configuration with which the RoIB can process events at 100 kHz.

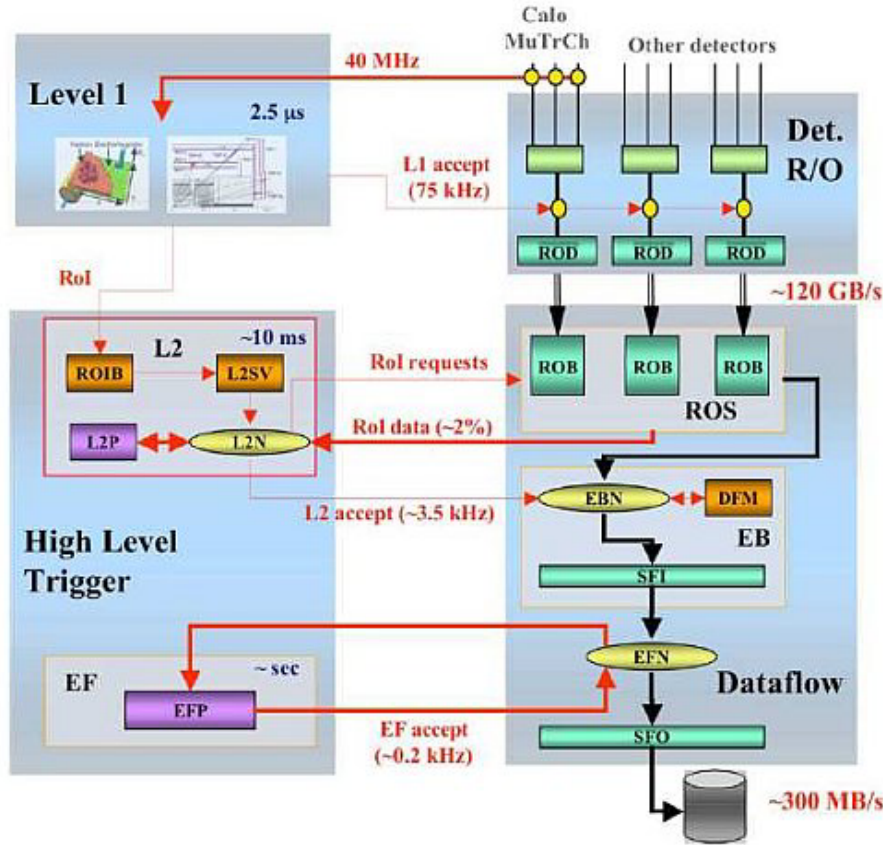


Figure 3.15. A schematic of the Run I ATLAS TDAQ. Data flow is depicted by black arrows and message flow by red. The L2 and the EF run separate sets of algorithms on the data. Applications running in this system are configured under segments that make up a partition.

Special cards installed on the ANL PCs emulate elements of the Trigger and Data Acquisition (TDAQ) system. Two quad s-link transmitter (QUEST) cards are used to supply L1 event fragments to the RoIB via a VME crate with a VME Single Board Controller (VMESBC) that houses custom VME cards that combine L1 fragments. A Four Input Links for Atlas Readout (FILAR) card receives data fragments from the RoIB and transmits it via a highly integrated PCIx interface to the HLTSV. A Two Input Links for Atlas (TILAR) card functions just as a FILAR card but with two less inputs and a PCIe interface. Figure 3.16 shows a chartflow of how the data fragments flow in a partition on this test bed: A QUEST card reads data from simple text files and transmits the fragments to the RoIB. After being processed by the RoIB the fragments are relayed to the HLTSV via a FILAR or a TILAR card (tests were done with both cards and the rates were assessed independently). The HLTSV then assigns fragments to HLTUs and also relays them to the ROS. Since

these components of data-flow are located on multiple PCs, multiple optical cables facilitate inter-PC connection.

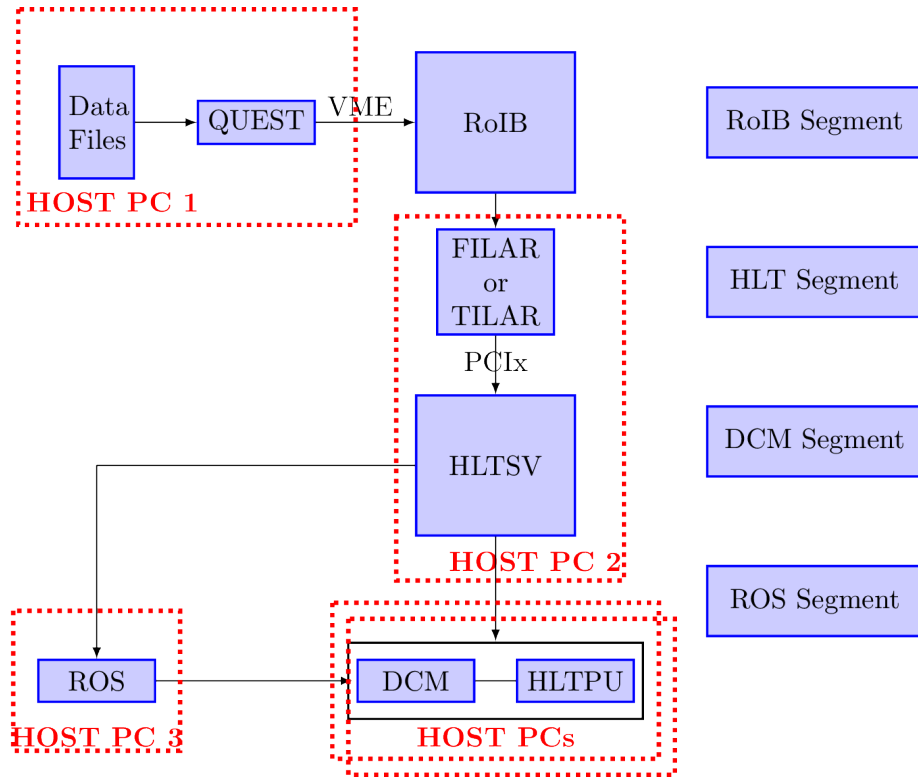


Figure 3.16. A flow-chart showing data flow in a partition at ANL’s test bed.

Table 3.2 shows the PC specifications on the test bed and the special cards installed on those PCs. The PCs are identified as $ustb^*$, where $*$ is an integer in $[0, 21]$ and $ustb$ stands for ‘US Test Bed’.² Since $ustb16$ hosts the **FILAR** card, the **HLTSV** application must run on $ustb16$. $ustb3$, $ustb4$ and $ustb10$ are called *blade* PCs because they are single board ATCA computers that do not have PCIe or PCIx slots for **FILAR** or **TILAR** cards.

There are three potential bottlenecks to the **RoIB/HLTSV** rate. First is the link from the **RoIB** to the **FILAR** card. Second is the PCIx connection from the **FILAR** card to the **HLTSV** and third is the CPU memory on which the **HLTSV** runs. It was shown at Point 1 that the maximum rate of transferring fragments from the **RoIB** to the **FILAR** cards using one link is around 60 kHz. Using two optical fibres for the link would therefore achieve a 100 kHz rate of fragment transfer. This leaves two bottlenecks in the system, where the CPU bottleneck is very dominant. Just like

²Not all integers in $\{0, 21\}$ are used, because there are only 13 PCs

Cards	PC	Architecture		CPUs		Cores	HT		Cache [MB]	Memory [MB]
		32 Bits	64 Bits	1	2		Yes	No		
FILAR	ustb16	✓		✓		4		✓	6.1	4 012
QUEST	ustb14	✓		✓		4		✓	6.1	4 012
	ustb21	✓			✓	8		✓	6.1	4 018
TILAR	ustb0	✓		✓		4		✓	6.1	4 012
	ustb11	✓			✓	8		✓	6.1	4 018
ROBINNP	ustb12		✓		✓	8		✓	6.1	3 921
VMESBC	ustb7	✓		✓		1		✓	0.5	511
	ustb1		✓		✓	8	✓		8.2	12 183
	ustb3		✓		✓	8	✓		8.2	3 910
	ustb4		✓		✓	8	✓		8.2	3 910
	ustb10		✓		✓	12	✓		12.3	12 187
	ustb13		✓	✓		4		✓	6.1	3 920
	ustb20		✓		✓	8		✓	6.1	4 019

Table 3.2. Linux run PCs on the [ANL](#) Test Bed. They have diversely varying CPU strength and hardware structure, so some custom-made cards can only be installed on specific computers. *HT* stands for hyperthreading. The cores are the total number of cores in all the physical CPUs. **FILAR** and **TILAR** cards transmit data fragments from the [RoIB](#) to the [HLTSV](#). The **QUEST** cards supplies data fragments to the [RoIB](#). Although ustb1, ustb3 and ustb10 are the most powerful, none can host any custom cards because they have a very thin structure.

in Run I, the data flow in the Run II [DAQ](#) uses the *pull* architecture, as opposed to the *push* architecture. In the pull architecture when the HLTPU is done processing event fragments it sends a message to the [HLTSV](#), which requests a set of fragments from the [RoIB](#). In tdaq 05-02-00, the **FILAR** card is limited by a single buffer whereas in tdaq 05-03-00 the buffer size is increased to 100. Such a large buffer size causes problems with the driver – version 05-03-00 of TDAQ that limits the **FILAR** card buffer size to 16 was used in these studies. The 100-buffer and 16-buffer versions are referred to as A and B respectively.

Table 3.3 shows some of the parameters that can be configured to optimize the [HLTSV](#) rate when running the [RoIB](#). The [HLTSV_DCMTest](#) is the application that handles [DCM](#) functionalities. The NumberOfCores is the number of cores on which [DCMs](#) run on. It is the same as the number of [DCMs](#) in the system. L2ProcessingTime is the time it takes to run the [L2](#) algorithms within HLTPUs. The EventBuildingTime is the time it takes to build the event if it is accepted by the [L2](#) algorithms. The [HLTSVApplication](#) is the application that runs the [HLTSV](#). The NumberOfAssignedThreads are the core threads assigned to the [HLTSV](#).

Application	Parameter
HLTSV_DCMTTest	NumberOfCores
	L2ProcessingTime
	EventBuildingTime
HLTSVApplication	NumberOfAssignedThreads

Table 3.3. Parameters that have the most impact on the **HLTSV** rate in a partition.

There are other applications whose configurations remain constant in these studies, other than being moved around from one PC to the other to determine their effect on the **HLTSV** rate. The **ROS** functionality is ran by an application called **testROS** and the **RoIB** by **RoIBApplication**. The **RoIBApplication** is always placed on **ustb7** because that is the **VMESBC** as shown in Table 3.2. Text files that contain data fragments are always on **ustb14** and they are named *testi.d* where *i* is an integer ranging from 1 to 11. The respective segments are called **RoIBSegment**, **HLT**, **DCM-Segment** and **ROS**.

To test the **HLTSV** rate dependance on these parameters, an **unoptimized** partition in which the PCs available as **DCMs** are **ustb13**, **ustb21** and **ustb12** was created. The **HLTSVApplication** was put on **ustb16** and the **testROS** on **ustb11**. The **RoIBSegment** was placed on **ustb20**, **HLT** on **ustb16**, **DCM-Segment** on **ustb13** and **ROS** on **ustb11**. This configuration, which is shown in Figure 3.17, is referred to here as **Configuration 1**. Figures 3.18, 3.19 and 3.20 show how the rate depends on each of the variables in Table 3.3 , while the other variables are held constant.

Using the plots in Figures 3.18, 3.19, 3.20 it can be claimed that (25,5,3)³ is the optimal configuration; it was used as a starting point in the rest of the study. To test the CPU bottleneck, random data fragments were generated internally in the PC that hosts the **HLTSV** and by-passed the **FILAR** card. Data obtained through this method is referred to as *Internally Generated Data* (IGD). Tests could therefore be conducted on powerful PCs that cannot host a **FILAR** card. The **HLTSVApplication** was put on **ustb3** and **ustb10** was used just for the **DCMs**. The **HLTSVApplication** parameters were configured as (25,5,4). All other components of the partition remained identical to Configuration 1. The schematic diagram on the left of Figures 3.21 and 3.22 shows this setup. In this configuration, the optimized rate was not expected to increase by running **tdaq 05-03-00** (which has a default of **FILAR** 100 buffers) instead of **tdaq 05-02-00** (1 buffer) because the **RoIB** was by-passed. This achieved a rate of 68 kHz. Adding another node to the **DCM** (**ustb4**) boosted the rate to a stable 107 kHz. The image on the right of Figure 3.22 shows this new configuration, which is referred to here as **Configuration 2**. Adding more than two **DCM** nodes did not improve the rate. This implies that with at least two **DCMs** a 100 kHz rate is achievable on

³In this notation we put (NumberOfCores,L2ProcessingTime,NumberOfAssignedThreads)

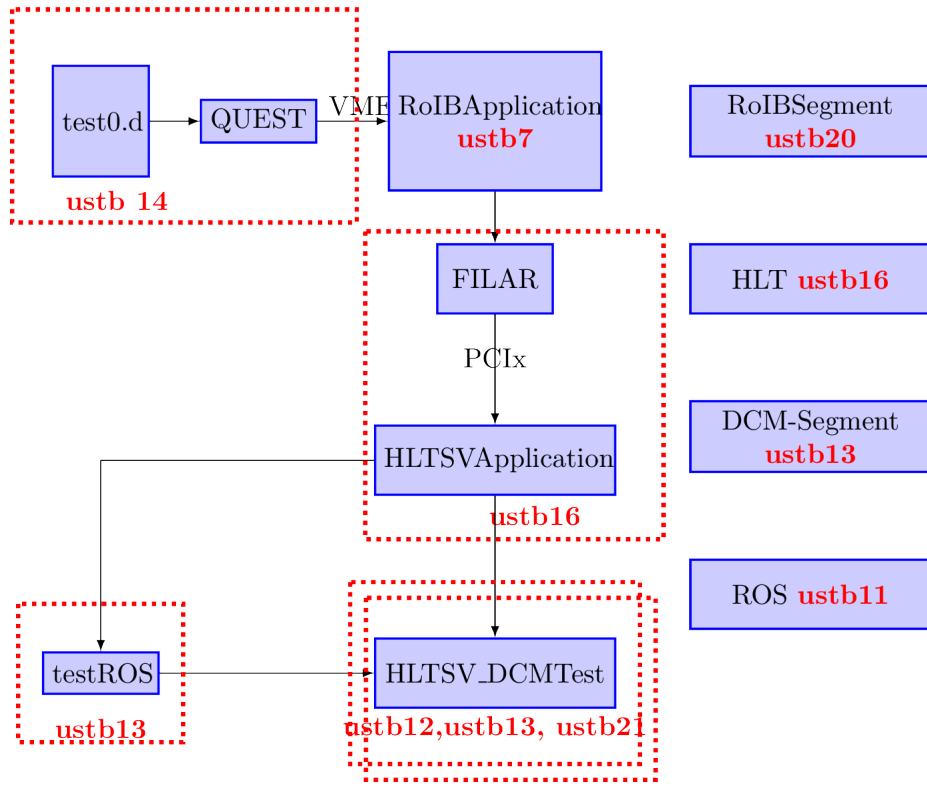


Figure 3.17. A flow-chart showing **Configuration 1** of the partition. This configuration was used to determine the optimal values of the parameters in Table 3.3 by producing the plots in Figures 3.18, 3.19 and 3.20.

a powerful enough PC. Moving the HLTSVApplication to uстb16 (which has fewer number of cores and lower cache memory) gave an unstable rate ranging from 65 kHz to 80 kHz. The same behavior was observed in both tdaq 05-03-00 versions A and B⁴ as well.

To achieve a reproducible rate without the RoIB with the HLTSVApplication on uстb16, NumberOfThreads were varied to find a value with a minimal rate fluctuation as shown in Figure 3.23. The error bars represent the rate fluctuation. Notice that at 7 threads, the rate stabilizes. HLTSVApplication configuration was then changed to (25,5,7). In addition to that, all segments (HLT, ROS, DCM) were placed on uстb21. The HLTSV_DCM application ran on uстb10 and uстb4. The partition was hosted by uстb13. The image in Figure 3.24(a) shows a schematic of a version of Configuration 2 but with the above changes; the rate still stabilized at 107 kHz. This configuration is referred to as **Configuration 2a**. With the HLTSVApplication on uстb16, (**Configuration 2b**, Figure 3.24(b)) the rate stabilizes at 85 kHz. Because

⁴Reminder: The FILAR card in A has 100 buffers and in B has 16 buffers

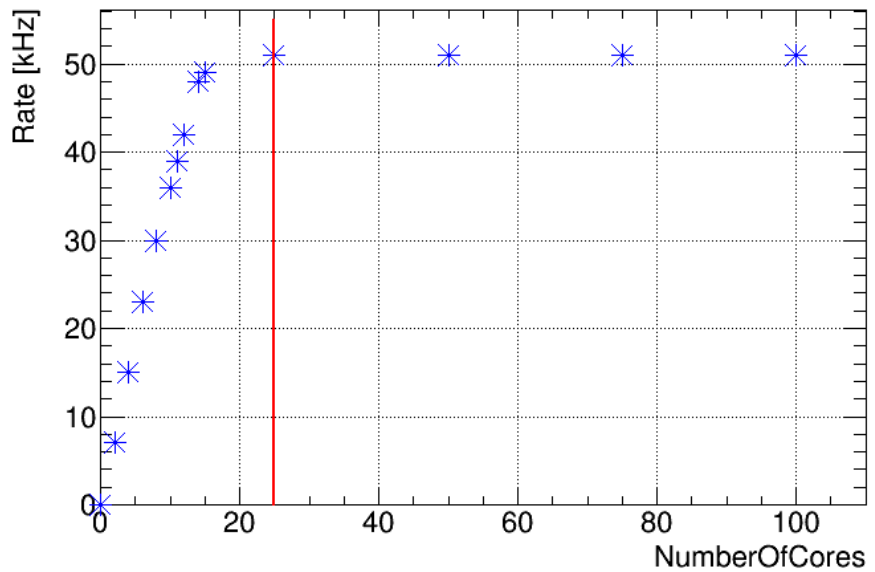


Figure 3.18. Plot showing the number of Cores maxes the rate at 25. The number of cores available on ustb13, ustb21 and ustb12 sums up to 20. An additional data point would show that the Number of Cores maxes at 20 .

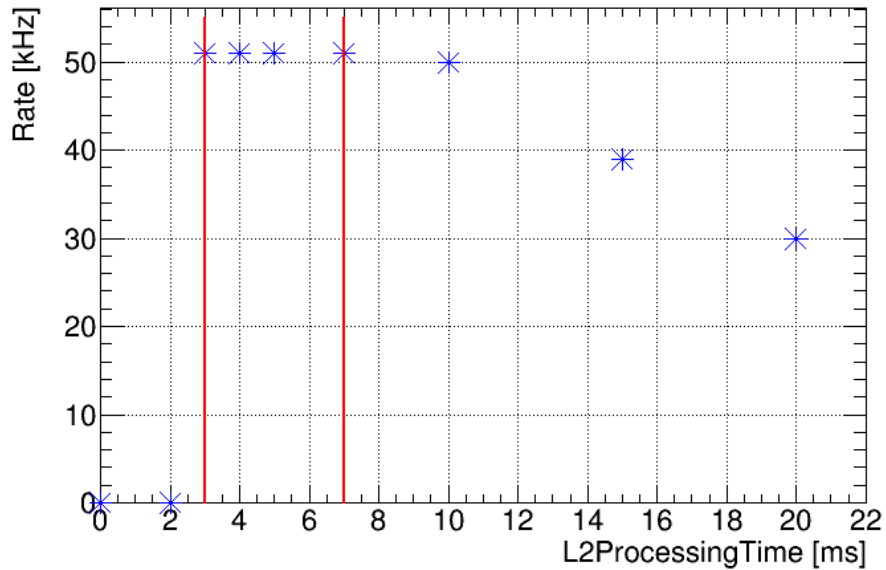


Figure 3.19. Plot showing the processing time less than 3 ms is not physical. Above that, it makes sense that the rate would decrease .

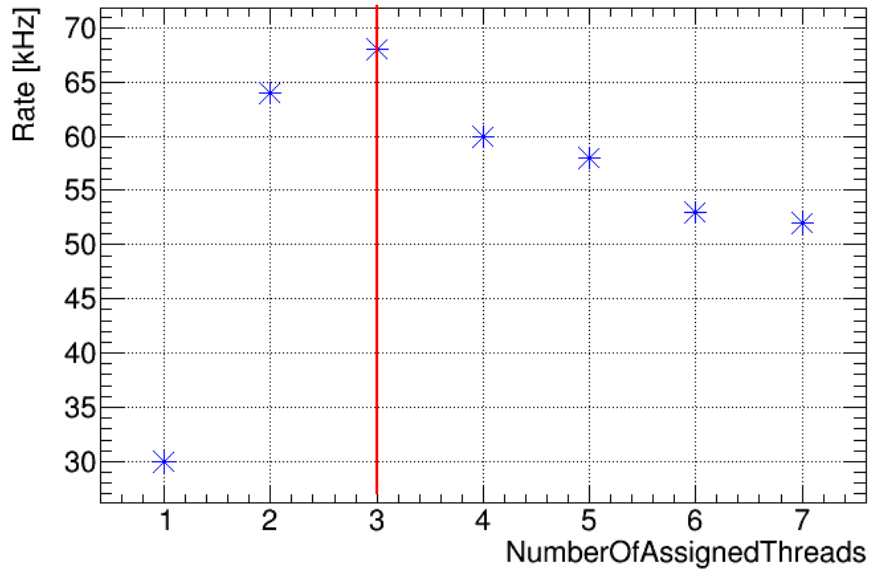


Figure 3.20. Plot showing the number of threads assigned to the [HLTSV](#).

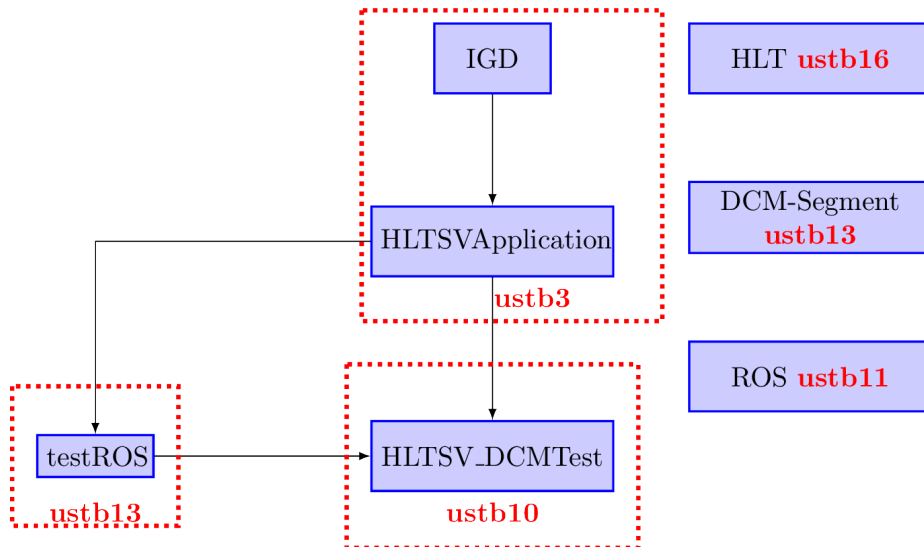


Figure 3.21. Flow chart showing configuration for running the partition without the RoIB. The HLTSVApplication host generates random numbers in place of data. The HLTSVApplication was (25,5,4). The [DCMs](#) and the HLTSVApplication were run on the test bed's most powerful PCs. 68 kHz was achieved by this configuration.

ustb16 has fewer cores and lower cache memory than ustb3, this implies that the rate decreases because of the CPU bottleneck. To eliminate the possibility that this

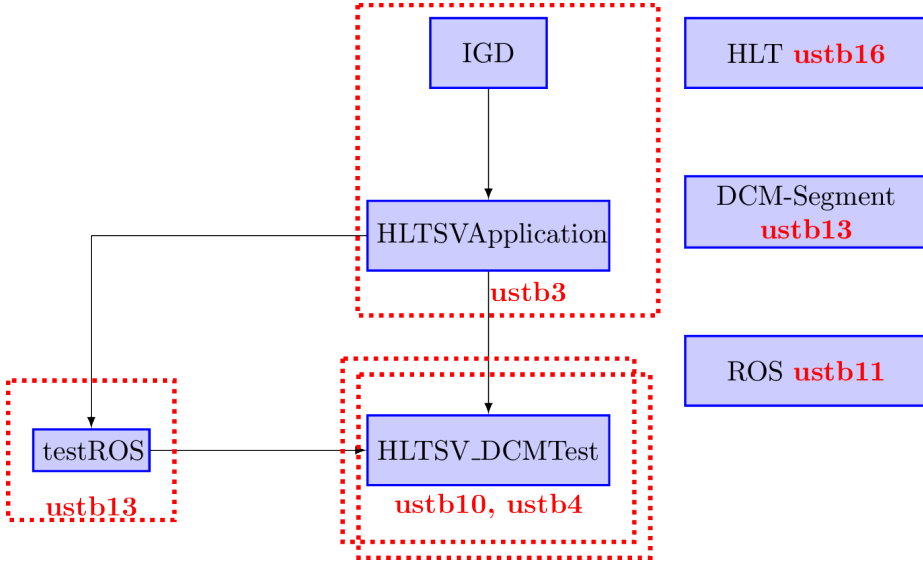


Figure 3.22. Flow chart showing **Configuration 2**. The only difference between this configuration and the one on the left is that there is an additional **DCM** node (ustb4). The rate was boosted to 107 kHz by adding this node. The **HLTSV** can therefore achieve 100 kHz if it runs on a capable PC.

decrease in rate is dependent on the PC architecture⁵ the HLTSVApplication was moved to ustb12, (**Configuration 2c**, Figure 3.24(c)) which has identical memory to ustb16 but is 64-bit; the rate was 85 kHz as well.

Adding a 1-input **RoIB** to this system lowered the **HLTSV** rate even further to 55 kHz. Tests were performed with two and three **RoIB** inputs as well, referred to as **Configuration 3** and shown in Figure 3.25. In this configuration the RoIBSegment was added to ustb21 as well. The rate successively fell with increasing inputs as expected. The third column in Table 3.4 summarizes these rates. The CPU bottleneck therefore does not permit measurement of the rate of fragment transfer between the **RoIB** and the **HLTSV**.

Tdaq 05-03-00 was expected to improve the rates when running partitions with the **RoIB**. Rate changes were not expected for those partitions that do not include the **RoIB**. This is because the main difference between tdaq 05-02-00 and tdaq 05-03-00 is the **FILAR** buffer size. Partitions with no **RoIB** do not use the **FILAR** card so no improvement was expected. For Configurations 2a and 2b the rates were identical to the tdaq 05-02-00 for both version A and B of tdaq 05-03-00. Configuration 2c in both versions A and B produced largely varying rates ranging between 56 kHz and 93 kHz. The average rate over 12 data points for A and B was 81 kHz and 82.5 kHz

⁵ustb16 is 32-bit whereas ustb3 is 64-bit

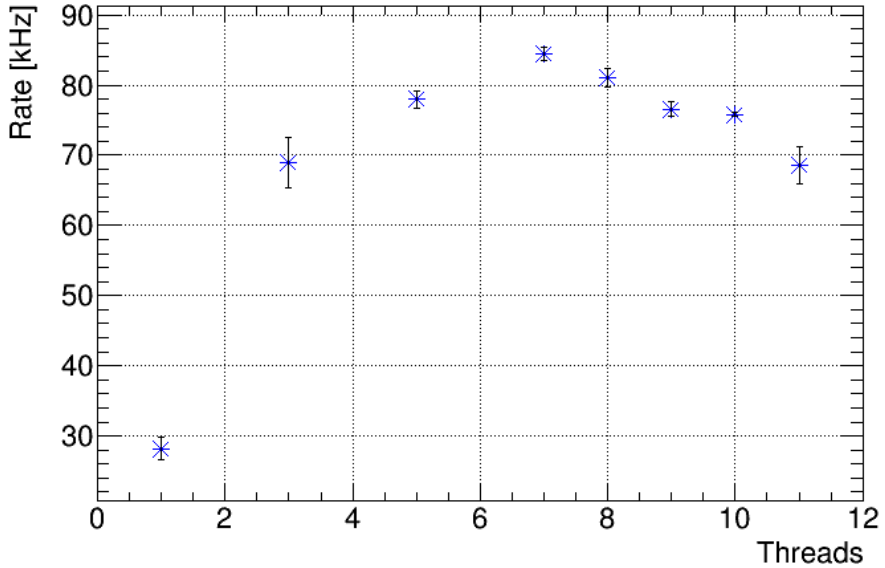


Figure 3.23. Plot showing rate variation with the number of threads. At 7 number of threads the rate is highest and the most stable. The error bars show the instability.

respectively for Configuration 3 (See Table 3.4). These large variations were observed only when the HLTSVApplication was on 32-bit PCs.

For Configuration 3 varying rates were observed in both A and B versions of tdaq 05-03-00. Figure 3.26 shows the rates recorded for these two versions with the RoIB included. The rates recorded in Table 3.4 are averages over the data points in Figure 3.26. Although there is a significant increase in rates from tdaq 05-02-00 to tdaq 05-03-00, due to the instabilities and few data points it is impossible to categorically identify an increase in rate from A to B.

To rule out the possibility of the instabilities stemming from the **FILAR** card, tests similar to Configuration 3 were performed using the **TILAR** card. Instead of replacing the FIILAR with the **TILAR** on ustb16, the **TILAR** and the **FILAR** cards were installed on ustb11; it was therefore necessary to run the HLTSVApplication on ustb11. Table 3.5 and Table 3.6 show the rates for these tests. The instabilities still existed. Again, for unstable rates the entries are just averages over a few data points so it was not possible to tell if there is an improvement from version A to version B of tdaq 05-03-00. There seemed to be an improvement however from tdaq 05-02-00 to tdaq 05-03-00. Also, higher rates were generally observed when the **FILAR** card.

	Configuration	tdaq 05-02-00 [kHz]	tdaq 05-03-00 A [kHz]	tdaq 05-03-00 B [kHz]
Without RoIB	2a	107	107	107
	2b	85	85	85
	2c	85	81 (v)	82.5 (v)
With RoIB	3 (1 input)	55	76 (v)	73 (v)
	3 (2 input)	49	62 (v)	74 (v)
	3 (3 input)	44	59 (v)	62 (v)

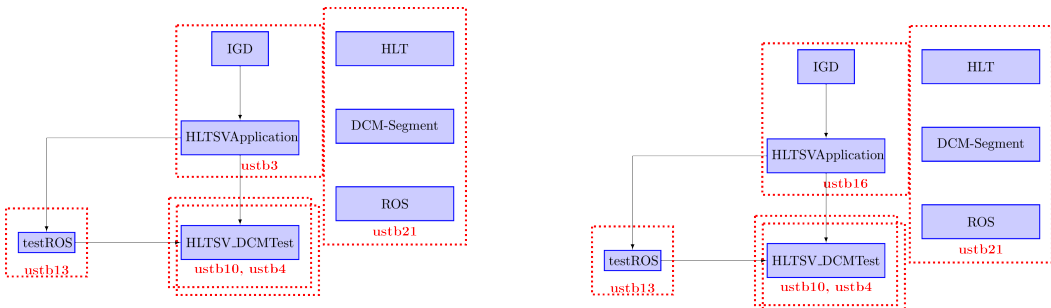
Table 3.4. Summary of HLTSV rates for all tested configurations in all releases of the tdaq software. The *v* next to a rate indicates that the rate recorded is an average over multiple rates because of the large rate variations. Version A and B of software differ over the number of buffers available to the FILAR card; 100 for A and 16 for B. For tdaq 05-02-00 the buffer size is 1. There is a general increase in the rate from tdaq 05-02-00 to tdaq 05-03-00.

Number of RoIB Inputs	tdaq 05-02-00 [kHz]	tdaq 05-03-00 A [kHz]	tdaq 05-03-00 B [kHz]
1	43	60 (v)	57 (v)
2	40	54 (v)	54 (v)
3	36	49 (v)	54 (v)

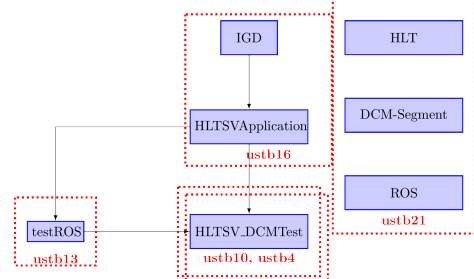
Table 3.5. Summary of HLTSV rates with the RoIB in all releases of the tdaq software using the TILAR card. The configuration is similar to Configuration 3, but with HLTSVApplication running on ustb11. The large variations in rates were still observed so there was nothing wrong with the FILAR card.

Number of RoIB Inputs	tdaq 05-03-00 B [kHz]
1	70 (v)
2	63 (v)
3	55 (v)

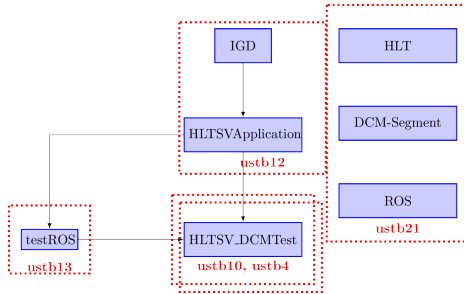
Table 3.6. Summary of HLTSV rates with the RoIB in version B of tdaq 05-03-00 using the FILAR card. The configuration is similar to Configuration 3, but with HLTSVApplication running on ustb11. The average rates observed are larger than those observed with a TILAR card as shown in Table 3.5.



(a) Configuration 2a: When the HLTSVApplication is on ustb3, the rate maxes at 107 kHz. ustb3 is 64-bit. Here its configuration is (25,5,7). This rate ensures a stable rate when the RoIB is added



(b) Configuration 2b: Moving the HLTSVApplication to ustb16 decreases the rate to 85 kHz. ustb16 is 32-bit and has lower number of cores than ustb3



(c) Configuration 2c: Moving the HLTSVApplication to ustb12 achieves 85 kHz maximum as well. ustb12 is 64-bit but has less memory than ustb3. The rates quoted here are from tdaq 05-02-00 (see Table 3.4.) HLTSV rate measurements are hampered by CPU memory and number of cores

Figure 3.24. Illustrations of 3 variations of Configuration 2.

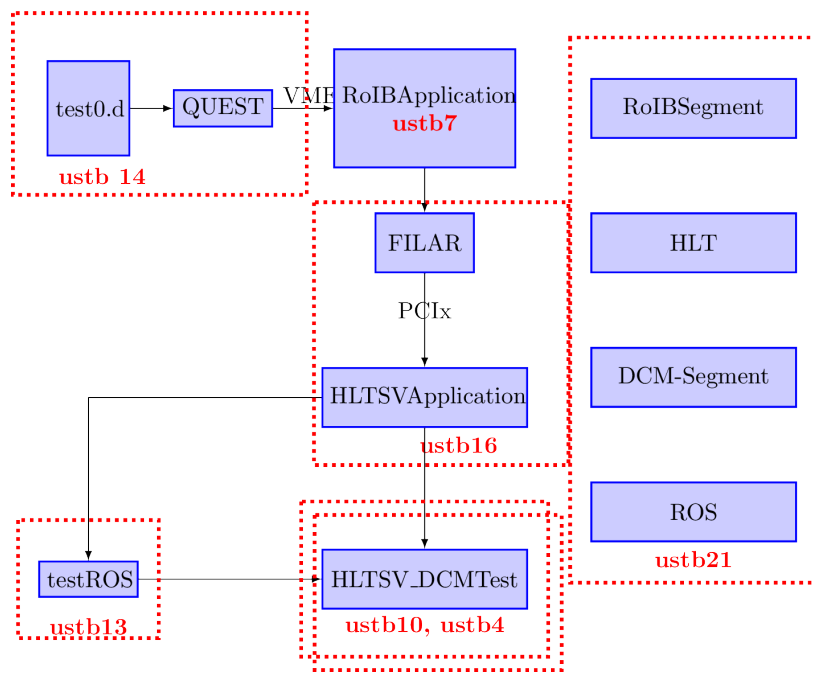


Figure 3.25. Configuration 3: The `RoIB` is added and real data fragments are read. The rate maxes at 55 kHz with 1 `RoIB` input (see Table 3.4) .

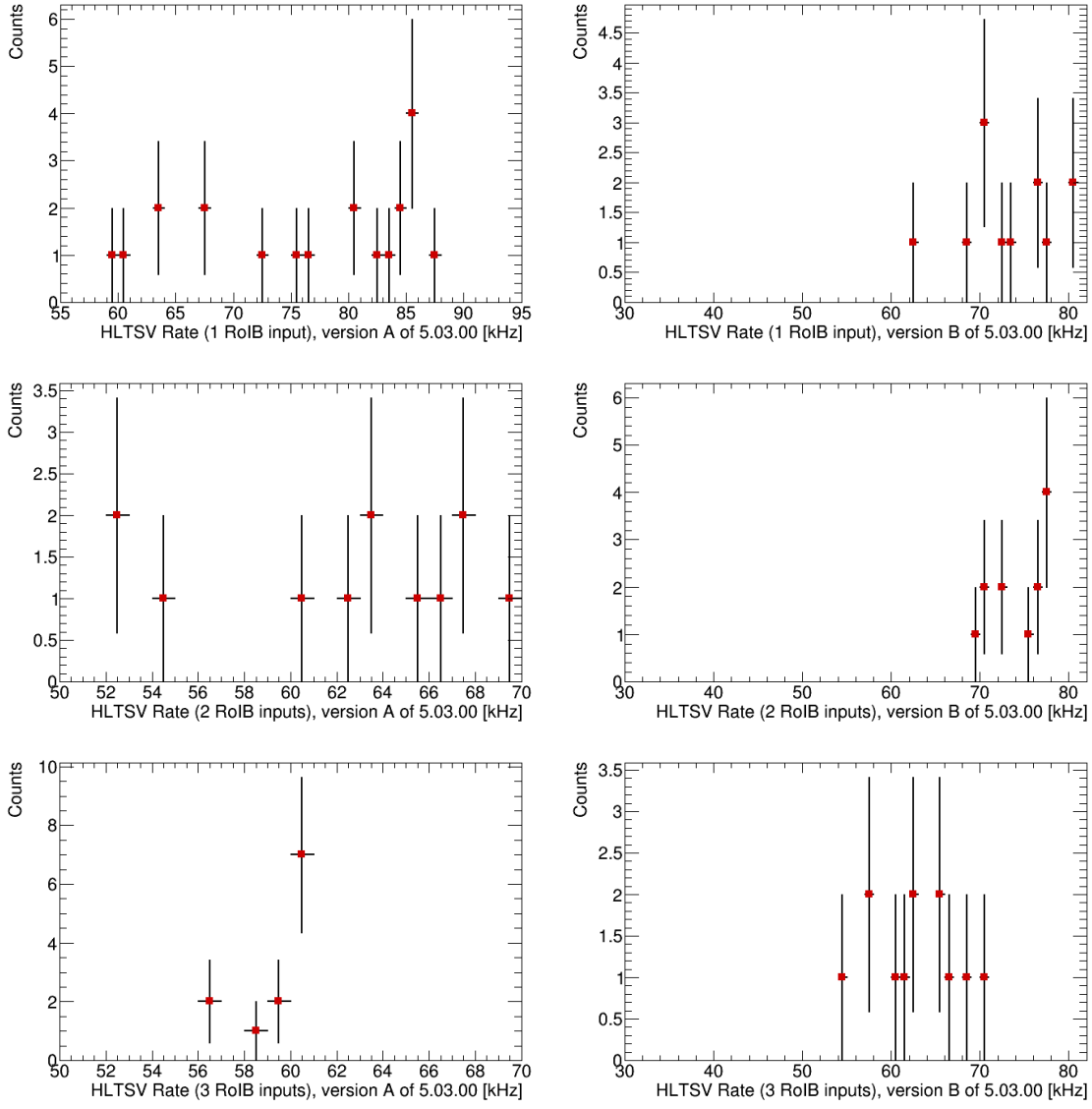


Figure 3.26. Plots showing rate variations under several configurations. Each plot shows rates recorded independently but under Configuration 3. Differences between versions A and B are extensively discussed in the text. These large variations are still not understood, but they are only observed when the HTSVAapplication is running of 32-bit PCs. Their averages are entered in Table 3.4.

Chapter 4

ATLAS Simulation Chain

Simulations are widely used to predict rates of physics processes and their kinematic properties. Within ATLAS, Monte Carlo methods are the simulation of choice. The process of producing the simulation data is referred to in this Chapter as the ‘ATLAS Simulation Chain’. This chain essentially comprises three stages. First is the ‘Event Generation’, during which pp collisions are simulated and physics processes at a high energy scale are generated. In addition, parton showers and subsequent hadronizations are simulated. Second is the ‘Detector Simulation’, during which the particle traversal in the ATLAS detector is simulated. During ‘Digitization’, detector simulation output is converted to ‘digits’. The digitized simulation data is eventually passed through the standard ATLAS Trigger system and saved on disk just like real data.

This chapter is divided into two sections. Event generation is discussed in Section 4.1. Here, cross section for physics processes is formulated, the parton shower is developed, and hadronization models are presented. In addition, Monte Carlo generators used in this thesis are presented. Section 4.2 discussed the ATLAS detector simulation and the subsequent treatment of simulation data.

4.1 Event Generation

As discussed in Section 2.1.2.1, theoretical interpretation of physical processes depends on the energy scales at which they occur. Processes during and after a pp collision occur at a wide range of energy scales, from the TeV to the MeV scale. The factorization theorem [65] fortunately enables separation of cross section calculations at high energy scales from those at low energy scales. The separation is encoded in the factorization factor $\mu_F(Q)$ which is a function of the energy scale Q . For pp collisions at the LHC Q is taken to be such that the produced system can be contained in a radius of just below a femtometer. Theories at these energy scales are then renormalized according to the renormalization group [66]. The renormalization is encoded in the parameter μ_R which, as discussed in Section 2.1.2.1 is a function of the coupling constant α_S . The production cross section of a system X in a pp collision is then formulated as

$$\sigma_{pp \rightarrow X} = \sum_{a,b} \int dx_a dx_b f_a(x_a, \mu_F^2) f_b(x_b, \mu_F^2) \times \sigma_{ab \rightarrow X}(x_a p_a, x_b p_b, \mu_F^2, \mu_R^2) \quad (4.1)$$

The functions $f_a(f_b)$ are the Parton Distribution Functions (PDFs) that describe the probability of a parton of flavor $a(b)$ to have fraction $x_a(x_b)$ of the proton momentum $p_a(p_b)$ at an energy scale determined by μ_F . Since QCD cannot predict all the partons in a proton, PDF shapes are obtained by fitting their ad-hoc analytical forms to experimental data. Some of the groups that maintain these PDFs are CTEQ [67], NNPDF [68], HERAPDF [69], and MSTW [70]. Figure 4.1 shows an example of PDFs obtained from several the MSTW group.

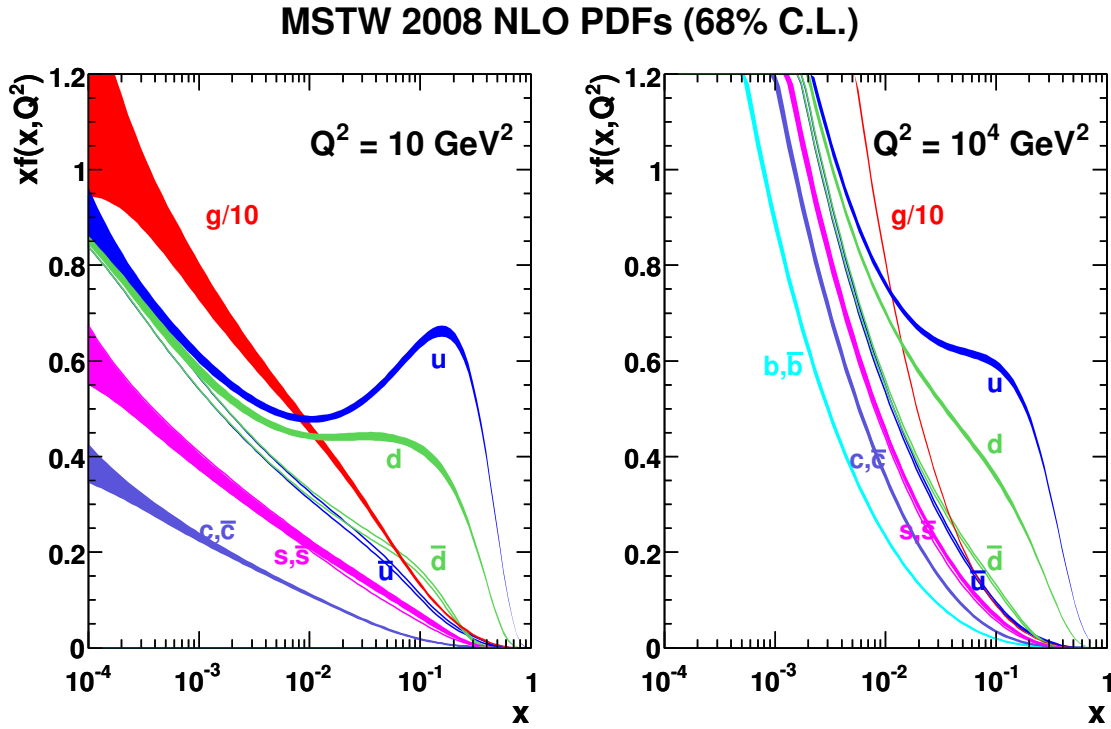


Figure 4.1. Parton distribution functions obtained from the MSTW group. This image was obtained from Ref. [71].

$\sigma_{ab \rightarrow X}$ is the parton level production cross section for system X . The process $ab \rightarrow X$ is known as the ‘hard scatter’. The cross section depends on μ_R^2 , and can be expanded into Equation 4.2.

$$\hat{\sigma}_{ab \rightarrow X} = \sum_{k=0}^{\infty} \int d\Phi_{X+k} \left| \sum_{l=0}^{\infty} \mathcal{M}_{X+k}^l \right|^2 \quad (4.2)$$

\mathcal{M}_{X+k}^l is a matrix element that encodes the amplitude of the process $ab \rightarrow X + k$, where k are the additional partons in the final state. The index l indicates the number of additional corrections to the process, colloquially known as ‘loops’. Essentially, k represents real emmisions from the production in the sense that the additional final state partons alter the final state configuration of the process, and l represents virtual emmisions because the final state remains unchanged. The leading order (LO) matrix element for production of X is \mathcal{M}_X^0 while the LO matrix element for production of $X + k$ is \mathcal{M}_{X+k}^0 . $l = 1$ is known as next to leading order (NLO) and $l = 2$ is next to next to leading order (NNLO). During simulation, the sum in Equation 4.2 is normally truncated, at NNLO at best. The matrix elements are integrated over the phase space of the $X + k$ system and the integral is summed over an infinite number of final state partons. This sum is in practice also truncated after a few terms.

Divergences may arise in the cross section when two final state partons become collinear or when a final state parton becomes collinear with an initial state parton. They may also happen when a final state parton emits a gluon with such a small transverse momentum that the resulting gluon and the parton have an indistinguishable angular separation. The former are known as collinear emissions and the latter as soft emissions. The probability for a parton to not split or emit another parton, that may cause divergences, is encoded in the Sudakov form factor [72]. It will be referred to frequently in later sections. Virtual corrections from loops l also cause divergences. The KLN theorem [73] however guarantees that at any order, divergences from virtual corrections cancel divergences from collinear splitting and soft emissions. So, $\hat{\sigma}_{ab \rightarrow X}$ remains accurate up to high order correction pertubations.

To generate a heavy system through an elastic pp collision the KMR model, introduced in Section 2.2.2, is used. Without loss of generality, the system discussed here is the Higgs boson system, and the process is referred to as the exclusive Higgs process. The collision occurs at a relatively smaller energy scale, $\mu_F^2 \sim m_H$, than the energy scale for inelastic collisions. Consequently, formulation of the corresponding cross section takes a slightly different approach than Equation 4.1, and is encoded in

$$\sigma_{pp(gg) \rightarrow ppH} \propto \hat{\sigma}(gg \rightarrow H) \left(\int \frac{dQ_t^2}{Q_t^4} f_g(x_1, x'_1, Q_t^2, \mu_F^2) f_g(x_2, x'_2, Q_t^2, \mu_F^2) \right)^2 \quad (4.3)$$

where $\hat{\sigma}(gg \rightarrow H)$ is the parton-level cross-section for the gluon fusion process that produces the Higgs boson, which is calculated at LO using matrix elements introduced above. The functions f_g are the generalized gluon densities. These are a non-trivial combination of the gluon PDFs and the Sudakov form factor. The Sudakov form factor is introduced because the process of interest is that in which the initial

state gluons do not radiate any other gluons. The generalized gluon densities take x_1, x_2 , which are equivalent to Equation 4.1's x_a, x_b , and the factorization scale μ_F^2 as inputs. The variables x'_1 and x'_2 are the fractions of the momentum carried by the exchanged third gluon with respect to the momenta of protons P_1 and P_2 . Finally, the gluon densities are integrated over the exchanged (third) gluon transverse momentum Q_t . Figure 4.2 illustrates the production of the exclusive Higgs boson, with labels of the parameters discussed above.

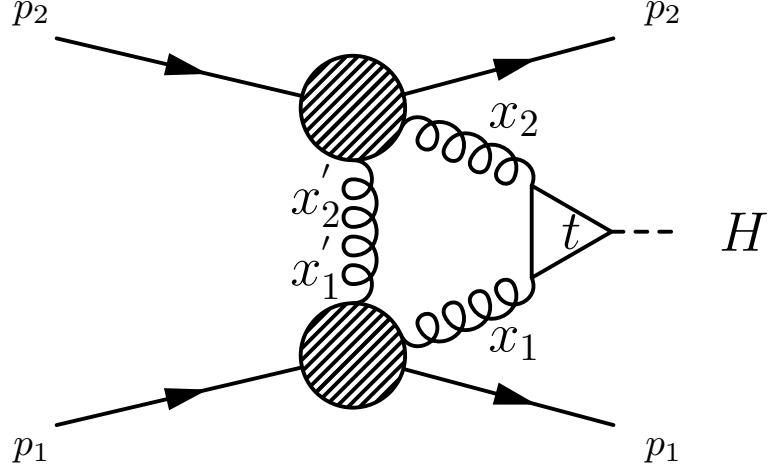


Figure 4.2. Feynman diagram for the exclusive Higgs boson production.

4.1.1 Parton Shower Development

In simulation, shower development is achieved by perturbatively expanding on the hard scatter process. For a pp collision with k final state partons and differential cross section $d\sigma_k$, the differential cross section of a process with $k + 1$ final state partons is

$$d\sigma_{k+1} = d\sigma_k \times \frac{\alpha_S(t)}{2\pi} P_{a,bc}(z) \frac{dt}{t} dz \frac{d\phi}{2\pi} \quad (4.4)$$

where the additional parton is obtained from a split or emission from one of the k partons, which for reference can be called the ‘original parton’. In the multiplicative factor, t is the energy of the original parton, z is the fraction of the energy carried by the additional parton in relation to t , and ϕ is the angular separation between the additional and the original partons. $P_{a,bc}$ is the probability that a parton of flavor a splits or transforms into partons of flavor b and c . So during simulation, given an

energy scale t , Equation 4.4 is sampled and partons are emitted at an energy scale t' . If t' is below a threshold scale, the shower development is terminated. Otherwise, the process is repeated recursively for each parton. The threshold for t' known as the infrared cut-off, and it is about 1 GeV. Figure 4.3 shows a schematic of a parton shower developed in this manner.

4.1.2 Hadronization

Hadronization is the process that occurs immediately following the parton shower, when colored partons combine to form color-singlet hadrons. These hadrons are dominated by pseudoscalar and vector mesons, and spin-1/2 and spin-3/2 baryons. They are referred to as primary hadrons, and the hadrons that they decay to are referred to as secondary hadrons. The hadronization energy scale by construction is equal to the infrared cut-off of the parton shower. Phenomenological models are implemented in several event generators to describe hadronization, the most common being the *string* and *cluster* models.

The string model utilizes the observation from lattice QCD [74] that the potential between a color charge dipole grows linearly with the distance, r , between the two charges. The Coulomb potential from the electric charge, being inversely proportional to r , is negligible at large r . In the model, the potential between the two partons is represented by a quasi-elastic string that holds the two partons together. As r grows, it may become more favorable to produce a $q\bar{q}$ pair from the vacuum than to maintain a tight string. Each of the parton in the $t\bar{t}$ pair attaches itself to one of the partons in the original dipole through a new string, essentially doubling the number of dipoles in the system. Gluons can also be created from the vacuum as loops or ‘kinks’ on the string, and may subsequently split into a $q\bar{q}$ pair. Mass or flavor of the produced quarks and gluons is determined by the energy in the string breakup process. Because c and b quarks are heavy, they are rarely produced at the infrared cut-off scale (~ 1 GeV). Baryons are produced when pairs of di-quarks are formed during the string break-up, instead of a $q\bar{q}$.

The main idea behind the cluster model is that gluons at the end of the parton shower are forced to split to $q\bar{q}$ pairs. The flavor of these $q\bar{q}$ pairs is determined by the gluon energy. Again $b\bar{b}$ and $c\bar{c}$ are rarely produced at the 1 GeV energy scale. After the forced splits, a set of color-singlet hadrons is obtained by clustering pairs of quarks. Heavy singlets are allowed to decay to lighter ones at this stage. The formed clusters, in general, are regarded as excited mesons because they by construction will comprise two partons. They eventually decay to other hadrons that are more stable, including baryons.

All these particles are saved in a record that documents their production, decays and splits. This record is known as the ‘truth’ record.

4.1.3 Underlying Event and Pileup

Apart from the primary hard scatter partonic interaction, additional activity is more often than not observed within a pp collision. This additional activity is collectively referred to as the *underlying event*. The underlying event is dominated by additional partonic interactions. These additional interactions introduce additional parton showers in the event. These showers lower the resolution for measuring observables for the primary event, so they eventually have to be corrected for. Event generators are available that account for the underlying event and they are tuned to match what is observed in data.

Additional activity from other pp collisions within the same bunch is called *in-time pileup*, otherwise it is called *out-of-time pileup*. During Run I of the LHC, on average 20.7 extra pp collisions from pileup were observed. During Run II, this number was even larger. Pileup is factored into the simulated event during the detector simulation part of the chain, as will be discussed in Section 4.2.

Figure 4.3 illustrates the development of both the hard scatter event and a secondary event, which contributes to pileup events. The red blob in the figure represents the hard scatter event surrounded by parton showers and other particles undergoing Bremsstrahlung. The purple blob similarly represents the secondary pileup event. The light green blobs represent hadronization. The hadrons formed decay to the dark green blobs which continually decay until stable final state particles are reached. The yellow lines represent soft photon radiation.

4.1.4 Monte Carlo Generators

PYTHIA6 [76] is the standard event generator for ATLAS. Written in FORTRAN, it generates the hard scatter event at LO and implements the parton showering and hadronization models. Event generation uses both hard and soft scale models, so it is able to generate the underlying event as well. Its parameters were tuned to fit ATLAS conditions. A similar generator called PYTHIA 8 [77], which was written in C++, exists.

Because PYTHIA generators approximate the hard scatter event just to leading order, other generators are used to generate the hard scatter event and are interfaced to PYTHIA for parton showering and hadronization. POWHEG-Box [78–82] is one such NLO generator. It is normally interfaced to PYTHIA 8 for parton showering and hadronization. ALPGEN [83] is another leading order generator. However, it enables more sophisticated generation of certain final states such as those with a W or Z and multiple jets. It is also normally interfaced with PYTHIA 8. SHERPA [84], a leading order generator, is also usually interfaced with PYTHIA 8 for hadronization and parton showering. This is because it is expected to give a more accurate description of final states with a large number of partons, than PYTHIA 8.

HERWIG [85], written in FORTRAN, is another leading order generator popular within ATLAS. Its C++ counterpart, HERWIG++ [86], also exists. The underlying

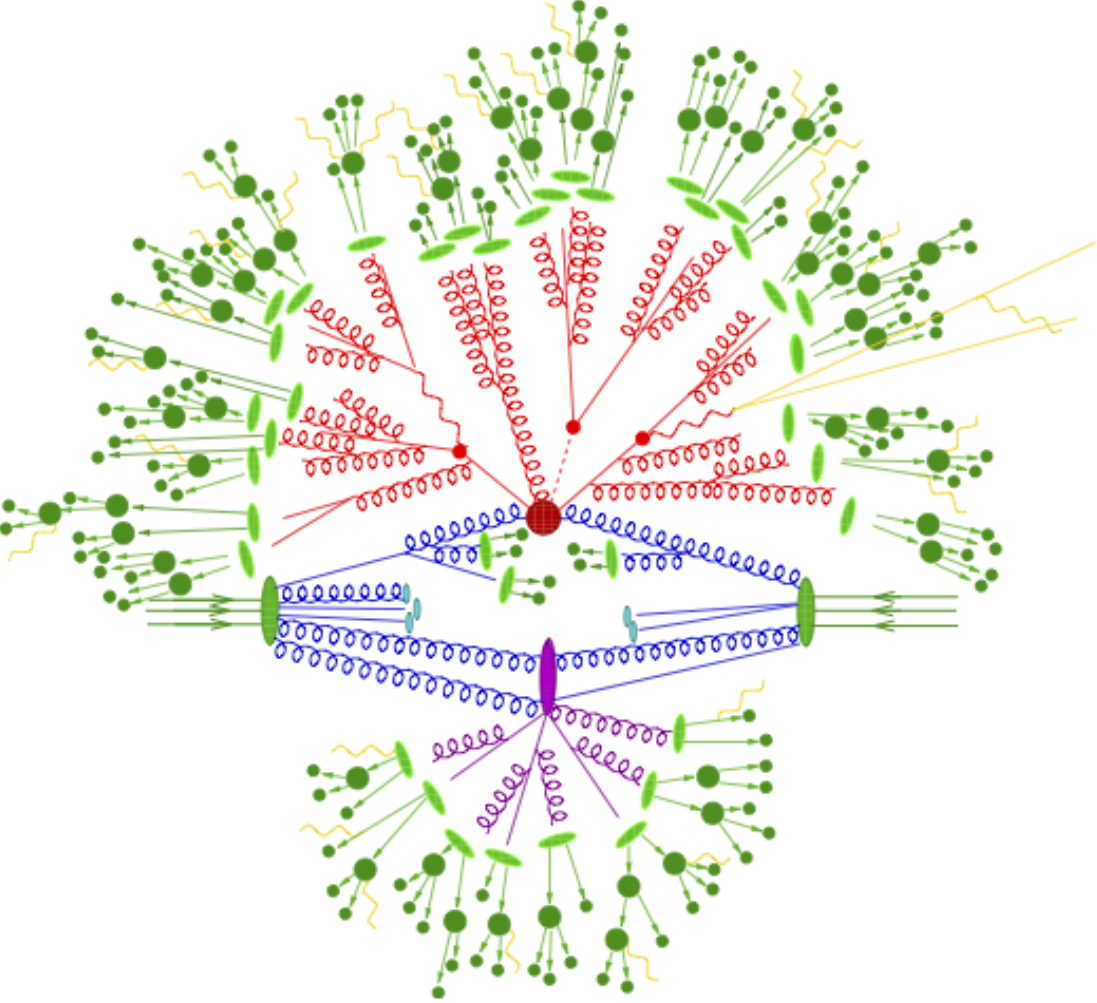


Figure 4.3. An illustration of the parton shower development, hadronization and hadron decays. Taken from Ref [75].

event is not included within HERWIG, so it is usually used with JIMMY [87] because JIMMY includes the underlying event. An NLO generator usually interfaced with HERWIG and JIMMY is MC@NLO [88]. It is used to produce events with t quarks because it provides a better representation of top quarks than PYTHIA 8. Another lesser known generator that is good at generating WW pairs is GG2WW [89].

There are some generators specific to exclusive processes. For the exclusive Higgs boson, FPMC [90] uses the KMR model to generate the process at leading order. Processes like the exclusive SM $\gamma\gamma \rightarrow W^+W^-$ and $\gamma\gamma \rightarrow \ell^+\ell^-$, are generated by HERWIG++. Parton showering and hadronization in both FPMC and HERWIG++ generators are implemented in JIMMY. Some other variations of exclusive processes are done best in LPAIR 4.0 [91]

While all Monte Carlo generators used in this thesis have been mentioned, this discussion is far from comprehensive. A more detailed discussion can be found in Ref [92].

4.2 Detector Simulation and Data Management

Particles with lifetimes such that they can traverse at least a femtometer from the collision point are considered stable. Hadrons from parton hadronization are also considered stable. These are run into a simulation of the ATLAS detector to mimic real particles.

Data used to simulate the ATLAS detector is stored in several databases. This data is made up of details describing physical volumes and material types. Physical volumes are used to model sub-detector components, made up of their corresponding material types. Ultimately, this data comprises a complex arrangement of hundreds of materials and hundreds of thousands of physical volumes. For example, calorimeter sub-detectors are made up of over 100 000 physical volumes that require about 40 MB of memory to load. The total memory required to load the entire ATLAS detector from these databases is almost 300 MB.

Simulation of the detector's response to particles is handled by GEANT4 [93]. GEANT4 is a toolkit that provides models of how particles traverse through several geometries and material types. During Run I, GEANT4 version 9.4 was used. Version 9.6 was used during Run II. This toolkit allows the ability to turn on and off detector components, reducing the memory needed to load the detector. It also allows realignments of sub-detectors to match simulation conditions to those in specific data runs. This flexibility has enabled several standardized detector setups that run faster than loading the whole detector. One of these setups that is used in this thesis is ATLFAST2 [94]; it uses full simulation for the Inner Detector and the Muon Spectrometer, but uses a simplified version of the calorimeter simulation.

Particle decays, such as photon conversions, are added to the truth record at this stage. The detector response, through so-called ‘hits’, is stored in a separate file. The hits are inputs to the digitization stage, where the analog signals are converted to ‘digits’. Other simulated pp collisions are overlaid on the primary collision at a known rate to mimic pileup effects. This rate would later be adjusted according to the rate extracted from data. Detector noise is also added to the event at this stage. The event is then passed through the L1 trigger system. Subsequent treatment of simulation data is identical to that of real data except that simulated events that fail the L1 trigger are not discarded. The failure is however recorded in the event. The output of both simulated data and real data is in the Raw Data Object (RDO) format. This output is finally passed through the HLT, and particles are reconstructed from the digitized signals. This reconstruction is discussed in the next chapter.

Chapter 5

Physics Objects

The link between the particles introduced in Chapter 2 and the experimental setup introduced in Chapter 3 is established in this chapter. The signatures printed by these particles in the ATLAS detector are referred to here collectively as *physics objects*. Dedicated algorithms are used to *reconstructed* these physics objects from detector electrical signals. In some cases, other algorithms are used to further *identify* the physics objects from the reconstructed objects. Reconstruction and identification procedures are described in this chapter in detail for each of the physics objects used in analyses discussed in Chapters 6 and 7. Photons were not directly used in either analysis, so their reconstruction and identification are not discussed here. Rather, sufficient references are supplied.

5.1 Tracks

As explained in Chapter 3, charged particles leave traces that describe their traversal paths in the ATLAS detector’s Inner Detector (ID) and the Muon Spectrometer (MS). These traces are known as *tracks*, and the methodology of recording these tracks is referred to as *tracking*. In Sections 3.2.1 and 3.2.3, it was shown that the MS exclusively tracks muons while the ID tracks any charged particles. Because of this difference in purpose, different approaches are taken when reconstructing tracks in the MS and ID. Since any relatively long-lived charged particles leave tracks in the ID, no separate identification schemes are applied to identify tracks in their own right. This section discusses tracking systems in the ID and MS.

5.1.1 Inner Detector Tracks

Track reconstruction in the Inner Detector begins with the identification of *spacepoints*. These are spatial points per sensor that were hit by a charged ionizing particle. These hits are collected in the Pixel Detector and the Semi-Conductor Tracker (SCT) which are collectively known as Silicon Detectors. In the Pixel Detector a hit on a pixel provides a 2-dimensional spacepoint, while a hit on an SCT sensor provides a 1-dimensional spacepoint; the other dimension in the SCT is provided by

another sensor glued back-to-back and at an angle to the aforementioned sensor, as described in Section 3.2.1. The spacepoints in the silicon detectors are fitted using the Kalman Fitter [95] which adds spacepoints to the fit recursively, making it convenient for online real time processing.

The result of each fit is characterized by a score that is calculated from the quality of the reconstructed track and the χ^2 value of the fit. Track quality is determined by the number and *type* of hits that it constitutes. The type of a hit refers to its location in the ID: Pixel Detector hits are given more weight than SCT hits. At this stage of reconstruction different tracks may share hits, leading to ambiguities. These ambiguities in hits are resolved by giving preference to a track with the highest score, refitting the other tracks without the ambiguous hits, and re-evaluating the scores. This process is repeated until all ambiguities are resolved.

Hits from the Transition Radiation Tracker (TRT) are also fitted using the Kalman Fitter to tracks reconstructed from the silicon detectors. If the score of the resultant track improves the score of the silicon track, the TRT component is added. Otherwise it is reconstructed as an independent track. Tracks from the TRT are sometimes used as seed for track reconstruction, but tracks used in this thesis are reconstructed with hits from the silicon detector as seeds.

Reconstructed tracks are parametrized by the point of their closest approach to either the beam-line or the interaction point (IP). The beam-line or the IP is known as the *perigee*. The perigee is in turn parametrized by *perigee parameters*. Using the beam-line as reference is a more useful parametrization because the beam-line does not always align perfectly with the z -axis. The most common perigee parameters are d_0 and z_0 , and their definitions are illustrated in Figure 5.1. d_0 is the signed distance of the track's closest point to the z -axis, and z_0 is its z -coordinate. Other parameters defined at the perigee are the charge-momentum ratio, the angle with the x -axis in the xy plane, and the angle with the z -axis in the rz plane. Figure 5.1 illustrates most of them.

If a group of tracks reconstructed in the ID are extrapolated to a single spatial point in the ID, that point is reconstructed as a vertex. A vertex essentially represents a point where a particle, or particles, decay or split into secondary particles that leave tracks in the ID. The vertex with the highest sum of track transverse momentum, p_T , is labeled the primary vertex (PV). This is the vertex at which the hard scatter occurs. Since the PV does not always coincide with the IP, track perigees are usually measured relative to the PV.

5.1.2 Muon Spectrometer Tracks

Seeds for MS track reconstruction are extracted from the precision sub-detectors: Cathode Strip Chambers (CSCs) and Monitored Drift Tubes (MDTs). From MDTs drift circles are processed, and from CSCs *clusters* are built. Signals from drift circles

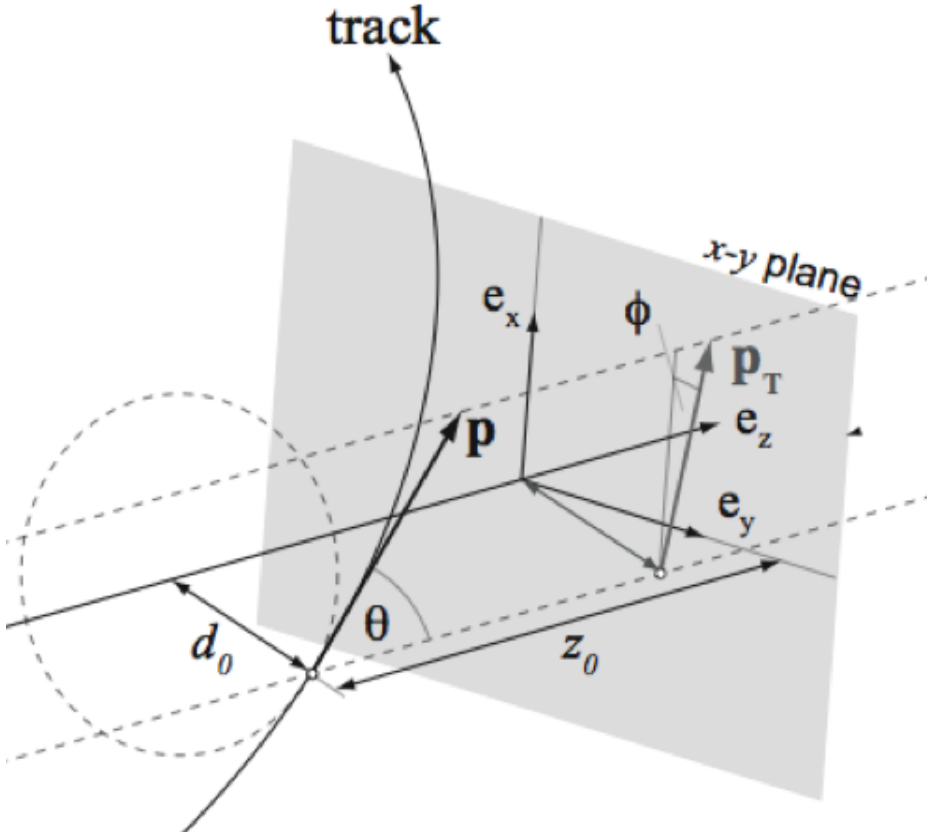


Figure 5.1. Illustration of perigee parameters. The most common of these are d_0 and z_0 . The perigee may be defined relative to either the beam-line or the interaction point. The analysis in Chapter 7 utilizes this choice. Illustration taken from Ref [96].

and clusters are used as inputs to pattern recognition algorithms to form *segments*, which are combined and fitted to form the reconstructed track.

Clusters in the CSCs are muon hits in each chamber that give a 1-dimensional measurement of position. Since CSCs are mounted on wheels in the end-caps and are segmented in ϕ , separate ϕ and η clusters are obtained. A set of clusters is fitted using the Hough transform method [97], which is more suited to fitting non-linear tracks than the Kalman Fitter, to form separate η and ϕ segments. Combining the two gives a 2-dimensional position and a direction to each cluster.

Segments in the MDTs are reconstructed from fitting drift circles measured from drift tubes in two neighboring stations. Two outer MDT hits are picked as seeds and straight lines are fitted between them, accounting for hits in the middle layer. With a minimum of 3 hits required to form a segment, the fit with the highest number of hits is picked. The quality of an individual hit in an MDT is best described by Figure 5.2. When the track path perfectly matches the drift radius the MDT is considered to be *on track*. When the drift radius is too small compared to the track path the MDT

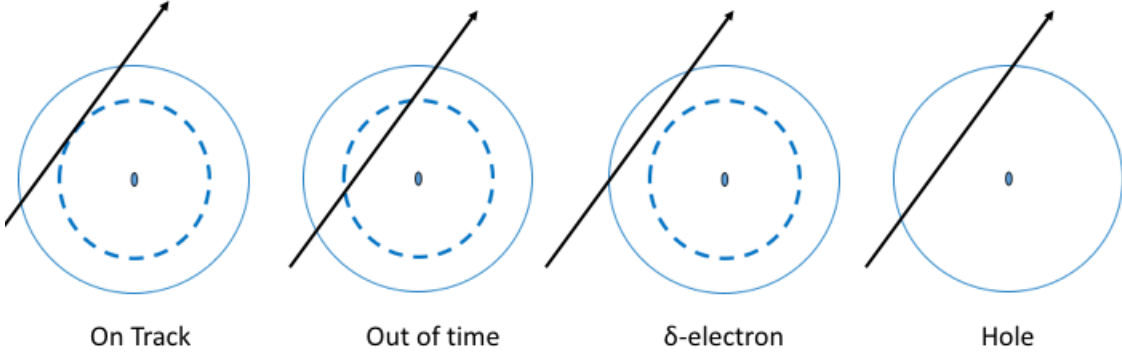


Figure 5.2. Illustration of track fitting in the MS. A track fit to an MDT can be any of 4 cases: track path coincides with drift circle (on track), is smaller than drift circle (out of time), is larger than drift circle (δ -electron), and no drift circle (hole). Track quality is evaluated by the multiplicity of these cases..

is referred to as having a δ -*electron*. When the drift radius is too large to match the track, the MDT is considered *out of time*, and when there is no drift circle the MDT is known as a *hole*. A segment is scored by $N_\delta + N_{out} + N_{hole}$, where the smaller the sum the higher the quality. Ambiguous segments are recursively resolved with the score, the χ^2 and the overall number of hits. Just like TRT hits, hits from the RPCs and TGCs are fitted to existing segments if they improve the segment score.

Full track reconstruction is done by fitting segments, starting from segments farthest from the IP and taking into account the bending caused by the magnetic field. Each track's χ^2 and number of hits are evaluated and used to recursively resolve ambiguities. Finally, the reconstructed tracks are extrapolated to the beam-line and their d_0 and z_0 are extracted.

5.2 Electrons

5.2.1 Reconstruction and Identification

Electrons reconstructed in the ATLAS detector are classified into *central* and *forward*, where central electrons are those within $|\eta| < 2.5$ and forward electrons are those within $2.5 < |\eta| < 4.9$. Since central electrons fall within the Inner Detector (ID)

coverage, they make use of both the EM Calorimeter and the ID measurements while forward electrons rely just on the calorimeter information. As a result, calorimeter requirements on forward electrons are much more stringent than on central electrons.

Central electrons are reconstructed by matching energy clusters in the EM Cal to tracks in the ID, where a cluster is a group of calorimeter cells. The sliding window algorithm (introduced in Section 3.2.4) is used to find these clusters by searching for calorimeter cells with energy deposits greater than 3 GeV in windows of size 3×5 calorimeter cells in $\eta \times \phi$ ¹. The window is made larger in the ϕ direction to account for any magnetic field effects. This cluster search begins in Layer 2 of the EM Cal. Upon locating the cluster center in Layer 2 energy deposits in the corresponding presampler, Layer 1 and Layer 3 are collected and summed. During Run I, using the sliding window algorithm, the efficiency for finding electrons with $E_T = 7$ GeV was 95%, 99% for those with $E_T = 15$ GeV and 99.9% for those with $E_T = 45$ GeV [98].

Forward electrons are reconstructed using *topological clusters* [99], whose clustering algorithm differs from the sliding window algorithm. Cells with large signal to noise ratio are used as seed and added to the cluster. The cluster grows by iteratively adding neighboring cells with a signal to noise ratio above a threshold slightly less than the seed threshold. Perimeter cells are added on the cluster by imposing an even lower energy threshold. This creates 3-dimensional clusters of varying energies. During Run I and Run II the seed threshold was 6 GeV and both the neighbor and perimeter thresholds were 3 GeV. This topological clustering scheme is known as EM 633, named after energy thresholds from seeds, neighbors and perimeters.

Only tracks with $p_T > 0.5$ GeV, at least two hits in the Pixel Detector, at least seven total hits from the Pixel Detector and the SCT are considered for matching clusters in the EM Cal. These tracks are extrapolated from their last hit in either the Silicon Detectors or the TRT to Layer 2 of the EM Calorimeter. A track and a cluster are considered a match if the cluster center and the track are within $|\Delta\eta| < 0.05$ and $|\Delta\phi| < 0.1$. The matching window in the ϕ coordinate is larger to allow for brehmsstrahlung losses due to the magnetic field. In the case of multiple tracks being matched to one cluster, preference is given to the tracks with most hits in the Silicon Detectors, based on the scoring method discussed in Section 5.1.1, and the smallest ΔR between the track and the EM Calorimeter cluster. A central electron is considered reconstructed if a cluster is matched to a track, otherwise it is reconstructed as a photon. To minimize background, only electrons with at least 5 GeV energy are reconstructed.

Effectively, a reconstructed electron is characterized by the following : the cluster energy, the estimate of the energy deposited in the ID, EM Calorimeter presampler energy, lateral cluster energy leakage and leakage of energy into the hadronic calorimeter. These five components are combined to estimate the total electron energy. At 0.5 MeV, the electron mass is taken as zero in the ATLAS detector. This

¹ The magnetic field bending plane in the ID is the $r\phi$ plane. The calorimeters may be subject to this field as well, albeit significantly weaker than in the ID

approximation makes the total electron transverse energy equal to its p_T . For central electrons the (η, ϕ) position is extracted from the tracks and for forward electrons it is extracted from the topological clusters.

Reconstructed electrons are grouped into categories of several identification requirements. The variables that define these categories describe cluster (which in turn describes an electron shower) and track properties, as well as criteria used for track-cluster matching.

Of prime importance in describing a shower is the extent of hadronic leakage and the lateral shower shape. Given that $E_{T,\text{had}1}$ is the transverse energy in Layer 1 of the hadronic calorimeter behind the electron cluster, $E_{T,\text{had}}$ is the transverse energy in the whole hadronic calorimeter section behind the electron cluster, η_2 is the η position of the cluster in the EM calorimeter, and E_T is the ratio of the cluster energy to $\cosh \eta_2$, the hadronic leakage is defined as

$$\text{Hadronic Leakage} = \begin{cases} E_{T,\text{had}1}/E_T, & \text{if } |\eta_2| < 0.8 \text{ and } |\eta_2| > 1.37 \\ E_{T,\text{had}}/E_T, & \text{if } 0.8 < |\eta_2| < 1.37 \end{cases} \quad (5.1)$$

The lateral shower shape is described by, among many other variables, $R_\eta(37)$ defined as

$$R_\eta(37) = E(237)/E(277) \quad (5.2)$$

where $E(237)$ is the energy deposited in Layer 2 of the EM Calorimeter in a rectangle of size 3×7 cell units in $\eta \times \phi$, centered around the cluster center. $E(277)$ is similarly the energy deposited in a rectangle of size 7×7 cell units. Hadronic leakage and lateral shower shapes are very efficient in rejecting π^\pm decays and wide showers. To reject electrons from π^0 decays Layer 1 of the EM Calorimeter is used because of its finer granularity in η . As already discussed in Section 3.2.4 π^0 decays result in two energy maxima. To search for these two energy maxima several variables are defined in a $0.125 \times 0.2 \Delta\eta \times \Delta\phi$ window around the cell with the highest energy deposit (the so-called hottest cell). Given that E_{2nd} is the energy deposited in the second hottest cell, that E_{min1} is the energy deposited in the cell with the least energy between the hottest and second hottest cell, $\Delta E = E_{2nd} - E_{min1}$ is an excellent variable for picking up the two energy maxima due to π^0 s.

While calorimeter shower analysis significantly reduces backgrounds due to charged hadron decays, background due to photon conversions are better reduced by track analysis. First, track quality requirements are demanded on candidate electron tracks: at least nine Pixel Detector hits where one of the hits must be in the B-layer, and the transverse impact parameter either with respect to the beamline or to the primary vertex is demanded to be less than a threshold value. To ensure track-cluster matching, in addition to the $\Delta\phi, \Delta\eta$ requirements discussed in the preceding section, the energy measurement from the calorimeter is compared to the p_T from the track bending.

Categorization of electron identification is successive and inclusive. This means that first a category with minimal requirements is defined; latter categories are just sub-sets of the first category, with more stringent requirements. The categories are a trade-off between the signal efficiency (ratio of identified electrons to reconstructed electrons) and background rejection. Reconstructed electrons that pass the first category requirements are referred to as *loose*. Subsequent categories are referred to as *medium* and *tight*. In general loose electrons pass hadronic leakage and lateral shower shape requirements. Medium electrons are additionally pass shower shape requirements in Layer 1, reducing π^0 contamination. Tight electrons additionally use track quality and track matching criteria to reduce backgrounds due to photon conversions.

Rather than directly imposing requirements on variables to distinguish between signal electrons and background objects, a multivariate technique is used for electron identification for analyses described in this text. The discriminant used is the log-likelihood function $\log d_{\mathcal{L}}$ [100], where

$$d_{\mathcal{L}} = \frac{\mathcal{L}_S}{\mathcal{L}_S + \mathcal{L}_B}, \quad (5.3)$$

where $\mathcal{L}_{S,B}$ are likelihood functions on signal electrons and background objects respectively. The $\mathcal{L}_{S,B}$ are functions of probability density functions (pdf) obtained by training a multivariate classifier on signal electrons or background objects from Monte Carlo simulations using variables discussed in the preceding paragraphs as inputs. A generalization of a likelihood function is

$$\mathcal{L}(\vec{x}) = \prod_{i=1}^n P_i(x_i) \quad (5.4)$$

where \vec{x} is a tuple of input variables and P_i is a pdf for variable i . Categorization into identification categories is achieved by directly cutting on $\log d_{\mathcal{L}}$, where $d_{\mathcal{L}}$ is computed using successively more variables for loose, medium and tight categories.

5.2.2 Measurement of efficiencies, corrections and uncertainties

This section quantifies the performance of the electron reconstruction and identification methods discussed so far.

5.2.2.1 Efficiency

Electron identification and reconstruction suffers from inefficiencies due to detector limitations. These inefficiencies are measured in data and in Monte Carlo simulation and compared, ultimately correcting the Monte Carlo simulation predictions.

The total efficiency of reconstructing and identifying electrons for use in an analysis can be factorized into its major components as

$$\epsilon_{total} = \epsilon_{reco} \times \epsilon_{id} \times \epsilon_{trigger} \times \epsilon_{isolation} \quad (5.5)$$

where ϵ_{reco} is the efficiency of reconstructing an electron once an electromagnetic cluster is found in the EM Calorimeter, and ϵ_{id} is the efficiency of categorizing the reconstructed electron as loose, medium or tight. $\epsilon_{trigger}$ is the efficiency of an identified electron to pass a particular trigger and $\epsilon_{isolation}$ is the efficiency of an electron that has passed the trigger to pass an isolation selection criteria. These efficiencies are computed successively. For example, an electron that passes the trigger selection must have also passed identification, and reconstruction. ϵ_{reco} is particularly important because it quantifies track reconstruction and track-cluster matching. Electrons, at a mass of 0.5 MeV, suffer more from brehmsstrahlung as they traverse material in the ID than heavier particles. This results in unpredictable deviations in the electron track path in the ID, leading to relatively poor reconstruction. ϵ_{id} on the other hand quantifies the performance of the Log Likelihood function described in the previous section. This section discusses the method for extracting ϵ_{id} and ϵ_{reco} .

For studies discussed in this text ϵ_{id} and ϵ_{reco} were extracted from $Z \rightarrow ee$ and $J/\psi \rightarrow e^+e^-$ events in data to cover a wide electron p_T range. In both these cases, the *tag-and-probe* method was utilized [101]. Here, one electron was fully reconstructed and identified with the highest efficiency possible. This is known as the tag electron. The other electron was used to probe the selection efficiency in question by requiring it to satisfy conditions either before or after the selection was applied. For $Z \rightarrow ee$ events, the tag electron was tightly identified, matched to a tight trigger electron, had $E_T > 20$ GeV and lied outside the calorimeter transition region ($1.37 < |\eta| < 1.52$). For $J/\psi \rightarrow e^+e^-$ events the tag electron was tightly identified, matched to a tight trigger electron object and have $E_T > 5$ GeV. In both cases, a tag object was required to be present, with a quality dependent on the type of efficiency being measured. For $Z \rightarrow ee$ events, m_T of the probe object and the tag electron was required to lie between 80 and 100 GeV.

To evaluate systematic uncertainties in the efficiencies being measured, several efficiency measurements with variations on the event selection criteria were performed. For example, the tag electron was modified or the background estimation was varied.

For ϵ_{id} a reconstructed electron was used as a probe. In $Z \rightarrow ee$ events this probe electron had to have $E_T > 10$ GeV. Measurements were extracted from two dimensions: electron E_T and η . The decision to bin measurements in η was motivated by the fact that brehmsstrahlung losses depend on the amount of material that the electron traverses in the ID, which is in turn dependent on η . Results from $Z \rightarrow ee$ and $J/\psi \rightarrow e^+e^-$ events were combined, including systematic uncertainties. Figure 5.3 shows these efficiencies binned in E_T and η , in both Monte Carlo simulation and data. In general, Monte Carlo simulation modelling agrees reasonably with data. The background rejection was also observed to be as large as 400.

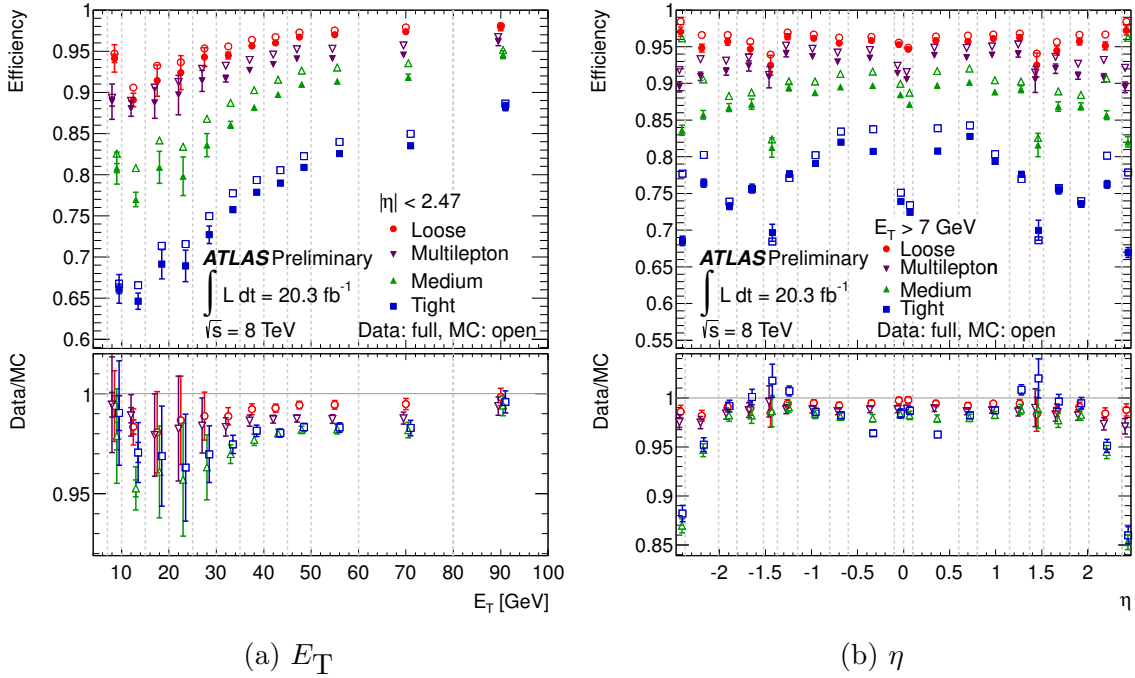


Figure 5.3. Plots of electron identification efficiencies during Run 1, binned in E_T , and η . Taken from Ref [101].

To measure ϵ_{reco} with $Z \rightarrow ee$ events an EM cluster was taken as the probe object. This cluster was required to be isolated from electrons, to reduce backgrounds from photons. Measurements were binned in E_T and η . Figure 5.4 shows the measurements obtained data and Monte Carlo simulations. Overall there is reasonable agreement between data and Monte Carlo predictions. For the data set used for the analysis in this text (2012), the reconstruction efficiencies are at least 90%.

5.2.2.2 Calibration

Electron energy loss in the material upstream or beyond the Lar calorimeters, or outside the EM cluster in η and ϕ , was corrected for using dedicated calibration schemes.

To determine these calibration parameters, a Boosted Decision Tree (BDT) was trained on Monte Carlo simulation to predict the true electron energy E_{true} from variables such as the EM cluster energy, position, leakages, and ratios of cluster energies in different layers of the Lar calorimeters. The training was categorized by E_T and η , whose binning were chosen to optimize energy responses in different regions of phase space. Calibration using this BDT was shown to improve energy resolutions by 10% [102].

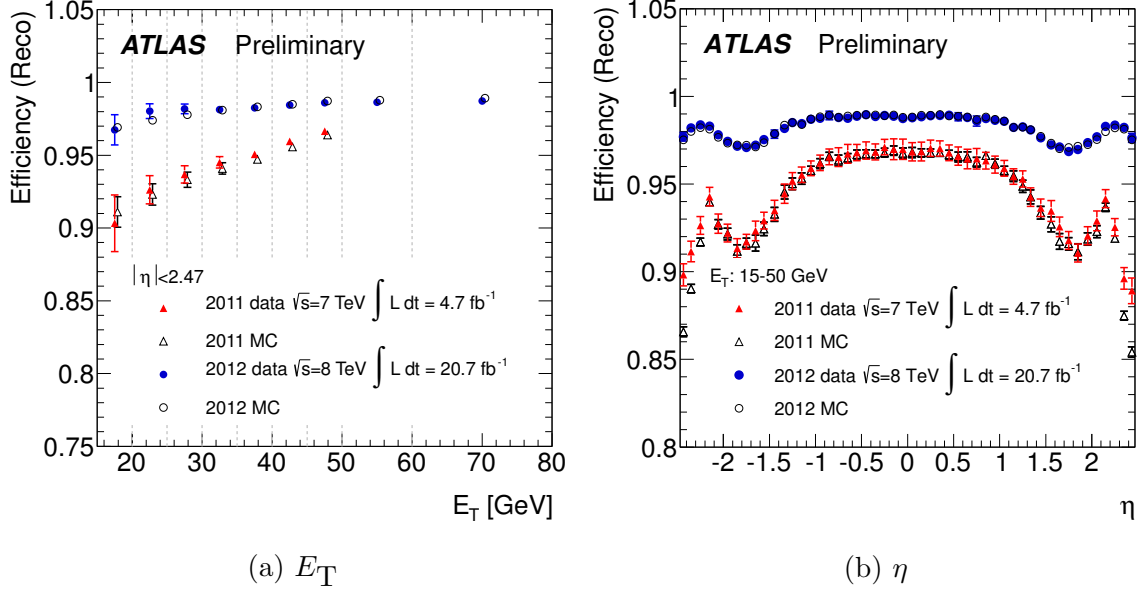


Figure 5.4. Plots of electron reconstruction efficiencies during Run 1, binned in E_T , and η . Taken from Ref [101].

Several other corrections were applied to electron candidates after the BDT calibration. For example, the energy scales in the first and second layers of the Lar calorimeters were equalized between data and Monte Carlo simulation. After that, the overall electron energy response in data was calibrated so that it agreed with the expectation from simulation using $Z \rightarrow ee$ events. These calibrations were categorized in η . The sensitivity of the results was evaluated by varying the event selection in data, and the quality of the electrons used.

After all these calibrations were applied the agreement between data and Monte Carlo simulation was validated in $J/\psi \rightarrow e^+e^-$ events, to test the performance in a different E_T regime. Figure 5.5 shows the invariant masses of the ee system in $J/\psi \rightarrow e^+e^-$ and $Z \rightarrow ee$ events, covering different E_T regimes. In the $Z \rightarrow ee$ case, distributions from data was compared to those from calibrated Monte Carlo simulation and uncalibrated Monte Carlo simulation. In the $J/\psi \rightarrow e^+e^-$ case, some of the background component was data-driven, so the calibrated data was compared to the sum of Monte Carlo simulation and the data-driven background. In both cases, agreement was within 2%.

Uncertainties in the electron energy scale stemmed from several sources. For example, uncertainties associated with calibrating individual Lar layers reached 0.15%. Those associated with the distribution of material upstream the Lar reached 0.3%. Added in quadrature, overall the uncertainty on energy scale varied from 0.04% to 0.4% depending on η . Forward electrons suffered the most. The relative uncertainty

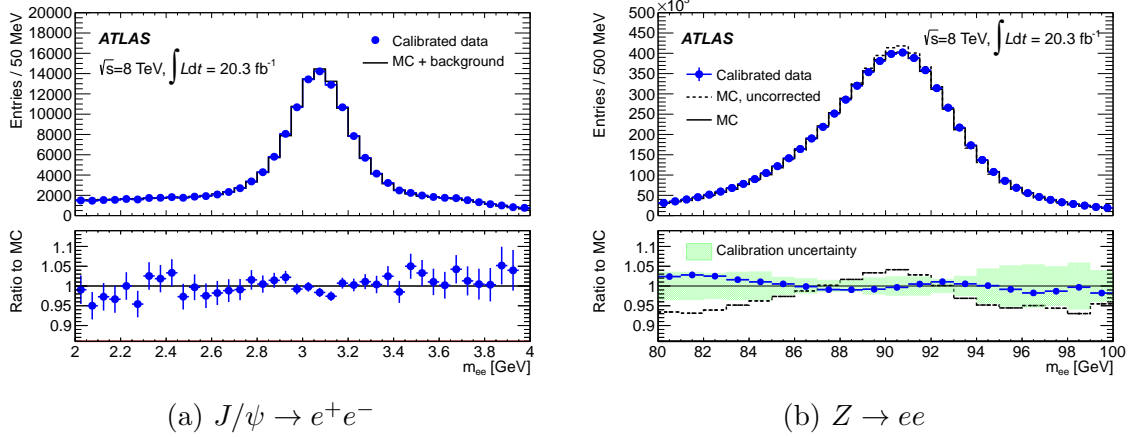


Figure 5.5. Plots of the invariant mass of the ee system in $J/\psi \rightarrow e^+e^-$ and $Z \rightarrow ee$ events in data, calibrated and uncalibrated Monte Carlo simulation. Taken from Ref [102].

on energy resolution was better than 10% for 50 GeV electrons, and asymptotically rose to 40% for higher energies.

5.3 Muons

5.3.1 Reconstruction and Identification

Every track reconstructed in the Muon Spectrometer is considered a muon track, after all ambiguities are resolved. Each of these tracks is further categorized into classes upon demanding further identification requirements. Muons identified just by tracks from the Muon Spectrometer are classified as *Stand-Alone Muons (SA)*. As mentioned in Section 5.1 these tracks are extrapolated to the IP, and energy losses from minimal ionizations in the calorimeters are corrected for. Muons constructed by combining and matching tracks from the MS and the ID are known as *Combined (CB)* muons. The overall quality of CB muons is characterized by the significance of the ratio of the track charge to its momentum q/p , the χ^2 of the combined MS-ID fit, and the number of ID track hits. For an ID track to be considered as a candidate for matching with an MS track it is required to have at least 1 hit in the Pixel Detector, 5 SCT hits, and fewer than 3 Pixel Detector or SCT holes. Other types of muons that are rarely used are *Segment Tagged (ST)* and *Calorimeter Tagged (CT)* muons. An ST muon is reconstructed if at least one of the MS segments is matched to an ID track, while a CT muon is reconstructed if some energy deposits consistent with a muon path in the calorimeters are matched to a track in the ID. Purity in these muon classes is ranked as follows: CB, ST, SA and CT. Overlaps between classes are resolved in the same order of preference. CB muons were used in both analyses

discussed in this Thesis while SA muons are normally used to determine the efficiency of measuring muons with the ID.

CB muons used in Run I were required to have at least 3 MDT hits in at least two layers. This rule was relaxed to at least 1 MDT layer and no more than 1 MDT hole in the region of $|\eta| < 0.1$, which is partially equipped because of service cables. During Run II muon classes were modified to mimic electron identification classes, i.e Loose, Medium and Tight. These classes contain more than one of the CB, ST, SA and CT categories. For example, the Medium class is a combination of CB and SA muons. For $|\eta| < 2.5$ CB muons are used with the same requirements demanded during Run I. For $|\eta| > 2.5$, which does not have ID tracking, SA muons are used. They are required to have hits in at least 3 MDT or CSC layers, and the significance of their q/p is required to be less than 7 to reduce contamination from muons from K and π^\pm decays. Medium muons are used in this Thesis for Run 2 data and CB muons are used for Run 1 data.

5.3.2 Measurement of efficiencies, corrections and uncertainties

Just like electron reconstruction, muons reconstruction suffers from inefficiencies and energy skews, especially in Monte Carlo simulation. Identification efficiencies in Monte Carlo are also not expected to match with those in data. Techniques to correct for this are discussed here.

5.3.2.1 Identification Efficiency

Identification and reconstruction efficiencies for muons are terms used rather inter-changeably. This is because as mentioned before, any track reconstructed in the MS and matched to a track in the ID is considered a muon. So, the only efficiency described in this text for muons is the identification efficiency, ϵ_{id} . Only ϵ_{id} for muons with $|\eta| < 2.5$ is discussed here. Otherwise, the reader is encouraged to read Ref [103]. For a thorough discussion of muon isolation efficiencies the reader is also encouraged to read the same reference.

Since muons with $|\eta| < 2.5$ are measured from both the ID and MS tracks, the tag-and-probe method is naturally appealing. Given two muons, one is used as the tag object and the other as the probe object. The identification efficiency can be factorized as

$$\epsilon_{id} = \epsilon_{id|ID} \times \epsilon_{ID}. \quad (5.6)$$

where $\epsilon_{id|ID}$ is the efficiency of a muon track in the ID to be identified as a muon², and ϵ_{ID} is the efficiency of a muon track to be reconstructed in the ID. The

²During Run I these categories were just CB, ST, CT, etc. During Run II the standard loose, medium, tight working points were used.

latter is efficiency is difficult to calculate, so it is approximated by $\epsilon_{ID|MS}$, which is the efficiency of reconstructing a muon track in the ID given that it has been reconstructed in the MS. Ultimately, the efficiencies in data, ϵ_{id}^{data} , and MC, ϵ_{id}^{MC} , are compared by taking their ratio as a scale factor. This cancels out any biases stemming from the tag-and-probe method.

To cover a wide range of muon p_T , efficiency measurements were performed using both $J/\psi \rightarrow \mu^+\mu^-$ and $Z \rightarrow \mu\mu$ events from data and MC. For $Z \rightarrow \mu\mu$ events the tag muon was required to satisfy the following:

1. medium quality, loose isolation and have $p_T > 24$ GeV;
2. impact parameter requirements to ensure that it originated from the primary vertex;
3. and be matched to the muon trigger.

The probe muon was required to have $p_T > 10$ GeV and be loosely isolated. For $J/\psi \rightarrow \mu^+\mu^-$ the tag muon was required to have $p_T > 5$ GeV, be of medium ID, and be matched to the muon trigger. Additionally, for both $J/\psi \rightarrow \mu^+\mu^-$ and $Z \rightarrow \mu\mu$ the probe muon was required to have a fully reconstructed muon within $\Delta R < 0.05$ around its location.

Efficiencies were extracted in bins of η, ϕ and p_T , as described in full detail in Ref [104]. Figure 5.6 shows identification efficiencies extracted from data for medium (Run II) and CB (Run I) muons in the region $0.1 < |\eta| < 2.5$. The high p_T region was covered by muons from $Z \rightarrow \mu\mu$ events while the low p_T region was covered by muons from $J/\psi \rightarrow \mu^+\mu^-$ events. Above about 20 GeV, the efficiency was observed to be independent from the muon p_T . Overall, the agreement between data and Monte Carlo simulation was observed to be within 1%.

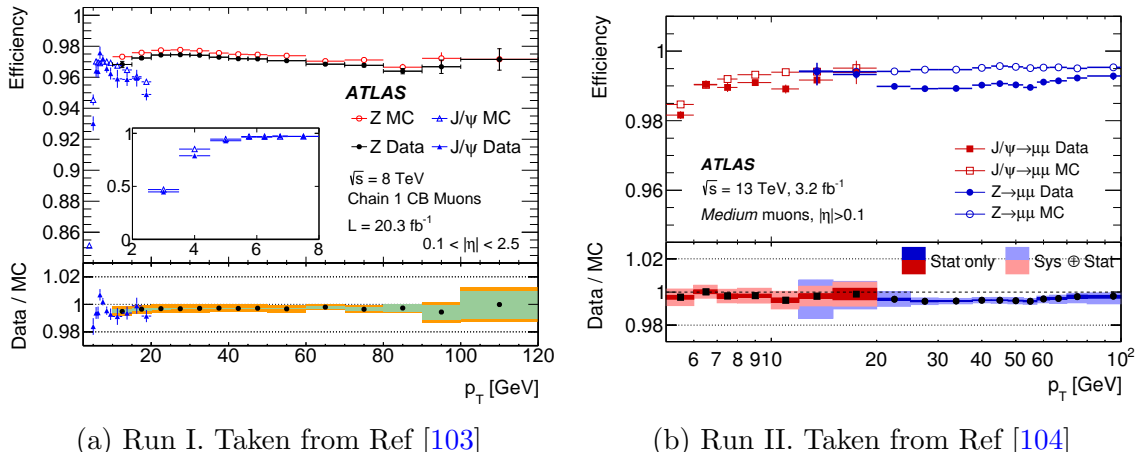


Figure 5.6. Plots of the muon identification efficiencies, binned in p_T . $Z \rightarrow \mu\mu$ events were used for high p_T muons while $J/\psi \rightarrow \mu^+\mu^-$ events were used for low p_T muons

The major systematic uncertainties affecting these results were found to be from the data-driven estimation of background processes, choice of cone size used to match probe muons to reconstructed muons, and kinematic distribution disagreements between probes in data and Monte Carlo simulation. The uncertainties due to background processes was calculated by varying a parameter used in the estimation by $\pm 100\%$. The cone size uncertainties were evaluated by varying the cone size by $\pm 50\%$. Distributions of probe kinematics in MC were weighted to agree with data. The shift was taken as a systematic uncertainty. After adding these and other [104] uncertainties in quadrature, the overall uncertainties on the identification efficiencies were less than 2%.

5.3.2.2 Momentum Scale and Smear

Just like with electrons, muons may lose energy as they traverse detector material upstream of the Muon Spectrometer (MS). This loss may also be mis-modelled in Monte Carlo simulations. While losses in the Inner Detector (ID) are very small and taken as negligible, losses the calorimeters cannot be neglected. Modelling of the magnetic field integral and detector dimensions in the ID and MS in Monte Carlo simulations may also differ from the true physical values. Energy loss and other forms of mismodelling must therefore be corrected in both data and Monte Carlo simulation. Effectively such corrections adjust the muon momentum by scale factors.

Fluctuations in muon energy losses in the calorimeters lead to uncertainties in the measured muon momentum. Magnetic field inhomogeneities, spatial hits displacements in the ID and MS, and misalignment of the MS all lead to larger uncertainties in the measured muon p_T in both the ID and MS. Accounting for these uncertainties broadens (or *smears*) the p_T resolution in MC to match the data. The corrected muon p_T in MC can be written as

$$p_T^{corr,MC} = \frac{p_T^{uncorr,MC} + \text{Sum of Scales}}{1 + \text{Sum of Smears}}, \quad (5.7)$$

where the scale and smear corrections are derived from data.

During both Run I and Run II, $J/\psi \rightarrow \mu^+\mu^-$ and $Z \rightarrow \mu\mu$ events from data were used as the source of muons with p_T lying in the range of 5 GeV to 300 GeV. Their energy distributions were compared to those predicted by Monte Carlo simulations. Muons from $J/\psi \rightarrow \mu^+\mu^-$ and $Z \rightarrow \mu\mu$ were required to be of medium³ identification, oppositely charged, within the ID acceptance, and have impact parameters that indicate that they originated from the same vertex, which is required to be the primary vertex in the event. The invariant mass of the system of two muons, $m_{\mu\mu}$, was required to be within 76 GeV and 106 GeV for $Z \rightarrow \mu\mu$ and within 2.65 GeV and 3.6 GeV for $J/\psi \rightarrow \mu^+\mu^-$ events. The $m_{\mu\mu}$ distributions were then used to extract correctional scale factors as described in detail in Ref [104]. Figure 5.7 shows such

³In Run I they were required to be CB muons.

distributions for uncorrected MC p_T , corrected MC p_T , and data p_T for muons from both $J/\psi \rightarrow \mu^+\mu^-$ events, using Run I and Run II data-sets. These distributions show that a correction for energy losses of about 1% was necessary. Depending on the p_T , resolution smearing corrections below 15% were applied.

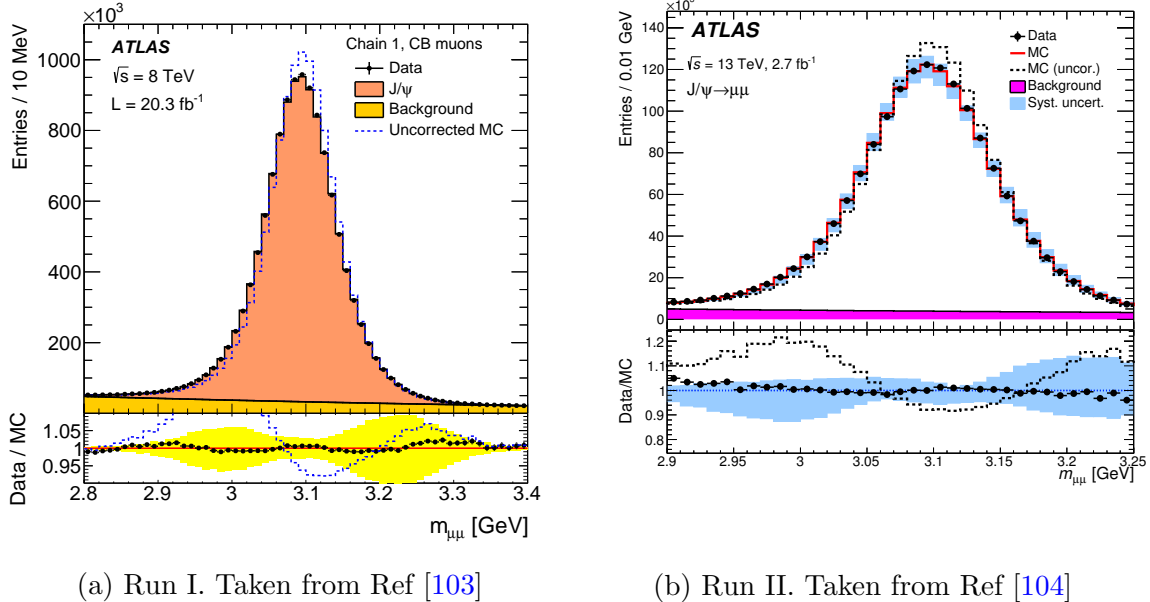


Figure 5.7. Plots showing comparisons of $m_{\mu\mu}$ distributions for muons from $J/\psi \rightarrow \mu^+\mu^-$ events in data, MC in which muon p_T is corrected and MC in which p_T is not corrected.

Systematic uncertainties in these corrections originate from imperfections in the model used for momentum correction, and in the fit used to extract correctional parameters. These were evaluated by varying several components when extracting the corrections. For example, the $m_{\mu\mu}$ window was varied by ± 5 GeV in $Z \rightarrow \mu\mu$ event selection. This variation had the most impact effect on results.

5.4 Jets

A *jet* in the ATLAS detector is a stream of collimated hadrons and other particles originating from a localized vertex. Although these jets can be formed from hadronic decays of heavy particles such as W or Z bosons, most are formed through scattering of gluons and quarks, and radiation of quarks inside the protons during a pp collision. Jets formed through the latter processes are referred to here as QCD multi-jets.

Due to asymptotic freedom [105], introduced in Section 2.1.2.1, although quarks and gluons cannot move freely at the GeV energy scales, they can move quasi-freely inside the barriers of hadrons and baryons. At the LHC hard-scatter energy scales (TeV) however, quarks and gluons may briefly move freely until their energies decrease. During this brief moment, quarks and gluons may radiate gluons, and gluons may split into $q\bar{q}$ pairs, as shown in Figure 2.1. This process repeats until a low-enough energy is reached, forming a parton shower. The $q\bar{q}$ pairs eventually hadronize to form high energy mesons such as π^\pm , neutral and charged K that propagate in more-or-less the same direction as the direction of the original quark or gluon. This collection of hadrons makes up a jet. A formal discussion of parton shower development and hadronization is in Sections 4.1.1 and 4.1.2.

5.4.1 The anti- kt clustering scheme

Several schemes have been developed to standardize the mechanism with which hadrons are incorporated into a jet [106]. The ideal scheme is expected to be insensitive to slight modifications to the jets through infrared emmissions or collinear splitting because such modifications are stochastic and difficult to predict. Moreover, it is expected to be easy to implement in an experimental setting. The jets used in these analyses are defined using the *anti- kt algorithm* [107], which takes topological clusters of calorimeter cells as inputs. The energy in the topological clusters corresponds to energy deposited by hadrons in the calorimeters.⁴

The jets are built from two types of topological clusters. For the first type, energy deposits in calorimeter cells are calibrated assuming that the particle is a neutral pion. This form of calibration is known as the electromagnetic (EM) scale because a neutral pion immediately decays to two photons that initiate an EM shower. Although this scale is correct for electromagnetic particles, it is not correct for hadrons. The second type of jet corrects for this offset in calibration by calibrating hadron energy deposits as if the particle is a charged pion. By first classifying each calorimeter cell energy deposit as EM or hadronic, each calorimeter cell is given an independent local weight; this process is therefore rightfully called *local cell signal weighting* (LCW). Although LCW is significantly slower than implementing the EM scale, it is a more accurate calibration scale.

Unlike topological clusters for forward electron reconstruction, topological clusters used for jet reconstruction use as seed calorimeter clusters with signal to noise ratio of 4. Additionally, signal to noise ratio for neighboring cells is required to not be less than 2. The topological cluster building scheme for jets is therefore 422, while for electrons it is 633.⁵ The definition for noise in calorimeter cells used in both these schemes is the sum of electronics noise and energy from pileup pp collisions. The pileup component of noise increases with the increase in pileup events. Because of

⁴ Details on how topological clusters are built from calorimeter cells were presented in Section 5.2.

⁵ See Section 5.2.1.

this, noise thresholds used during Run 1 jet reconstruction were lower than those during Run 2. Additionally, during Run 2 topological clusters were not allowed to start building from the EM Calorimeter presampler. This significantly reduced the number of jets from pileup events.

The anti- kt algorithm uses the metric defined in Equation 5.8 to determine cluster association in the position-energy phase space.

$$d_{ij} = \min(p_{T,i}^{-2}, p_{T,j}^{-2}) \frac{\Delta R_{ij}^2}{R^2}, \text{ where } \Delta R_{ij}^2 = (\eta_i - \eta_j)^2 + (\phi_i - \phi_j)^2 \\ d_{iB} = p_{T,i}^{-2} \quad (5.8)$$

The second equation in Equation 5.8 is meant to draw an association between a hadron and the incoming or outgoing proton beam, while the first definition assesses the relation between two hadrons. The R parameter is a solid angle that limits the window of hadron association. During both Run 1 and Run 2, jets were reconstructed with $R = 0.4$. This metric in Equation 5.8 is designed to be invariant under boosts in the z coordinate because it is made up of p_T , η and ϕ , which are also invariant under similar transformations.

The anti- kt algorithm proceeds as follows, starting with a list of topological clusters : The highest p_T cluster (*the hardest*) is found and indexed with i . d_{iB} and d_{ij} are evaluated, where j is the cluster closest to i , as determined by Equation 5.8. If $\min(d_{ij}, d_{iB}) = d_{ij}$, i and j are combined into a single cluster and the process is repeated, otherwise i is declared a final-state jet and removed from the cluster list. This process is repeated until no cluster remains in the seed list. The four-momentum of the resultant jet is the sum of the four-momenta from all the contributing clusters.

Starting with the hardest cluster, the anti- kt algorithm effectively groups low p_T clusters around the hardest cluster. This strategy is most convenient at the LHC, where the most important jets are usually of high p_T . Additionally, because the metric defined in Equation 5.8 includes a combination of an angle and energy it is insensitive to collinear splitting and infrared emmissions.

5.4.2 Performance and Calibration

Jet reconstructed using the anti- kt clustering scheme may have energy offsets due to several detector imperfections. These issues are corrected by calibrating several components of the jets. The following corrections or calibrations are applied sequentially.

5.4.2.1 Origin Correction

Topological clusters positions are computed relative the LHC's interaction point (IP). Reconstructed jet positions are therefore also computed relative the IP. Since the primary vertex from which the jet originates may not necessarily coincide with the

IP, the jet origin has to be adjusted. The scheme proceeds as follows: The primary vertex is searched for by selecting the vertex whose tracks have the largest sum of p_T . Topological clusters are repositioned to match the identified primary vertex. Jet four-momentum is recalculated with the new cluster four-momenta. The jet energy response and resolution are not affected by this correction, but the jet pseudorapidity resolution is improved. This is expected since the beam spot is significantly longer in the z direction (5 cm) than it is in the transverse plane (at most 1 mm).

5.4.2.2 Pileup Subtraction from each jet

The calibration scheme to subtract pileup contamination from each jet is done at an event by event, and jet by jet basis. The subtracted quantity in each jet p_T is the product of the jet p_T and the event *pileup density*, ρ , which is a measure of how many particles from pileup events were included in the jet. The assumption in this scheme is that particles from pileup should be uniformly distributed in $\eta \times \phi$. To determine each jet’s sensitivity to these particles, particles of infinitesimal p_T (known as *ghost* particles [108]) are added to the event and jet reconstruction is repeated. The number of ghost particles in each jet are used to parameterize the area, A_j , of the jet in $\eta \times \phi$. The median of p_T/A_j for all the jets in the event is picked as ρ for that event.

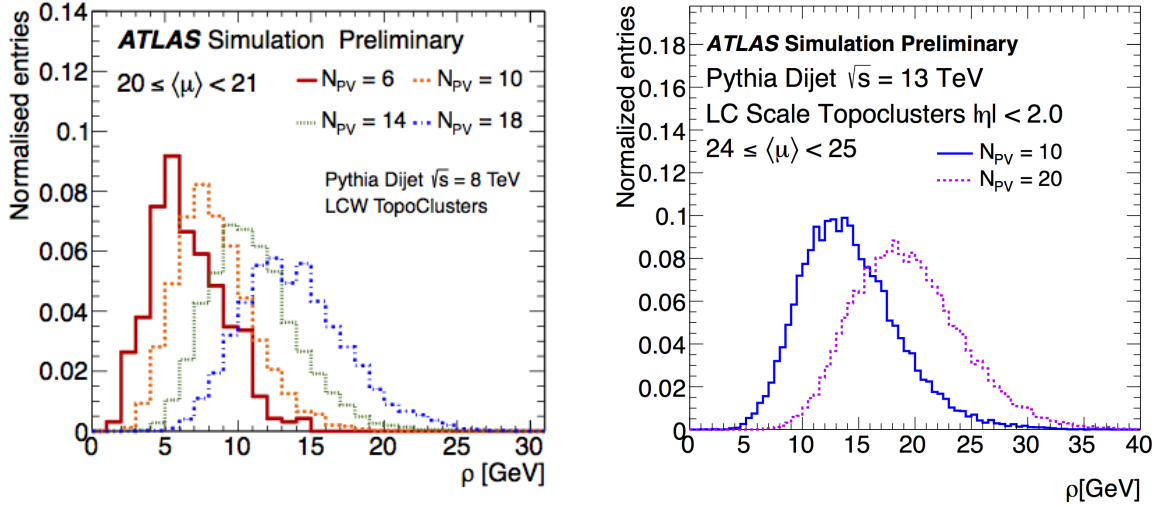
Figure 5.8(a) shows the ρ distributions from simulation events during Run 1, where the number of vertices, N_{PV} , is varied. The average ρ increases with N_{PV} as expected. The distributions shown in Figure 5.8(b) are similar to those in Figure 5.8(a) but with Run 2 settings. Any residual dependence of jet p_T on N_{PV} and the average number of interactions per bunch crossing $\langle\mu\rangle$ is further corrected from bins of N_{PV} and $\langle\mu\rangle$.

5.4.2.3 Energy Scale and Resolution

After calibrations schemes described so far have been applied, any remaining jet energy dependence on η and p_T is corrected by comparing the calculated jet energy and the true particle jet energy from MC simulation. A jet is matched to a true particle if the true particle is within its $\Delta R < 0.3$. The jet energy *response* (also known as *scale*⁶) \mathcal{R} is defined as the ratio of the reconstructed energy E^{reco} to the energy of the true particle jet E^{true} . Jet p_T *response* is defined similarly. Jet energy in simulation is finely binned in E^{true} and η_{det} bins, where η_{det} is the pseudo-rapidity in detector coordinates rather than the corrected η described in Section 5.4.2.1. The motivation for η_{det} parameterization is that problems may arise from transitioning from the barrel to end-cap calorimeters.

The jet energy response is measured in bins of E^{true} and η_{det} . The value in each bin is taken as the peak of a gaussian fit for all the values that fall in that bin. The

⁶These terms will be used interchangeably in this text



(a) ρ during Run 1, taken from Ref [109] (b) ρ during Run 2, taken from Ref [110]

Figure 5.8. Plots showing the pileup density ρ , the pileup contribution to jet p_T , at several number of vertices N_{PV} for jets reconstructed from LCW topological clusters.

energy *resolution* is then taken as the standard deviation of the said gaussian fit, so it is binned in the same manner as the energy response. For each η_{det} bin, a calibration function $\mathcal{F}(E^{reco})$ is obtained by a fit of (E^{reco}, \mathcal{R}) values for each E^{true} bin. The corrected jet energy is then defined for each η_{det} bin as

$$E^{corr} = E^{reco}/\mathcal{F}(E^{reco}) \quad (5.9)$$

where $1/\mathcal{F}(E^{reco})$ is the jet energy scale. A simple approximation, $\mathcal{F}(E^{reco}) = \langle E^{reco}/E^{true} \rangle$, was used in both Run I and Run II. In this approximation, $\mathcal{F}(E^{reco})$ is the average jet energy response per η_{det} bin. Figure 5.9(a) and 5.9(b) show the jet energy response for p_T^{true} and η_{det} respectively for simulated LCW anti-kt jets, with $R = 0.4$. The disagreement in the low p_T range is caused by non-perfect fits which were caused by non-Gaussian effects.

Studies described in the preceding paragraphs were performed with Monte Carlo simulations for several physics processes to evaluate the associated systematic uncertainties. These are $Z+jets$, $\gamma+jets$ and events with only 2 jets. Jets in the central region were observed to have at most 3% uncertainty in the jet energy scale, and those in the forward regions had at most 6%. The resolution was observed to increase with true p_T and with higher pseudorapidity. The total uncertainty on the resolution was calculated by varying the Gaussian fits (introduced in this section) by $\pm 1\sigma$. This uncertainty was observed to be at most 2%, varying with the true p_T .

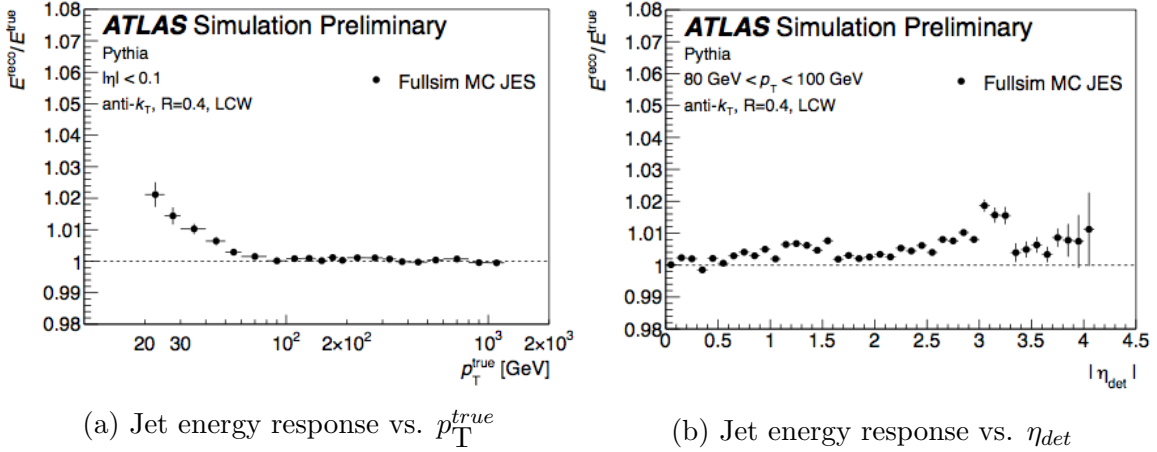


Figure 5.9. Plots showing the jet energy response for simulated LCW jets reconstructed with the anti- k_T algorithm at $R= 0.4$ is plotted against p_T^{true} and $|\eta_{det}|$. Taken from Ref [109].

5.4.2.4 Jets from pileup

Even after tracks from pileup events that get associated to jets are subtracted with the technique described in Section 5.4.2.2 are subtracted from the jet, jets that originate entirely from pileup events are not subtracted from the event. Techniques used to suppress such jets have evolved from Run 1 to Run 2.

During Run 1, the Jet Vertex Fraction (JVF) [111] was the main variable used to suppress jets from pileup interactions. In an event with multiple reconstructed vertices, JVF for a jet was used to determine the likelihood of it originating from each of the vertices. Thus, JVF is a function of the jet jet_i and reconstructed vertex V_j in the event. Precisely, it is defined as

$$JVF(jet_i, V_j) = \frac{\sum_m p_T(\text{track}_m^{jet_i}, V_j)}{\sum_n \sum_l p_T(\text{track}_l^{jet_i}, V_n)}, \quad (5.10)$$

where m runs over tracks associated with jet $_i$ and whose origin is V_j . n runs over all reconstructed vertices in the event and l runs over all tracks whose origin is V_n and associated with jet $_i$. For each of these tracks a $p_T > 500$ MeV requirement is demanded. For jets with no tracks, a value of -1 is assigned to JVF. During Run 1 the vertex of interest was the primary vertex, V_0 . $JVF(V_0)$ was used as a discriminant for each jet. Figure 5.10 shows the $JVF(V_0)$ distribution for simulation jets from the primary vertex (hard-scatter jets) and jets from pileup, for jets with $20 < p_T < 50$ GeV and $|\eta| < 2.4$. These jets were reconstructed using the LCW scale and the jet energy scale 5.4.2.3 (JES) was applied. Pileup jets tend to have low JVF because their tracks rarely originate from the primary vertex. Using $Z \rightarrow \mu\mu + \text{jets}$

events from simulation it was observed that pileup jets during Run 1 were suppressed to 2% for jets with $p_T \approx 20$ GeV and even to lower values for jets with higher p_T .

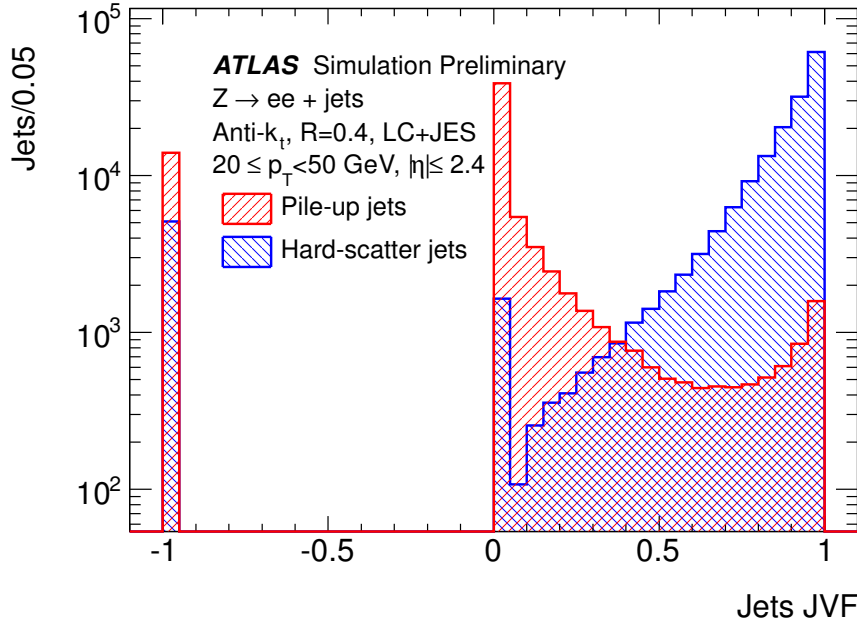


Figure 5.10. Plots showing the JVF distributions for pileup jets and jets from the primary vertex (hard-scatter), evaluated for the primary vertex. Taken from Ref [112].

Although reasonably efficient for low pileup (Run 1) conditions, JVF performance is reduced for higher pileup conditions. This is because JVF is dependent on the number of reconstructed vertices in the event; more tracks in the event makes the denominator in Equation 5.10 large, lowering JVF even for hard-scatter jets. Two variables were defined to correct for this. corrJVF corrects for the linear increase of the sum p_T of tracks from non-primary vertices ($\sum_{n \geq 1} \sum_l p_T^{trk_l}(V_n)$) with the number of pileup tracks (n_{trk}^{PU}) by scaling n_{trk}^{PU} with a correctional factor k . corrJVF evaluated at the primary vertex V_0 is then defined as

$$\text{corrJVF} = \frac{\sum_m p_T^{trk_m}(V_0)}{\sum_l p_T^{trk_l}(V_0) + \sum_{n \geq 1} \sum_l p_T^{trk_l}(V_n)} \quad (5.11)$$

The second variable used is R_{p_T} . It is defined as

$$R_{p_T} = \frac{\sum_h p_T^{trk_h}(V_0)}{p_T^{\text{jet}}} \quad (5.12)$$

where h runs over all the tracks associated with the jet and originating from the primary vertex, and the denominator is the calibrated reconstructed jet p_T after subtracting pileup tracks using the ghost tracks technique described in the previous section. Figures 5.11(a) and 5.11(b) show corrJVF and R_{p_T} respectively for hard-scatter and pileup jets. In both these variables, a value of -1 is assigned if the jet has no associated tracks. For those jets with associated tracks, corrJVF and R_{p_T} are reasonable discriminants.

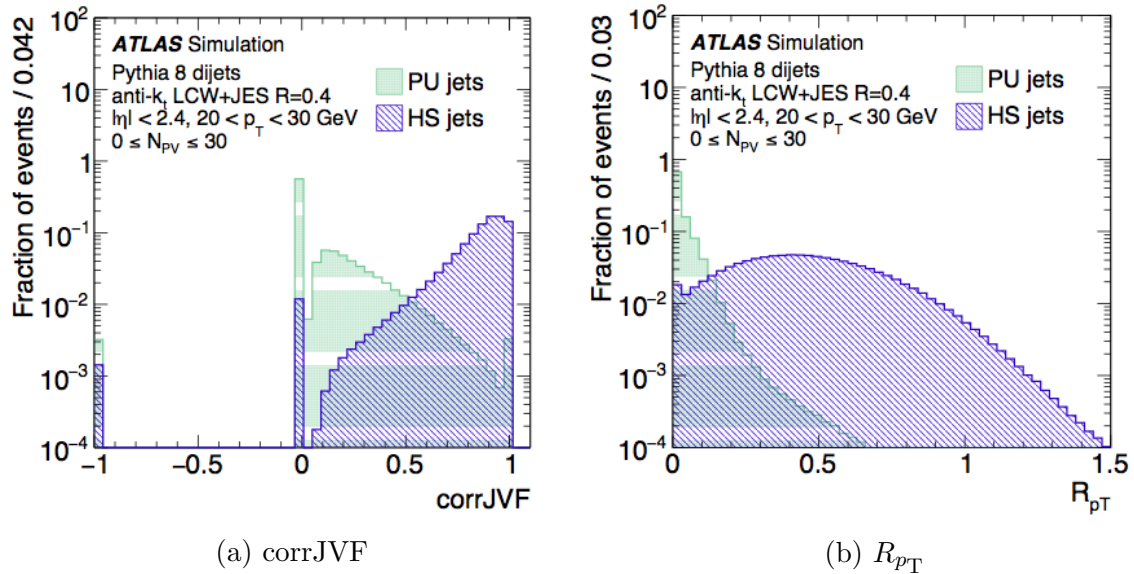


Figure 5.11. Plots showing distributions of variables used to correct for JVF's dependence on the number of reconstructed vertices, and hence number of pileup tracks, in an event. The distributions from pileup and hard-scatter jets are overlayed. The simulated jets are reconstructed with the LCW scale and the jet energy scale is applied. Taken from Ref [112].

During Run 2 a Jet Vertex Tagger (JVT), which makes use of corrJVF and R_{p_T} , is used. corrJVF and R_{p_T} define a 2-dimensional space in which every reconstructed jet resides. The k-nearest neighbor (kNN) model [113] is used to determine the likelihood of a jet to be from hard-scatter (signal) or from pileup (background). This model is trained on a sample of signal and background for jets with p_T in the range of 20 GeV and 50 GeV and $|\eta| < 2.4$, where 100 nearest neighbors are used to determine the likelihood for a jet to be signal or background. Figure 5.12 shows the fake rate from pileup jets versus the efficiency from hard scatter jets from simulation using JVT and other discriminants discussed in this section; the JVT curve shows that it is the most optimal of all the other pileup suppression techniques.

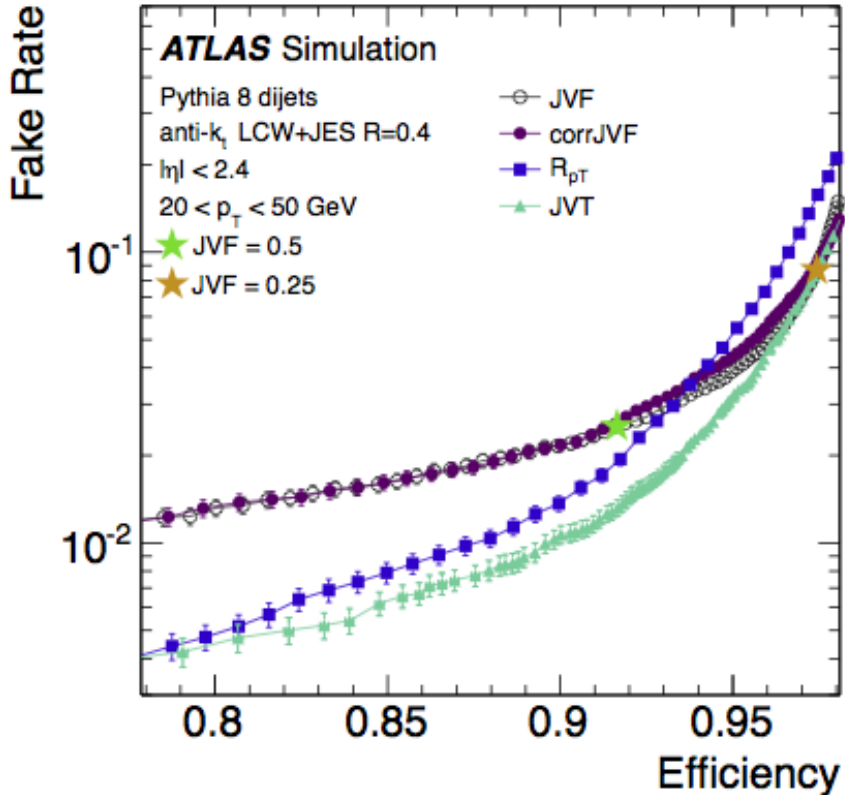


Figure 5.12. Plots showing the fake rate from pileup jets versus efficiency hard scatter jets for JVF, corrJVF, R_{pT} , and JVT. JVT uses a kNN model in corrJVF- R_{pT} space where 100 neighbors determine whether a jet is from pileup or from hard scatter. Taken from Ref [112].

Uncertainties associated with JVF and JVT were calculated by shifting the JVF or JVT selection by variations that account for the extent to which the jet correction is mis-modelled for jets originating from the primary vertex. These uncertainties vary between 2 and 6% depending on the jet p_T and pseudorapidity.

5.4.3 B-Tagging

Jets initiated by b -quarks are common signatures in many processes. For example, in $gg \rightarrow t\bar{t}$ each top quark decays weakly to a bottom quark which then initiates a jet. Several techniques are available that tag a jet as b -quark initiated. b -tagging techniques typically exploit the relatively high lifetime of the b -hadrons, which is of the order of 1.5 ps. To put this into perspective, a b -hadron with $p_T = 50$ GeV will typically traverse several mm before decaying to c -hadrons or some other light-flavor

hadrons. This section discussed two types of b -tagging techniques whose details can be found in Ref [114].

The first technique parameterizes the b -hadron lifetime by the impact parameters of the tracks in a jet with respect to the primary vertex. The most efficient of algorithms that implement this technique is IP3D. It proceeds as follows: For a jet, each track's transverse impact parameter with respect to the primary vertex d_0 and its longitudinal impact parameter z_0 are extracted. A 2-dimensional function of the significance of d_0 ($d_0/\sigma(d_0)$), and the significance of z_0 ($z_0/\sigma(z_0)$) is evaluated and compared to 2-dimensional probability density functions for b and light flavor jet hypotheses for each track. These prior probability density functions are obtained from Monte Carlo simulations. The ratio of the b -jet likelihood to the light flavor jet likelihood is taken as the track weight. The weight for the jet is then the sum of logarithms of the individual track weights. A simpler version of this algorithm is the IP2D, which replaces the 2-dimensional function with a 1-dimensional function of $z_0/\sigma(z_0)$.

The second technique constructs a secondary vertex at which the b -hadron decays. The secondary vertex is built by vertices from pairs of tracks with large displacements from the primary vertex. These two-track vertices are required to have a fit with a χ^2 lower than a threshold value. Additionally, vertices compatible with long lived particles and photon conversions are not considered. When building the two-track vertices into the secondary vertex two-track vertices contributing the largest χ^2 are removed if the secondary vertex's χ^2 is larger than a threshold value. The distance between the primary vertex and the secondary vertex is the discriminant used for identifying b -jets. One algorithm that implements this technique is called SV1. It uses the Log Likelihood Ratio method, where the likelihoods are constructed from two distributions: The first is a 2-dimensional distribution of secondary vertex mass versus its energy. The second is a 2-dimensional distribution of the number of two-track vertices in the secondary vertex versus the ΔR between the jet axis and the primary-secondary vertices axis.

Another algorithm that constructs a secondary vertex using a slightly different approach is called JetFitter. This algorithm runs a trained artificial neural network on the jet, looping through each vertex (apart from the primary) that has at least two tracks. The neural network takes variables that describe the vertex in question and has output nodes for either a b -vertex or a light flavor vertex. The discriminant to select b -jets from light flavor jets is taken as the logarithm of the ratio of values in the b -node to the value in the light flavor node.

5.4.3.1 Performance and Uncertainties

During Run 2 the b -tagging algorithms discussed in this section were combined. More specifically, in 2015 the combined algorithm was MV2c20 while in 2016 the algorithm used was called MV2c10. These two algorithms combine IP2D, IP3D, SV1

and JetFitter [115], where the variables from each of standalone algorithms were used as inputs to a Boosted Decision Tree (BDT). The BDT was trained using jets initiated by b -quarks as signal. The background was a composition of light-flavor jets, c -jets and jets from a hadronic τ lepton. In MV2c20, 20% of the background was made up of c -jets while in MV2c10 10% of the background was made up of c -jets. It was shown that even though MV2c10 provides similar light-jet rejection to that provided by MV2c20, it provides 40% more c -jet rejection. Thus, analyses presented in this text use only MV2c10. Regardless, it is worthwhile to compare the performance of MV2c10 against MV2c20.

Figure 5.13 shows the performance of the MV2c10 BDT output for b -, c -, and light flavor jets in $t\bar{t}$ events. A nominal selection criterion was imposed on the BDT output such that the b -jet selection efficiency is 77%. This working point varied with needs. For example, in Section 6.2 the working point was such that the b -jet selection efficiency was 70%.

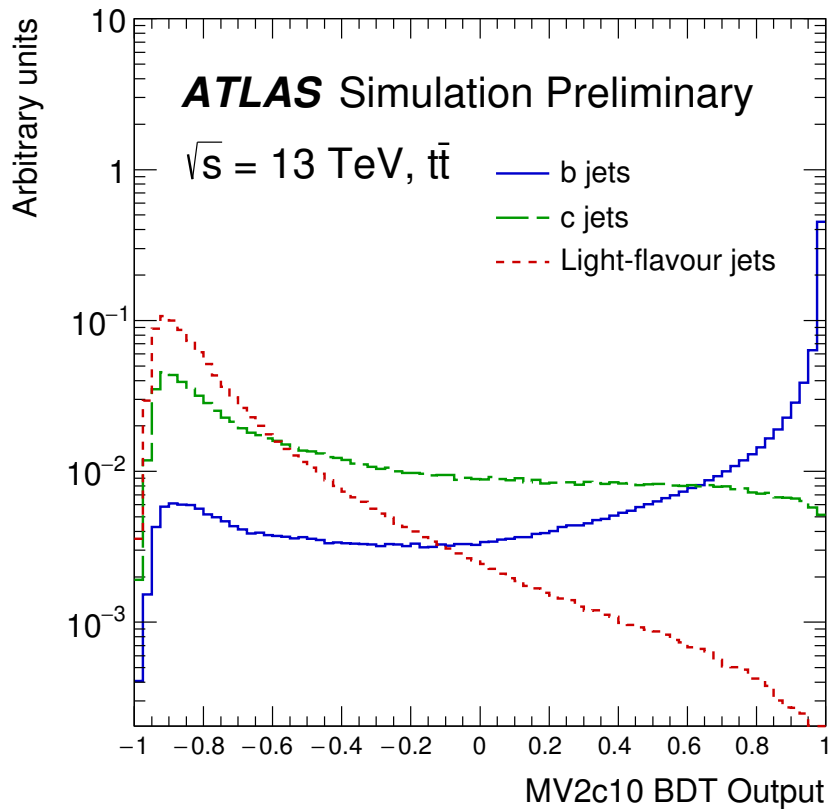


Figure 5.13. Plots showing the MV2c10 BDT output, taken from Ref [115].

Figure 5.14(a) shows the b -jet selection efficiencies, plotted against jet p_T , using the BDT outputs from MV2c10 and MV2c20. The working point was 77% efficiency. There is no significant difference between the two algorithms. Figure 5.14(b) shows the c -jet rejection, plotted against jet p_T , using the BDT outputs from MV2c10 and MV2c20, at a 77% efficiency working point. MV2v10 shows much more improved rejections. That is why it was the algorithm of choice in the analysis discussed in Chapter 6.

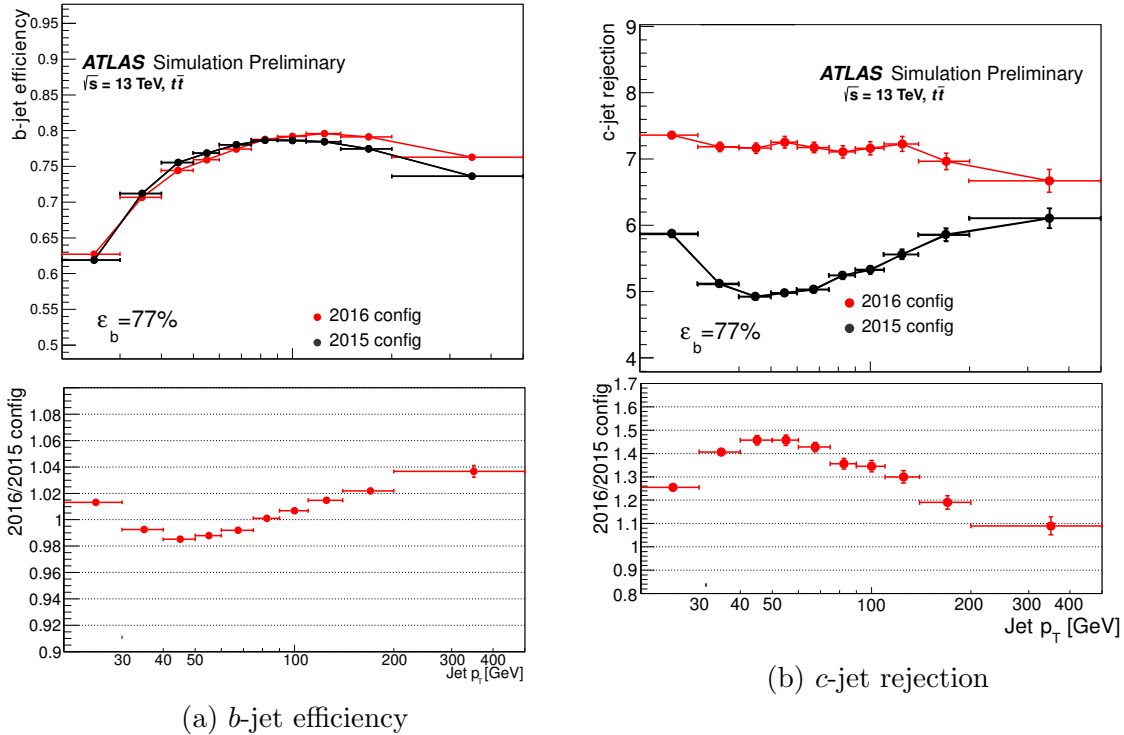


Figure 5.14. Plots showing the b -jet efficiency and c -jet rejection parametrized with jet p_T , for the MV2c10 (2016 config) and the MV2c20 (2015 config) algorithms, at a 77% b -jet selection efficiency working point. Taken from Ref [115].

b -tagging efficiencies in Monte Carlo simulations were corrected to match efficiencies obtained in regions in data rich in the physics processes modelled by the said Monte Carlo simulations. Uncertainties on the b -tagging efficiencies were evaluated by shifting the BDT output value by an up and a down value, and evaluating the impact on the physics process prediction. More analysis-specific details on this in Section 6.2.

5.5 Taus

As discussed in Section 2.1, of all leptons the τ lepton has the smallest mean lifetime of 2.9×10^{-13} s ($c\tau \approx 87 \mu\text{m}$), decaying inside the LHC beam pipe.⁷ Also the heaviest of all the leptons, the τ lepton is the only lepton heavy enough to decay to hadrons, with a branching ratio of approximately 65%. The said hadrons are dominated by neutral and charged pions, although 2.7% of the time the τ lepton decays to kaons.

5.5.1 Reconstruction and Identification

When a τ lepton decays hadronically it is referred to as a hadronic τ , otherwise it is reconstructed as the electron or muon that it decays to (See Sections 5.2 and 5.3). In either case, there is a ν_τ in the final decay products. Since this ν_τ is invisible in the ATLAS detector the hadronic τ is reconstructed through its visible decay products, which are referred to as $\tau_{\text{had-vis}}$. As discussed in Section 2.1 the τ lepton is restricted to decaying to an odd number of charged mesons, with decreasing branching ratios as the odd number increases. In ATLAS the most common hadronic τ decays constitute 1 or 3 charged pions, sometimes with associated neutral pions.

5.5.1.1 Reconstruction

The $\tau_{\text{had-vis}}$ signature in ATLAS comprises some energy deposits in the calorimeters, matched to 1 or 3 ID tracks.⁸ $\tau_{\text{had-vis}}$ with 1 matched track are called *1-prong*, and those with 3 matched tracks are called *3-prong*. Since neutral pions decay as $\pi^0 \rightarrow \gamma\gamma$, a significant component of the energy is deposited in the electromagnetic calorimeters for those τ lepton decays that include neutral pions.

The largest background to the hadronic τ is the QCD jet, although electrons and muons can be reconstructed as $\tau_{\text{had-vis}}$ as well. With a smaller transverse mass, $\tau_{\text{had-vis}}$ components from a hadronic τ tend to be more collimated than those from a QCD jet for a given p_T . Moreover, due to higher particle multiplicity in a QCD jet, a QCD jet tends to have a higher ID track multiplicity than a hadronic τ for a given p_T . These two differences are used to reduce the QCD jet background contamination, as discussed in Section 5.5.1.2.

Topological clusters in all jets with $p_T > 10$ GeV and $|\eta| < 2.5$, reconstructed as discussed in Section 5.4, are used as seeds by the τ reconstruction algorithm. Tracks from the ID that satisfy the selection criteria shown in Table 5.1 are matched to the $\tau_{\text{had-vis}}$ candidate, using the center of the vector sum of all the topological clusters (henceforth known as the $\tau_{\text{had-vis}}$ center) as reference. This reference point may not be the same as the center of the reconstructed jet because the jet center undergoes corrections described in Section 5.4.2. Tracks from the ID that lie within $\Delta R < 0.2$

⁷The LHC beam pipe has an external diameter of about 5.3 cm.

⁸ ≥ 5 ID tracks are very rare.

around the $\tau_{\text{had-vis}}$ center are counted as tracks from the τ decay. The τ candidate is then classified as either 1-prong or 3-prong, depending on the number of tracks found within $\Delta R < 0.2$. Energy from topological clusters that lie within $\Delta R < 0.2$ around the $\tau_{\text{had-vis}}$ center are summed up to compute the total transverse energy E_T of the $\tau_{\text{had-vis}}$ candidate, which is taken as equal to p_T , on account of the small τ lepton mass. The $\tau_{\text{had-vis}}$ is then characterized by p_T , η and ϕ , where η, ϕ are the $\tau_{\text{had-vis}}$ center coordinates. Further, the following regions in relation to the $\tau_{\text{had-vis}}$ center are defined:

1. $\Delta R < 0.1$, as the *calo-core* region;
2. $\Delta R < 0.2$, as the *core* region;
3. and $0.2 < \Delta R < 0.4$, as the *isolation ring*.

Selection Criteria
$p_T > 1 \text{ GeV}$ Number of b-Layer hits ≥ 1 Number of Pixel Detector hits ≥ 2 Number of Silicon Detector hits ≥ 7 $ d_0 < 1.0 \text{ mm}$ $ z_0 \sin \theta < 1.5 \text{ mm}$

Table 5.1. Selection criteria for tracks from the Inner Detector that are matched to τ -jet candidates.

5.5.1.2 Identification against QCD Jets

To further reduce the fraction of QCD jets that are reconstructed as $\tau_{\text{had-vis}}$, a separate identification algorithm is applied on the reconstructed hadronic τ lepton. Several variables, designed to exploit the differences in shower width and track multiplicity between hadronic τ jets and QCD jets, are used. Only a few are discussed here, but for a more detailed discussion the reader should consult Ref [116].

1.

$$f_{\text{core}} = \frac{\sum_{i \in \text{calo-core}} E_{T,i}^{\text{EM}}}{\sum_j^{\Delta R_i \in \text{core}} E_{T,j}^{\text{EM}}}$$

is the fraction of transverse energy deposited in topological clusters in the core-calorimeter region, to that deposited in the core region. The energy deposits are calibrated at the EM scale. For studies used in this analysis, a more pile-up robust version of this variable is $f_{\text{core}}^{\text{corr}}$ used, after correcting for pile-up events by taking into account the number of vertices with at least 2 tracks in the event.

2.

$$f_{\text{track}} = \frac{p_T^{\text{leadTrk}}}{\sum_{j \in \text{core}} E_{T,j}^{EM}}$$

is the ratio of the transverse momentum of the track with the highest transverse momentum, to energy deposits in the core region of the $\tau_{\text{had-vis}}$. Here, a pile-up corrected version $f_{\text{track}}^{\text{corr}}$ is used, just like in the f_{core} case.

3.

$$R_{\text{track}} = \frac{\sum_i^{\Delta R_i < 0.4} (p_{T,i} \times \Delta R_i)}{\sum_i^{\Delta R_i < 0.4} p_{T,i}}$$

is the transverse radius defined by the $\tau_{\text{had-vis}}$ tracks, weighted by the p_T of the tracks.

Some variables were showed stronger discrimination strength when applied either to 1-prong or 3-prong $\tau_{\text{had-vis}}$. For example, for 1-prong $\tau_{\text{had-vis}}$ candidates the impact parameter significance ($d_0/\delta d_0$) of the track with the highest p_T , and the number of tracks in the isolation ring are used. For 3-prong $\tau_{\text{had-vis}}$ candidates the maximal ΔR between the $\tau_{\text{had-vis}}$ tracks and its center, and the invariant mass of the track system are used.

With these and other variables each $\tau_{\text{had-vis}}$ candidate lies in a multivariate hyper-space. Monte-Carlo simulations are used to train Boosted Decision Trees (BDTs). $Z \rightarrow \tau\tau$ and $W \rightarrow \tau\nu$ events from simulated samples are used as signal to train the BDT on τ leptons while QCD multi-jets from data are used to train the BDT on QCD jets. The BDT is trained in several distinct categories to maximize its classification strength. The first categorization is n -prong, separating the candidates according to their associated tracks. The second categorization is the reconstructed τ p_T . The p_T ranges are $0 \rightarrow 45$ GeV, $45 \rightarrow 100$ GeV, and $100 \rightarrow \infty$ GeV. The last categorization is the number of vertices in the event, to get a handle on pileup effects. The number of vertices are categorized into ranges of $1 \rightarrow 3$, $4 \rightarrow 7$, and $8 \rightarrow \infty$.

There are three working points for τ identification. *Loose* is defined at a target signal selection efficiency of 70% for 1-prong and 65% for 3-prong $\tau_{\text{had-vis}}$. Likewise, the *medium* working point targets a signal efficiency of 60% for 1-prong and 55% for 3-prong $\tau_{\text{had-vis}}$. Lastly, the *tight* working point targets a signal efficiency of 40% for 1-prong and 35% for 3-prong.

5.5.1.3 Identification against electrons and muons

As already hinted, electrons and muons may also be reconstructed as hadronic τ leptons. This is more common for electrons than it is for muons because muons rarely deposit most of their energy in the calorimeters. Since an electron is likely to be associated with one track, 1-prong $\tau_{\text{had-vis}}$ suffer a lot more electron contamination than 3-prong electrons.

A BDT is used to train hadronic τ signal and electron backgrounds. Monte Carlo simulation samples of $Z \rightarrow \tau\tau$ and $Z \rightarrow ee$ are used for these respective tasks.

Both the electron and τ candidates are required to pass $p_T > 20$ GeV. The $\tau_{\text{had-vis}}$ is further required to pass the BDT loose selection criteria. Upon overlap between and electron and a $\tau_{\text{had-vis}}$, an electron is preferred. The BDT was trained in categories of $|\eta| < 1.37$, $1.37 < |\eta| < 2.0$, $2.0 < |\eta| < 2.3$ and $|\eta| > 2.3$.

Apart from $f_{\text{core}}^{\text{corr}}$, $f_{\text{track}}^{\text{corr}}$ and R_{track} some variables that enhanced electron/ τ separation were used. These are

1.

$$f_{\text{iso}} = \frac{\sum_{i \in \text{isolation ring}} E_{T,i}^{\text{EM}}}{\sum_j^{\Delta R < 0.4} E_{T,j}^{\text{EM}}},$$

compares the width of the electron and $\tau_{\text{had-vis}}$ showers. Although the electron shower is not expected to be much wider than the $\tau_{\text{had-vis}}$ shower, some differences at the core level are expected;

2. and f_{HT} , the ratio of high-threshold to low-threshold hits in the TRT. Electrons, being lighter than pions (from the τ decay), have higher Lorentz factors (γ). So they are expected to produce more high-threshold hits in the TRT than hadronic τ leptons.

5.6 Missing Energy

The longitudinal momentum of the proton constituents during pp collisions at the LHC is not known. Rather, the total transverse momentum of these constituents is expected to be insignificantly smaller than the longitudinal momentum. So, the total transverse momentum before a pp collision can be taken as zero. Due to conservation of momentum, it should also be zero after the collision. In other words, transverse momentum imbalance, also known as *missing transverse energy (MET, or E_T^{miss})*, is expected to be zero if all decay products were detectable by the ATLAS detector.

Neutrinos leave no signature in the ATLAS detector; they are invisible. Their presence is inferred by the presence of E_T^{miss} , whose x and y components are defined as

$$E_{x(y)}^{\text{miss}} = E_{x(y)}^{\text{miss},e} + E_{x(y)}^{\text{miss},\gamma} + E_{x(y)}^{\text{miss},\tau} + E_{x(y)}^{\text{miss,jets}} + E_{x(y)}^{\text{miss},\mu} + E_{x(y)}^{\text{miss,soft}}, \quad (5.13)$$

where each term is either the negative sum of p_T components, or the negative sum of cell energies, weighted according to their position in η and ϕ as follows :

$$E_x^{\text{miss,term}} = \sum_{i=1}^{N_{\text{cell}}^{\text{term}}} E_i \sin \theta_i \cos \phi_i \quad \text{and} \quad E_y^{\text{miss,term}} = \sum_{i=1}^{N_{\text{cell}}^{\text{term}}} E_i \sin \theta_i \sin \phi_i. \quad (5.14)$$

The $E_{x(y)}^{\text{miss,soft}}$ term is called the *soft term*, and the sum of the other terms is collectively called the *hard term*. Reconstruction of the soft and hard terms differs slightly between Run I and Run II, as discussed in Sections 5.6.1 and 5.6.2. To

avoid ambiguities in the detector signals used to construct the physics objects used in the hard term, a priority list is defined. Electrons, having the highest purity, are considered first, followed by photons, hadronic τ leptons, muons and finally jets. This means that objects low in the priority list are removed from the list if they share detector signals with objects higher in the priority list.

Approximating the neutrino masses with zero, $\mathbf{E}_T^{\text{miss}} = \mathbf{p}_T^{\text{miss}}$. These two quantities are therefore used interchangeably in this text.

The magnitude of $\mathbf{E}_T^{\text{miss}}$ is then

$$E_T^{\text{miss}} = \sqrt{(E_x^{\text{miss}})^2 + (E_y^{\text{miss}})^2} \quad (5.15)$$

and its ϕ direction is

$$\phi^{\text{miss}} = \arctan(E_y^{\text{miss}}, E_x^{\text{miss}}). \quad (5.16)$$

The scalar sum of the p_T of all the objects in the event is then

$$\sum E_T = \sum_{i \in \text{hard}} p_{T,i} + \sum_{j \in \text{soft}} p_{T,j}. \quad (5.17)$$

5.6.1 Run I Reconstruction

While the hard term in Run I reconstruction is formulated as in Equation 5.13, the soft term is formulated as

$$E_{x(y)}^{\text{miss,soft}} = E_{x(y)}^{\text{miss,softjets}} + E_{x(y)}^{\text{miss,CellOut}} + (E_{x(y)}^{\text{miss,calo},\mu}), \quad (5.18)$$

where the parentheses on one of the terms hint towards a caveat.

$E_{x(y)}^{\text{miss},e}$, $E_{x(y)}^{\text{miss},\gamma}$ and $E_{x(y)}^{\text{miss},\tau}$ are calculated from cells in clusters associated with electrons, photons and hadronic τ leptons respectively. The electrons and photons are calibrated at the electromagnetic scale, while the hadronic τ leptons are calibrated with the LCW scheme. Electrons, photons and hadronic τ leptons used for this calculation are required to have at least 10 GeV in p_T . While electrons are required to pass the medium identification criteria, photons and hadronic τ leptons are required to pass the tight identification criteria. While both $E_{x(y)}^{\text{miss,softjets}}$ and $E_{x(y)}^{\text{miss,jets}}$ use LCW-calibrated jets reconstructed as in Section 5.4, the former uses jets with $7 < p_T < 20$ GeV and the latter uses jets with $p_T > 20$ GeV. Calorimeter cells not associated to any reconstructed object are calibrated using the LCW scheme and used to reconstruct $E_{x(y)}^{\text{miss,CellOut}}$.

And now the $E_{x(y)}^{\text{miss,calo},\mu}$ caveat: When a muon is isolated from calorimeter jets, as determined by $\Delta R = 0.3$, $E_{x(y)}^{\text{miss},\mu}$ is reconstructed from the muon p_T measured in the Muon Spectrometer and corrected for the energy lost in the calorimeters. In this case, $E_{x(y)}^{\text{miss,calo},\mu}$ is not used in Equation 5.13. Otherwise, $E_{x(y)}^{\text{miss},\mu}$ is reconstructed

from the muon p_T measured in the Muon Spectrometer and $E_{x(y)}^{\text{miss,calo},\mu}$ is not used in Equation 5.13.

The object selection criteria used to construct E_T^{miss} described in this section is constant. This means that E_T^{miss} is constant for each event, even if the physics objects in that event are selected with a different criteria.

5.6.1.1 Performance and Uncertainties

Performance of this E_T^{miss} reconstruction scheme was tested in $W \rightarrow l\nu$, $Z \rightarrow ll$ and events with only two jets. Performance in data was compared to expected performance in Monte Carlo simulation. In $W \rightarrow l\nu$ events the E_T^{miss} is expected to be reconstructed from the neutrino. In $Z \rightarrow ll$ no E_T^{miss} is expected, except from imperfections in the reconstruction scheme. Figures 5.15(a) and 5.15(b) show E_T^{miss} distributions in regions in data rich in $Z \rightarrow ll$ and $W \rightarrow l\nu$ respectively.

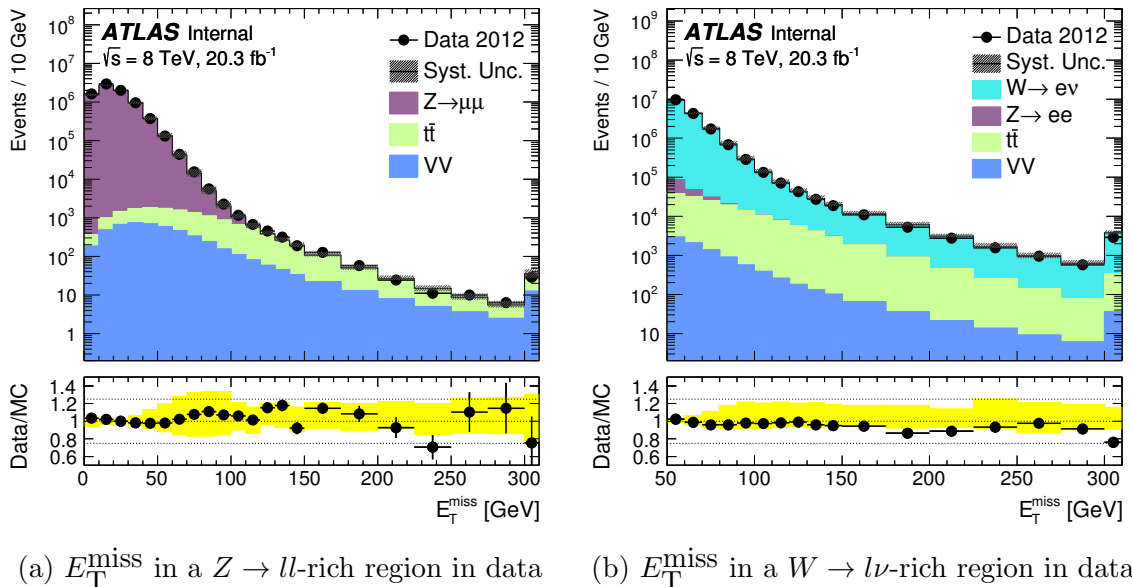


Figure 5.15. Plots showing distributions of E_T^{miss} in data, compared to predictions from Monte Carlo distributions, taken from Ref [117].

To quantify the E_T^{miss} performance, its resolution was approximated by the standard deviations $\sigma(E_{x(y)}^{\text{miss}} - E_{x(y)}^{\text{miss,true}})$ as functions of $\sum E_T$. Since no E_T^{miss} was expected in $Z \rightarrow ll$ events, these standard deviations were reduced to $\sigma(E_{x(y)}^{\text{miss}})$. In $W \rightarrow l\nu$ events $E_{x(y)}^{\text{miss,true}}$ was obtained from Monte Carlo simulation, so resolutions

were studied only in simulation. Contrastingly, in $Z \rightarrow ll$ events resolutions in data and in Monte Carlo simulation were compared. Either way, these resolutions were observed to fall between 5 and 30 GeV, worsening with increasing $\sum E_T$.

Uncertainty in the E_T^{miss} scale was propagated from the scale uncertainties in the individual terms. The uncertainties in the electron, muon, jets, and hadronic τ terms were obtained by methods described in Sections 5.2, 5.3, 5.4, and 5.5. The scale uncertainties in the $E_{x(y)}^{\text{miss,softjets}}$ and $E_{x(y)}^{\text{miss,CellOut}}$ terms, collectively known as *soft terms*, were evaluated by varying energy scales in the topological clusters that contributed to those terms in Monte Carlo simulation. After the scale uncertainties from all terms in Equation 5.13 were evaluated, the overall scale uncertainty on E_T^{miss} using $W \rightarrow l\nu$ Monte Carlo events was found to be about 2.6%.

5.6.2 Run II Reconstruction

The hard terms during Run II reconstruction are formulated just like in Equation 5.13. The selection criteria for the physics objects is however not constant, and consequently E_T^{miss} varies with the physics object selection. The Run II E_T^{miss} used in this thesis is further discussed in Section 6.2.

To evaluate the performance of this reconstruction method a base physics object selection was used. The calibration schemes for each of these objects was identical to those used during Run I reconstruction. Electrons, photons and hadronic τ leptons were required to not fall in the transition region between the central and end-cap calorimeters. Electrons were required to pass the medium selection criteria and have $p_T > 10$ GeV. Photons were required to be tightly identified, have $p_T > 25$ GeV. Hadronic τ leptons were required to be of medium quality and have $p_T > 20$ GeV. Muons were required to be of medium quality, fall in $|\eta| < 2.7$ and have $p_T > 10$ GeV. All jets used had $p_T > 20$ GeV and $|\eta| > 2.4$, or $p_T > 50$ GeV and $|\eta| < 4.5$. Any jets with $20 < p_T < 50$ GeV and $|\eta| < 2.4$ were required to pass additional selection criteria, discussed in Ref [118]; other criteria to resolve overlaps between objects are also discussed in the same Ref.

The soft term was reconstructed from the p_T of tracks in the Inner Detector not associated to any of the physics objects discussed in the preceding paragraph. These tracks were required to have at least 400 MeV in p_T and satisfy all track quality criteria discussed in Section 5.1. In addition, these tracks were required to originate from the primary vertex. This additional requirement enabled the soft term to be pileup-robust.

5.6.2.1 Performance and Uncertainties

Performance of E_T^{miss} was tested in $Z \rightarrow ll$ and $W \rightarrow l\nu$ events, just like during Run I. Figures 5.16(a) and 5.16(b) show the E_T^{miss} distributions in regions in data rich in those two processes respectively. There is reasonable agreement between data

and Monte Carlo prediction. To quantify this performance, the same approximation for resolution discussed in Section 5.6.1 was used. In $Z \rightarrow \mu\mu$ events, resolutions obtained in data and Monte Carlo simulations agreed within at most 10%, with most of the disagreement at high $\sum E_T$. The worst resolution was about 20 GeV in both cases. In $W \rightarrow \mu\nu$ events resolutions were also evaluated with respect to $E_{x(y)}^{\text{miss, true}}$, using Monte Carlo simulation. The worst resolution was 25 GeV.

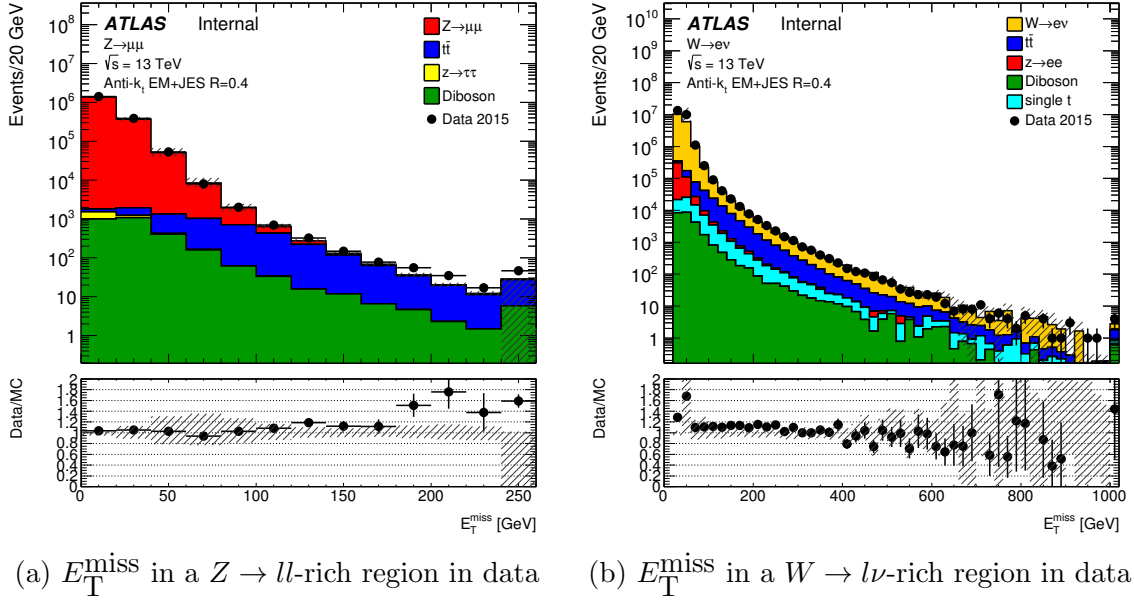


Figure 5.16. Plots showing distributions of E_T^{miss} in data, compared to predictions from Monte Carlo distributions, taken from Ref [118].

Uncertainties on the E_T^{miss} scale were determined from comparisons between data and Monte Carlo simulation. Alternative event generators were used. These were observed to be a few percent [118].

Chapter 6

Charged Higgs Search

A search for evidence of the charged Higgs boson from LHC collisions is presented in this chapter. Potential charged Higgs boson masses were scanned from 200 to 2000 GeV. Observations in this data-set indicate that it is consistent with the Standard Model predictions, rather than predictions from the hMSSM. Exclusion limits were set on the production cross section of the charged Higgs boson times the branching ratio of its decay to a τ lepton and a τ neutrino. In Section 6.1 the data-sets used in the search are presented. Data obtained from LHC collisions is referred to as *data*, while data obtained from simulation is just referred to as *simulation*. In Section 6.2 physics object selection criteria are presented, adding to the criteria presented in Chapter 5. In Section 6.3 the criteria to select events with a charged Higgs boson signature are introduced. Treatment of backgrounds to the charged Higgs boson is discussed in Section 6.4, with the associated systematic uncertainties discussed in Section 6.5. Final event yields are presented in Section 6.6, and their statistical assessment is discussed in the same section.

6.1 Data and Simulation

Data used for this analysis was collected by the ATLAS detector during Run II of the LHC. The LHC parameters and conditions during this data-taking period are discussed in Chapter 3. Only data from runs during which proton beams were stable¹ were considered. The total integrated luminosity of this data-set is 14.7 fb^{-1} , 3.2 fb^{-1} of which was collected in 2015. The rest was collected in 2016. Uncertainties on the 2016 and 2015 luminosities were 3.7% and 2.1% respectively. The impact of these uncertainties on the final results of this search is discussed in Section 6.6.

Expected signal and background events were computed using Monte Carlo (MC) simulation, as discussed in detail in Chapter 4. As discussed in Section 2.3.2, for high m_{H^+} the charged Higgs boson is produced in association with a top quark. Such a production mode is dominated by the 4FS and 5FS diagrams shown in Figure 6.1. Since the 4FS and 5FS diagrams have similar topologies [119], without loss of generality sig-

¹Stable beams are those that have a stable energy of 6.5 TeV.

nal samples were generated only from the 4FS diagram. Using the NNPDF23LO [120] PDF set, hard scatter events were generated by MADGRAPH5_aMC@NLO [121] version 2.2.2. Underlying events were generated by PYTHIA 8 [77] version 8.186, whose parameters were tuned to match parameters, called A14 [122], observed in data. Parton showering, fragmentation and hadronization were handled by PYTHIA [123] version 6.428. Taking the mass of the top quark as 172.5 GeV, 18 signal samples with $200 \text{ GeV} \leq m_{H^+} \leq 2000 \text{ GeV}$ were independently generated.

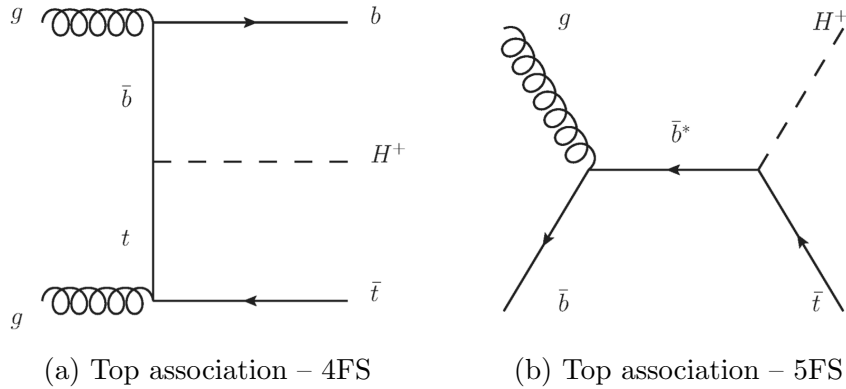


Figure 6.1. Leading order Feynman diagrams for the charged Higgs boson production.

The $t\bar{t}$ process, shown in Figure 6.2, is the most dominant process with a top quark in the final state at the LHC [124]. It is therefore expected to be the most dominant background to the charged Higgs boson produced in association with a top quark. The next dominant source of top quarks at the LHC is the *single top* process, produced through any of the s-, t- or Wt-channels shown in Figure 6.3. The hard scatter events for $t\bar{t}$, Wt- and s-channel single top processes were generated by POWHEG-Box [78–82] version 2 at NLO, using the CT10 [125, 126] PDF set. POWHEG-Box version 1 was used to generate the t-channel single top hard scatter event, using the CT10F4² PDF set. Again, the mass of the top quark was set at 172.5 GeV. Using the CTEQ6L1 [127] PDF set PYTHIA version 6.428 was used to model parton showering, fragmentation and the underlying event. These models were tuned with the Perugia 2012 [128] parameters. While the $t\bar{t}$ cross section was calculated to NNLO+NNLL, single top processes were normalized to NNLO cross sections.

$t\bar{t}$ and single top processes are collectively referred to in this search as *Top*.³

Events containing a W or Z boson and some associated jets are also expected to be a significant background to the signal. Their hard scatter events were generated

²The ‘F4’ indicates that this is a 4FS version of the standard CT10 PDF set

³Not to be confused with the *top* quark, which will either be in full small caps, or abbreviated to *t*.

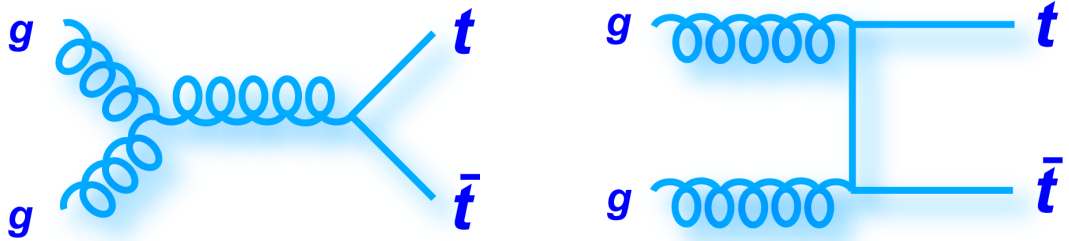


Figure 6.2. Leading order Feynman diagrams for $t\bar{t}$ production at the LHC. Taken from Ref [129].

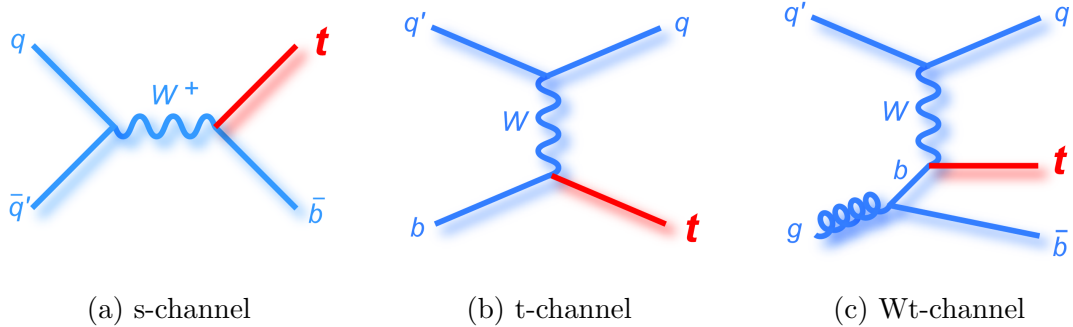


Figure 6.3. Leading order Feynman diagrams for single top quark production at the LHC. Taken from Ref [129].

by MADGRAPH5_aMC@NLO version 2.2.2 with the NNPDF23LO PDF set. PYTHIA 8 was used to generate the underlying events, while PHOTOS [130] was used to radiate photons from charged leptons. All the cross sections were normalized to NNLO.

Events with two vector bosons and associated jets, referred to collectively as VV or *Diboson*, were generated by POWHEG-BOX version 2 interfaced with PYTHIA version 8.186 for the parton shower models. The CT10 PDF set was used to model gluon and quark momenta in the protons. Cross sections were normalized to NLO.

Bottom and charm quark decays were produced and decayed by EVTGEN [131] version 1.2.0. Pileup events were added to these events with PYTHIA version 8 using the MSTW2008LO [71, 132, 133] PDF set. Just like in signal, parton showering, hadronization and fragmentation models in PYTHIA version 8 were also tuned with the A14 parameter set.

6.2 Object Selection

Physics objects used in this search are jets, hadronic τ leptons, electrons, muons and missing transverse energy. Reconstruction and identification of these objects from detector signals is discussed in detail in Chapter 5. This section summarizes other selection criteria imposed on these physics objects, specific to this analysis.

Basic jet reconstruction is discussed in Section 5.4. Of the jets that were reconstructed using the anti- k_T algorithm with $\Delta R = 0.4$, only those with $p_T > 25$ GeV and $|\eta| < 2.5$ were considered. For jets with $p_T < 60$ GeV, the Jet Vertex Tagger (JVT) was used to reduce effects from pileup events. The b-tagging algorithm described in Section 5.4.3 was applied on each jet that passed this selection criteria, ultimately assigning to it a *b-tagging score*. The working point for the score used to identify b-tagged jets in this analysis corresponds to a 70% efficiency in identifying b-jets in $t\bar{t}$ events, at a background rejection rate of 400.

Primary reconstruction of hadronic τ leptons is discussed in Section 5.5. Since every hadronic τ decay includes a ν_τ in its final state, the reconstruction was performed only on the visible components of the decay products. The reconstructed object, which estimates the τ lepton, is referred to here as a $\tau_{\text{had-vis}}$. Treatment of $\tau_{\text{had-vis}}$ was separated into 1-prong and 3-prong candidates, corresponding to decays to 1 π^\pm or 3 π^\pm respectively. A boosted decision tree (BDT) was trained to distinguish $\tau_{\text{had-vis}}$ candidates from jets initiated by quarks or gluons. Loose and medium working points on the BDT output were used for different purposes in this search. The loose working point corresponds to 70% and 65% identification efficiencies on the 1-prong and 3-prong $\tau_{\text{had-vis}}$ candidates. The medium working point corresponds to 55% and 40% identification efficiencies on the 1-prong and 3-prong $\tau_{\text{had-vis}}$ candidates. In both cases, the background rejection rate was found to be of $\mathcal{O}(10^2)$. All $\tau_{\text{had-vis}}$ candidates were required to have $p_T > 40$ GeV and $|\eta| < 2.3$.

Electron and muon reconstruction and identification is discussed in detail in Sections 5.2 and 5.3. Loosely identified and loosely isolated electrons were selected. To further ensure that the electrons originated from the primary vertex, $|z_0 \sin \theta| < 0.5$ and $|d_0/\sigma_{d_0}| < 5$ were imposed. Electron candidates that satisfied these selection criteria were additionally required to have $p_T > 20$ GeV, and be within $|\eta| < 2.47$, excluding transition between the barrel and end-cap regions $1.37 < |\eta| < 1.52$. Muons were also loosely identified and isolated. In addition, impact parameter selection criteria were imposed on them to ensure that they originated from the primary vertex: $|z_0 \sin \theta| < 0.5$ and $|d_0/\sigma_{d_0}| < 3$. Those that satisfied these requirements were required to have $p_T > 20$ GeV and be within $|\eta| < 2.5$.

Overlap between the physics objects discussed above were resolved using the following priority list: $\mu \rightarrow e \rightarrow \tau_{\text{had-vis}} \rightarrow \text{jet}$. If an electron was found within $\Delta R < 0.2$ of a reconstructed muon, the electron was removed from the list of physics objects in that event. This is because since electrons experience photon radiation and brehmsstrahlung at a higher rate than muons, they are more difficult to reconstruct.

If a $\tau_{\text{had-vis}}$ was reconstructed within $\Delta R < 0.2$ of an electron or muon, the $\tau_{\text{had-vis}}$ was removed. Likewise, if a jet was reconstructed within $\Delta R < 0.2$ of an electron, muon or τ lepton, the jet was removed from the list.

E_T^{miss} , the magnitude of the missing transverse momentum, was reconstructed after all the other physics objects were identified and overlaps were resolved. It was reconstructed as the negative vector sum of all the reconstructed and calibrated objects, and the reconstructed tracks that were not associated to any physics objects. All these objects were required to originate from the hard scatter event. This association with the hard scatter event reduced effects from pileup events on the reconstructed E_T^{miss} .

Table 6.1 summarizes all the physics object selection criteria for this analysis.

Physics Object	Selection Criteria
Jets	anti- k_T with $\Delta R = 0.4$ $p_T > 25$ GeV, $ \eta < 2.5$ JVT for $p_T < 60$ GeV
b -tagged Jets	b -tagging score at 70% efficiency working point
$\tau_{\text{had-vis}}$	BDT score working point at 55%(40%) efficiency for 1(3)-prong for medium BDT score working point at 70%(65%) efficiency for 1(3)-prong for loose $p_T > 40$ GeV, $ \eta < 2.3$
Electrons	Loose ID Loose Isolation $p_T > 20$ GeV, $ \eta < 2.47$ excluding $1.37 < \eta < 1.52$
Muons	Loose ID Loose Isolation $p_T > 20$ GeV, $ \eta < 2.5$

Table 6.1. Selection criteria for physics objects.

6.3 Event Selection

Evidence for the charged Higgs boson was searched for in events in which the Higgs boson decays to a τ lepton and a ν_τ . In these events, the τ lepton decays hadronically and is reconstructed as a $\tau_{\text{had-vis}}$. The 4FS and 5FS topologies for such events, signal events, are respectively

$$gb \rightarrow [t][H^+] \rightarrow [(jj)b][(\tau_{\text{had-vis}} + E_T^{\text{miss}})] \quad (6.1)$$

and

$$gg \rightarrow [tb][H^+] \rightarrow [(jj)bb][(\tau_{\text{had-vis}} + E_T^{\text{miss}})]. \quad (6.2)$$

In the terminology of Equations 6.1 and 6.2 a b -tagged reconstructed jet is represented by b , otherwise it is represented by j . Table 6.2 summarizes the selection criteria optimized to select signal events as represented by Equations 6.1 and 6.2 and minimize the level of background contamination. These selection criteria define the *signal region*. This section discusses each component of these selection criteria.

Before pre-selection, measures were taken to reduce the number of events originating from instrumental effects such as intra-beam interactions and proton losses upstream of the interaction point.⁴ This was achieved by requiring the following :

1. no jet with $p_T > 25$ GeV that fails the `BadLoose` quality selection criteria discussed in Section 5.4;
2. at least one vertex with two or more tracks. This selection is designed to identify the primary vertex to which all the physics objects should point;
3. the SCT, Tile and LAr Calorimeters not be in an error or unknown state;
4. and the event must be considered *complete* by the TTC.⁵

These selection criteria are collectively referred to as *clean-event* in the rest of this chapter.

	Selection
pre-selection	Pass trigger <code>HLT_xe70_tc_1cw</code> (<code>HLT_xe90_mht</code>) for 2015(2016) data Exactly one $\tau_{\text{had-vis}}$ with $p_T > 40$ GeV At least 3 jets with $p_T > 25$ GeV No muon or electron
full selection	At least one b -tagged jet $E_T^{\text{miss}} > 150$ GeV $m_T > 50$ GeV

Table 6.2. Signal region definition. Additionally, measures were taken to ensure that events originated from inelastic pp collisions and no jets originated from unwanted experimental effects.

The event topology presented in Equations 6.1 and 6.2 suggests several options to trigger on when selecting such events. One could use a trigger that demands presence of a $\tau_{\text{had-vis}}$, some E_T^{miss} , or both the $\tau_{\text{had-vis}}$ and some E_T^{miss} . The least stringent $\tau_{\text{had-vis}}$ -only trigger available on both the 2015 and 2016 trigger menu required presence of a $\tau_{\text{had-vis}}$ with $p_T > 160$ GeV in the event. Since the topology in Equations 6.1 and 6.2 is not biased towards high- p_T τ leptons, a $\tau_{\text{had-vis}}$ -only

⁴Proton losses from the beam may induce cascades that may eventually reach the ATLAS detector. These cascades would be reconstructed as jets.

⁵See Section 3.2.4 for a more formal definition of ‘complete’.

trigger was not chosen. The least stringent of all unprescaled triggers that require presence of both a $\tau_{\text{had-vis}}$ and some E_T^{miss} required the $\tau_{\text{had-vis}}$ to have at least 35 GeV in p_T and $E_T^{\text{miss}} > 70$ GeV. Likewise, the least stringent unprescaled trigger that requires the presence of just E_T^{miss} required $E_T^{\text{miss}} > 70$ GeV. The efficiencies of the E_T^{miss} -only and the $E_T^{\text{miss}} + \tau_{\text{had-vis}}$ triggers when selecting signal events in Monte Carlo simulation were found to be comparable. Thus, there was no advantage in using an $E_T^{\text{miss}} + \tau_{\text{had-vis}}$ trigger over an E_T^{miss} -only trigger.

To avoid imposing selection criteria on the $\tau_{\text{had-vis}}$, only E_T^{miss} -only-based triggers were considered. Figure 6.4 shows signal selection efficiency distributions for several of E_T^{miss} -only triggers on a signal sample with $m_{H^+} = 200$ GeV, binned in E_T^{miss} . The naming convention for these triggers can be generalized to

`Level_xeMissingEnergyCut_MissingEnergyReco`.

`Level` indicates the level in the trigger system at which the trigger is active. In this case, the level is `HLT`, denoting the Higher Level Trigger. At this level the E_T^{miss} may be reconstructed using either topological clusters, in which case `MissingEnergyReco` is `tc_lcw`, or jet energies, in which case `MissingEnergyReco` is `mht`. Otherwise, the E_T^{miss} is reconstructed using energy recorded in calorimeter cells. For $100 < E_T^{\text{miss}} < 200$ GeV, the most efficient trigger is `HLT_xe70_tc_lcw`, which accepts events with $E_T^{\text{miss}} > 70$ GeV.

While `HLT_xe70_tc_lcw` was the least stringent E_T^{miss} -only trigger during the 2015 data-taking period, `HLT_xe90_mht` was the least stringent in the 2016 data-taking period. Events from the 2015 data-set were therefore triggered with `HLT_xe70_tc_lcw`, and events from the 2016 data-set were triggered with `HLT_xe90_mht`.

In addition to trigger requirements, the pre-selection criteria required events to have exactly one $\tau_{\text{had-vis}}$. The said $\tau_{\text{had-vis}}$ was also required to have $p_T > 40$ GeV. At least 3 reconstructed jets with $p_T > 25$ GeV were required to be present. Since the topologies in Equations 6.1 and 6.2 do not include electrons or muons, the event was also required to have no electrons or muons.

For the full selection at least one b -tagged jet was demanded. Additionally, the event had to have $E_T^{\text{miss}} > 150$ GeV and $m_T > 50$ GeV, where m_T is the transverse mass of the $\tau_{\text{had-vis}}, E_T^{\text{miss}}$ system :

$$m_T = \sqrt{2p_T^\tau E_T^{\text{miss}}(1 - \cos \Delta\phi_{\tau, E_T^{\text{miss}}})}. \quad (6.3)$$

Figures 6.5(a) and 6.5(b) show expected E_T^{miss} and m_T ‘n-1’ distributions after the full selection criteria has been applied,⁶ for backgrounds where the $\tau_{\text{had-vis}}$ was reconstructed from a τ lepton and for several signal samples. Vertical black lines

⁶These are distributions where all the selection criteria has been applied except the criteria based on the variable being plotted.

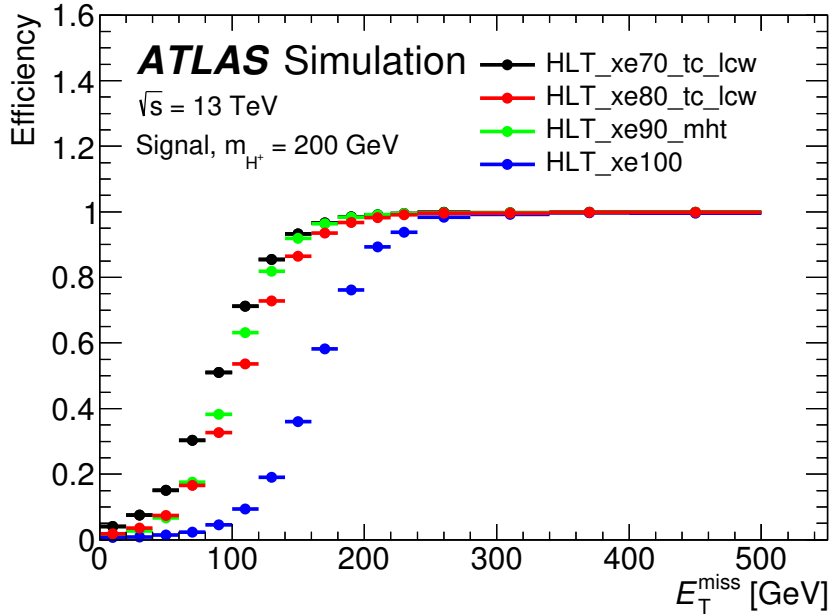


Figure 6.4. Plots of the efficiencies of several E_T^{miss} -based triggers, obtained from simulation of signal with $m_{H^+} = 200$ GeV.

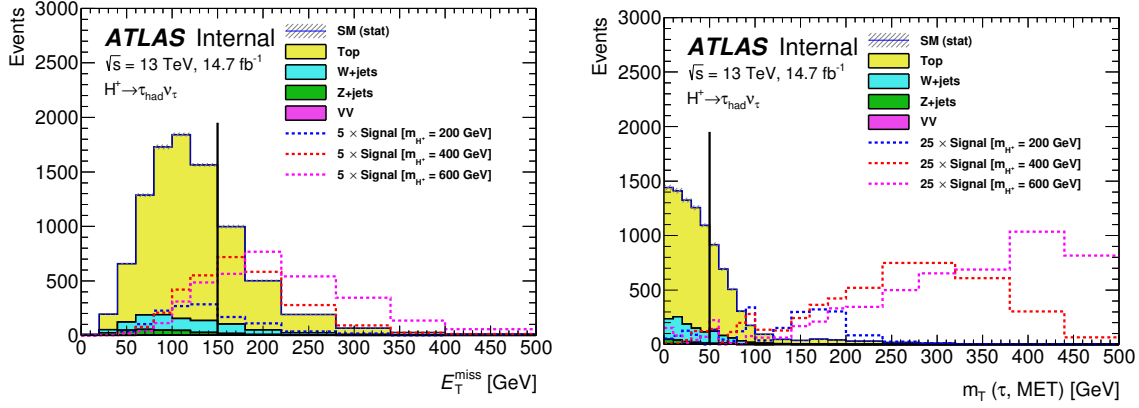
show the point at which E_T^{miss} and m_T are cut on. As already been predicted, it is expected that the Top background dominates, followed by the $W + \text{jets}$ background.

Treatment of backgrounds where the $\tau_{\text{had-vis}}$ is reconstructed from objects other than τ leptons is discussed in Sections 6.4.2 and 6.4.1.

Events in which E_T^{miss} is mismeasured and is aligned to the τ direction are suppressed by the m_T requirement. Moreover, events from which $m_T < 50$ GeV are likely to contain $W^+ \rightarrow \tau\nu$ processes rather than signal. The E_T^{miss} requirement suppresses background from QCD multijets.

6.3.1 Trigger Efficiency

Although trigger decisions in Monte Carlo simulation are sufficient to evaluate and compare trigger efficiencies as demonstrated by Figure 6.4, they may not perfectly model trigger decisions in data. As shown in Table 6.2, trigger decisions in simulation are essential in predicting background processes that contaminate the signal region. To account for this potential mis-modelling, efficiencies in simulation were corrected to those in data. The efficiencies from data were extracted from a dedicated control region and binned in E_T^{miss} . The trigger efficiency in data, in an E_T^{miss} bin was then defined as



(a) Expected E_T^{miss} distributions in the signal region, minus $E_T^{\text{miss}} > 150$ GeV
(b) Expected m_T distributions in the signal region, minus $m_T > 50$ GeV

Figure 6.5. N-1 distributions after the full selection criteria have been applied. The black vertical line marks the point at which the variable being plotted is cut on.

$$\epsilon = \frac{\text{control region selection} + \text{Trigger}}{\text{control region selection}} \quad (6.4)$$

where the ‘Trigger’ is either `HLT_xe70_tc_lcw` or `HLT_xe90_mht`. Both triggers require the event to pass an L1 trigger that demands at least 50 GeV in online E_T^{miss} . Apart from passing the clean-event selection, the control region selection is defined as follows :

1. exactly one loosely identified and loosely isolated electron, trigger matched to `HLT_e26_lhtight_iloose_L1EM20VH`;
2. exactly one loosely identified $\tau_{\text{had-vis}}$ with at least 26 GeV;
3. and at least two reconstructed jets, one of which must be b -tagged.

A similar control region with exactly one muon and no electrons was also considered. m_T and E_T^{miss} distributions in the 1-electron control region are shown in Figure 6.6. Here, contributions from processes in which jets are reconstructed as $\tau_{\text{had-vis}}(j \rightarrow \tau)$, or those in which non- τ leptons are reconstructed as $\tau_{\text{had-vis}}(l \rightarrow \tau)$, were estimated using methods described in Section 6.4. As will become clearer in the said section, application of those methods in this region requires some careful extrapolations that compensate for differences in topological structures in the two regions. Estimations shown in Figure 6.6 are rather ad-hoc because they do not take into account these differences. Consequently, there is an obvious mis-modelling of physics processes in the low E_T^{miss} and m_T regions, as shown by the disagreement between data and simulation. Reasonable agreement between data and predictions is observed at $E_T^{\text{miss}} > 50$ GeV. Since trigger thresholds studied were at minimum

$E_T^{\text{miss}} = 70$, disagreements in the low E_T^{miss} and low m_T regions did not have significant impact on measurements.

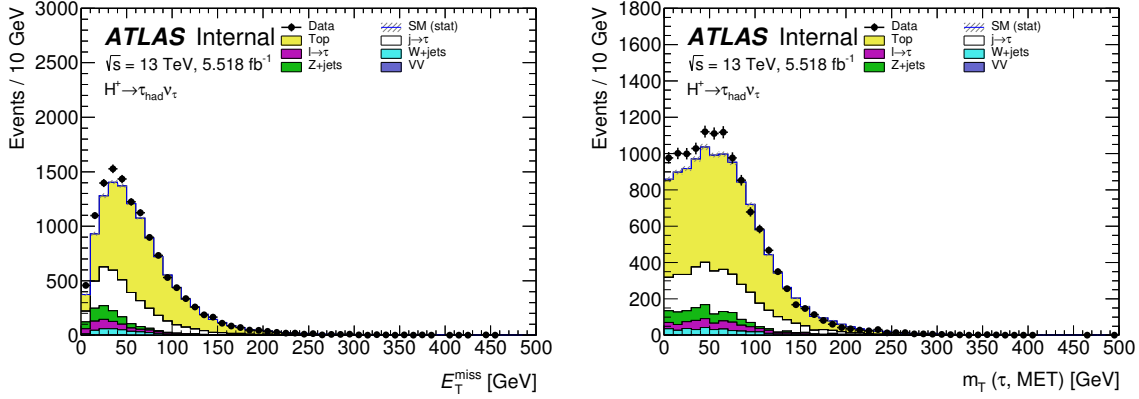


Figure 6.6. E_T^{miss} and m_T distributions in the control region used to measure trigger efficiencies. Since trigger thresholds studied were at minimum $E_T^{\text{miss}} = 70$, disagreements in the low E_T^{miss} and low m_T regions did not have significant impact on measurements.

To obtain continuous efficiency distributions, the binned efficiencies from data were fitted to the error function, parametrized as

$$F(x) = p_0 \cdot \left[1 + \text{erf} \left(\frac{x - p_1}{p_2} \right) \right] + p_3 \quad (6.5)$$

where initial values for the p_i were repeatedly changed until an optimal fit was obtained. The optimization of the fit was quantified by the χ^2 distribution. This procedure was done separately for the 2015 and 2016 datasets. The efficiency distributions and their respective fits are shown in Figures 6.7(a) and 6.7(b), reaching 100% efficiency at about $E_T^{\text{miss}} = 250$ GeV. In these plots the region from which most of the events in the signal region lie, $150 < E_T^{\text{miss}} < 250$ GeV, is marked with vertical dashed lines.

6.4 Background Modelling

Backgrounds are categorized into 3 classes that are defined according to the source of the $\tau_{\text{had-vis}}$. If the $\tau_{\text{had-vis}}$ is reconstructed from a τ lepton, it is referred to as a *true* $\tau_{\text{had-vis}}$. Treatment of this category has been briefly discussed in Section 6.3 and is discussed in more detail in Section 6.4.3. Events in which a $\tau_{\text{had-vis}}$ is reconstructed from an electron or muon constitute the $l \rightarrow \tau$ background. More on

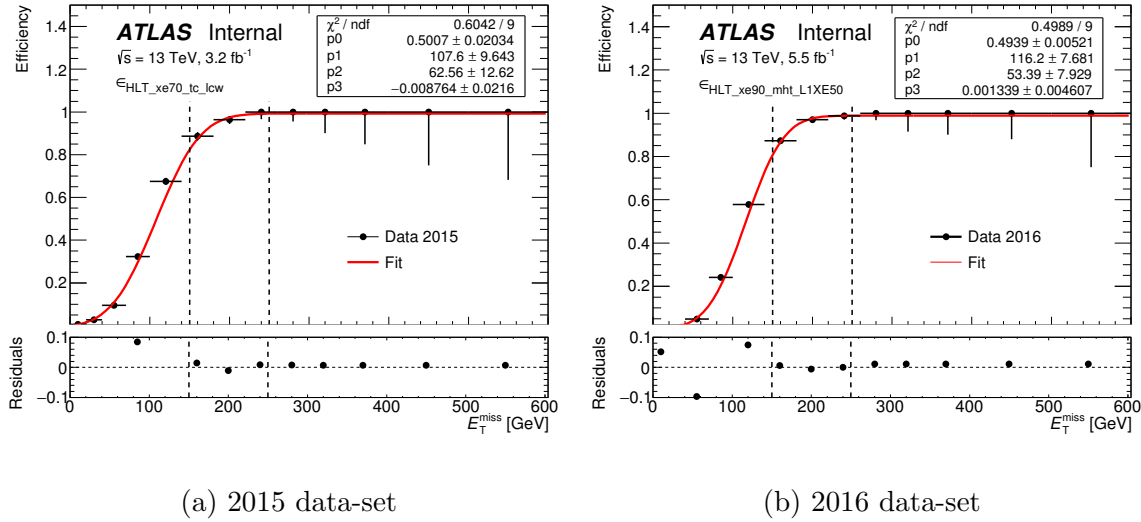


Figure 6.7. Plots showing trigger efficiency fits.

this in Section 6.4.1. Events in which a $\tau_{\text{had-vis}}$ is reconstructed from a jet, be it from a quark or gluon, constitute the $j \rightarrow \tau$ background. More on this in Section 6.4.2. The $j \rightarrow \tau$ and $l \rightarrow \tau$ backgrounds are collectively referred to here as the *Mis-ID*⁷ backgrounds.

6.4.1 Lepton to τ

For the $l \rightarrow \tau_{\text{had-vis}}$ backgrounds only the $e \rightarrow \tau_{\text{had-vis}}$ contribution is estimated; the $\mu \rightarrow \tau_{\text{had-vis}}$ background contamination in the signal region was found to be an order of magnitude smaller. Backgrounds in which a $\tau_{\text{had-vis}}$ is matched in ΔR to an electron are applied a scale factor, which encodes the probability of an electron to fake a $\tau_{\text{had-vis}}$. This scale factor is dependent on whether the reconstructed $\tau_{\text{had-vis}}$ is 1-prong or 3-prong, so separate computations are performed. This scale factor was also observed to be dependent on η , so it was parametrized accordingly.

To measure these scale factors the following $Z \rightarrow ee$ control region is designed

- exactly one electron matched to a single electron trigger;
 - exactly one medium $\tau_{\text{had-vis}}$ with charge opposite to the electron;
 - no b -tagged jets; and
 - $m_T(e, E_T^{\text{miss}}) < 40 \text{ GeV}$

Here, the electron is used as a tag, and the $\tau_{\text{had-vis}}$ as a probe. To ensure that the $\tau_{\text{had-vis}}$ and the electron originate from the Z , the mass of the $e - \tau_{\text{had-vis}}$ system is restricted to between 80 GeV and 100 GeV.

The scale factors were computed as the ratio of events that pass all selection criteria to those that pass all but not necessarily the presence of the $\tau_{\text{had-vis}}$. This

⁷For ‘misidentified τ ’.

computation was performed in both data and simulation. In data, non- $Z \rightarrow ee$ events were subtracted from data before the calculation was performed. Figure 6.8 shows these scale factors, parametrized in η . They range from 0.5% to 2.5%.

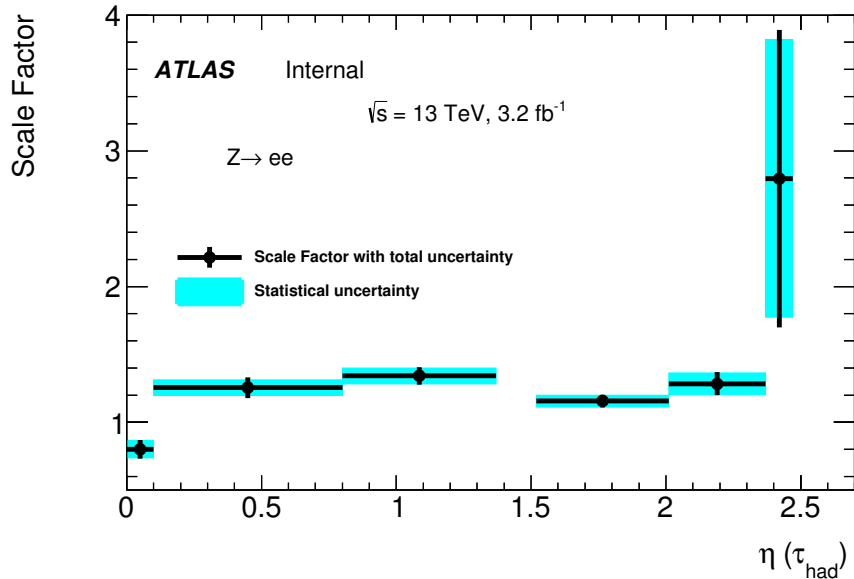


Figure 6.8. Plot showing the probability of an electron to fake a $\tau_{\text{had-vis}}$, parametrized in η .

6.4.2 $j \rightarrow \tau$ backgrounds

The *Fake Factor Method (FFM)*, described in this section, is used to estimate $j \rightarrow \tau$ backgrounds. The strategy is to extrapolate to the signal region the number of events where a $\tau_{\text{had-vis}}$ is reconstructed from a quark or gluon initiated jet, from a control region rich with quark or gluon initiated jets. The extrapolation is handled by scale factors, referred to as *Fake Factors (FF)*. During this extrapolation large uncertainties are accrued from differences between the said control region and the signal region. To minimize them, the control region is designed to be as close to the signal region as possible. The control region used here, referred to as the *anti- τ* region, only differs from the signal region in that the reconstructed $\tau_{\text{had-vis}}$ fails the identification criteria required in the signal region. More specifically, the *anti- τ* region is identical to the signal region except that its $\tau_{\text{had-vis}}$ is required to be not loose and its jet BDT score is required to be greater than 0.5. Events in which a quark or gluon initiated jet fakes a τ lepton in the signal region, N_{fakes}^τ , are therefore estimated by weighting events in the *anti- τ* region, $N_{\text{fakes}}^{\text{anti-}\tau}$, with FF as summarized in Equation 6.6.

$$N_{\text{fakes}}^{\tau} = N_{\text{fakes}}^{\text{anti-}\tau} \times \text{FF} \quad (6.6)$$

The FF are measured from a region in data that is rich in quark or gluon initiated jets. This *measurement* control region must be different from the control region in which the FF are applied (e.g the one described in the preceding paragraph). It is however similar in the sense that the $\tau_{\text{had-vis}}$ is required to pass the same identification criteria. In this case it is required to be not loose and have a jet BDT score greater than 0.5. In that respect, it is referred to as the *anti- τ -id*⁸ region. A similar control region, but with the $\tau_{\text{had-vis}}$ required to pass the identification criteria that is demanded in the signal region, is also defined. This is called the τ -id control region. The number of events in the anti- τ -id control region, $N_{\text{anti-}\tau\text{-id}}$, and the number of events in the τ -id region, $N_{\tau\text{-id}}$, are extracted. The fake factors are then computed as

$$\text{FF} = \frac{N_{\tau\text{-id}}}{N_{\text{anti-}\tau\text{-id}}} \quad (6.7)$$

6.4.2.1 Pre-validation

To test the effectiveness of this method, fake factors from $t\bar{t}$ simulation are applied on $t\bar{t}$ events after a different selection criteria has been applied. Simulated $t\bar{t}$ events with exactly one not loose $\tau_{\text{had-vis}}$ make up the anti- τ -id region. Similarly, events with exactly one medium $\tau_{\text{had-vis}}$ make up the τ -id region. Since the probability of a jet being mis-identified as a $\tau_{\text{had-vis}}$ depends on the jet substructure, FF are parameterized in terms of parameters that describe the jet substructure. These are

1. Transverse momentum of the $\tau_{\text{had-vis}}$, p_T^{τ} . This parameter is sensitive to the gluon or quark fractions in the jet;
2. τ decay mode. This is essentially a measure of the number of pions that the τ lepton decays to; and
3. b -tagger weight.

The FF obtained in the $t\bar{t}$ MC simulation are applied to $t\bar{t}$ events that pass the preselection criteria defined in Table 6.2. Figure 6.9 shows comparisons between estimation using FF and direct MC estimation.

6.4.2.2 FF measurement control regions

Two regions in data that are rich in jets reconstructed as $\tau_{\text{had-vis}}$ are used to extract FF. One of these regions is designed to be dominated by QCD multi-jet events, while the other is dominated by $W + \text{jets}$ events. The former will be referred to as the *multi-jet* region while the latter as the $W + \text{jets}$ region. The fraction of jets that are initiated by quarks in the multi-jet region is roughly the same as the fraction

⁸To emphasize, this is not to be confused with the anti- τ region in which the FF are applied.

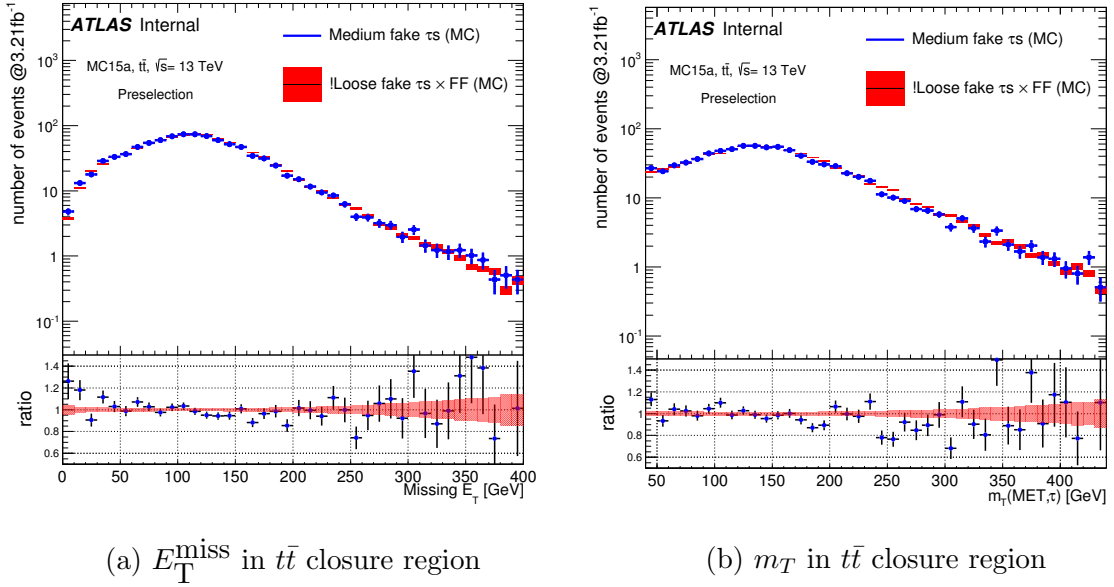
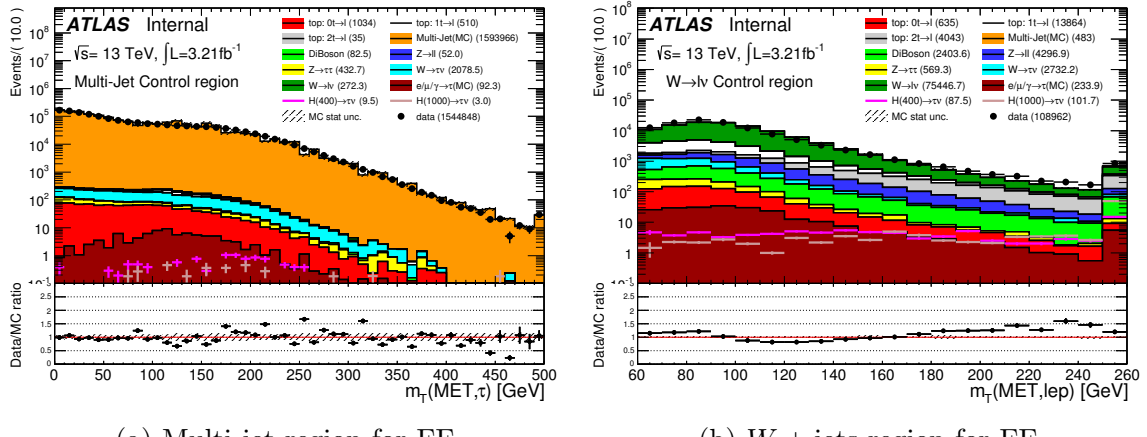


Figure 6.9. Plots showing the comparison of estimations using direct MC versus the FF method.

of jets that are initiated by gluons in the same region. In contrast, the $W + \text{jets}$ region is dominated by jets initiated by light-flavor quarks. Since the substructure of jets is expected to depend on their source, it is necessary to evaluate the impact of these different sources on the final results. The multi-jet region is used as the nominal region for measuring FF. Measurements taken from $W + \text{jets}$ are used as a systematic variation corresponding to the inclusion of a higher fraction of light-flavor quarks.

The multi-jet region is similar to the signal region. It differs from the signal region in that it requires 0 b -tagged jets and $E_T^{\text{miss}} < 80$ GeV. Figure 6.10(a) shows m_T distributions for processes that pass this selection criteria. The $W + \text{jets}$ region is more different to the signal region than the multi-jet region. E_T^{miss} is required to be at most 150 GeV, exactly one electron or muon must be present, no b -tagged jets, and $m_T(e/\mu, E_T^{\text{miss}}) > 60$ GeV. Figure 6.10(b) shows m_T distributions in this region.

Figures 6.11(a) and 6.11(b) show the FF obtained from the multi-jet region. They are parametrized in p_T computed separately for 1-prong and 3-prong $\tau_{\text{had-vis}}$ candidates. Figure 6.11(a) is from 2015 data while Figure 6.11(b) is from 2016 data. The binning in p_T was optimized to have a minimal statistical uncertainty in each bin. For 2016 data the FF dependence on the b -tag weight was insignificant so it wasn't pursued further.



(a) Multi-jet region for FF

(b) $W + \text{jets}$ region for FF

Figure 6.10. Plots showing m_T distributions in the multi-jet and the $W + \text{jets}$ control regions.

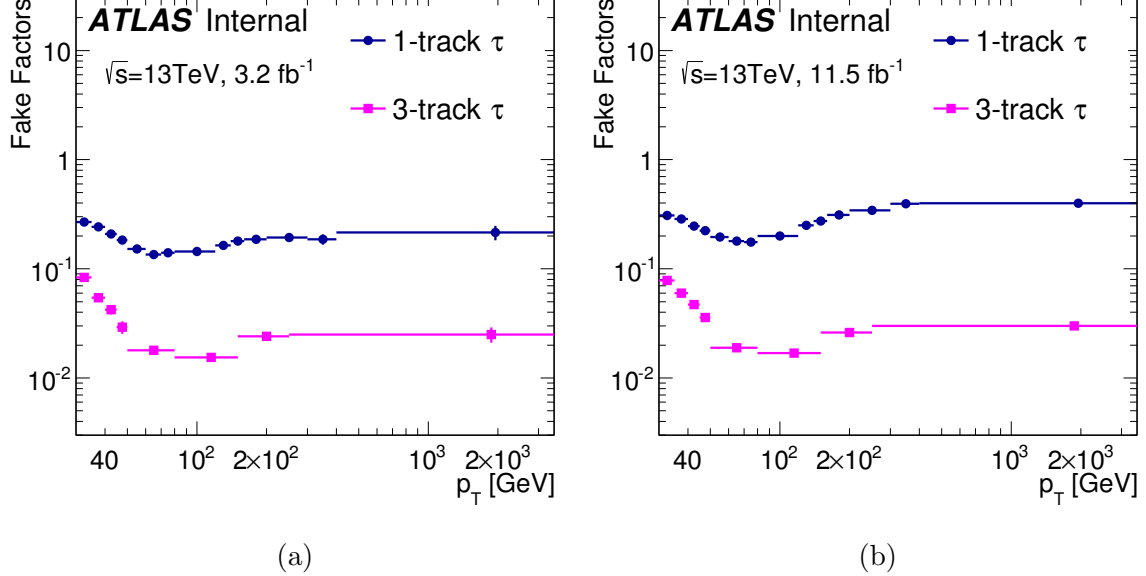


Figure 6.11. Plots showing the measured FF parametrized in $\tau_{\text{had-vis}} p_T$.

6.4.2.3 Validation

The FF shown in Figure 6.11 were validated in several control regions. First is the multi-jet control region from which these FF were measured. Figure 6.12 shows the estimated $j \rightarrow \tau$ contribution in this region, using the FFM. Overall, the estimation shows good FF modelling in this region.

To evaluate the FF robustness to change in jet composition, two control regions were used. As already mentioned, the $W + \text{jets}$ region is dominated by jets initiated

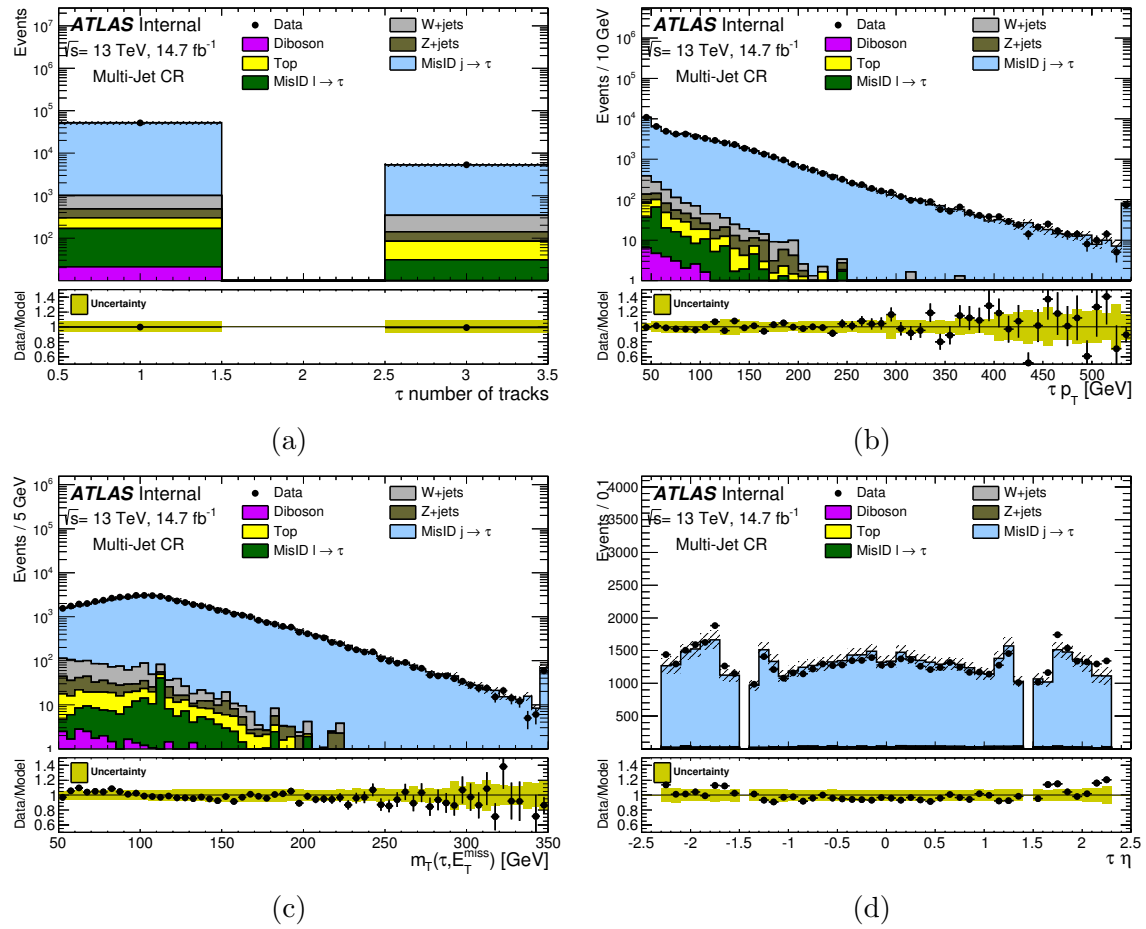


Figure 6.12. FF closure plots in the multi-jet measurement control region.

by light-flavored quarks. Contrastingly, a region rich in $t\bar{t}$ events is dominated by jets initiated by heavy-flavored quarks. These two regions were used to evaluate the impact of heavy versus light-flavored quarks on FF modelling, and vice-versa. Figure 6.13 and Figure 6.14 show the estimated $j \rightarrow \tau$ background using the FF method in the $W +$ jets and $t\bar{t}$ control regions respectively. The modelling in the $W +$ jets control region is good, while the modelling in the $t\bar{t}$ control region shows an overall event underestimation. The statistical uncertainties in the $t\bar{t}$ control region are larger, indicating that the observed underestimation may be statistical in nature.

6.4.3 True $\tau_{\text{had-vis}}$ backgrounds

True $\tau_{\text{had-vis}}$ backgrounds are estimated from Monte Carlo simulation. Such backgrounds expected in the signal region are shown in Figures 6.5(a) and 6.5(b). Top and $W +$ jets processes are expected to dominate these backgrounds, while a few $Z +$ jets and $V V$ events are also expected to contaminate the signal region.

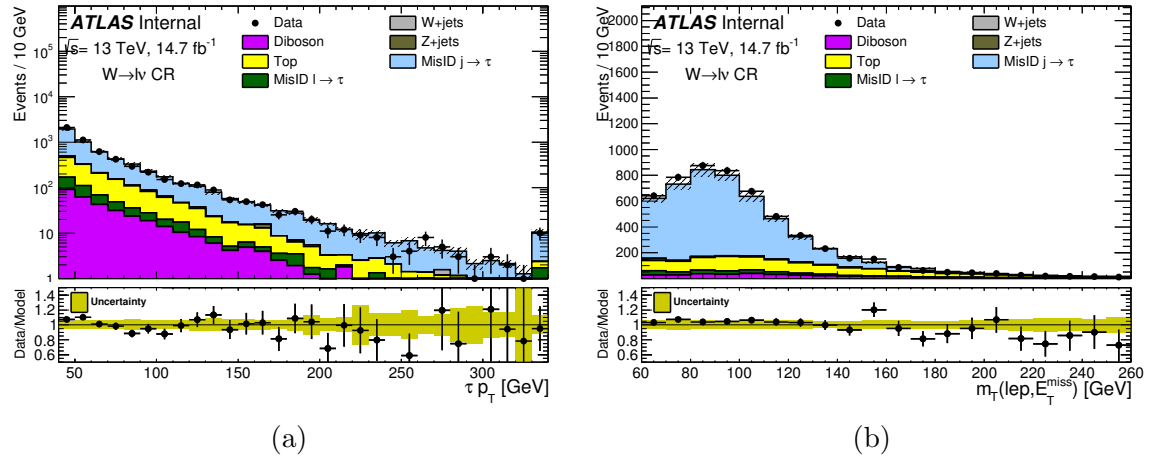


Figure 6.13. FF closure plots in the $W + \text{jets}$ control region.

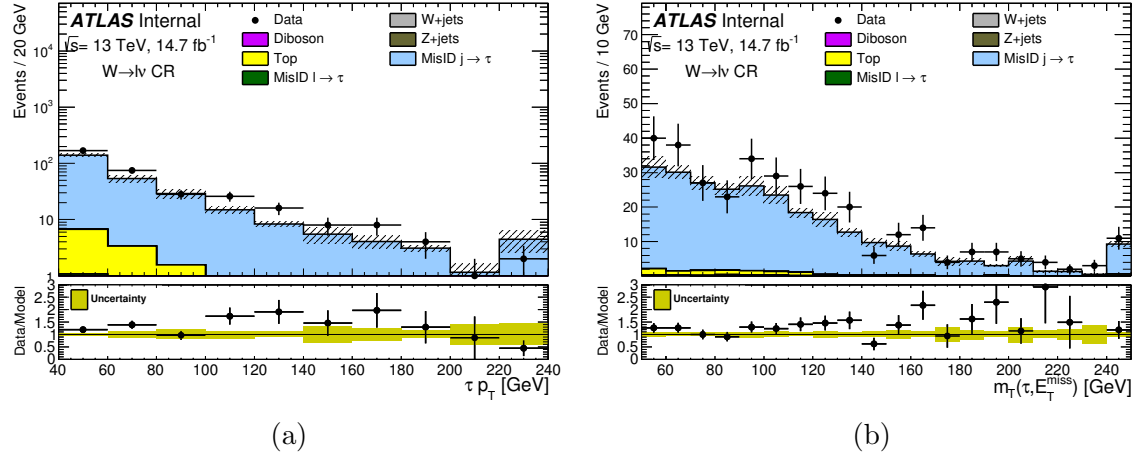


Figure 6.14. FF closure plots in the $t\bar{t}$ control region.

$t\bar{t}$ may be mis-classified as signal when one of the top quarks decays leptonically as

$$\begin{aligned} t &\rightarrow W^+ b \rightarrow \tau \nu_\tau \quad \text{and the other as,} \\ t &\rightarrow W^+ b \rightarrow q q b. \end{aligned} \tag{6.8}$$

In this topology, the ν_τ is reconstructed as E_T^{miss} and the τ as $\tau_{\text{had-vis}}$; the three quarks from the other top decay may be reconstructed as jets, one of which may be b -tagged. The $m_T(\tau, \nu_\tau)$, is usually low in this topology because the $\tau_{\text{had-vis}}$ and E_T^{miss} are expected to be aligned in ϕ . The secondary method of $t\bar{t}$ signal contamination is when both top quarks decay leptonically and one of the leptons is not identified or reconstructed. In this case m_T is expected to be high because the

E_T^{miss} is a reconstruction of two ν_τ . A single top can get mis-classified as signal when the top quark decays leptonically, and the associated quarks are reconstructed as jets. Note that only the Wt -channel has multiple jets in the leading order calculation. So, contribution of single top to the signal region is relatively smaller than that of $t\bar{t}$.

$W + \text{jets}$ events enter the signal region when the W^+ decays to a τ lepton and a ν_τ . Since the signal region requires at least 3 jets in the event, $W + \text{jets}$ only enters the signal region if it has 3 or more associated jets.

Since $t\bar{t}$ and $W + \text{jets}$ are the most dominant backgrounds processes in the signal region, dedicated control regions in data are devised to assess their modelling in simulation. For this assessment to be extrapolated to the signal region, these control regions are designed to be as close as possible to it. They are also designed to have as few signal events as possible to reduce bias.

The $t\bar{t}$ control region differs from the signal region in that 2 or more b -tagged jets and $m_T < 100$ GeV are required. The b -tagged jets requirement is justifiable from Equation 6.8. The low m_T selection is to maximize $t\bar{t}$ events in which one of the top quarks decays to a τ lepton, while refraining from the high m_T region that is part of the signal region. With this selection criteria the $t\bar{t}$ control region has a small overlap with the signal region, but the expected signal contamination is about one order of magnitude smaller than the expected fraction of $H^+ \rightarrow \tau^+\nu$ events in the signal region. Kinematic distributions in this region are shown in Figure 6.15.

The $W + \text{jets}$ control region differs from the signal region in that it requires events to have no b -tagged jets and have $mT < 100$ GeV. This region is orthogonal to the signal region, and yet close to the signal region in phase space. Kinematic variables are shown in Figure 6.16.

6.5 Systematic Uncertainties and Statistical Methods

6.5.1 Systematic Uncertainties

Systematic uncertainties considered in this analysis are grouped into experimental and theoretical categories. Regardless of the category, the procedure for evaluating each uncertainty's impact on the analysis results is the same:

1. a parameter that corresponds to that uncertainty is shifted by $\pm 1\sigma$ from the nominal value;
2. this shift may propagate to the final event yields, the shapes of key kinematic distributions such as m_T , or both;
3. and finally, shape and yield shifts are both examined for each systematic variation in this analysis.

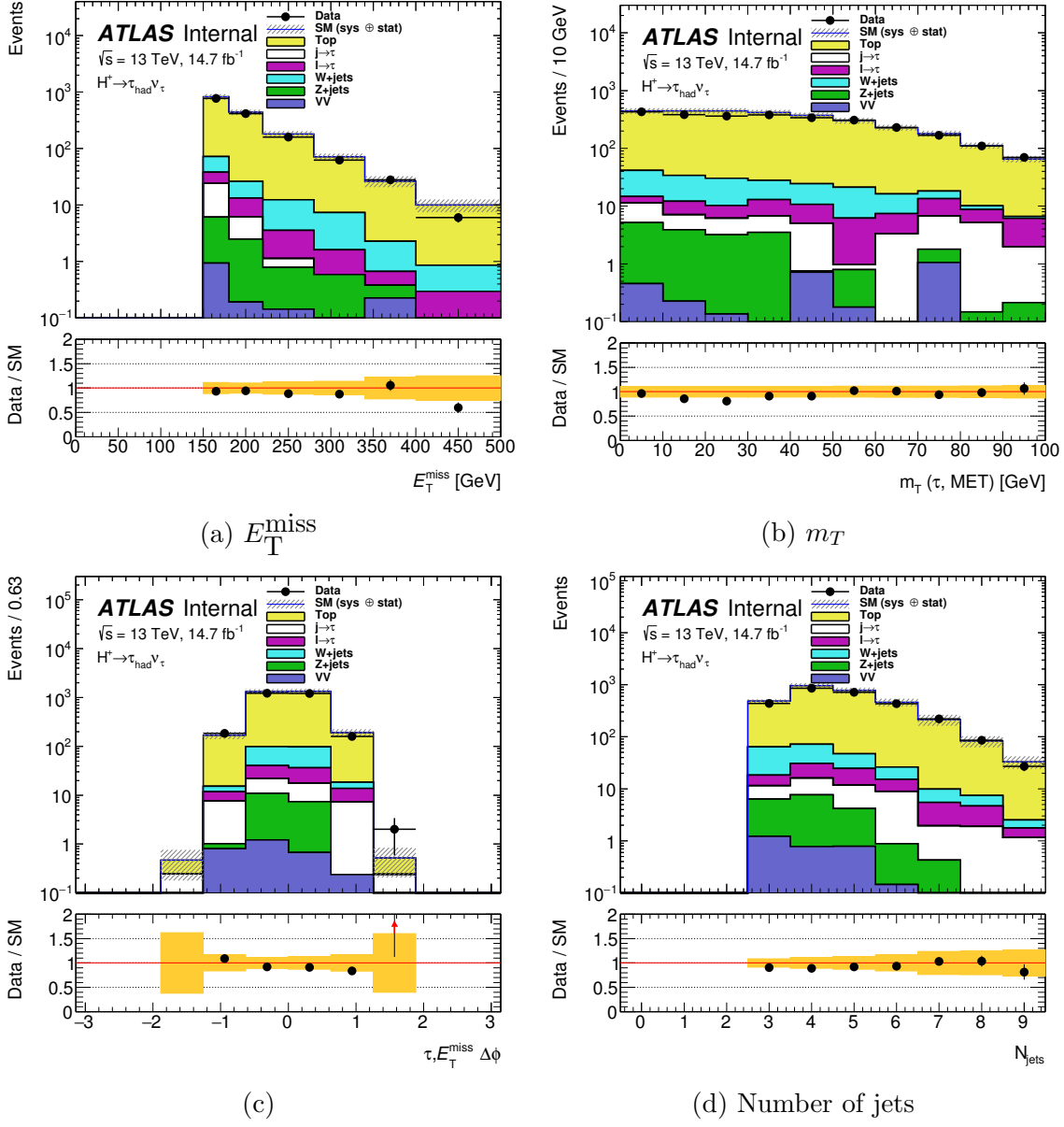


Figure 6.15. Plots showing kinematic distributions in the $t\bar{t}$ control region.

6.5.1.1 Experimental Systematic Uncertainties

Experimental systematic uncertainties include uncertainties on reconstruction efficiencies, identification efficiencies, energy scales, or momentum scales of all the physics objects used in the analysis. These objects are electrons, jets, and the $\tau_{\text{had-vis}}$. These variations were propagated to the hard term component of E_T^{miss} . An additional uncertainty was also considered on the E_T^{miss} soft term. The uncertainty

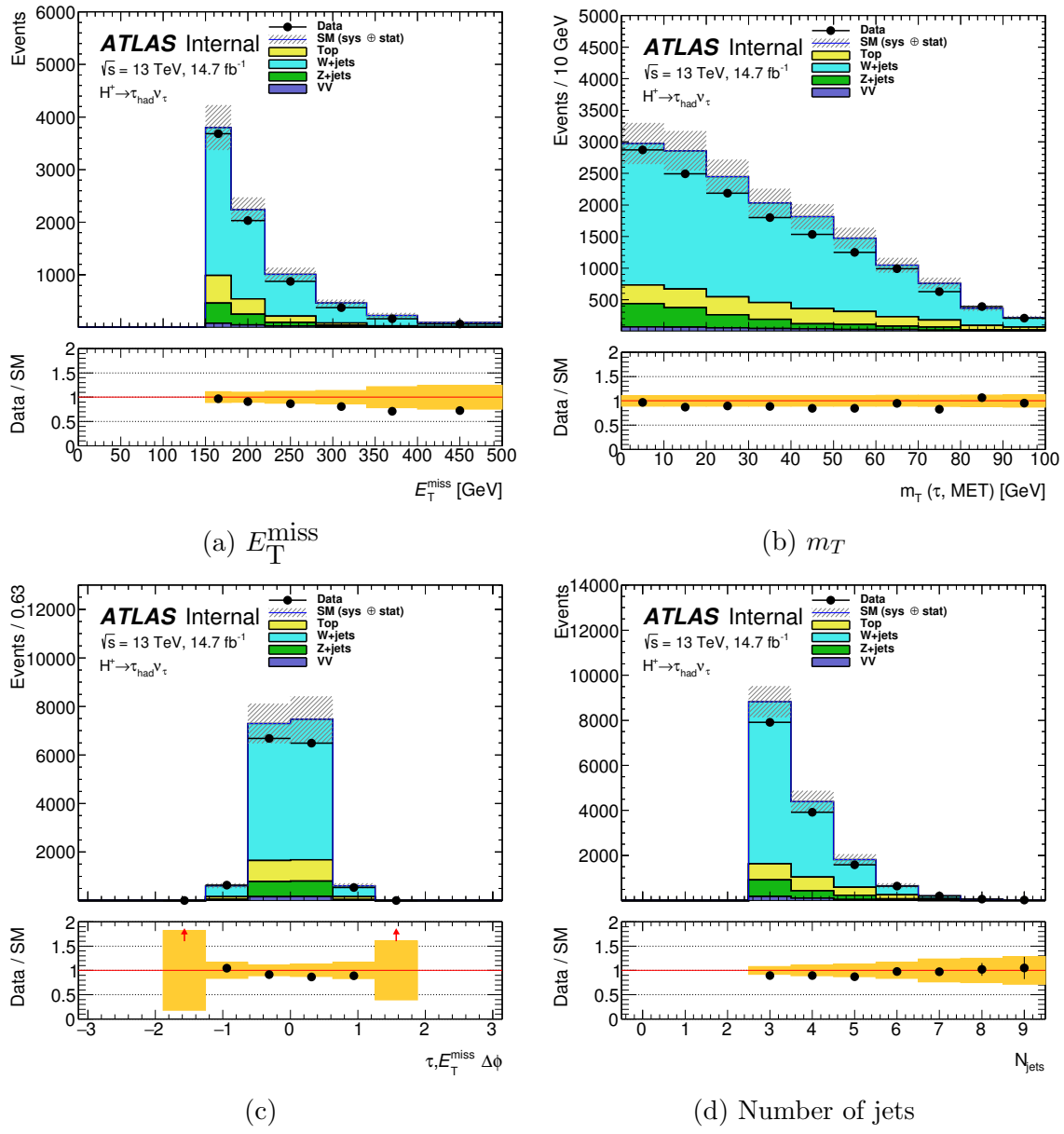


Figure 6.16. Plots showing kinematic distributions in the $W + \text{jets}$ control region.

due to b -tagging efficiency was also considered. Table 6.3 shows the impact of the most dominant uncertainties on $t\bar{t}$ and several of the expected yields. Uncertainties related to electrons and muons were found to be negligibly small.

The procedures for obtaining systematic uncertainties for $\tau_{\text{had-vis}}$, jet and b -tagging are discussed in Chapter 5.

The systematic uncertainty associated with the trigger efficiency is a combination of the following uncertainties :

Variation	$t\bar{t}$		Signal $m_{H^+} = 400$ GeV		Signal $m_{H^+} = 1000$ GeV		Signal $m_{H^+} = 2$ TeV	
	up (%)	down (%)	up (%)	down (%)	up (%)	down (%)	up (%)	down (%)
$\tau_{\text{had-vis}}$ reconstruction efficiency	-2.8	2.8	2.4	2.4	-2.1	2.1	-2.2	2.2
$\tau_{\text{had-vis}}$ ID efficiency	-11.2	11.2	-7.7	7.7	-7.3	7.3	-8	8
$\tau_{\text{had-vis}}$ -lepton OLR	-1.2	1.2	-1.7	1.7	-2.3	2.3	-2.4	2.4
$\tau_{\text{had-vis}}$ energy scale	-6.4	6.1	-4.8	4.0	-1.2	1.5	1.8	-0.4
Jet energy scale	-10	11	-4.4	4.8	-1.8	2.6	-1.1	1.9
b -tagging efficiency	-2	2	2	-2	1.7	-1.6	1.5	-1.5
E_T^{miss} soft term scale/resolution	2.1	-2.1	-1.6	1.6	< 0.1	< 0.1	< 0.1	< 0.1
Trigger efficiency	-3	3	-1	1	0.2	0.2	< 0.1	< 0.1

Table 6.3. Experimental systematic uncertainties.

1. statistical uncertainties in each bin of the efficiency distribution;
2. identification of $\tau_{\text{had-vis}}$ in the control region used to measure the trigger efficiency;
3. identification of the electron in the said control region;
4. and jet reconstruction in the said control region.

Statistical uncertainties in each bin of the turn-on curve are assumed to follow a Poisson distribution. Identification of the $\tau_{\text{had-vis}}$ was evaluated by varying its identification criteria from loose to medium, and tight. The same variation technique was applied to the electron object. The number of reconstructed jets requirement was varied between a minimum of two and three.

Uncertainties associated with fake factors, described in Section 6.4.2, were also observed to be significantly large. As already mentioned, the object from which the reconstructed jet is initiated (light flavor quark, heavy flavor quark or gluon) affects the values of the measured fake factors. The minimum jet BDT score required for jets in the anti- τ -id region was varied to allow different composition of reconstructed jets. Since the nominal selection is 0.5, the $\pm 1\sigma$ variations were taken as 0.4 and 0.6 respectively. These variations affect both the shape of the m_T distribution in the signal region, and the overall yield of accepted events. The effect on the latter is about 20%. The effect of the former is shown in Figure 6.17. The number of $\tau_{\text{had-vis}}$ matched to true τ leptons in $N_{\text{fakes}}^{\text{anti-}\tau}$, when computing N_{fakes}^τ in Equation 6.6 was also generously varied by 50%. This variation affects both the shape of the m_T distribution in the signal region and the final accepted event yield. The latter is shifted by about 6%. The last significant source of uncertainty in the fake factor method is due to statistical uncertainties in the measurement control samples. This only affects the event yield by about 3%. No m_T shape shifts were observed.

6.5.1.2 Theoretical Systematic Uncertainties

Theoretical uncertainties include uncertainties due to the choice of the QCD renormalization and factorization scales, choice of parton distribution functions, and tunes applied to the parton shower and underlying event models. These uncertainties

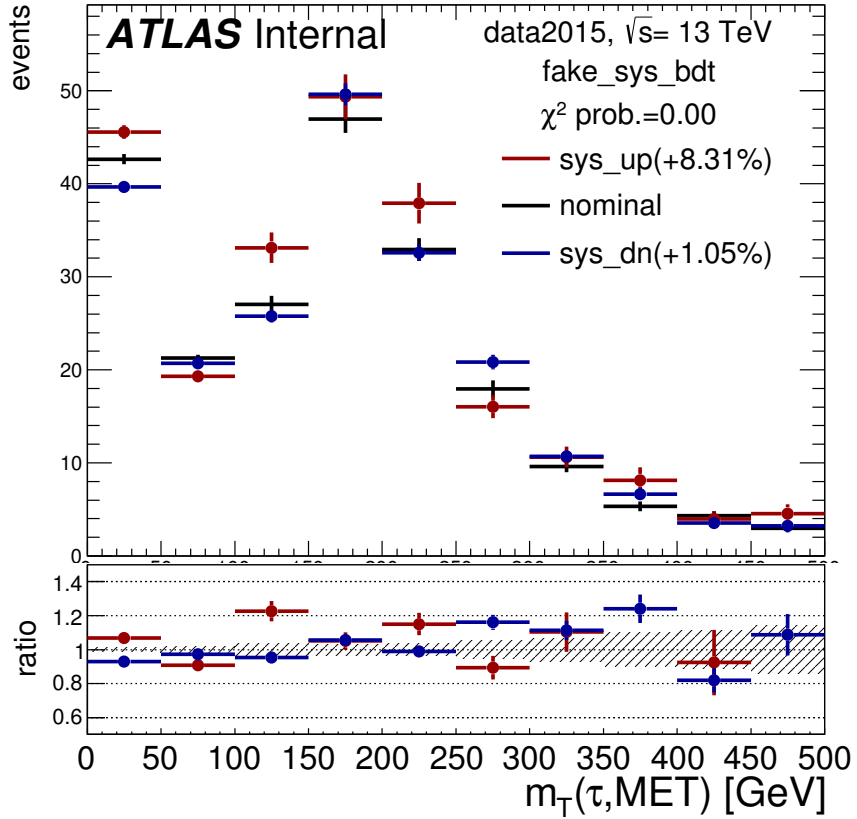


Figure 6.17. Plots showing m_T distributions with variation in jet BDT score selection criteria.

were computed for signal samples and the most dominant backgrounds, which are $t\bar{t}$ and $W + \text{jets}$.

For signal samples, the QCD renormalization scale μ_R and factorization scale μ_F were varied by a factor of 0.5 and 2.0 to evaluate their impact on the expected signal yields. This impact was shown to be less than 5%. Table 6.4 shows the percentage impact on the individual variations on several m_{H^+} . The largest variation was symmetrized and taken as the QCD scale uncertainty for that mass point.

Dependence on the parton distribution function (PDF) set choice is evaluated by LHAPDF [134]. For a sample generated with PDF set *A*, LHAPDF is able to compute weights for each event, such that the dataset would be equivalent to a dataset generated with PDF set *B*. By taking NNPDF23_nlo_as_0118_qed as the nominal PDF set, 3 variations were then examined : NNPDF30_nlo_as_0118_nf_4, CT14nlo_NF4, and MSTW2008nlo68cl_nf4. The largest variation was symmetrized and taken as the error on the PDF choice. This variation was found to have less than 1% impact on the results for all signal samples.

Mass (GeV)	$\mu_R \times \mu_F$ (% diff)							
	0.5 × 0.5	0.5 × 1.0	0.5 × 2.0	1.0 × 0.5	1.0 × 2.0	2.0 × 0.5	2.0 × 1.0	2.0 × 2.0
200	-8	1.7	7	-7	4	-8	-2	2
500	-5	-1	2	-3	2	-2	1	2
800	-4	-1	1	-2	1	-1	1	2
1000	-4	-1.3	0.6	-2	1.5	0.7	1	2

Table 6.4. Theoretical systematic uncertainties on the signal acceptance (in %) due to the QCD scale. The factorization scales are varied by a factor of 2 for up and down variations.

Uncertainties due to parton shower and underlying event tunes were considered for $m_{H^+} = 200, 500$, and 800 GeV. The A14 tune with the NNPDF set comes with a set of systematic variations that were empirically found to cover the total uncertainty in the data used to tune parton shower and underlying event models. A pair of these variations, *Var1*, covers underlying event effects. Another pair, *Var2*, covers jet structure effects. 3 other pairs, *Var3a*, *Var3b* and *Var3c*, cover aspects of extra jet production. The up and down variations were symmetrized and summed in quadrature to obtain their full impact. Table 6.5 summarizes the percentage impact of each symmetrized variation.

Mass (GeV)	Var1 (%)	Var2 (%)	Var3a (%)	Var3b (%)	Var3c (%)
200	2	7	8	10	10
500	4	4	5	4	6
800	4	4	5	8	1

Table 6.5. Theoretical systematic uncertainty on the signal acceptance due to choice of parton shower and underlying event tune.

QCD scale, choice of parton shower and underlying event tunes, and choice for matrix element generator were evaluated for $t\bar{t}$. The impact on the predictions was evaluated by generating Monte Carlo simulation samples with the respective variations and imposing signal region selection criteria on them. POWHEG +PYTHIA version 8 samples were used as the nominal samples. Separate samples with more final state radiation (FSR) and less FSR were also generated. MADGRAPH5_aMC@NLO+HERWIG++ and POWHEG +HERWIG++ samples were generated to evaluate the impact of using different matrix element generators. The impact of using different parton showering and underlying event tunes was computed by comparing POWHEG +PYTHIA version 8 and POWHEG +HERWIG++ samples.

QCD scale and PDF choice uncertainties were shown to be less than 5%. Shift on the event yield due to FSR was shown to be approximately 7%, for the choice of matrix element generator it was 15%, and for the choice of parton shower and underlying event tunes it was 16%. Effects of these variations on the shape of the $m_T(\tau, \nu)$ distribution were also examined, after normalizing the samples to the same NNLO+NNLL cross section.

Various selection criteria in the $W +$ jets control region were varied to evaluate the systematic uncertainties on the $W +$ jets background. All these variations were shown to be less than 3%. Since contributions from other background process in the signal region are very small, their systematic variations were taken as negligible.

6.5.2 Statistical Methods

The m_T distributions for signal samples with $200 < m_{H^+} < 2000$ GeV, and background processes in the signal region are used to test for the presence of charged Higgs bosons with m_{H^+} in the $200\rightarrow 2000$ GeV mass range in data. This procedure involves tests on two hypotheses : that the data is fully described by the known Standard Model processes, called the *background-only* (b) hypothesis; and that some signal is required to explain the observed data, called the *signal+background* ($s+b$) hypothesis. Since the signal true cross section $\sigma_{H^+}^{Obs}$ is not known a-priori, a parameter of interest (POI)

$$\mu = \frac{\sigma_{H^+}^{Obs}}{\sigma_{H^+}^{Exp}} \quad (6.9)$$

is defined to parametrize the $s+b$ hypothesis into $\mu.s + b$. Here, $\sigma_{H^+}^{Exp}$ is the expected cross section from phenomenological models introduced in Chapters 2. A test can be made independent of $\sigma_{H^+}^{Exp}$ by setting it equal to 1; this would make the POI μ equal to the true cross section $\sigma_{H^+}^{Obs}$. In any case $\mu \geq 0$, where $\mu = 0$ reduces the $s+b$ hypothesis to the background-only hypothesis.

Since the number of events in the signal region is usually small, the m_T distributions used for these tests are optimally binned to minimize statistical uncertainties. For an m_T distribution with N bins, the expected number of events in each bin can be parametrized as

$$E_i = \mu.s_i + b_i \quad (6.10)$$

where i runs from 0 to N . Variables s_i and b_i are the expected signal and background events in the i -th bin respectively. These events follow a Poisson probability distribution with means s_i and b_i respectively. The statistical methods described here are based on the *binned likelihood function*, L , which is a product of Poisson probability terms over all the N bins

$$L(\mu) = \prod_{i=0}^N \frac{(E_i)^{n_i}}{n_i!} \exp(-E_i) \quad (6.11)$$

s_i and b_i are affected by the systematic uncertainties discussed in Section 6.5.1. More specifically, the s_i and b_i probability distributions become wider when the systematic uncertainties are accounted for. A set of P systematic uncertainties can be included in the statistical method as *nuisance parameters*, $\theta = (\theta_1, \dots, \theta_P)$, transforming s_i and b_i as $s_i \rightarrow s_i(\theta)$ and $b_i \rightarrow b_i(\theta)$ respectively. Likewise, the binned likelihood function is transformed as

$$L(\mu) \rightarrow L(\mu, \theta) = \prod_{i=0}^N \frac{(\mu \cdot s_i(\theta) + b_i(\theta))^{n_i}}{n_i!} \exp(\mu \cdot s_i(\theta) + b_i(\theta)) \cdot \prod_{k=1}^P \rho(\theta_k). \quad (6.12)$$

From the binned likelihood function a test statistic called the *profile likelihood ratio*

$$q_\mu = -2 \ln \left(\frac{L(\mu, \hat{\theta})}{L(\hat{\mu}, \hat{\theta})} \right) \quad (6.13)$$

is created, where $\hat{\mu}$ and $\hat{\theta}$ are parameters that maximize the likelihood functions. The $\hat{\theta}$ parameters are the nuisance parameters that maximize the likelihood function for a given μ value.

The compatibility between data and a given hypothesis is quantified by computing a p -value. This is the probability of observing results as incompatible with data or worse, given that said hypothesis. For the $s + b$ hypothesis, the p -value is

$$p_{s+b} = \int_{q_{\text{obs}}}^{\infty} f(q|s+b) dq \quad (6.14)$$

where $f(q|s+b)$ is the probability distribution function of the test statistic q given the $s + b$ hypothesis. For the b hypothesis the p -value is

$$p_b = \int_{q_{\text{obs}}}^{\infty} f(q|b) dq \quad (6.15)$$

where $f(q|b)$ is the probability distribution function of the test statistic q given the b hypothesis. Figure 6.18 illustrates how these p_b is computed from a distribution of $f(q|b)$ and an observed q_{obs} in data.

These p -values are converted to a *significance*, defined as the number of standard deviations Z at which a normally distributed variable with 0 mean would give a one-sided tail area equal to the p -value.

From Equations 6.14 and 6.15 a confidence level (CL) of the $s + b$ hypothesis is defined as

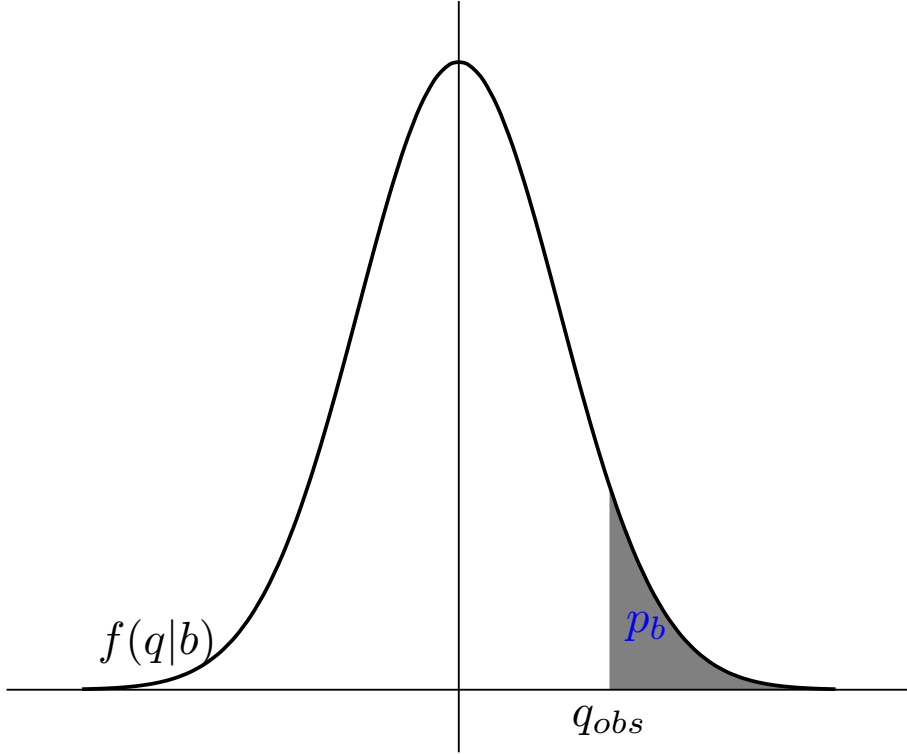


Figure 6.18. p_b illustration from a distribution of $f(q|b)$ and an observed q_{obs} in data.

$$CL_s(\mu) = \frac{CL_{s+b}}{CL_b} = \frac{p_{s+b}}{1 - p_b} \quad (6.16)$$

A 95% CL upper limit on μ is set by finding the μ at which $CL_s = 0.05$, using the asymptotic approximation.

6.6 Results

6.6.1 Expected and Observed Event Yields

After all background processes have been estimated, and their associated systematic uncertainties have been evaluated, final kinematic distributions in the signal region were examined. Figure 6.19 shows such n-1 distributions for E_T^{miss} and m_T . The black vertical lines show the values at which the selection criteria for the plotted variables were imposed. The yellow band in the ratio plot encodes the overall systematic and statistical uncertainties, summed in quadrature. In Figure 6.19 this band is shown only in the signal region because that is where the systematic uncertainties were evaluated. Table 6.6 shows the expected event yields from background processes and the observed yield from 14.7 fb^{-1} of data, accumulated during the 2015 and 2016 data taking periods.

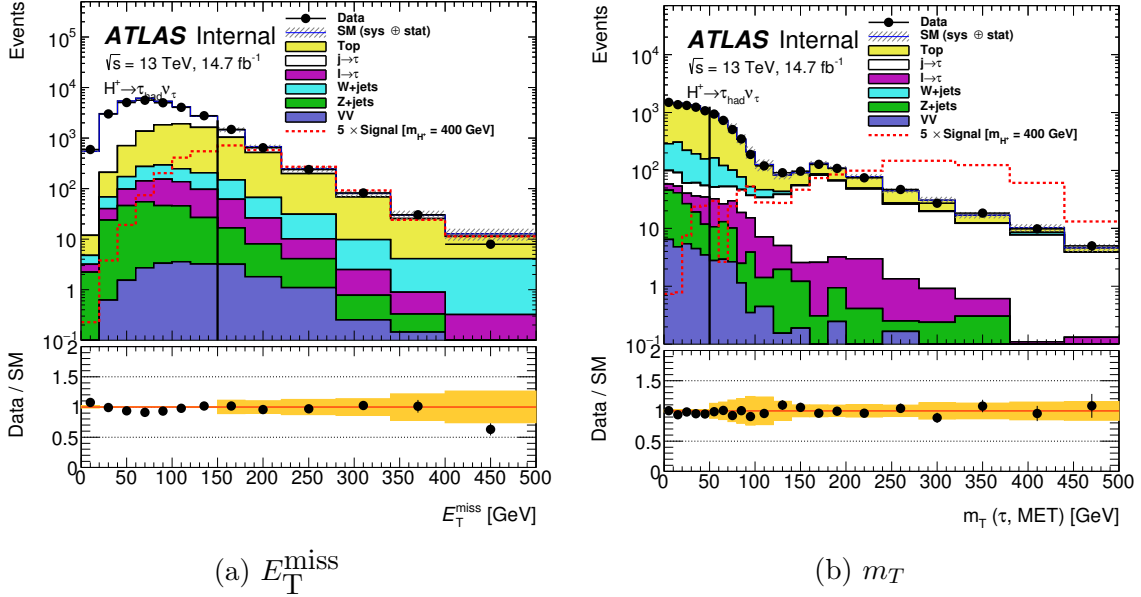


Figure 6.19. Plots showing the m_T and E_T^{miss} distributions in the signal region.

Category	Source	Event Yield
True $\tau_{\text{had-vis}}$	$t\bar{t} + \text{Single Top}$	$2880 \pm 770 \pm 25$
	$W \rightarrow \tau\nu$	$265 \pm 51 \pm 18$
	$Z \rightarrow \tau\tau$	$44.3 \pm 7.1 \pm 7.6$
	VV	$13.8 \pm 2.2 \pm 1.7$
$j \rightarrow \tau$	All processes	$1170 \pm 110 \pm 16$
$l \rightarrow \tau$	All processes	$126 \pm 25 \pm 6.5$
Total Background		$4500 \pm 779 \pm 36.4$
Data (14.7 fb^{-1})		4645

Table 6.6. Expected event yields in the signal region, compared to observed event yields from data.

Figures 6.20 and 6.21 show distributions of other kinematic variables in the signal region. These are the p_T, η, ϕ of the $\tau_{\text{had-vis}}$, the number of reconstructed jets, the number of b -tagged reconstructed jets and the $\Delta\phi(\tau, E_T^{\text{miss}})$. All these figures show that the $t\bar{t}$ background with true $\tau_{\text{had-vis}}$ is the most dominant.

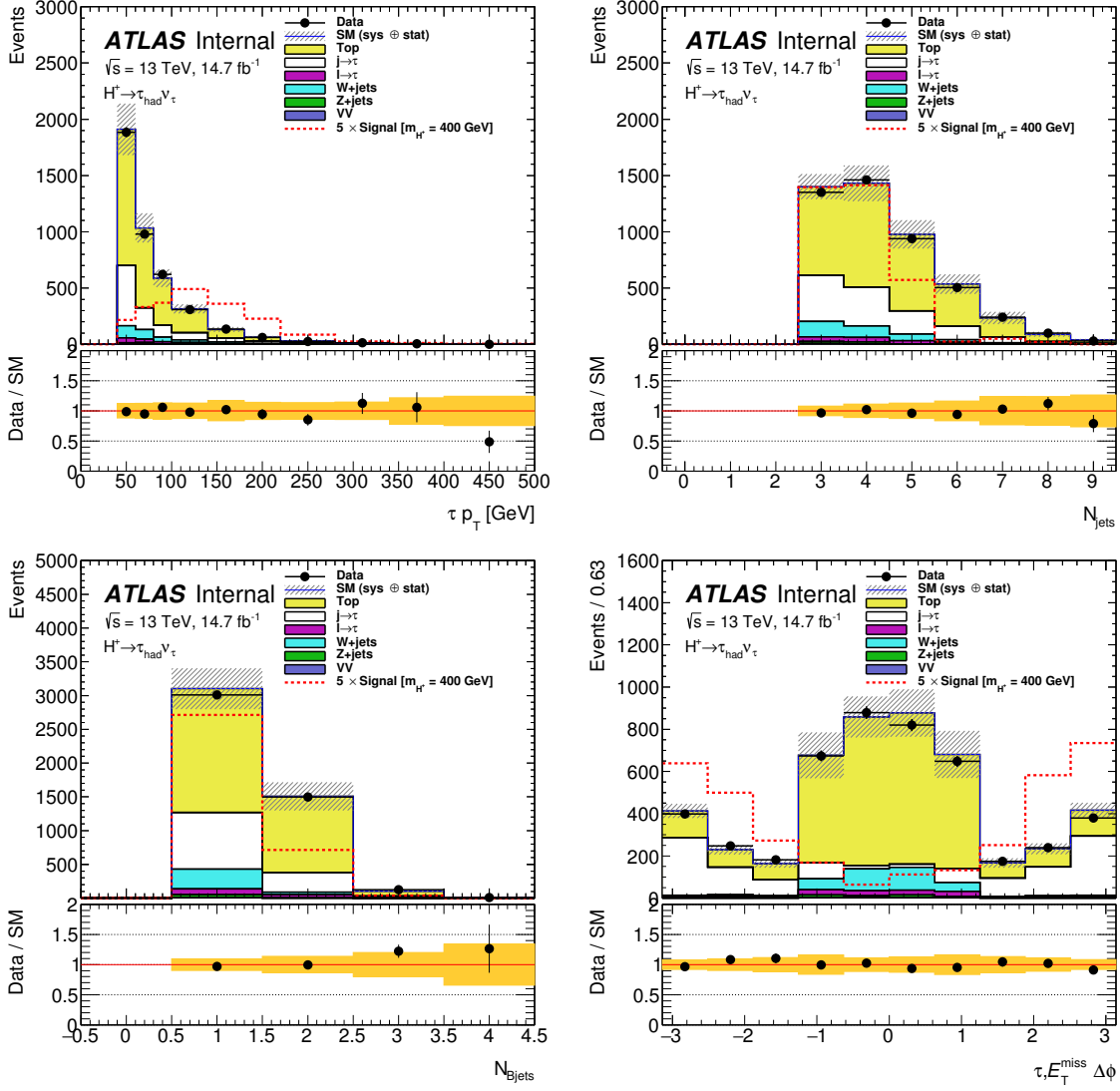


Figure 6.20. Plots showing distributions of $\tau_{\text{had-vis}} p_T$, number of reconstructed jets, number of b-tagged jets and the angular separation between the $\tau_{\text{had-vis}}$ and E_T^{miss} , in the signal region.

6.6.2 Statistical Analysis

Results were tested for evidence of existence of charged Higgs bosons with m_{H^+} ranging from 200–2000 GeV. For each of the mass points, $\sigma_{H^+}^{\text{Exp}}$ was set at 1 to make the parameter of interest $\mu = \sigma_{H^+}^{\text{Obs}}$. Here, the said cross section is the product of the production cross section and branching ratio of the topologies introduced in Equations 6.1 and 6.2. The test statistic q_0 , where $\mu = 0$ in Equation 6.13, was used to test the compatibility of observed data with the background-only hypothesis. The

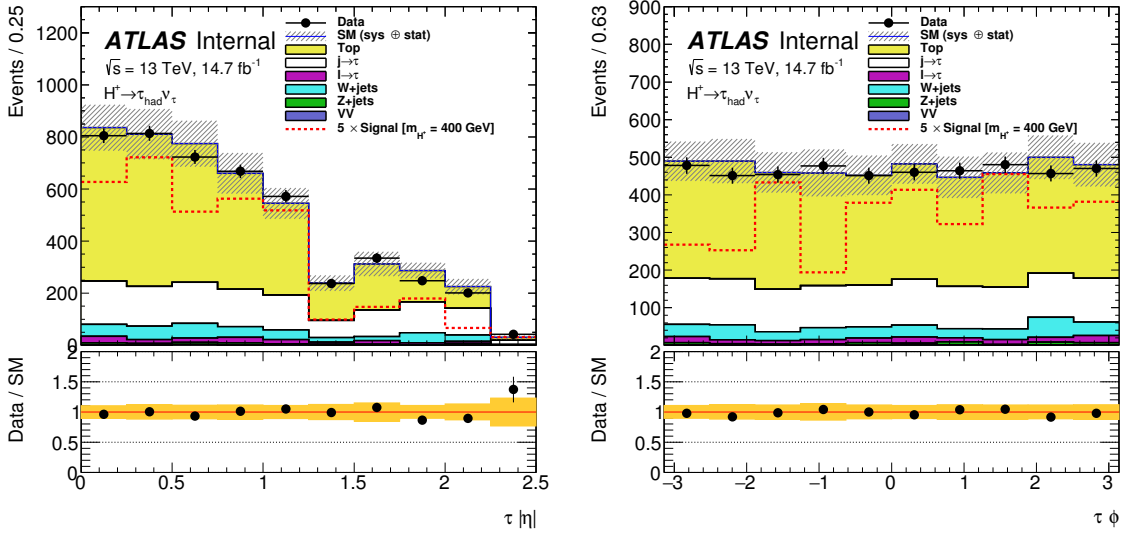


Figure 6.21. Plots showing distributions of $\tau_{\text{had-vis}}$ η and ϕ in the signal region.

probability distribution function $f(q|b)$ was estimated using the asymptotic approximation [135] which supposes an artificial data-set called the ‘Asimov data-set’.⁹

The systematic uncertainties discussed in Section 6.5.1 were included as nuisance parameters. Table 6.7 shows the list of all such uncertainties and the processes (components) to which they were applied. Those that affect more than one component were treated as correlated or anti-correlated, whichever was applicable. Otherwise, it was assumed that they were uncorrelated. Those whose impact on the expected event yield or m_T shape is less than 0.5% were removed from the list. The $\pm 1\sigma$ variations were symmetrized by taking the one with the largest impact on the result, unless there was an explicit reason for an asymmetry.

The test of the observed data against the background-only hypothesis shows that the data is consistent with the Standard Model prediction. Hence, exclusion limits on $\mu = \sigma_{H^+}^{Obs}$ were set by rejecting the $s + b$ hypothesis at 95% confidence level using the CL_s procedure, where $CL_s(\mu)$ is defined as in Equation 6.16. Expected exclusion limits were computed assuming the $s + b$ hypothesis, and using the artificial Asimov data-set which was approximated by the sum of all the expected backgrounds. Observed exclusion limits are computed using the $s + b$ hypothesis, and using the total observed data. Figures 6.22 and 6.23 show the expected and observed exclusion limits for m_{H^+} ranging from 200–2000 GeV. In the former figure, systematic uncertainties were not included in the computation of the exclusion limits. In the latter, the systematic uncertainties were included. The solid line denotes the observed limits and the dashed line denotes the expected limits at 95% confidence levels. The green and

⁹This data-set is defined such that if used to evaluate estimators of all parameters, true values of those parameters are obtained

Contribution to total background (%)	Description	signal	true τ (MC) 72	$j \rightarrow \tau$ (Data) 25	$l \rightarrow \tau$ (MC) 3
NUIP_alpha_xxx					
JET_Globally-reduced_X	jet energy scale: 19 components	✓	✓	✓	✓
JET_Flavor_X	jet energy scale: 3 components	✓	✓	✓	✓
JET_JER_NP_X	jet energy resolution: 8 components	✓	✓	✗	✓
TAUS_TRUEHADTAU_SME_TES	$\tau_{\text{had-vis}}$ energy scale: 3 components	✓	✓	✗	
bjet_xyz	b -jet identification SFs: 6 b , 4 c and 10 light components	✓	✓	✓	✓
MET_SoftTrk_xyz	E_T^{miss} soft term: 2 resolution, 1 scale component	✓	✓	✗	✓
met_xyz	E_T^{miss} trigger efficiency measurement: 3 components	✓	✓	✗	✓
signal_xyz	theoretical uncertainty on signal acceptance: QCD scale and PSUE	✓			
ttbar_xzy	theoretical uncertainty on $t\bar{t}$ acceptance and m_T shape: scale, PSUE, ME			✓	
ttbar_norm	$t\bar{t}$ cross section			✓	
UWSF	$W \rightarrow \tau\nu$ scale factor uncertainty			✓	
lep_sf	$\ell \rightarrow \tau_{\text{had-vis}}$ scale factor				✓
tau_ID	$\tau_{\text{had-vis}}$ identification: 2 components (all and high p_T)	✓	✓	✓	
tau_RECO	$\tau_{\text{had-vis}}$ reconstruction efficiency	✓	✓	✓	
tau_ELEOLR	$\tau_{\text{had-vis}}/\text{electron}$ overlap removal	✓	✓	✓	
tau_ff_stat	statistics in FF method				✓
tau_ff_bdt	jet composition in FF method				✓
tau_ff_prompt_tau	mis-id prompt $\tau_{\text{had-vis}}$ modelling in MC				✓

Table 6.7. Description of each of the nuisance parameters, along with the samples they were applied to. If the same nuisance parameter was applied to different backgrounds, all correlations were kept. A '✓' indicates that the systematic uncertainty was considered and included in the fit. A '✗' indicates that the systematic uncertainty was considered but not included in the fit, otherwise the given systematic uncertainty is not applied to the given background.

yellow shaded regions represent the $\pm 1\sigma$ and $\pm 2\sigma$ uncertainty bands respectively. An illustrative signal prediction in the hMSSM benchmark scenario at $\tan \beta = 60$ is also

overlaid. Without systematic uncertainties the limits are slightly more stringent than with systematic uncertainties. Figure 6.23 shows that the m_{H^+} range from 200→540 GeV for $\tan\beta = 60$ is excluded by these observed exclusion limits.

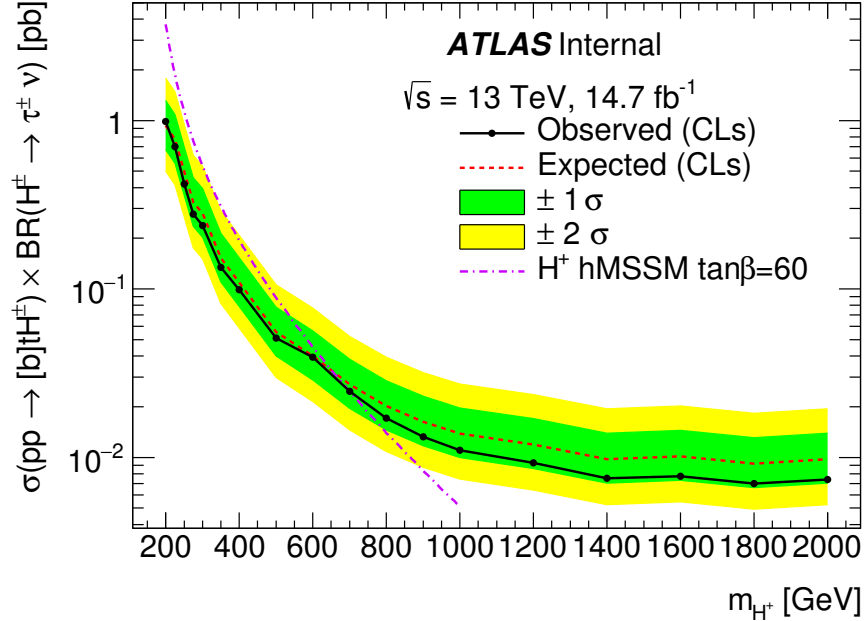


Figure 6.22. Plots of the expected and observed limits on $\mu = \sigma_{H^+}^{Obs}$, without including systematic uncertainties in the background and signal predictions.

To evaluate the impact of the individual limits on exclusion limits shown in Figure 6.23 the limit-setting procedure was repeatedly performed without including each of the systematic uncertainties. Table 6.8 summarizes the impacts of groups of these systematic uncertainties for $m_{H^+} = 200$ GeV and $m_{H^+} = 1$ TeV. The percentage impact was obtained by comparing the nominal expected limit and the expected limit computed without considering each of these groups of uncertainties. Evidently, the largest impact is from fake factors and $t\bar{t}$ background modelling.

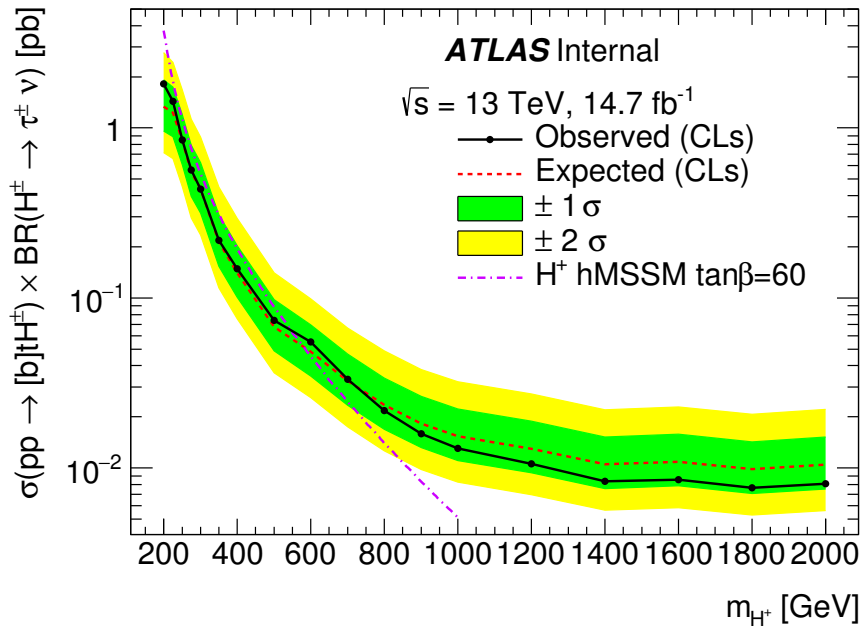


Figure 6.23. Plots of the expected and observed limits on $\mu = \sigma_{H^+}^{Obs}$. Systematic uncertainties were included in the background and signal predictions.

Category	Source of systematic uncertainty	Impact on the expected limit (in %)	
		$m_{H^+} = 200$ GeV	$m_{H^+} = 1000$ GeV
Experimental	luminosity	1.5	0.9
	trigger	< 0.1	< 0.1
	$\tau_{had-vis}$	1.0	1.4
	jet	3.0	0.2
	E_T^{miss}	< 0.1	< 0.1
Fake factors	FF	0.8	4.7
Signal and background models	$t\bar{t}$ modelling	13.2	3.5
	H^+ signal modelling	1.4	1.4

Table 6.8. Impact of various sources of uncertainty on the expected 95% CL exclusion limit.

Chapter 7

Exclusive Higgs Search

A search for evidence of the exclusively produced SM Higgs boson from LHC collisions is presented in this chapter. The only mass probed was 125 GeV for the SM Higgs boson. Exclusion limits were set on the total production cross section of the exclusive SM Higgs boson. In Section 7.1 the data-sets used in the search are presented. Data obtained from LHC collisions is referred to as *data*, while data obtained from simulation is just referred to as *simulation*. In Section 7.2 physics object selection criteria are presented, adding to the criteria presented in Chapter 5. In Section 7.3 the criteria to select events with a charged Higgs boson signature are introduced. Treatment of backgrounds to the charged Higgs boson is discussed in Section 7.4, with the associated systematic uncertainties discussed in Section 7.6. Final event yields are presented in Section 7.7, and their statistical assessment is discussed in the same section.

7.1 Data and Simulation

Data used for this analysis was collected by the ATLAS detector during Run I of the LHC, with parameters and conditions set as discussed in Chapter 3. Only data from runs during which proton beams were stable were considered. The total integrated luminosity amounted to 20.2 fb^{-1} . All of the data was collected during 2012. The total uncertainty on the luminosity value is 2.1%. The impact of this uncertainty on final results in this search are discussed in Section 7.6.

The expected signal (Figure 7.1), was obtained by generating 500 000 Monte Carlo simulation events. The generator used was the Forward Physics Monte Carlo (FPMC) [90]. This is a generator dedicated to generate exclusive events in which a large mass is produced from the proton momentum exchange. In this case, the large mass is the Standard Model Higgs boson. The PDF set used was H1 [136], measured at the HERA collider [137]. Since there are no underlying events in exclusive processes, no underlying event generator was used. Parton showering, fragmentation and hadronization were handled by HERWIG version 6.5 [85].

There are several background process that mimic the exclusive Higgs boson signature in the ATLAS detector. Justification as to why they qualify to be backgrounds

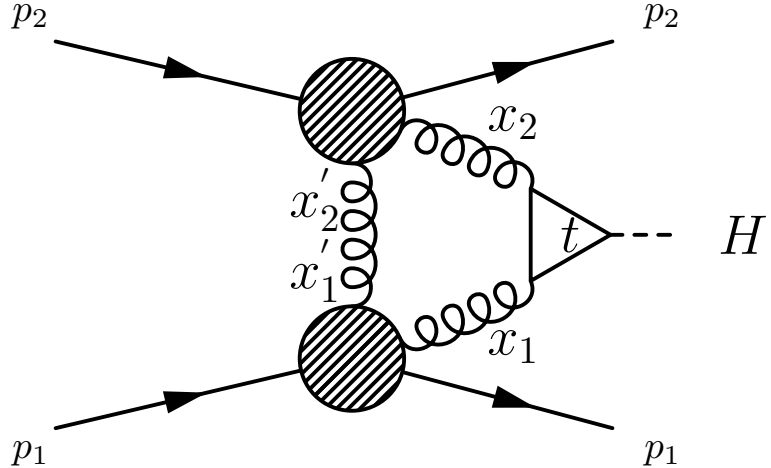


Figure 7.1. Leading order Feynman diagram for the exclusive Higgs production.

is discussed in Section 7.4. While estimation of their contribution was in some cases data-driven, Monte Carlo generators were used to generate several of them. They are categorized into exclusive and inclusive categories.

The most important exclusive processes that were considered here were the exclusive production of W^\pm pairs. While exclusive W^\pm pairs can be produced through gluon fusion, production through photon exchange has a much higher cross section. 500 000 events were generated using HERWIG++ [86] version 2.6.3, which also handled fragmentation, parton showering and hadronization. This generator used the equivalent photon approximation (EPA) introduced in Section 2.2. This generator only handles elastic production (See Figure 2.10). This means that estimation of single and double dissociative contributions had to be data-driven.

The second most important exclusive processes were the exclusive production of leptons, referred to here as the di-leptons. They are produced through photon exchange, so the EPA mechanism is used in calculating their cross sections. 300 000 elastic $\gamma\gamma \rightarrow \tau^+\tau^-$, 800 000 $\gamma\gamma \rightarrow \mu^+\mu^-$, and 800 $\gamma\gamma \rightarrow e^+e^-$ events were generated using HERWIG++. Just like in the exclusive W^\pm pair case, fragmentation, parton showering and hadronization were processed within HERWIG++ as well. The single and double dissociative di-lepton samples were produced using LPAIR [91] version 4.0, save for the $\tau\tau$ decay mode. LPAIR is a generator dedicated to lepton pair production. Unfortunately, it does not incorporate τ leptons in the generation. Single dissociative $\gamma\gamma \rightarrow \tau^+\tau^-$ processes were therefore generated using PYTHIA 8 [77]. No Monte Carlo generator to date has produced double dissociative $\gamma\gamma \rightarrow \tau^+\tau^-$, so these samples were unavailable.

Inclusive WW backgrounds have several production modes. These are

1. quark-induced $q\bar{q} \rightarrow WW$;
2. gluon-induced $gg \rightarrow WW$;
3. and $gg \rightarrow H \rightarrow WW$, with $m_H = 125$ GeV.

The $q\bar{q} \rightarrow WW$ and $gg \rightarrow H \rightarrow WW$ samples were generated using Powheg version 1.0 [81]. This generator was interfaced to PYTHIA 8 for parton showering, hadronization and simulation of the underlying event. $gg \rightarrow WW$ events were generated by the GG2WW [89] generator, interfaced to HERWIG version 6.5 for parton showering, hadronization and underlying event generation. In all these generators, the CT10NLO PDF set was used. Parton showering, hadronization and underlying event models in PYTHIA 8 and HERWIG were tuned using the AU2 [138] and the AUET2 [139] tunes.

$W + \text{jets}$ and $Z + \text{jets}$ processes were modelled using Alpgen [83] interfaced to Pythia6 [76] using the Perugia 2011C [140] tune and CTEQ6L1 PDF [141] set. Additional $Z + \text{jets}$ samples were generated with Alpgen interfaced to Herwig+Jimmy. Other $Z + \text{jets}$ samples, generated using Powheg+Pythia8 and Sherpa1.4 with CT10 NLO PDF, were also used for additional background studies.

Diboson processes such as $WZ(\gamma^*)$, $W/Z + \gamma$ and ZZ are referred to here as VV . The WZ and ZZ samples were generated using Powheg+Pythia with the AU2 tune and CT10 NLO PDF set. $W\gamma$ and $W\gamma^*$ samples were generated, respectively, using Alpgen (interfaced to Herwig+Jimmy) and Sherpa.

$t\bar{t}$ and single top processes were generated with Powheg and MC@NLO.

7.2 Object Selection

The physics objects used in this analysis are electrons, muons, jets and missing transverse energy. Tracks, regardless of what physics object they are associated with, are also used. Reconstruction and identification of these objects is discussed in detail in Chapter 5. This section summarizes other selection criteria imposed on these objects, specific to this analysis.

Track reconstruction is discussed in Section 5.1.1. Tracks used here are those reconstructed from the Inner Detector (ID). Other than satisfying all the track quality criteria outlined in the said section, they were required to have left at least 1 hit in the Pixel Detector, and 4 hits in the Semi-Conductor Tracker (SCT). Additionally, they were required to have p_T of at least 400 MeV.

Electron reconstruction and identification is discussed in Section 5.2.1, along with the associated corrections and calibrations. The electrons used here were reconstructed from matches between calorimeter energy deposits and ID tracks. Since the ID is limited to $|\eta| < 2.47$ and the transition region between the barrel and end-cap calorimeters ($1.37 < |\eta| < 1.52$) is a dead region, electron candidates are required to not be in the calorimeter transition region while being within $|\eta| < 2.47$. So, only central electrons were considered. They were also required to pass the very tight likelihood identification selection criteria and have p_T of at least 10 GeV. The electron p_T was calibrated and corrected as discussed in Section 5.2.2. Additional isolation criteria

were applied to suppress backgrounds from jets that were reconstructed as electrons, both in the calorimeter and tracking measurements. As shown in Section 5.2.2, such background contamination is energy (or p_T) dependent, so these isolation criteria were binned in electron E_T and p_T , where E_T was measured from the calorimeters and p_T was measured from the ID. The variable of interest in defining isolation is $EtCone30$ (or $PtCone30$): the E_T (or p_T) in a cone of $\Delta R < 0.3$ around the electron candidate, excluding E_T (or p_T) from the electron candidate. The isolation criteria is such that $EtCone30$ ($PtCone30$) is less than a certain fraction of the electron, E_T (p_T). Table 7.1 shows this isolation selection criteria for electrons.

	Condition	Isolation Criterion
Calorimeter	$E_T^e < 15 \text{ GeV}$	$EtCone30/E_T^e < 0.20$
	$15 \leq E_T^e < 20 \text{ GeV}$	$EtCone30/E_T^e < 0.24$
	$E_T^e \geq 20 \text{ GeV}$	$EtCone30/E_T^e < 0.28$
Track	$p_T^e < 15 \text{ GeV}$	$PtCone30/p_T^e < 0.06$
	$15 \leq p_T^e < 20 \text{ GeV}$	$PtCone30/p_T^e < 0.08$
	$p_T^e \geq 20 \text{ GeV}$	$PtCone30/p_T^e < 0.10$

Table 7.1. Electron isolation criteria.

Muon reconstruction and identification is discussed in Section 5.3.1. In this analysis, combined (CB) muons were used. These use information from both the muon spectrometer (MS) and the ID. Apart from the selection criteria outlined in Section 5.3.1, these muons were required to have $p_T > 10 \text{ GeV}$ and be within $|\eta| < 2.47$ because of the ID pseudorapidity limitation. Tracks from the ID were also required to have at least 1 hit in the Pixel Detector and 5 hits in the SCT. Holes in the SCT (see Figure 5.2) were not allowed to be more than 2. Isolation criteria similar to that applied on electron candidates were also applied on muon candidates, to suppress background from jets reconstructed as muons. Table 7.2 lists the isolation criteria.

In contrast to electron and muon selection criteria in the charged Higgs boson search, electrons and muons in this analysis were not required to satisfy any selection criteria based on the impact parameters or their significance.

Jet reconstruction is discussed in Section 5.4. Jets used in this analysis were reconstructed using the anti- k_T algorithm with $R = 0.4$. They were also required to fall within $|\eta| < 4.5$ and have at least 25 GeV in p_T to suppress jets from pileup. While

	Condition	Isolation Criterion
Calorimeter	$p_T^\mu < 15 \text{ GeV}$	$\text{EtCone30}/p_T^\mu < 0.06$
	$15 \leq p_T^\mu < 20 \text{ GeV}$	$\text{EtCone30}/p_T^\mu < 0.12$
	$20 \leq p_T^\mu < 25 \text{ GeV}$	$\text{EtCone30}/p_T^\mu < 0.18$
	$p_T^\mu \geq 25 \text{ GeV}$	$\text{EtCone30}/p_T^\mu < 0.30$
Track	$p_T^\mu < 15 \text{ GeV}$	$\text{PtCone30}/p_T^\mu < 0.06$
	$15 \leq p_T^\mu < 20 \text{ GeV}$	$\text{PtCone30}/p_T^\mu < 0.08$
	$p_T^\mu \geq 20 \text{ GeV}$	$\text{PtCone30}/p_T^\mu < 0.12$

Table 7.2. Muon isolation criteria.

energy scale and resolution corrections were applied on these jets, all corrections that depend on the position of the primary vertex were not applied. Examples of such corrections are the origin correction, JV and JVT.¹ Reasons for refraining from such corrections will become clearer in the following sections.

Reconstruction of missing transverse energy, E_T^{miss} , is discussed in Section 5.6. In particular, the E_T^{miss} used here reconstructed the soft terms in the E_T^{miss} from calorimeter energy deposits that were not associated to any other physics objects.

7.3 Event Selection

Evidence for the exclusive Higgs boson was searched for in events in which the Standard Model Higgs boson decays to a pair of W^\pm bosons, which in turn decay leptonically. This leptonic decay includes τ leptons, but only those that decay leptonically. Effectively, the final state leptons are electrons and muons. The topology for this decay channel is therefore

$$gg \rightarrow [H] \rightarrow [W^+][W^-] \rightarrow [l][l][E_T^{\text{miss}}], \quad (7.1)$$

where l represents the leptons: μ or e .

The topology in Equation 7.1 is the same topology used to search for the inclusive Higgs boson in Ref [142]. The event selection criteria in this analysis mimics the same selection criteria in Ref [142]. Here, the flavor of the two leptons was required to be opposite to suppress backgrounds from $Z \rightarrow ee$ or $Z \rightarrow \mu\mu$ events. Signal events were therefore required to have only two leptons of different flavor satisfying the se-

¹JVT was developed for use during Run II anyway.

lection criteria outlined in Section 7.2. The impact parameters of the lepton tracks with respect to the beamline in the ID, z_0 , were required to be less than 1.0 mm from each other. In addition, the charges of the two leptons were required to be opposite because the SM Higgs boson is neutral to electromagnetic charge.

Of the two leptons in signal events, the one with the largest p_T is referred to as the *leading* lepton, otherwise it is the *sub-leading* lepton. The leading lepton was required to have at least 25 GeV in p_T and the sub-leading lepton was required to have at least 15 GeV in p_T . Moreover, the mass of the di-lepton system, $m_{\ell\ell}$, was required to be at least 10 GeV. This selection is referred to as the *pre-selection*. Recalling that only different flavor lepton pairs are considered, the symbol $m_{\ell\ell}$ is used interchangeably with $m_{e\mu}$ to represent the transverse mass of the di-lepton system.

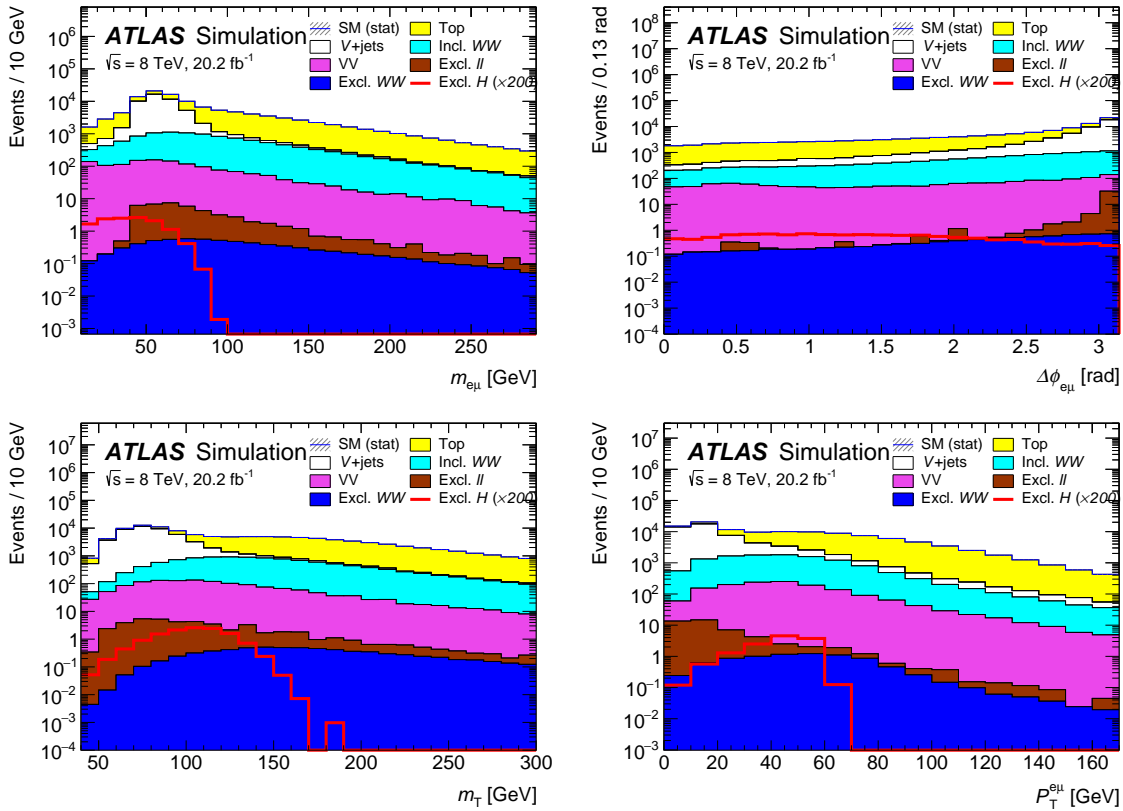


Figure 7.2. Plots showing the expected signal and background distributions after pre-selection.

Figure 7.2 shows expected distributions for several kinematic quantities for background and signal after the pre-selection criteria has been applied. Contributions from all the backgrounds are stacked on each other to total the Standard Model (SM) prediction. The hashed lines on the SM prediction is the statistical uncertainty,

obtained by assuming that the predicted number of events follow a Poisson distribution. The signal prediction is not stacked on the background, and is scaled by 200 for better visibility. While these distributions were predicted by simulation, a full discussion on background treatment is detailed in Section 7.4.

The mass of the di-lepton system, $m_{e\mu}$, has already been introduced above. While most of the backgrounds have reasonably high $m_{e\mu}$, almost all the signal is expected to fall in the $m_{e\mu} < 100$ GeV region, after all the pre-selection criteria has been applied. In particular, the WW distributions tend to have high $m_{e\mu}$ than the signal. This is expected because with a spin-0 quantum number, the Higgs boson decays to final state leptons that have a smaller angular separation than the leptons from WW decays. This small angular separation lowers $m_{e\mu}$. This hints towards additional selection criteria dependent on the mass and angular separation of the di-lepton system. Figure 7.2 shows both $m_{e\mu}$ and $\Delta\phi_{e\mu}$, where most of the signal lies in the region $\Delta\phi_{e\mu} < 2.0$.

The transverse mass, m_T , of the di-lepton- E_T^{miss} system shown in Figure 7.2 is defined as

$$m_T = \sqrt{(E_T^{e\mu} + E_T^{\text{miss}})^2 - |\mathbf{p}_T^{e\mu} + \mathbf{p}_T^{\text{miss}}|^2}, \quad (7.2)$$

where $E_T^{e\mu} = \sqrt{|\mathbf{p}_T^{e\mu}|^2 + m_{e\mu}^2}$ and $|\mathbf{p}_T^{\text{miss}}| = E_T^{\text{miss}}$. This quantity essentially is the mass of the Higgs boson, so it is expected to peak at 125 GeV and have a small tail that is mostly in the region $m_T < 140$ GeV.

The transverse mass of the di-lepton system, $p_T^{\ell\ell}$ or $p_T^{e\mu}$, is expected to be relatively higher for signal than it is for backgrounds such as $V+\text{jets}$ and exclusive di-leptons. QCD multi-jets, not shown in Figure 7.2, are also expected to have low $p_T^{e\mu}$ when the jets are mis-identified as leptons. To suppress these backgrounds, a selection of $p_T^{e\mu} > 30$ GeV was imposed.

A dedicated selection was also developed to separate exclusive from inclusive events. This criterion is referred to here as the *exclusivity selection* or Δz_0^{iso} in short. Its performance in simulation and data was tested, and is formally introduced in the next two sections.

From the distributions in Figure 7.2 the following additional selection were applied to isolate Higgs-like events from the W^+W^- spectrum: $m_{\ell\ell} < 55$ GeV, $m_T < 140$ GeV and $\Delta\phi_{\ell\ell} < 1.8$. This selection was found to be optimal without any additional E_T^{miss} criteria.

Table 7.3 summarizes all the selection criteria discussed in this section. Figure 7.3 shows the expected m_T distributions in the signal region, minus the m_T selection criterion. Modified distributions will be shown in later sections after several calibrations and corrections have been applied to the background processes. In any case, exclusive and inclusive W^+W^- was expected to dominate the background processes that contaminated the signal region.

	Selection
Preselection	Oppositely charged $e\mu$ final states $p_T^{\ell_1} > 25$ GeV and $p_T^{\ell_2} > 15$ GeV $m_{e\mu} > 10$ GeV
	$p_T^{e\mu} > 30$ GeV Exclusivity selection, Δz_0^{iso}
Spin-0 Higgs boson	$m_{e\mu} < 55$ GeV $\Delta\phi_{e\mu} < 1.8$ $m_T < 140$ GeV

Table 7.3. Event selection criteria.

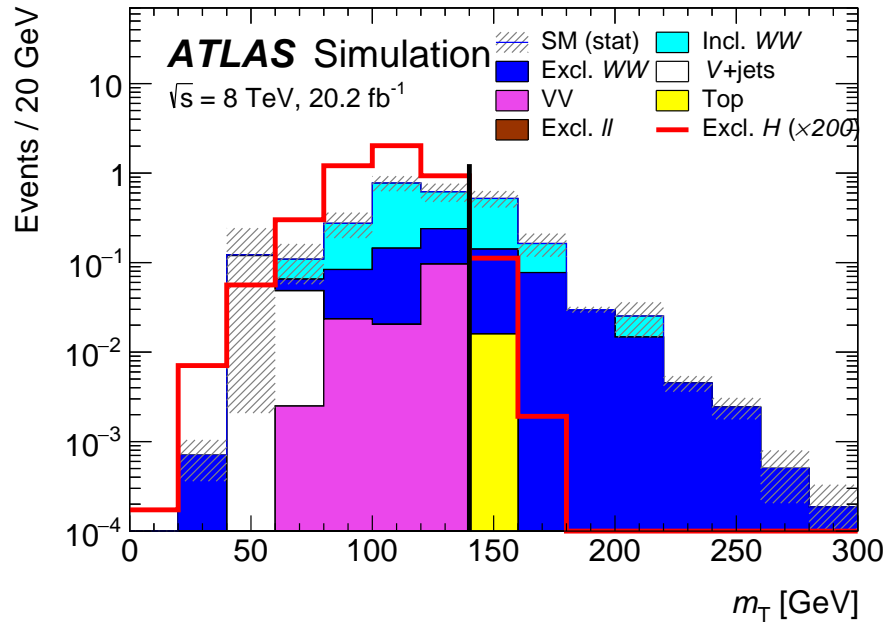


Figure 7.3. Plots showing the preliminary expected m_T distributions in the signal region, minus the m_T selection.

7.3.1 Exclusivity Selection

The exclusivity selection developed in this analysis is based on the final state particles shown in the topology in Equation 7.1. With only two leptons in the final state, these exclusive events are expected to have exactly two tracks in the event. These tracks are in turn expected to be matched to the said leptons.

As mentioned in previous sections, tracks in this analysis were parametrized by impact parameters measured with respect to the beamline. It is worth mentioning that the most common track parametrization in ATLAS is with respect to the primary vertex (PV), defined as the vertex with the highest track sum p_T . The default ATLAS primary vertex is referred to as PV in this text, and the vertex from which two tracks in exclusive processes originate is referred to as the di-lepton vertex. The probability that a track from pileup events is mistakenly associated with the PV, especially in events that have few tracks, is substantial. When that happens, the position of the PV in the z coordinate may get distorted. This, as will be shown in the next paragraphs, would reduce the efficiency of the exclusivity selection. So an effort to refrain from using quantities that rely on the ATLAS PV was made.

As shown in Chapter 5, the fit method used to reconstruct tracks is different from that used to reconstruct electron tracks in the ID. In addition, the measured ID hits for muons candidates may be different as the combined MS+ID track fit is used for CB muons. Thus, matching tracks to leptons is necessary. A track was considered matched to a lepton track if it satisfied the following conditions :

1. passes all track quality selection criteria;
2. has at least 2 GeV in p_T ;
3. $\Delta z_0(\text{track}, \text{lepton})$ is less than 1 mm;
4. and $\Delta R(\text{track}, \text{lepton})$ is less than 0.01.

In the case where a track is matched to both leptons in the event, preference is given to the lepton closest in z_0 , measured with respect to the beamline. Figure 7.4 shows the number of tracks matched to electrons and muons in the simulated signal sample of events. Electrons, since they undergo brehmsstrahlung at a higher rate than muons, have a larger fraction of two matched tracks than muons. It is not expected to match 3 or more tracks to either of the leptons.

To ensure that the two leptons in the event are indeed from the di-lepton vertex, their z_0 positions, z_0^1 and z_0^2 , were required to be within 1 mm of each other. The 1 mm value was arrived at after measuring the z_0 resolution in both data and simulation and observing that they safely agree within 1 mm. The position of the di-lepton vertex in z_0 , z_0^{av} , was then taken as the average of z_0^1 and z_0^2 . Tracks not matched to either of the leptons were tested for absolute distance in z_0 from z_0^{av} . Figure 7.5 illustrates this geometry. For Δz_0^{iso} , the closest unmatched track (also referred to as an *extra* track) was required to be at least 1 mm way from z_0^{av} .

Although Δz_0^{iso} was observed to be sensitive to pileup events, the signal selection efficiency in the pileup range expected during the Run I data taking period was not terrible. At worst the signal efficiency was about 50%, when the number of pileup

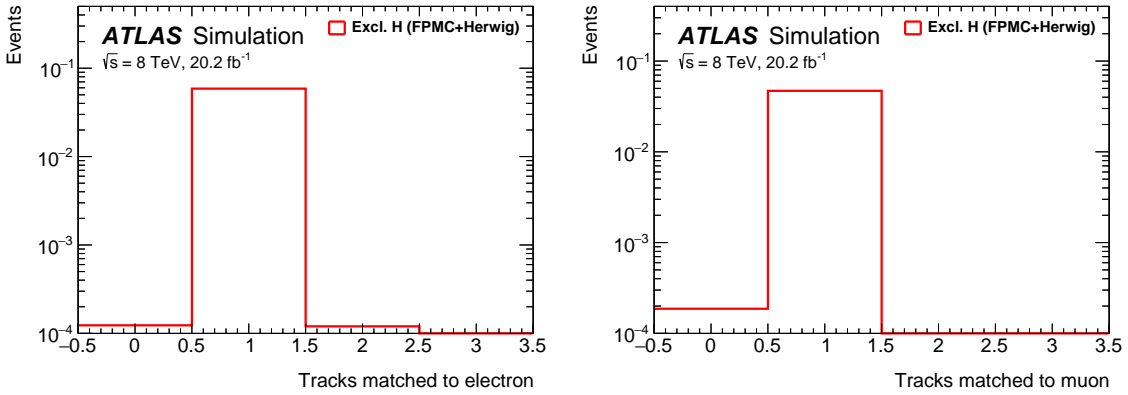


Figure 7.4. Plots showing the number of tracks matched to the electron (left) and the muon (right) tracks.

$$z_0^{av} = (z_0^1 + z_0^2)/2$$

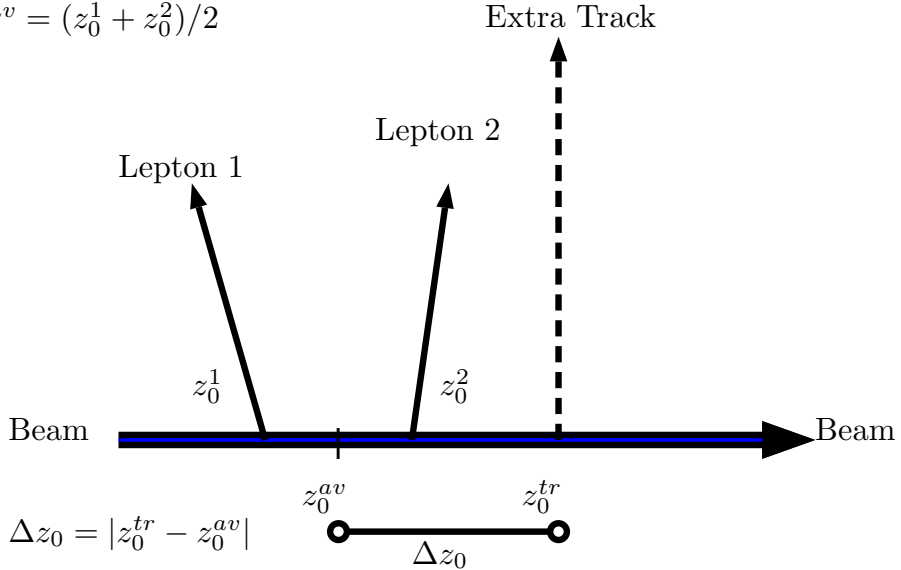


Figure 7.5. Illustration of the geometry of the exclusivity selection criteria.

events (μ) was greater than 30. During Run I, the average number of pileup events was 20.7. Figure 7.6 shows the signal efficiency of this selection, simulated using FPMC, plotted against the number of pileup event, μ . For $\mu = 20.7$, the efficiency was found to be around 58% in simulation. This was compared to the efficiency measured in data, as discussed in the next section.

7.3.2 Performance and calibration of exclusivity

The exclusivity selection introduced in the previous section was tested for several inconsistencies in data and simulation. First, since background rejection with

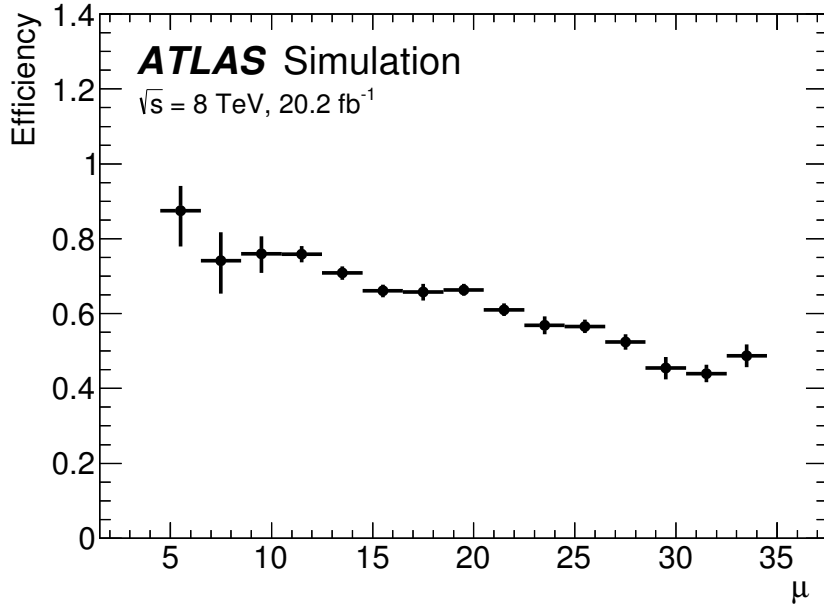


Figure 7.6. Plot of the efficiency of the exclusivity selection, extracted from the exclusive Higgs boson signal simulation, is plotted against the average number of interactions per beam crossing μ .

this selection in simulation is dependent on the modelling of the underlying event, it is reasonable to expect difference in performance in different Monte Carlo generators as well as in data. Second, the equivalent photon approximation (EPA) is known to overestimate the cross section of elastic processes such as elastic di-leptons or elastic W^\pm pairs [143, 144]. It was worthwhile to reproduce this over-estimation using Δz_0^{iso} as a cross check. Third, SD and DD Monte Carlo simulation for exclusive W^\pm pairs is not available. A mechanism to estimate these contributions was developed in the context of Δz_0^{iso} .

This section discusses three studies. The underlying event modelling in several Monte Carlo generators were calibrated to match the underlying event in data. The EPA overestimation of elastic cross sections were reproduced using the Δz_0^{iso} selection criteria. SD and DD contributions to the exclusive W^\pm pairs was estimated. These three studies essentially tested the performance of Δz_0^{iso} and enabled its calibration.

7.3.2.1 Calibration of the underlying event

To calibrate the underlying event modelling across different generators, $Z \rightarrow \mu\mu$ events in data were used for comparison. $Z \rightarrow ee$ samples were also used separately to cross check the results. The reason for using Z events is that while they are a good source of leptons, they are so many in data that statistical uncertainties are kept at

a minimum. The Z events were isolated by requiring each of the two muons to have at least 20 GeV in p_T and have $80 < m_{\mu\mu} < 100$ GeV. Δz_0^{iso} was then applied, essentially requiring no unmatched tracks in $\pm \Delta z_0 < 1$ mm. The $\pm \Delta z_0$ window was varied to study systematic uncertainties on the results.

The following generators were used to simulate $Z \rightarrow \mu\mu$ events :

1. ALPGEN+PYTHIA6;
2. ALPGEN+HERWIG;
3. SHERPA;
4. and POWHEG +PYTHIA8.

Figure 7.7 shows the agreement between data and simulations from these generators. Circles and squares are respectively before and after the exclusivity selection was applied. Before exclusivity, all the generators predict $Z \rightarrow \mu\mu$ events to a reasonable agreement with data. After exclusivity, several disagreements between data and simulation, and also between simulations from the different generators, were observed. This is a symptom of poor underlying event modelling.

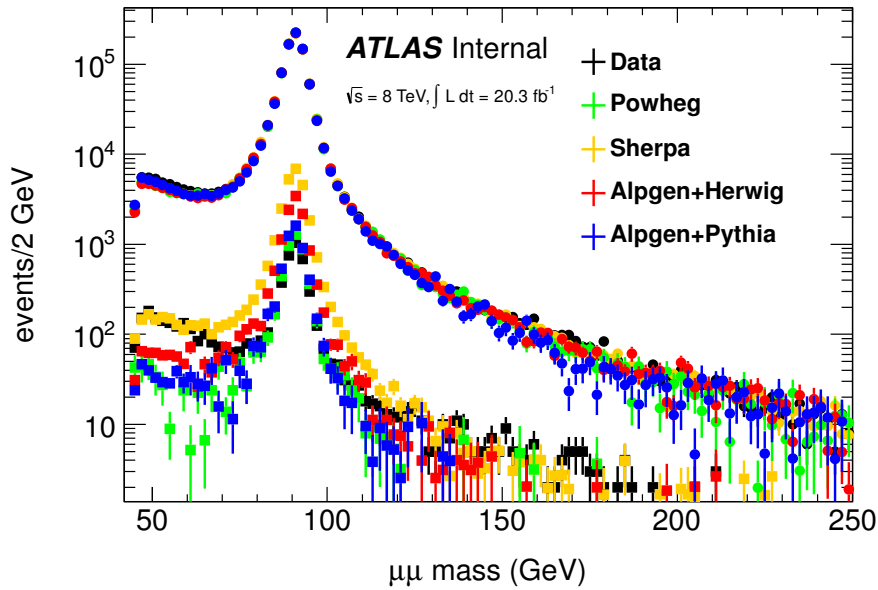


Figure 7.7. The rejection of $Z \rightarrow \mu\mu$ between data and simulation. Simulated samples are normalized to the data. Circles are before Δz_0^{iso} was applied, and squares are after Δz_0^{iso} was applied.

The fraction of events that passed Δz_0^{iso} in simulation, $n_{MC}^{\text{exc}}/n_{MC}^{\text{inc}}$, and the fraction of events that passed Δz_0^{iso} in data, $n_{data}^{\text{exc}}/n_{data}^{\text{inc}}$, were compared through scale factors

$$f_{n_{trk}}^{sim} = \frac{n_{MC}^{exc}/n_{MC}^{inc}}{n_{data}^{exc}/n_{data}^{inc}}, \quad (7.3)$$

where sim is P for POWHEG +PYTHIA8, AH for ALPGEN+HERWIG, AP for ALPGEN+PYTHIA6, and S for SHERPA. n_{trk} is the number of tracks required in the exclusivity window, 0 being the nominal. To improve the statistical uncertainties after Δz_0^{iso} , measurements with n_{trk} equal to 1 and 1→4 were also done. Exclusivity window sizes other than 1 mm were used to study the impact of systematic uncertainties on the results. Results for this study are shown in Table 7.4.

$n_{trk}, \Delta z_0^{\text{iso}}$	f_n^P	f_n^S	f_n^{AH}	f_n^{AP}
0, 1.0 mm	0.581	0.128	0.206	0.692
0, 1.25 mm	0.549	0.113	0.194	0.679
0, 1.5 mm	0.537	0.103	0.189	0.663
0, 2.5 mm	0.494	0.084	0.176	0.613
0, 4.0 mm	0.308	0.074	0.170	0.579
1-4, 1.0 mm	0.876	0.571	0.393	0.853
1, 1.5 mm	0.681	0.324	0.247	0.736

Table 7.4. Measured $f_{n_{trk}}^{sim}$ values for several different Monte Carlo generators, under different exclusivity settings. Exclusivity window sizes other than 1 mm were used to study the impact of systematic variations on the results.

To use the scale factors in Table 7.4 to calibrate processes other than Z decays these scale factors were extrapolated to a wider di-muon mass range. In particular, the stability of event yields after imposing Δz_0^{iso} at di-muon masses other than between 80 and 100 GeV needed to be quantified. These simulation yields were measured in bins of $44 \rightarrow 60$ GeV, $60 \rightarrow 90$ GeV, $90 \rightarrow 116$ GeV and $116 \rightarrow 200$ GeV. In all bins, SHERPA had the minimal statistical uncertainties, so its results were compared to those from the other three generators. Quantities shown in Table 7.5 are ratios of yields from the different generators to the yields from SHERPA after the Δz_0^{iso} selection. A generous 20% variation on the nominal yield (SHERPA) covers yields from all other generators.

7.3.2.2 Di-lepton check

As mentioned above, the EPA is known to overestimate the elastic contribution to exclusive processes that occur by exchanging a pair of photons. This section discusses a study that reproduces this overestimation within uncertainties, thereby validating Δz_0^{iso} .

Mass [GeV]	ALPGEN+HERWIG	ALPGEN+PYTHIA6	POWHEG+PYTHIA8
44–60	0.81 ± 0.02	0.84 ± 0.03	0.99 ± 0.09
60–90	1.04 ± 0.02	0.98 ± 0.03	1.01 ± 0.02
90–116	1.00 ± 0.01	1.02 ± 0.02	1.00 ± 0.02
116–200	0.89 ± 0.10	1.04 ± 0.19	0.76 ± 0.10

Table 7.5. Ratio of the exclusivity selection efficiency in Drell-Yan $\mu^+\mu^-$ production as a function of dimuon mass of different generators to SHERPA. Only statistical uncertainties are shown. The statistical uncertainty from SHERPA is included and contributes 2.9%, 0.8%, 0.7% and 5.7% in the four mass regions.

Since elastic, SD and DD Monte Carlo simulation samples for exclusive di-leptons were available, exclusive di-leptons were used for this study. The strategy was to isolate exclusive di-muons in data, entangle the elastic component, and compare it with the prediction from EPA. From this comparison, a scale factor than normalizes the EPA prediction to data was extracted and compared to previous studies of a similar nature. The basic selection required that each of the muons have $p_T > 20$ GeV, $m_{\mu\mu} > 45$ GeV excluding a ± 15 GeV window around the Z mass, and Δz_0^{iso} . Elastic di-muons tend to populate the low $p_T^{\mu\mu}$ region, as shown in Figure 7.8, where all the basic selection criteria described above were applied. So, a selection of $p_T^{\mu\mu} < 3$ GeV was additionally applied. The major background to the exclusive di-muons in this region was Drell-Yan di-muons; every other background was negligible. Clearly, in Figure 7.8 there is an overestimation of processes from simulation.

Acoplanarity, defined as $1 - \Delta\phi_{\mu\mu}/\pi$, is a good discriminant when disentangling elastic from SD and DD processes. This is expected, since $\Delta\phi_{\mu\mu}$ is dependent on $p_T^{\mu\mu}$. In this study, acoplanarity distributions from simulation after applying the selection criteria described in the preceding paragraphs were fit to the acoplanarity distribution from data, after the same selection criteria was applied. The yields from the fit were then extracted, comparing the elastic prediction to data minus everything else.

The acoplanarity distributions before the fit are shown in Figure 7.9. Clearly, SD, DD and Drell-Yan have similar shapes. For the fit, SD, DD and Drell-Yan contributions were summed up and treated as one process. The Drell-Yan background was varied by $\pm 20\%$ to evaluate systematic variations in modelling $f_{n_{trk}}^{\text{sim}}$. The binning and range of acoplanarity distributions were also varied to evaluate systematic uncertainties. These uncertainties were shown to impact results by about 7%. Figure 7.10 shows the post-fit acoplanarity distributions, with simulation stacked on top of each other and the total agreeing with the data. From this fit a scale factor $f_{EL} = 0.76 \pm 0.04$ (stat.) ± 0.07 (sys.) was extracted. This value agrees within uncertainties with previous predictions [143], which cover a range between 0.73 and 0.75.

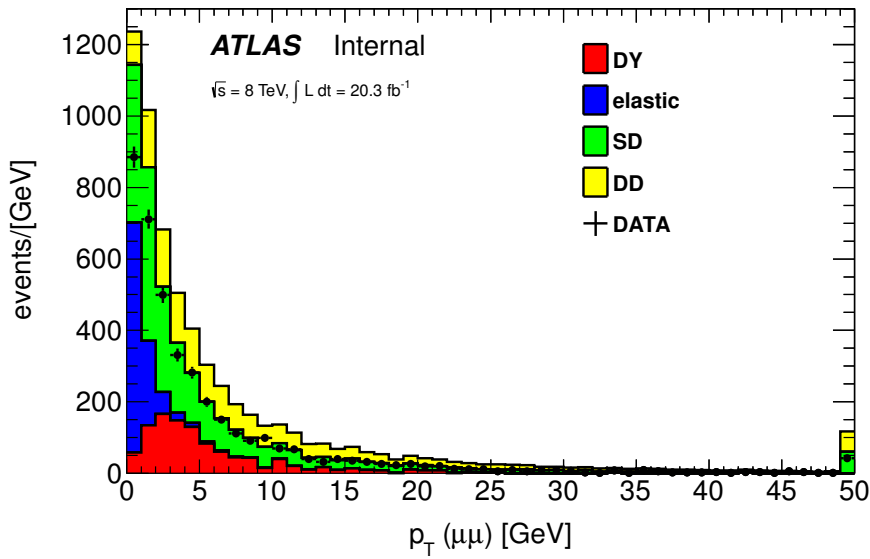


Figure 7.8. Plots showing the exclusive (1.0 mm) di-muon $p_T^{\mu\mu}$ distributions predicted and observed. The highest bin includes overflow. No scale factors are applied to elastic or SD or DD predictions.

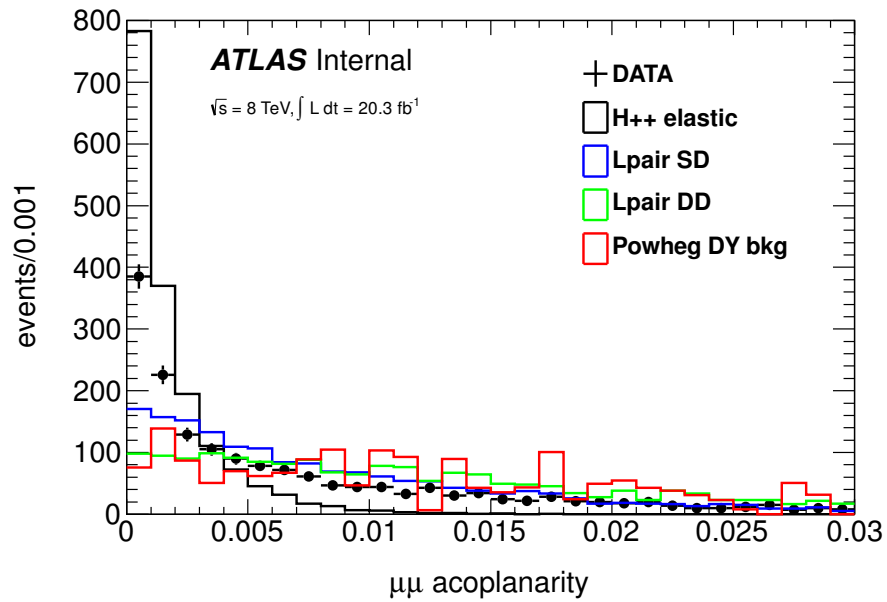


Figure 7.9. Plots of acoplanarity distributions for elastic, SD, DD and Drell-Yan each normalized to the data.

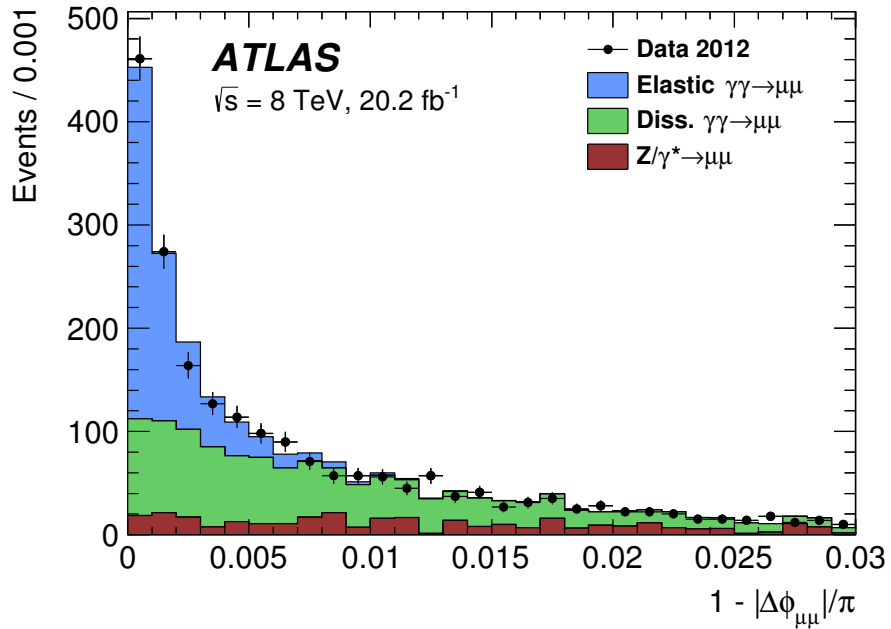


Figure 7.10. Plots of dimuon acoplanarity distributions after applying the exclusivity selection and requiring $p_T^{\mu\mu} < 3$ GeV. The expected Drell-Yan shape and the elastic and combined SD and DD (Dissociative) shapes normalized from the fit are stacked. This fit determines the factor f_{EL} .

A separate study independent of the fit method was also done to test the robustness of f_{EL} . This involved making an explicit selection based on acoplanarity in addition to the basic requirements already discussed above, counting the yields and re-calculating an estimate to f_{EL} . For acoplanarity less than 0.003, 899 events were observed in data, 764 elastic dimuons were predicted by EPA, and 340, 67 and 64 SD, DD and Drell-Yan events were also predicted respectively. This corresponds to an estimate to f_{EL} of $0.71 \pm 0.03(\text{stat}) \pm 0.01(\text{sys})$. Similarly, tightening the acoplanarity selection to be less than 0.0015 yielded $0.73 \pm 0.03(\text{stat}) \pm 0.01(\text{sys})$. These results fall well within the uncertainties of the results obtained from the fit method.

Δz_0^{iso} was tested for robustness against pileup by testing its performance in events with a selection identical to the one prior to the fit plus an acoplanarity cut, with the difference that one extra track was allowed in the exclusivity window. For exclusive processes, this extra track has to be from pileup because there is no underlying event. As such, the Δz_0 between this extra track and the di-lepton vertex is expected to be uniformly distributed, showing no clear peaks. Figure 7.11 shows the Δz_0 distributions for the extra track in exclusive and $Z \rightarrow \mu\mu$ events. For exclusive processes these distributions are uniform while for $Z \rightarrow \mu\mu$ they peak at 0. This shows that for $Z \rightarrow \mu\mu$ the extra track is from the underlying event. The

acoplanarity cut was tightened and loosened and an estimate of f_{EL} was computed at each variation. All the f_{EL} estimates fell within $\pm 10\%$, showing that Δz_0^{iso} has an a 10% pileup uncertainty.

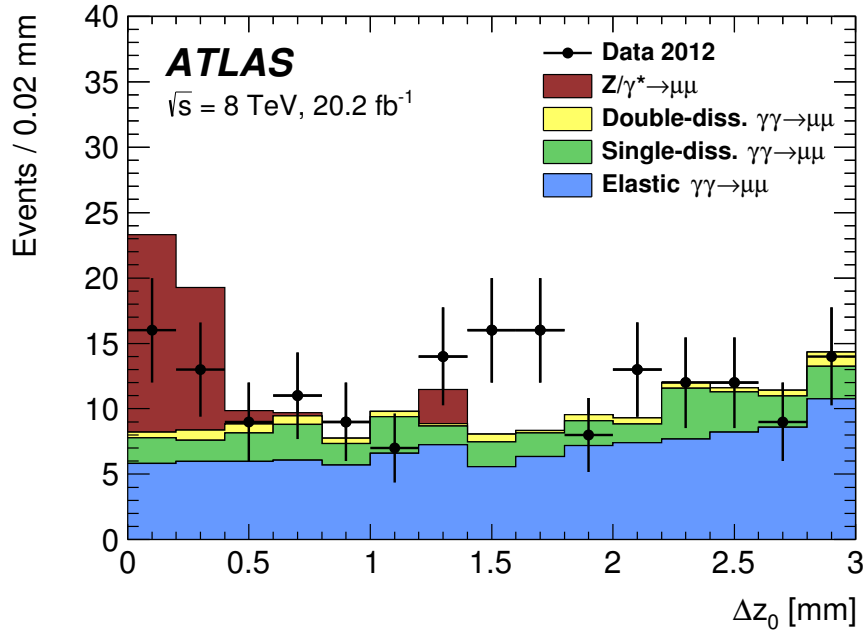


Figure 7.11. Plots of absolute Δz_0 of the extra track to the lepton vertex in the region defined by acoplanarity < 0.0015 . The exclusivity requirement was changed to select exactly one extra track within 3 mm. The exclusive predictions are scaled by a factor of 0.70.

Since electrons are also in the signal final state, these studies were repeated using $Z \rightarrow ee$ events. Due to the fact that electrons undergo brehmsstrahlung at a much higher rate than muons, results in the $Z \rightarrow ee$ channel carried a much higher error. In particular, when an electron radiates a photon (which pair produces electrons), the extra track that the radiated electron produces in the ID may be counted as an extra track by Δz_0^{iso} . This phenomenon is referred to here as *electron self-veto*. For acoplanarity less than 0.003 the estimate to f_{EL} obtained through $Z \rightarrow ee$ events was about 0.67. For acoplanarity less than 0.0015 it was 0.68. These results correspond to a $3.0 \pm 2.5\%$ difference with the results obtained from $Z \rightarrow \mu\mu$. This difference was taken as the uncertainty due to the electron self-vetoing itself.

7.3.2.3 Photon flux

This section discusses the estimation of SD and DD W^\pm contributions to the exclusive W^\pm pair production. This is an important estimation because it propagates to the estimation of the exclusive W^\pm pair contamination in the exclusive Higgs boson signal region.

Since exclusive di-lepton production is identical to exclusive W^+W^- production, this study was conducted with exclusive di-leptons. The results were then applied to exclusive W^+W^- . The strategy was to isolate exclusive di-leptons with high mass in data and taking the ratio of the data minus background to the elastic di-lepton prediction. This ratio was then applied to the elastic W^+W^- prediction to account for the SD and DD contributions. As before the leptons used were di-muons, each of at least 20 GeV in p_T . To suppress di-muons from W^+W^- decays, $m_{\mu\mu}$ was required to be at least 160 GeV. After applying Δz_0^{iso} , 244 events were observed in data were 17.4 was predicted to be from Drell-Yan, 0.4 from inclusive W^+W^- and 2.4 from exclusive W^+W^- . The predictions were corrected using the $f_{n_{trk}}^{\text{sim}}$ calibrations. From these quantities a scale factor

$$f_\gamma = \frac{N_{\text{Data}} - N_{\text{Background}}^{\text{POWHEG}}}{N_{\text{Elastic}}^{\text{HERWIG}++}} \Bigg|_{m_{\mu\mu} > 160 \text{ GeV}} = 3.30 \pm 0.22(\text{stat.}) \pm 0.06(\text{sys.}), \quad (7.4)$$

was calculated, where N_{Data} is the number of events in data, $N_{\text{Background}}^{\text{POWHEG}}$ is the expected number of background events, and $N_{\text{Elastic}}^{\text{HERWIG}++}$ is the expected number of elastic $\gamma\gamma \rightarrow \mu^+\mu^-$ candidates directly from HERWIG++, i.e, the unscaled EPA prediction. Drell-Yan processes were the major contribution to the total background events and inclusive and exclusive W^+W^- contributed less than 10%. To estimate the systematic uncertainties, the Drell-Yan contribution was varied by $\pm 20\%$. Figure 7.12 shows the $m_{\mu\mu}$ and m_{ee} distributions for the exclusive di-leptons after applying f_{EL} to the elastic contribution and scaling the SD distribution such that the sum of the elastic and SD contributions corresponds to $f_\gamma \times N_{\text{Elastic}}^{\text{HERWIG}++}$. These corrected predictions agree very well with the data.

The distributions in Figure 7.12 show that while f_γ was extracted from the invariant di-lepton mass greater than 160 GeV, its value is rather insensitive to this choice of cut.

From the above-mentioned di-muon sample in data, the Δz_0^{iso} selection efficiency was measured. It was observed to be 0.58 ± 0.06 , where the 10% uncertainty arose from pileup modelling. This measurement agrees very well with the Δz_0^{iso} efficiency measured in the exclusive Higgs boson signal samples.

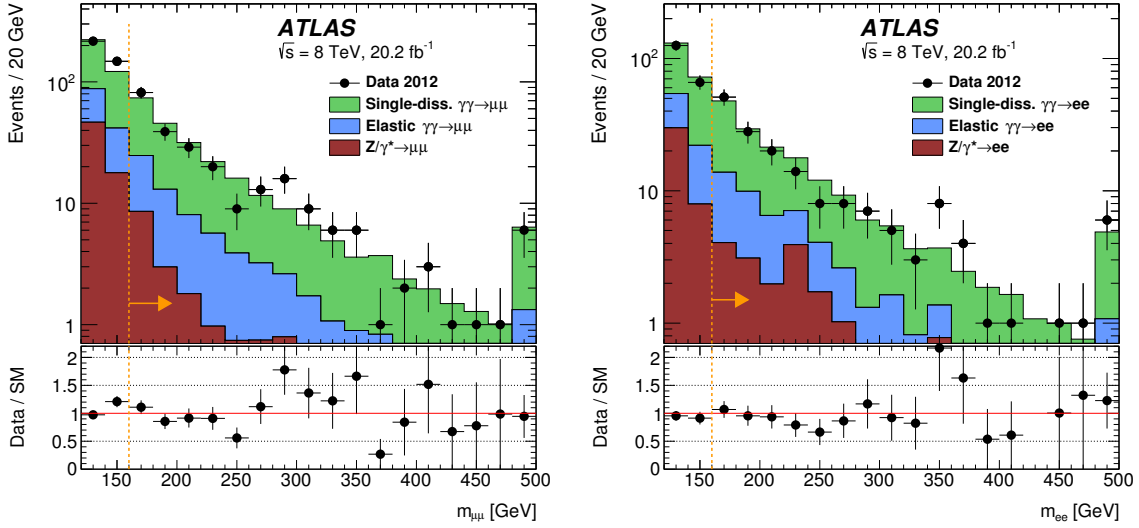


Figure 7.12. Plots of the dilepton invariant mass distribution for muon candidates (left) and electron candidates (right). The elastic yield is scaled by $f_{\text{EL}} = 0.76$ and the SD distribution is scaled to bring the sum of the elastic and SD contributions to the HERWIG++ prediction for the elastic process multiplied by the f_γ factor in the mass region above 160 GeV. The last bin includes overflow.

7.4 Modelling of background processes

Backgrounds to the signal region, as defined in Section 7.3, are categorized into exclusive and inclusive backgrounds. This section discusses modelling of these backgrounds in light of the scale factors that have been discussed so far.

7.4.1 Exclusive backgrounds

Figure 7.3 shows that the only major exclusive background expected to contaminate the signal region exclusive W^+W^- , even though several selection criteria listed in Table 7.3 were dedicated to suppressing the W^+W^- spectrum. As discussed in Section 7.3.2, SD and DD simulation samples for exclusive W^+W^- do not exist. f_γ , defined in Equation 7.4, was applied on the HERWIG++ prediction of elastic W^+W^- to account for the SD and DD components of exclusive W^+W^- . No other corrections were applied. Section 7.5.1 discusses a dedicated region in data used to validate modelling of exclusive W^+W^- .

The second significant exclusive background to the signal region is exclusive di-leptons, specifically exclusive $\gamma\gamma \rightarrow \tau^+\tau^-$. The different flavor selection criteria suppresses all the other exclusive di-leptons to the extent that they are insignificant. f_γ was also applied on the HERWIG++ prediction of elastic $\gamma\gamma \rightarrow \tau^+\tau^-$ to account for the SD and DD contributions to the exclusive $\gamma\gamma \rightarrow \tau^+\tau^-$. Since exclusive di-

leptons are produced in a manner similar to exclusive W^+W^- , the exclusive W^+W^- validation region in data hinted in the preceding paragraph also serves to validate modelling of exclusive di-leptons.

No other exclusive backgrounds significantly contaminated the signal region.

7.4.2 Inclusive backgrounds

Figure 7.3 shows that the major inclusive backgrounds that contaminate the signal region are inclusive W^+W^- , VV , $V+\text{jets}$ and Top. VV backgrounds are a collection of all non- W^+W^- processes such as ZZ , ZW and $W\gamma$. $V+\text{jets}$ are a collection of $W+\text{jets}$ and Drell-Yan. Top backgrounds are the sum of $t\bar{t}$ and single-top processes. Figure 7.3 also shows that the most dominant of all of these inclusive processes was inclusive W^+W^- . Estimation of inclusive W^+W^- 's estimation was rather complex. Several calibrations and corrections were made on the original PYTHIA8 prediction. These calibrations and corrections are discussed in the next two sub-sections.

From Figure 7.3 it is clear that while inclusive W^+W^- events were expected to dominate inclusive backgrounds, the sum of all other inclusive backgrounds was expected to be significantly less than the inclusive W^+W^- contribution. For this reason, all inclusive backgrounds, apart from inclusive W^+W^- , were sometimes treated collectively. The next sub-sections clarify this strategy.

7.4.2.1 Inclusive W^+W^- normalization

From previous measurements [142, 145], it is known that the NLO prediction for the $q\bar{q} \rightarrow W^+W^-$ process as provided by POWHEG+PYTHIA8 underestimates the observed inclusive W^+W^- event yield. It was therefore necessary to understand the simulation of this background before requiring the exclusivity selection. A control region close in phase space to the signal region was chosen for this purpose. It had the same definition as the signal region except: $55 < m_{e\mu} < 110$ GeV, $\Delta\phi_{e\mu} < 2.6$ to reduce Drell-Yan background, no jets to reduce $t\bar{t}$ background, and no requirement on exclusivity. This region was dominated by inclusive W^+W^- production, with a purity of 60%.

After subtracting the predicted backgrounds from data, $(20 \pm 5)\%$ more data was observed than is predicted by POWHEG+PYTHIA8. To correct for this, a normalization factor of $1.20 \pm 0.05(\text{stat.})$ was therefore taken as a correction to the cross-section and applied to the inclusive W^+W^- prediction in all regions of phase space, as done in Ref. [142]. A summary of the event yields in this region, where the inclusive W^+W^- prediction was scaled by $1.20 \pm 0.05(\text{stat.})$, is shown in Table 7.6. Several kinematic distributions in this control region after applying the normalization factor to the POWHEG+PYTHIA8 prediction are also shown in Fig. 7.13. Clearly, the Monte Carlo predictions agree reasonably well with data observations.

Background	Event Yield
Inclusive W^+W^-	1913.54 ± 8.78
VV	369.65 ± 195.60
$t\bar{t}$	211.39 ± 1.79
$W+jets$	196.47 ± 24.40
$Z \rightarrow \tau\tau$	160.08 ± 4.91
Single Top	112.09 ± 1.37
Other	36.39 ± 0.25
Total SM	2999.61 ± 197.42
Data	2995

Table 7.6. Summary of background yields in the control region used to correct POWHEG+PYTHIA8's prediction of inclusive W^+W^- processes.

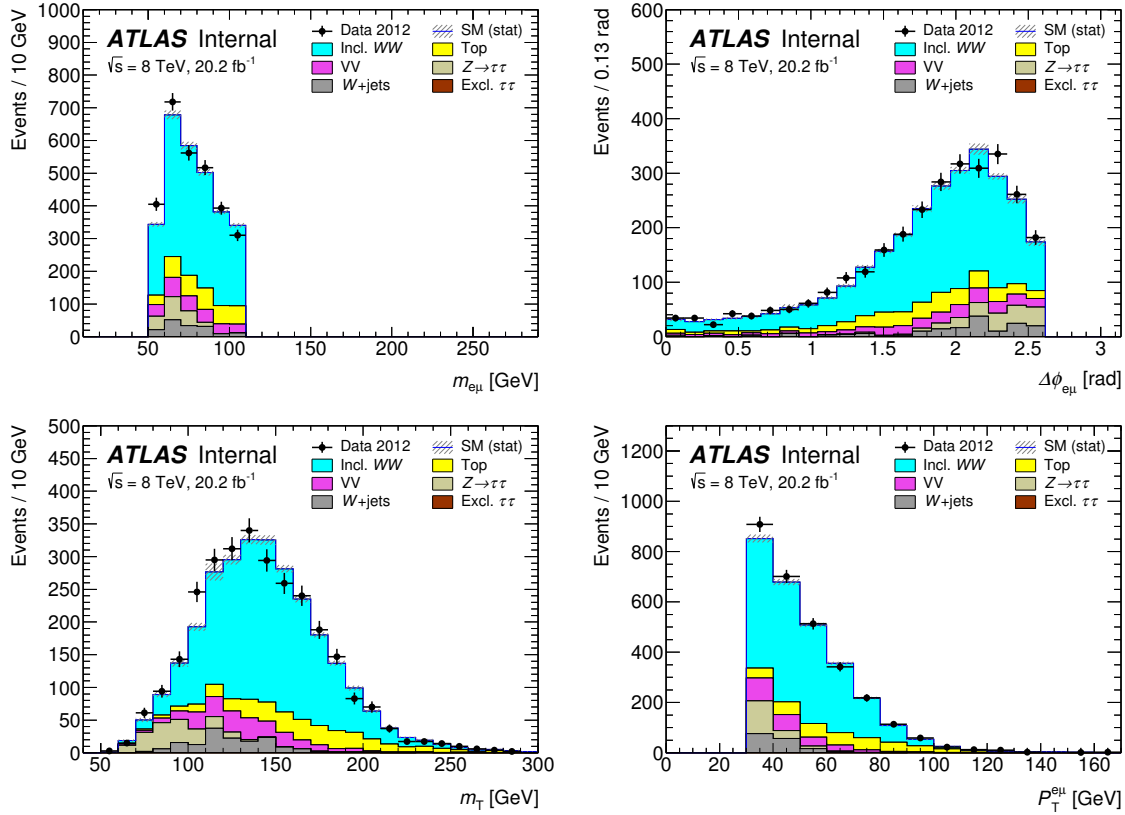


Figure 7.13. Plots showing $m_{e\mu}$, $\Delta\phi_{e\mu}$, m_T and $p_T^{e\mu}$ distributions in an inclusive W^+W^- -rich region.

	Selection
Preselection	Oppositely charged $e\mu$ final states $p_T^{\ell 1} > 25$ GeV and $p_T^{\ell 2} > 20$ GeV $m_{e\mu} > 20$ GeV
	$p_T^{e\mu} > 30$ GeV Exclusivity selection, allowing 1 to 4 tracks ²

Table 7.7. Selection criteria for the region used to study inclusive W^+W^- events.

7.4.2.2 Inclusive W^+W^- and other backgrounds

While the study discussed in the preceding sub-section demonstrates that the inclusive W^+W^- prediction after correction with the $1.20 \pm 0.05(\text{stat.})$ normalization factor was reasonable, validation of modelling of inclusive W^+W^- after the exclusivity selection was necessary. A dedicated control region in data that isolated inclusive W^+W^- events to a reasonable purity was defined for this purpose. The region definition is listed in Table 7.7.

The strategy here was to loosen the exclusivity selection slightly by allowing 1 to 4 extra tracks in the exclusivity window rather than allowing 0 tracks. While this loose selection allowed many inclusive W^+W^- events to be selected, rejection of other backgrounds was rather unoptimized. These backgrounds are $W+\text{jets}$, Drell-Yan and Top. They are referred to here as *Other Backgrounds*. Exclusive processes such as exclusive W^+W^- and exclusive $\gamma\gamma \rightarrow \tau^+\tau^-$, being well calibrated by f_γ , were subtracted from the data. This strategy therefore studies the sum of inclusive W^+W^- and other backgrounds. Expected and observed event yields in this data region are listed in Table 7.8, and kinematic distributions are shown in Figure 7.14.

The true value of the sum of inclusive W^+W^- and other backgrounds in this control region is bound by two estimates. The upper bound is the observed number of events in data, minus the sum of VV and exclusive backgrounds. The lower bound is a special case where there is no contribution from the other backgrounds, leading to contribution only from the inclusive W^+W^- , as predicted by POWHEG+PYTHIA8. These two estimates were extrapolated to a region with the same selection criteria but the nominal Δz_0^{iso} selection.³ In this region, the lower bound corresponds to the optimistic case where the other background contribution is completely rejected by Δz_0^{iso} , while the upper bound corresponds to the case where all observed candidates

³In other words, extrapolated from the 1 to 4 track region to the 0 track region

Processes	Inclusive W^+W^-
Inclusive W^+W^-	102 ± 20
Exclusive W^+W^-	5.5 ± 0.4
Exclusive $\tau^+\tau^-$	1.2 ± 0.2
Other diboson	10.9 ± 2.2
Other background	27.4 ± 6.2
Total SM	147 ± 21
Data	191

Table 7.8. Event yields in the inclusive W^+W^- -rich region.

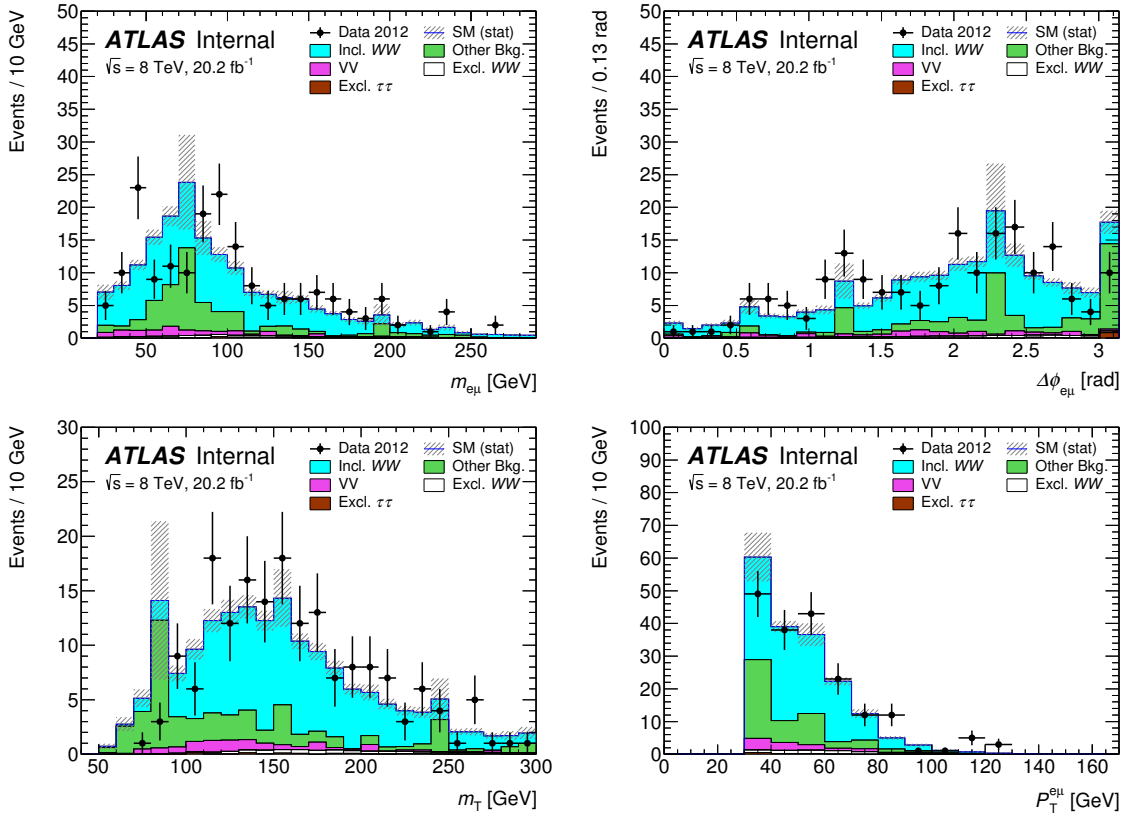


Figure 7.14. Plots showing $m_{e\mu}$, $\Delta\phi_{e\mu}$, m_T and $p_T^{e\mu}$ distributions in the inclusive W^+W^- -rich region.

in the ‘1 to 4’-track control region are suppressed by the same factor as the inclusive W^+W^- process. The average of the two estimates was taken as the better estimate to the true value of the sum of inclusive W^+W^- and other backgrounds, when the nominal Δz_0^{iso} selection criterion was applied. Comparing this estimate to the predic-

tion by POWHEG+PYTHIA8, a flat scale factor was extracted to correct for overall exclusivity mis-modelling by Monte Carlo simulation.

The extrapolation of upper and lower bounds from the 1 to 4-track region to the nominal Δz_0^{iso} region was done through

$$N_0^{\text{Estimated}} = N_{1-4}^{\text{Estimated}} \times \frac{N_{WW,0}^{\text{Predicted}}}{N_{WW,1-4}^{\text{Predicted}}}. \quad (7.5)$$

Here, $N_0^{\text{Estimated}}$ and $N_{1-4}^{\text{Estimated}}$ are the estimates for the lower bound or upper bound in the nominal Δz_0^{iso} and 1 to 4-track region respectively. $N_{WW,0}^{\text{Predicted}}$ and $N_{WW,1-4}^{\text{Predicted}}$ are respectively the number of inclusive W^+W^- events predicted by POWHEG+PYTHIA8 for the zero-track and 1 to 4-track regions. Extrapolation of the lower bound is trivial: since $N_{1-4}^{\text{Estimated}} = N_{WW,1-4}^{\text{Predicted}}$ the estimate in the nominal Δz_0^{iso} region $N_0^{\text{Estimated}}$ becomes $N_{WW,1-4}^{\text{Predicted}}$. For upper bound assumes that other backgrounds can be extrapolated using $N_{WW,0}^{\text{Predicted}} / N_{WW,1-4}^{\text{Predicted}}$. The average of these two estimates was taken as the overall estimate. Half the difference of the two estimates was taken as an additional contribution to the uncertainty in this extrapolation.

This extrapolation yields an estimate of 6.6 ± 2.5 inclusive W^+W^- events in the Δz_0^{iso} region. In other words, for POWHEG+PYTHIA8 prediction to match this value, a normalization factor of 0.79 was necessary. So in the signal region, a 0.79 scale factor was applied to the inclusive W^+W^- prediction from Monte Carlo simulation.

7.5 Validation of background modelling

The section discusses validation of background modelling. Two regions in data were defined to validate modelling of exclusive and inclusive backgrounds.

Since the major exclusive background is exclusive W^+W^- , a region that enhanced such events is discussed here. This region also contains a significant contribution from inclusive W^+W^- , so it demonstrates the validity of the inclusive W^+W^- modelling techniques discussed in the preceding sections.

Although $Z \rightarrow \tau\tau$ events were not expected to be very significant in the signal region, studying background composition in a region of data rich in $Z \rightarrow \tau\tau$ events reinforced that all the other backgrounds were reasonably well-modelled.

7.5.1 Exclusive W^+W^-

While the 1 to 4-track region introduced in Table 7.7 was rich in inclusive W^+W^- events, replacing the 1 to 4-track selection criterion with the nominal Δz_0^{iso} selection criterion suppressed the inclusive W^+W^- events and enhanced the exclusive W^+W^- events. This is the exclusive W^+W^- validation region.

Although this region was discussed in Section 7.4.2.2, validation kinematic distributions are presented in this section. Figure 7.15 shows such distributions. The inclusive W^+W^- contribution was scaled by 0.79 as discussed in Section 7.4.2.2. The

exclusive W^+W^- and $\tau\tau$ estimates were scaled by f_γ . Contributions from VV were very small. Any other background processes were insignificantly small in comparison to the inclusive W^+W^- contribution.

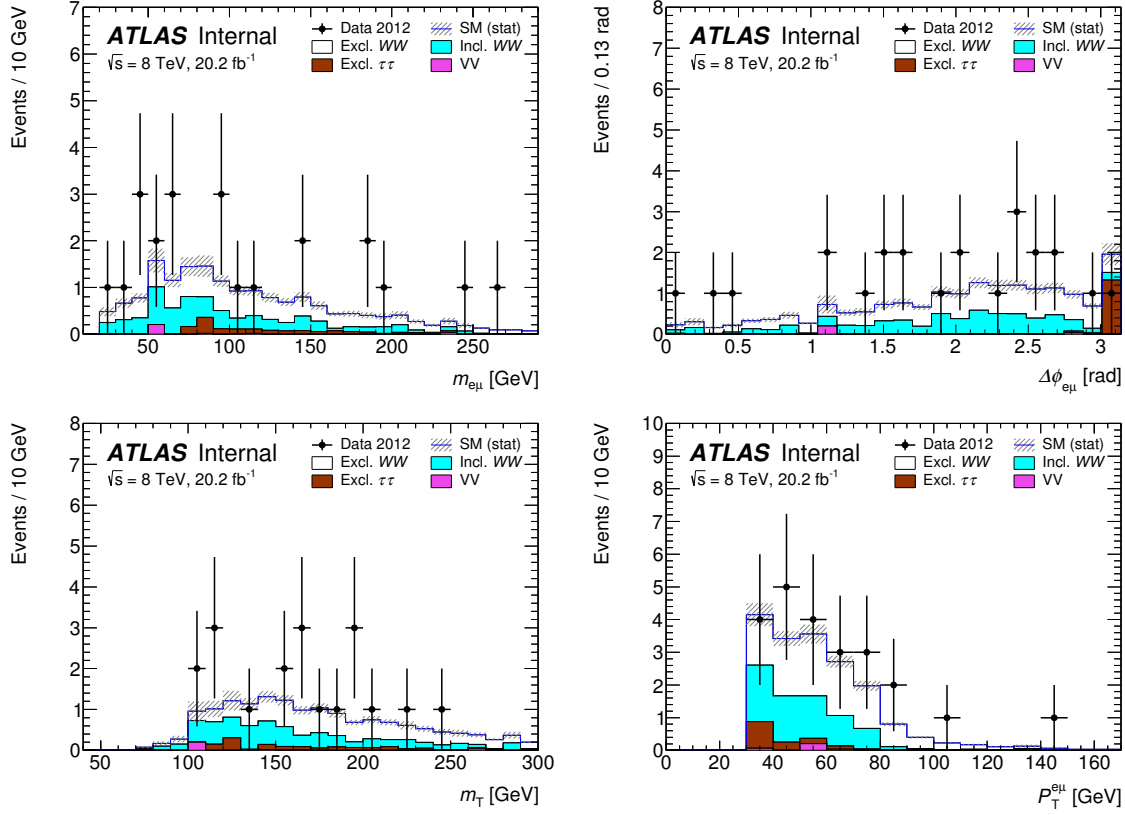


Figure 7.15. Plots showing $m_{e\mu}$, $\Delta\phi_{e\mu}$, m_T and $p_T^{e\mu}$ distributions in the exclusive W^+W^- validation region.

Overall Figure 7.15 shows reasonable agreement between data and predictions. A slight underestimation of exclusive W^+W^- was observed across all the distributions. From counting the yields from all the processes and comparing them with the observed data, a normalization factor of 1.57 ± 0.62 was extracted, to be additionally applied to the exclusive W^+W^- contributions in the signal region. The uncertainty in this normalization factor resulted from propagation of uncertainties of each of the numbers that went into the calculation.

7.5.2 Inclusive $Z \rightarrow \tau\tau$

A $Z \rightarrow \tau\tau + \text{jets}$ -rich region was defined in data to validate background modelling in an environment dominated by inclusive processes. Table 7.9 summarizes the

definition of this region. Figure 7.16 shows some kinematic distributions in this validation region, after all the selection criteria summarized in Table 7.9 were applied. The general slight disagreement between data and simulation was attributed to the mismodelling of the transverse momentum of the Z , p_T^Z . This mismodelling is well documented in Ref [146]. While considerable efforts are normally applied to reweight the Z p_T , $Z \rightarrow \tau\tau$ events were not a primary background in this analysis so such reweighting was observed to have insignificant effects on results.

	Selection
Preselection	Lepton p_T 25, 15 GeV OS and different flavour leptons $m_{\ell\ell} > 10$ GeV
$Z \rightarrow \tau\tau$	$p_T^{\ell\ell} < 30$ GeV $m_{\ell\ell} < 80$ GeV
Exclusivity	$ z_0^1 - z_0^2 < 1.0$ mm $\Delta z_0 > 1.0$ mm

Table 7.9. $Z \rightarrow \tau\tau$ validation region definition.

7.6 Systematic Uncertainties and Statistical analysis

This section summarizes the sources of systematic uncertainties in this search. The most important of these sources are listed in table 7.10. The errors on the various scale factors, $f_\gamma = 3.30 \pm 0.23$ and $f_{EL} = 0.76 \pm 0.04 \pm 0.07$ were included in the analysis as systematic uncertainties. For $Z + \text{jets}$, the estimate of 20% comes from the exclusivity calibration method described in Section 7.3.2. Details on the flux factor and WW background uncertainties are discussed in Sections 7.3.2.3 and sec:incWW respectively.

The systematic uncertainties associated to the physics objects were estimated using methods discussed in Chapter 5. They are listed in table 7.11. The systematics in tables 7.10 and 7.11 are uncorrelated, so they were added in quadrature.

The statistical framework used to evaluate results of this search are identical to those used in the search for the charged Higgs boson. See Section 6.5 for more details.

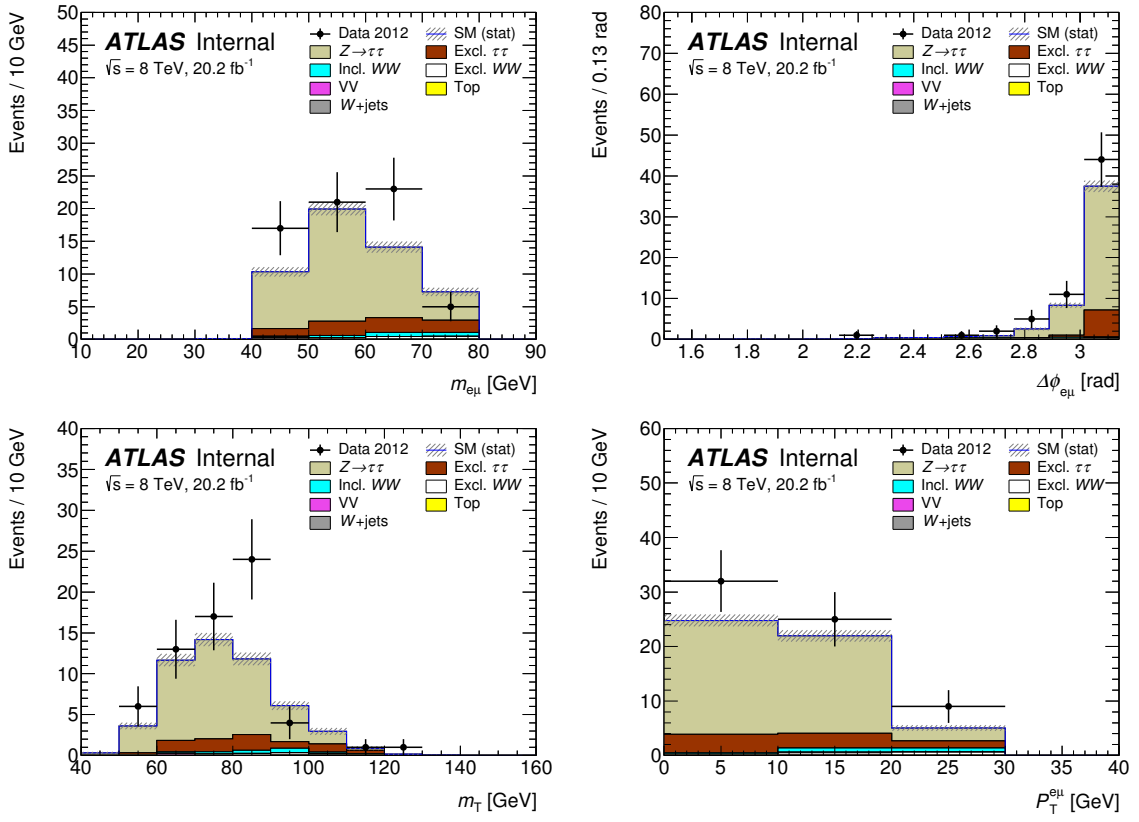


Figure 7.16. Plots showing $m_{e\mu}$, $\Delta\phi_{e\mu}$, m_T and $p_T^{e\mu}$ distributions in the $Z \rightarrow \tau\tau$ validation region.

Source of Uncertainty	Exclusive WW	Exclusive Higgs	Exclusive $\tau\tau$	Inclusive WW	$Z+jets$
Exclusivity	10%	10%	—	—	—
f_γ	7%	—	—	—	—
f_{EL}	—	—	10%	—	—
Background	—	—	—	38%	20%

Table 7.10. Most important sources of systematic uncertainties and their contribution to the event yields. The largest ones come from estimates of background. Dashed lines imply that the source was not directly applicable to that particular process.

7.7 Results

7.7.1 Expected and observed event yields

After the event selection criteria for the signal region was finalized, and the background modelling validated, final kinematic distributions in the signal region were examined. Figure 7.17 shows n-1 distributions for $\Delta\phi_{e\mu}$, $m_{e\mu}$, m_T and $p_T^{e\mu}$. N-1

Source of Uncertainty	Excl. Higgs [%]	Incl. WW [%]	Excl. WW [%]	ggF H. [%]
Electron Resolution	0.02	0.05	0.06	0.05
Electron Energy Scale	0.75	0.24	0.59	0.67
Muon Energy Scale	0.11	0.03	0.04	0.07
Electron ID & Reco.	1.55	1.26	1.28	1.35
Muon ID	0.32	0.32	0.32	0.32
Single Electron Trigger SF	0.45	0.31	0.32	0.35
Single Muon Trigger SF	0.64	0.47	0.53	0.53
Elec-Muon Trigger SF	0.01	0.01	0.01	0.01
Total Lepton	1.92	1.44	1.57	1.67
JES {				
EtaModelling	—	0.33	—	—
EtaStatMethod	—	0.08	—	—
FlavComp	—	0.04	—	—
FlavResp	—	0.45	—	—
HighPt	—	0.04	—	—
NPDetector1	—	0.17	—	—
NPModelling1	—	0.45	—	—
NPV	—	0.16	—	—
PilePt	—	0.04	—	—
PileRho	—	0.26	—	—
Total JES	—	0.8	—	—
Luminosity	1.90	1.90	1.90	1.90

Table 7.11. List of all systematic uncertainties associated with the reconstruction of physics objects. Chapter 5 discusses methods with which these uncertainties were calculated. The individual uncertainties were assumed to be uncorrelated so they were added in quadrature.

distributions show event yields and shapes in the signal region, minus the selection criteria specific to the distribution being plotted. All the scale factors discussed in the preceding sections were applied to correctly model the backgrounds. For the exclusive W^+W^- process, f_γ was multiplied by 1.57 to match validation results observed in Section 7.5. The inclusive W^+W^- process was scaled by 0.79. As discussed in Section 7.4.2.2, applying this background implicitly adds the $Z \rightarrow \tau\tau$ background to the inclusive W^+W^- background. The rest of the backgrounds were scaled by their respective scale factors to account for the mis-modelling of the underlying event in simulation.

A summary of the yields in the signal region is shown in Table 7.12. Six events were observed in data, while 3.00 ± 0.78 events were expected from all the background processes; 0.023 ± 0.003 events were expected from signal, where the quoted uncertainty is the sum in quadrature of systematic uncertainties and simulation statistical uncertainties.

	Excl. H Signal	Data	Total Bkg	Incl. W^+W^-	Excl. W^+W^-	Other Bkg
Preselection	0.065 ± 0.005	129018	120090	12844	43	107200
$p_T^{e\mu} > 30 \text{ GeV}$, $m_{e\mu} < 55 \text{ GeV}$, $\Delta\phi_{e\mu} < 1.8$	0.043 ± 0.004	18568	17060	2026	5.7	15030
Δz_0^{iso} requirement	0.023 ± 0.003	8	4.7 ± 1.3	1.4 ± 0.5	3.1 ± 1.3	0.2 ± 0.1
$m_T < 140 \text{ GeV}$ [Signal Region]	0.023 ± 0.003	6	3.0 ± 0.8	1.0 ± 0.4	1.8 ± 0.8	0.2 ± 0.1

Table 7.12. Summary of signal and background yields at different stages of the Higgs boson event selection. Only major background sources are listed explicitly. All the other background sources are summed up in the ‘Other’ category. For the background, the uncertainties are only shown for the yields after exclusivity selection, where they are relevant for the measurement. They include the systematic and statistical components, added in quadrature.

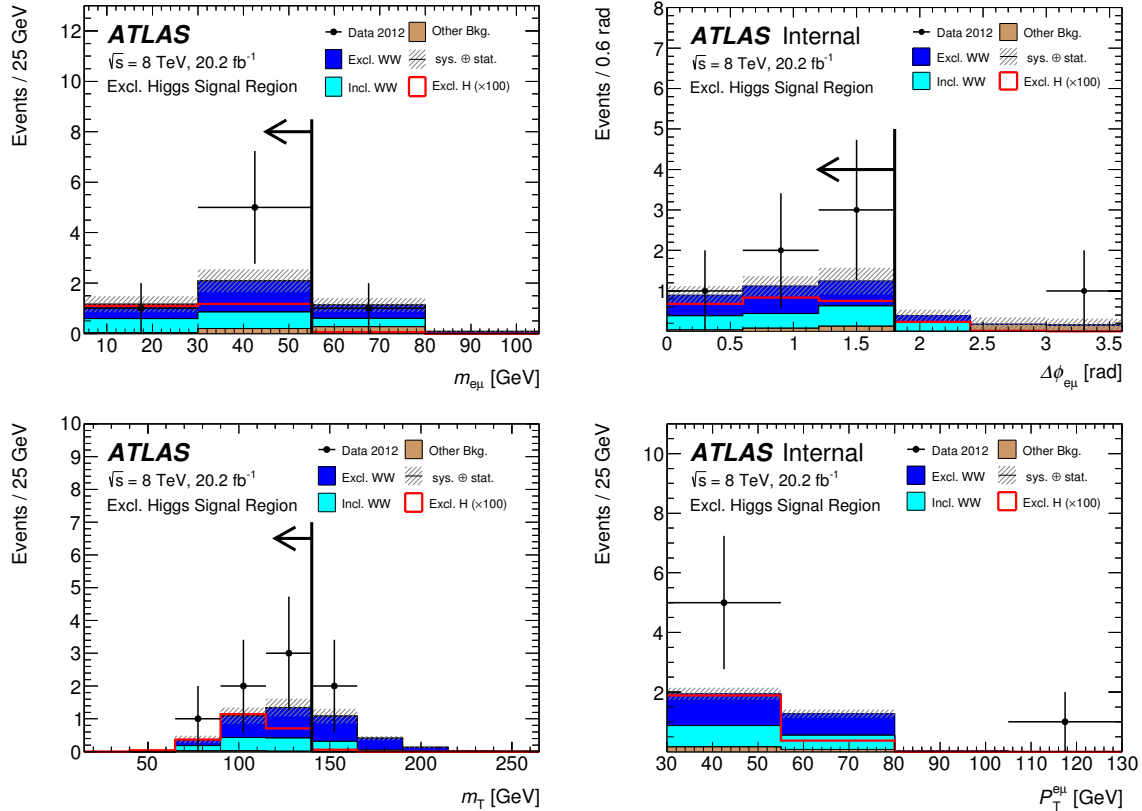


Figure 7.17. Plots showing $m_{e\mu}$, $\Delta\phi_{e\mu}$, m_T and $p_T^{e\mu}$ distributions in the signal region, minus the selection criteria for the variable being plotted.

7.7.2 Statistical Analysis

The results presented in the preceding sub-section were tested for evidence of exclusive Higgs production in LHC Run I data. For a Standard Model Higgs boson with $m_H = 125 \text{ GeV}$, σ_H^{Exp} was set at 1 to make the parameter of interest

$+2\sigma$ [pb]	$+1\sigma$ [pb]	Expected [pb]	-1σ [pb]	-2σ [pb]	Observed [pb]
1.6	1.0	0.7	0.5	0.4	1.2

Table 7.13. Upper limits on σ_H [pb] at 95% CL. The $\pm 1\sigma$ and $\pm 2\sigma$ uncertainties quoted here are on the expected upper limit.

$\mu = \sigma_H^{obs}$. The test statistic q_0 , where $\mu = 0$ in Equation 6.13, was used to test the compatibility of observed data with the background-only hypothesis. The rest of the statistical analysis is identical to that described in Section 6.6.2, including the treatment of systematic uncertainties. The discrepancy between the observed data and expected event yields corresponded to a 1.1σ upward fluctuation from the expected Standard Model results. This fluctuation is not significant enough to prove existence of the exclusive Higgs boson. Expected limits on the exclusive Higgs boson cross section were therefore set, using the CL_s procedure, where $CL_s(\mu)$ is defined as in Equation 6.16.

Table 7.13 shows a summary of the 95% CL upper limits on the exclusive Higgs boson total production cross-section. The observed upper limit is 1.2 pb, which is 1.1σ higher than the expected upper limit of 0.7 pb. The statistical uncertainty in the predicted background dominates the uncertainty involved in calculating this upper limit, while systematic uncertainties worsen the upper limits by at most 10%. This upper limit value is 400 times the cross-section predicted [27]. However, the limit would not change if the model prediction, which is for elastic production only, increased by an order of magnitude. This limit calculation inherently assumes that the acceptance and efficiency for dissociative events is not significantly different than for elastic events, hence the associated systematic uncertainty is insignificant.

Chapter 8

Conclusion

To be filled after the defense date

Bibliography

- [1] S. L. Glashow. “Partial-symmetries of weak interactions”.
In: *Nuclear Physics* 22.4 (1961), pp. 579 –588. ISSN: 0029-5582.
DOI: [http://dx.doi.org/10.1016/0029-5582\(61\)90469-2](http://dx.doi.org/10.1016/0029-5582(61)90469-2). URL: <http://www.sciencedirect.com/science/article/pii/0029558261904692>.
- [2] S. Weinberg. “A Model of Leptons”.
In: *Phys. Rev. Lett.* 19 (21 1967), pp. 1264–1266.
DOI: [10.1103/PhysRevLett.19.1264](https://doi.org/10.1103/PhysRevLett.19.1264).
URL: <http://link.aps.org/doi/10.1103/PhysRevLett.19.1264>.
- [3] O. S. Bruning et al. “LHC Design Report Vol.1: The LHC Main Ring”.
In: (2004).
- [4] Y. Fukuda et al. “Evidence for oscillation of atmospheric neutrinos”.
In: *Phys. Rev. Lett.* 81 (1998), pp. 1562–1567.
DOI: [10.1103/PhysRevLett.81.1562](https://doi.org/10.1103/PhysRevLett.81.1562). arXiv: [hep-ex/9807003 \[hep-ex\]](https://arxiv.org/abs/hep-ex/9807003).
- [5] ATLAS and CMS Collaborations.
“Combined Measurement of the Higgs Boson Mass in pp Collisions at $\sqrt{s} = 7$ and 8 TeV with the ATLAS and CMS Experiments”.
In: *Phys. Rev. Lett.* 114 (2015), p. 191803.
DOI: [10.1103/PhysRevLett.114.191803](https://doi.org/10.1103/PhysRevLett.114.191803). arXiv: [1503.07589 \[hep-ex\]](https://arxiv.org/abs/1503.07589).
- [6] G. Arnison et al. “Experimental observation of isolated large transverse energy electrons with associated missing energy at $s=540$ GeV”.
In: *Physics Letters B* 122.1 (1983), pp. 103 –116. ISSN: 0370-2693.
DOI: [http://dx.doi.org/10.1016/0370-2693\(83\)91177-2](http://dx.doi.org/10.1016/0370-2693(83)91177-2). URL: <http://www.sciencedirect.com/science/article/pii/0370269383911772>.
- [7] M. Banner et al.
“Observation of single isolated electrons of high transverse momentum in events with missing transverse energy at the {CERN} pp collider”.
In: *Physics Letters B* 122.5–6 (1983), pp. 476 –485. ISSN: 0370-2693.
DOI: [http://dx.doi.org/10.1016/0370-2693\(83\)91605-2](http://dx.doi.org/10.1016/0370-2693(83)91605-2). URL: <http://www.sciencedirect.com/science/article/pii/0370269383916052>.

- [8] R. Brandelik et al. “Evidence for Planar Events in e+ e- Annihilation at High-Energies”. In: *Phys. Lett.* B86 (1979), pp. 243–249.
DOI: [10.1016/0370-2693\(79\)90830-X](https://doi.org/10.1016/0370-2693(79)90830-X).
- [9] D. P. Barber et al. “Discovery of Three-Jet Events and a Test of Quantum Chromodynamics at PETRA”. In: *Phys. Rev. Lett.* 43 (12 1979), pp. 830–833.
DOI: [10.1103/PhysRevLett.43.830](https://doi.org/10.1103/PhysRevLett.43.830).
URL: <http://link.aps.org/doi/10.1103/PhysRevLett.43.830>.
- [10] C. Campagnari and M. Franklin. “The Discovery of the top quark”. In: *Rev. Mod. Phys.* 69 (1997), pp. 137–212.
DOI: [10.1103/RevModPhys.69.137](https://doi.org/10.1103/RevModPhys.69.137). arXiv: [hep-ex/9608003 \[hep-ex\]](https://arxiv.org/abs/hep-ex/9608003).
- [11] X. Gong. “Divergence of the normalization for real Lagrangian surfaces near complex tangents”. In: *ArXiv Mathematics e-prints* (June 1995). eprint: [math/9506202](https://arxiv.org/abs/math/9506202).
- [12] N. V. Krasnikov and A. A. Pivovarov. “Renormalization schemes and renormalons”. In: *Mod. Phys. Lett.* A11 (1996), pp. 835–852.
DOI: [10.1142/S0217732396000849](https://doi.org/10.1142/S0217732396000849). arXiv: [hep-ph/9602272 \[hep-ph\]](https://arxiv.org/abs/hep-ph/9602272).
- [13] V. Derkach and M. Malamud. “Weyl function of a Hermitian operator and its connection with characteristic function”. In: *ArXiv e-prints* (Mar. 2015). arXiv: [1503.08956 \[math.SP\]](https://arxiv.org/abs/1503.08956).
- [14] Y. Nambu. “Axial Vector Current Conservation in Weak Interactions”. In: *Phys. Rev. Lett.* 4 (7 1960), pp. 380–382.
DOI: [10.1103/PhysRevLett.4.380](https://doi.org/10.1103/PhysRevLett.4.380).
URL: <http://link.aps.org/doi/10.1103/PhysRevLett.4.380>.
- [15] T. Aaltonen et al. “Precise measurement of the W -boson mass with the CDF II detector”. In: *Phys. Rev. Lett.* 108 (2012), p. 151803.
DOI: [10.1103/PhysRevLett.108.151803](https://doi.org/10.1103/PhysRevLett.108.151803). arXiv: [1203.0275 \[hep-ex\]](https://arxiv.org/abs/1203.0275).
- [16] S. Schael et al. “Precision electroweak measurements on the Z resonance”. In: *Phys. Rept.* 427 (2006), pp. 257–454.
DOI: [10.1016/j.physrep.2005.12.006](https://doi.org/10.1016/j.physrep.2005.12.006). arXiv: [hep-ex/0509008 \[hep-ex\]](https://arxiv.org/abs/hep-ex/0509008).
- [17] G. Aad et al. “Observation of a new particle in the search for the Standard Model Higgs boson with the ATLAS detector at the LHC”. In: *Phys. Lett.* B716 (2012), pp. 1–29.
DOI: [10.1016/j.physletb.2012.08.020](https://doi.org/10.1016/j.physletb.2012.08.020). arXiv: [1207.7214 \[hep-ex\]](https://arxiv.org/abs/1207.7214).

- [18] D. Ghosh et al. “Looking for an Invisible Higgs Signal at the LHC”. In: *Phys. Lett.* B725 (2013), pp. 344–351.
DOI: [10.1016/j.physletb.2013.07.042](https://doi.org/10.1016/j.physletb.2013.07.042). arXiv: [1211.7015 \[hep-ph\]](https://arxiv.org/abs/1211.7015).
- [19] L. C.S. W. Group. *LHC Higgs Cross Sections*.
<https://twiki.cern.ch/twiki/bin/view/LHCPhysics/CrossSections>. 2016.
- [20] M. S. Costa, V. Goncalves, and J. Penedones. “Conformal Regge theory”. In: *JHEP* 12 (2012), p. 091. DOI: [10.1007/JHEP12\(2012\)091](https://doi.org/10.1007/JHEP12(2012)091). arXiv: [1209.4355 \[hep-th\]](https://arxiv.org/abs/1209.4355).
- [21] M.-S. Chen et al. “Lepton pair production from two-photon processes”. In: *Phys. Rev.* D7 (1973).
- [22] V. Budnev et al. “The process $pp \rightarrow \gamma\gamma$; $pp \rightarrow e^+e^-$ and the possibility of its calculation by means of quantum electrodynamics only”. In: *Nucl. Phys.* B63 (1973).
- [23] A. Abulencia et al. “Observation of exclusive electron-positron production in hadron-hadron collisions”. In: *Phys. Rev. Lett.* 98 (2007).
- [24] J. Adams et al. “Production of e^+e^- pairs accompanied by nuclear dissociation in ultra-peripheral heavy ion collisions”. In: *Phys. Rev.* C70 (2004).
- [25] “Exclusive photon-photon production of muon pairs in pp collisions at $\sqrt{s} = 7$ TeV”. In: *JHEP* 01 (2012). DOI: [10.1007/JHEP01\(2012\)052](https://doi.org/10.1007/JHEP01(2012)052).
- [26] “Search for exclusive or simi-exclusive photon pair production and observation of exclusive and semi-exclusive electron pair production in pp collisions at $\sqrt{s} = 7$ TeV”. In: *JHEP* 11 (2012). DOI: [10.1007/JHEP11\(2012\)080](https://doi.org/10.1007/JHEP11(2012)080).
- [27] V. Khoze, A. Martin, and M. Ryskin. “Prospects for new physics observations in diffractive processes at the LHC and Tevatron”. In: *Eur.Phys.J.* C23 (2002), pp. 311–327. DOI: [10.1007/s100520100884](https://doi.org/10.1007/s100520100884). arXiv: [hep-ph/0111078 \[hep-ph\]](https://arxiv.org/abs/hep-ph/0111078).
- [28] A. D. Martin and M. Ryskin. “Unintegrated generalized parton distributions”. In: *Phys. Rev.* D64 (2001), p. 094017. DOI: [10.1103/PhysRevD.64.094017](https://doi.org/10.1103/PhysRevD.64.094017). arXiv: [hep-ph/0107149 \[hep-ph\]](https://arxiv.org/abs/hep-ph/0107149).
- [29] P. Fayet. “Supersymmetry and weak, electromagnetic and strong interactions”. In: *Physics Letters B* 64.2 (1976), pp. 159 –162. ISSN: 0370-2693.
DOI: [http://dx.doi.org/10.1016/0370-2693\(76\)90319-1](http://dx.doi.org/10.1016/0370-2693(76)90319-1). URL: <http://www.sciencedirect.com/science/article/pii/0370269376903191>.

- [30] A. Djouadi et al. “The post-Higgs MSSM scenario: Habemus MSSM?”
In: *Eur. Phys. J.* C73 (2013), p. 2650.
DOI: [10.1140/epjc/s10052-013-2650-0](https://doi.org/10.1140/epjc/s10052-013-2650-0). arXiv: [1307.5205 \[hep-ph\]](https://arxiv.org/abs/1307.5205).
- [31] T. D. Lee. “A Theory of Spontaneous T Violation”.
In: *Phys. Rev. D* 8 (4 1973), pp. 1226–1239.
DOI: [10.1103/PhysRevD.8.1226](https://doi.org/10.1103/PhysRevD.8.1226).
URL: <http://link.aps.org/doi/10.1103/PhysRevD.8.1226>.
- [32] S. Myers. “The LEP collider, from design to approval and commissioning”.
In: 1991. URL: <http://doc.cern.ch/cernrep/1991/91-08/91-08.html>.
- [33] H. Wiedemann. *Particle accelerator physics; 3rd ed.* Berlin: Springer, 2007.
URL: <https://cds.cern.ch/record/1083415>.
- [34] M. Benedikt. *LHC Design Report: The LHC injector chain*.
LHC design report v. 3. CERN, 2004. ISBN: 9789290832393.
URL: <https://books.google.fr/books?id=4WLLAAAACAAJ>.
- [35] T. A. Collaboration et al.
“The ATLAS Experiment at the CERN Large Hadron Collider”.
In: *Journal of Instrumentation* 3.08 (2008), S08003.
URL: <http://stacks.iop.org/1748-0221/3/i=08/a=S08003>.
- [36] S. Chatrchyan et al. “The CMS experiment at the CERN LHC”.
In: *JINST* 3 (2008), S08004. DOI: [10.1088/1748-0221/3/08/S08004](https://doi.org/10.1088/1748-0221/3/08/S08004).
- [37] S. Amato et al. “LHCb technical proposal”. In: (1998).
- [38] T. A. Collaboration. “The ALICE experiment at the CERN LHC”.
In: *Journal of Instrumentation* 3.08 (2008), S08002.
URL: <http://stacks.iop.org/1748-0221/3/i=08/a=S08002>.
- [39] N. Arkani-Hamed et al.
“Physics Opportunities of a 100 TeV Proton-Proton Collider”. In: (2015).
arXiv: [1511.06495 \[hep-ph\]](https://arxiv.org/abs/1511.06495).
- [40] A. Collaboration. *Public Results 2012, ATLAS Experiment*. <https://twiki.cern.ch/twiki/bin/view/AtlasPublic/LuminosityPublicResults>. 2016.
- [41] A. Collaboration. *Public Results 2016, ATLAS Experiment*. <https://twiki.cern.ch/twiki/bin/view/AtlasPublic/LuminosityPublicResultsRun2>. 2016.
- [42] ATLAS Collaboration.
“The ATLAS Experiment at the CERN Large Hadron Collider”.
In: *JINST* 3 (2008), S08003. DOI: [10.1088/1748-0221/3/08/S08003](https://doi.org/10.1088/1748-0221/3/08/S08003).
- [43] ATLAS Collaboration.
“The ATLAS Inner Detector commissioning and calibration”.
In: *Eur. Phys. J. C* 70 (2010), p. 787.
DOI: [10.1140/epjc/s10052-010-1366-7](https://doi.org/10.1140/epjc/s10052-010-1366-7). arXiv: [1004.5293 \[hep-ex\]](https://arxiv.org/abs/1004.5293).

- [44] F. Hugging. “The ATLAS pixel detector”.
In: *IEEE Transactions on Nuclear Science* 53.3 (2006), pp. 1732–1736.
ISSN: 0018-9499. DOI: [10.1109/TNS.2006.871506](https://doi.org/10.1109/TNS.2006.871506).
- [45] G. Aad et al.
“Operation and performance of the ATLAS semiconductor tracker”.
In: *JINST* 9 (2014), P08009. DOI: [10.1088/1748-0221/9/08/P08009](https://doi.org/10.1088/1748-0221/9/08/P08009).
arXiv: [1404.7473 \[hep-ex\]](https://arxiv.org/abs/1404.7473).
- [46] T. A. T. collaboration. “The ATLAS Transition Radiation Tracker (TRT) proportional drift tube: design and performance”.
In: *Journal of Instrumentation* 3.02 (2008), P02013.
URL: <http://stacks.iop.org/1748-0221/3/i=02/a=P02013>.
- [47] D.-L. Pohl. “Overview of the ATLAS Insertable B-Layer (IBL) Project”.
In: *PoS* RD13 (2013), p. 012.
- [48] P Puzo. “{ATLAS} calorimetry”. In: *Nuclear Instruments and Methods in Physics Research Section A: Accelerators, Spectrometers, Detectors and Associated Equipment* 494.1–3 (2002). Proceedings of the 8th International Conference on Instrumentation for Colliding Beam Physics, pp. 340 –345.
ISSN: 0168-9002.
DOI: [http://dx.doi.org/10.1016/S0168-9002\(02\)01490-0](http://dx.doi.org/10.1016/S0168-9002(02)01490-0). URL: <http://www.sciencedirect.com/science/article/pii/S0168900202014900>.
- [49] ATLAS Collaboration.
“Readiness of the ATLAS liquid argon calorimeter for LHC collisions”.
In: *Eur. Phys. J. C* 70 (2010), p. 723.
DOI: [10.1140/epjc/s10052-010-1354-y](https://doi.org/10.1140/epjc/s10052-010-1354-y). arXiv: [0912.2642 \[hep-ex\]](https://arxiv.org/abs/0912.2642).
- [50] ATLAS Collaboration.
“Readiness of the ATLAS Tile Calorimeter for LHC collisions”.
In: *Eur. Phys. J. C* 70 (2010), p. 1193.
DOI: [10.1140/epjc/s10052-010-1508-y](https://doi.org/10.1140/epjc/s10052-010-1508-y). arXiv: [1007.5423 \[hep-ex\]](https://arxiv.org/abs/1007.5423).
- [51] ATLAS Collaboration.
“Commissioning of the ATLAS Muon Spectrometer with cosmic rays”.
In: *Eur. Phys. J. C* 70 (2010), p. 875.
DOI: [10.1140/epjc/s10052-010-1415-2](https://doi.org/10.1140/epjc/s10052-010-1415-2). arXiv: [1006.4384 \[hep-ex\]](https://arxiv.org/abs/1006.4384).
- [52] G. Cattani and the RPC group. “The Resistive Plate Chambers of the ATLAS experiment: performance studies”.
In: *Journal of Physics: Conference Series* 280.1 (2011), p. 012001.
URL: <http://stacks.iop.org/1742-6596/280/i=1/a=012001>.

- [53] K. Nagai. “BEAUTY ’96 Thin gap chambers in ATLAS”. In: *Nuclear Instruments and Methods in Physics Research Section A: Accelerators, Spectrometers, Detectors and Associated Equipment* 384.1 (1996), pp. 219 –221. ISSN: 0168-9002.
 DOI: [http://dx.doi.org/10.1016/S0168-9002\(96\)01065-0](http://dx.doi.org/10.1016/S0168-9002(96)01065-0). URL: <http://www.sciencedirect.com/science/article/pii/S0168900296010650>.
- [54] T. Liu and E. Diehl.
 “Proceedings of the 2nd International Conference on Technology and Instrumentation in Particle Physics (TIPP 2011) Calibration and Performance of the Precision Chambers of the ATLAS Muon Spectrometer”. In: *Physics Procedia* 37 (2012), pp. 543 –548. ISSN: 1875-3892.
 DOI: <http://dx.doi.org/10.1016/j.phpro.2012.02.404>. URL: <http://www.sciencedirect.com/science/article/pii/S1875389212017373>.
- [55] T. Argyropoulos et al. “Cathode strip chambers in ATLAS: Installation, commissioning and in situ performance”. In: *IEEE Trans. Nucl. Sci.* 56 (2009), pp. 1568–1574.
 DOI: [10.1109/TNS.2009.2020861](https://doi.org/10.1109/TNS.2009.2020861).
- [56] ATLAS Collaboration. “Performance of the ATLAS Trigger System in 2010”. In: *Eur. Phys. J. C* 72 (2012), p. 1849.
 DOI: [10.1140/epjc/s10052-011-1849-1](https://doi.org/10.1140/epjc/s10052-011-1849-1). arXiv: [1110.1530 \[hep-ex\]](https://arxiv.org/abs/1110.1530).
- [57] W. Buttinger. “The ATLAS Level-1 Trigger System”. In: *Journal of Physics: Conference Series* 396.1 (2012), p. 012010.
 URL: <http://stacks.iop.org/1742-6596/396/i=1/a=012010>.
- [58] S. Agostinelli et al. “Geant4—a simulation toolkit”. In: *Nuclear Instruments and Methods in Physics Research Section A: Accelerators, Spectrometers, Detectors and Associated Equipment* 506.3 (2003), pp. 250 –303.
 ISSN: 0168-9002.
 DOI: [http://dx.doi.org/10.1016/S0168-9002\(03\)01368-8](http://dx.doi.org/10.1016/S0168-9002(03)01368-8). URL: <http://www.sciencedirect.com/science/article/pii/S0168900203013688>.
- [59] F. Winklmeier. “The ATLAS High Level Trigger infrastructure, performance and future developments”. In: *Real Time Conference, 2009. RT ’09. 16th IEEE-NPSS*. 2009, pp. 183–188.
- [60] D. A. et al.
 “The second level trigger of the ATLAS experiment at CERN’s LHC”. In: *IEEE Transactions on Nuclear Science* 51 (2004), pp. 909–914.
 DOI: [10.1109/TNS.2004.829977](https://doi.org/10.1109/TNS.2004.829977).
 URL: <http://hal.in2p3.fr/in2p3-00148815>.

- [61] A. Negri. “Infrastructure of the ATLAS Event Filter”. In: *IFAE 2006: Incontri di Fisica delle Alte Energie Italian Meeting on High Energy Physics*. Ed. by G. Montagna, O. Nicrosini, and V. Vercesi. Milano: Springer Milan, 2007, pp. 357–360. ISBN: 978-88-470-0530-3.
DOI: [10.1007/978-88-470-0530-3_66](https://doi.org/10.1007/978-88-470-0530-3_66).
URL: http://dx.doi.org/10.1007/978-88-470-0530-3_66.
- [62] J. Zhang. “ATLAS data acquisition”. In: *Real Time Conference, 2009. RT '09. 16th IEEE-NPSS*. 2009, pp. 240–243.
- [63] M. Barczyk et al.
“Online monitoring software framework in the ATLAS experiment”. In: *eConf C0303241* (2003), THGT003. arXiv: [hep-ex/0305096 \[hep-ex\]](https://arxiv.org/abs/hep-ex/0305096).
- [64] Argonne National Laboratory. <http://science.energy.gov/laboratories/argonne-national-laboratory/>. Accessed: 2016-06-27.
- [65] J. C. Collins, D. E. Soper, and G. F. Sterman.
“Factorization of Hard Processes in QCD”. In: *Adv. Ser. Direct. High Energy Phys.* 5 (1989), pp. 1–91.
DOI: [10.1142/9789814503266_0001](https://doi.org/10.1142/9789814503266_0001). arXiv: [hep-ph/0409313 \[hep-ph\]](https://arxiv.org/abs/hep-ph/0409313).
- [66] H. Sonoda.
“Wilson’s renormalization group and its applications in perturbation theory”. In: *APCTP/CQUeST Field Theory Winter School at Pohang Pohang, Korea, February 2-6, 2006*. 2006. arXiv: [hep-th/0603151 \[hep-th\]](https://arxiv.org/abs/hep-th/0603151).
- [67] K. Kovarik et al. “CTEQ nuclear parton distribution functions”. In: *PoS DIS2013* (2013), p. 274. arXiv: [1307.3454](https://arxiv.org/abs/1307.3454).
- [68] R. D. Ball et al. “Parton distributions with QED corrections”. In: *Nucl. Phys.* B877 (2013), pp. 290–320.
DOI: [10.1016/j.nuclphysb.2013.10.010](https://doi.org/10.1016/j.nuclphysb.2013.10.010). arXiv: [1308.0598 \[hep-ph\]](https://arxiv.org/abs/1308.0598).
- [69] J. Kretzschmar. “Proton Structure Measurements and the HERAPDF fit”. In: *24th Lake Louise Winter Institute: Fundamental Interactions (LLWI 2009) Lake Louise, Alberta, Canada, February 16-21, 2009*. 2009.
arXiv: [0906.1108 \[hep-ex\]](https://arxiv.org/abs/0906.1108). URL:
<https://inspirehep.net/record/822351/files/arXiv:0906.1108.pdf>.
- [70] G. Watt.
“MSTW PDFs and impact of PDFs on cross sections at Tevatron and LHC”. In: *Nucl. Phys. Proc. Suppl.* 222-224 (2012), pp. 61–80.
DOI: [10.1016/j.nuclphysbps.2012.03.008](https://doi.org/10.1016/j.nuclphysbps.2012.03.008). arXiv: [1201.1295 \[hep-ph\]](https://arxiv.org/abs/1201.1295).

- [71] A. D. Martin et al. “Parton distributions for the LHC”. In: *Eur. Phys. J.* C63 (2009), pp. 189–285.
DOI: [10.1140/epjc/s10052-009-1072-5](https://doi.org/10.1140/epjc/s10052-009-1072-5). arXiv: [0901.0002 \[hep-ph\]](https://arxiv.org/abs/0901.0002).
- [72] J. C. Collins. “Sudakov form-factors”. In: *Adv. Ser. Direct. High Energy Phys.* 5 (1989), pp. 573–614.
DOI: [10.1142/9789814503266_0006](https://doi.org/10.1142/9789814503266_0006). arXiv: [hep-ph/0312336 \[hep-ph\]](https://arxiv.org/abs/hep-ph/0312336).
- [73] T. Grandou. “The Kinoshita-Lee-Nauenberg (KLN) theorem”. In: *From thermal field theory to neural networks: A day to remember Tanguy Altherr. Proceedings, Meeting, Geneva, Switzerland, November 4, 1994.* 1994.
- [74] R. Gupta. “Introduction to lattice QCD: Course”. In: *Probing the standard model of particle interactions. Proceedings, Summer School in Theoretical Physics, NATO Advanced Study Institute, 68th session, Les Houches, France, July 28-September 5, 1997. Pt. 1, 2.* 1997, pp. 83–219.
arXiv: [hep-lat/9807028 \[hep-lat\]](https://arxiv.org/abs/hep-lat/9807028).
URL: <http://alice.cern.ch/format/showfull?sysnb=0284452>.
- [75] S. Höche. “Introduction to parton-shower event generators”. In: *Theoretical Advanced Study Institute in Elementary Particle Physics: Journeys Through the Precision Frontier: Amplitudes for Colliders (TASI 2014) Boulder, Colorado, June 2-27, 2014.* 2014.
arXiv: [1411.4085 \[hep-ph\]](https://arxiv.org/abs/1411.4085). URL:
<https://inspirehep.net/record/1328513/files/arXiv:1411.4085.pdf>.
- [76] T. Sjostrand, S. Mrenna, and P. Z. Skands. “PYTHIA 6.4 Physics and Manual”. In: *JHEP* 05 (2006), p. 026.
DOI: [10.1088/1126-6708/2006/05/026](https://doi.org/10.1088/1126-6708/2006/05/026). arXiv: [hep-ph/0603175 \[hep-ph\]](https://arxiv.org/abs/hep-ph/0603175).
- [77] T. Sjostrand, S. Mrenna, and P. Z. Skands. “A Brief Introduction to PYTHIA 8.1”. In: *Comput. Phys. Commun.* 178 (2008), pp. 852–867.
DOI: [10.1016/j.cpc.2008.01.036](https://doi.org/10.1016/j.cpc.2008.01.036). arXiv: [0710.3820 \[hep-ph\]](https://arxiv.org/abs/0710.3820).
- [78] S. Alioli et al. “A general framework for implementing NLO calculations in shower Monte Carlo programs: the POWHEG BOX”. In: *JHEP* 06 (2010), p. 043. DOI: [10.1007/JHEP06\(2010\)043](https://doi.org/10.1007/JHEP06(2010)043).
arXiv: [1002.2581 \[hep-ph\]](https://arxiv.org/abs/1002.2581).
- [79] S. Alioli et al. “NLO Higgs boson production via gluon fusion matched with shower in POWHEG”. In: *JHEP* 04 (2009), p. 002.
DOI: [10.1088/1126-6708/2009/04/002](https://doi.org/10.1088/1126-6708/2009/04/002). arXiv: [0812.0578 \[hep-ph\]](https://arxiv.org/abs/0812.0578).
- [80] P. Nason. “A New method for combining NLO QCD with shower Monte Carlo algorithms”. In: *JHEP* 11 (2004), p. 040.
DOI: [10.1088/1126-6708/2004/11/040](https://doi.org/10.1088/1126-6708/2004/11/040). arXiv: [hep-ph/0409146 \[hep-ph\]](https://arxiv.org/abs/hep-ph/0409146).

- [81] S. Frixione, P. Nason, and C. Oleari. “Matching NLO QCD computations with Parton Shower simulations: the POWHEG method”. In: *JHEP* 11 (2007), p. 070. DOI: [10.1088/1126-6708/2007/11/070](https://doi.org/10.1088/1126-6708/2007/11/070). arXiv: [0709.2092 \[hep-ph\]](https://arxiv.org/abs/0709.2092).
- [82] S. Alioli et al. “NLO vector-boson production matched with shower in POWHEG”. In: *JHEP* 07 (2008), p. 060. DOI: [10.1088/1126-6708/2008/07/060](https://doi.org/10.1088/1126-6708/2008/07/060). arXiv: [0805.4802 \[hep-ph\]](https://arxiv.org/abs/0805.4802).
- [83] M. L. Mangano et al. “ALPGEN, a generator for hard multiparton processes in hadronic collisions”. In: *JHEP* 07 (2003), p. 001. DOI: [10.1088/1126-6708/2003/07/001](https://doi.org/10.1088/1126-6708/2003/07/001). arXiv: [hep-ph/0206293 \[hep-ph\]](https://arxiv.org/abs/hep-ph/0206293).
- [84] T. Gleisberg et al. “Event generation with SHERPA 1.1”. In: *JHEP* 02 (2009), p. 007. DOI: [10.1088/1126-6708/2009/02/007](https://doi.org/10.1088/1126-6708/2009/02/007). arXiv: [0811.4622 \[hep-ph\]](https://arxiv.org/abs/0811.4622).
- [85] G. Corcella et al. “HERWIG 6: An Event generator for hadron emission reactions with interfering gluons (including supersymmetric processes)”. In: *JHEP* 01 (2001), p. 010. DOI: [10.1088/1126-6708/2001/01/010](https://doi.org/10.1088/1126-6708/2001/01/010). arXiv: [hep-ph/0011363 \[hep-ph\]](https://arxiv.org/abs/hep-ph/0011363).
- [86] M. Bahr et al. “Herwig++ Physics and Manual”. In: *Eur. Phys. J.* C 58 (2008).
- [87] J. M. Butterworth, J. R. Forshaw, and M. H. Seymour. “Multiparton interactions in photoproduction at HERA”. In: *Z. Phys.* C72 (1996), pp. 637–646. DOI: [10.1007/s002880050286](https://doi.org/10.1007/s002880050286). arXiv: [hep-ph/9601371 \[hep-ph\]](https://arxiv.org/abs/hep-ph/9601371).
- [88] S. Frixione et al. “NLO QCD corrections in Herwig++ with MC@NLO”. In: *JHEP* 01 (2011), p. 053. DOI: [10.1007/JHEP01\(2011\)053](https://doi.org/10.1007/JHEP01(2011)053). arXiv: [1010.0568 \[hep-ph\]](https://arxiv.org/abs/1010.0568).
- [89] T. Bineth et al. “Gluon-induced W-boson pair production at the LHC”. In: *JHEP* 12 (2006), p. 046. DOI: [10.1088/1126-6708/2006/12/046](https://doi.org/10.1088/1126-6708/2006/12/046). arXiv: [hep-ph/0611170 \[hep-ph\]](https://arxiv.org/abs/hep-ph/0611170).
- [90] M. Boonekamp et al. “FPMC: a generator for forward physics”. In: (2011). arXiv: [1102.2531](https://arxiv.org/abs/1102.2531).
- [91] J. Vermaseren. “Two-photon processes at very high energies”. In: *Nuclear Physics B* 229.2 (1983), pp. 347 –371. ISSN: 0550-3213. DOI: [http://dx.doi.org/10.1016/0550-3213\(83\)90336-X](http://dx.doi.org/10.1016/0550-3213(83)90336-X). URL: <http://www.sciencedirect.com/science/article/pii/055032138390336X>.

- [92] M. H. Seymour and M. Marx. “Monte Carlo Event Generators”. In: *Proceedings, 69th Scottish Universities Summer School in Physics : LHC Phenomenology (SUSSP69): St.Andrews, Scotland, August 19-September 1, 2012.* 2013, pp. 287–319. DOI: [10.1007/978-3-319-05362-2_8](https://doi.org/10.1007/978-3-319-05362-2_8). arXiv: [1304.6677 \[hep-ph\]](https://arxiv.org/abs/1304.6677). URL: <https://inspirehep.net/record/1229804/files/arXiv:1304.6677.pdf>.
- [93] S. Agostinelli et al. “Geant4—a simulation toolkit”. In: *Nucl. Instrum. Meth. A* 506 (2003), p. 250. DOI: [dx.doi.org/10.1016/S0168-9002\(03\)01368-8](https://doi.org/10.1016/S0168-9002(03)01368-8).
- [94] ATLAS Collaboration. *The simulation principle and performance of the ATLAS fast calorimeter simulation FastCaloSim.* ATL-PHYS-PUB-2010-013. 2010. URL: <http://cds.cern.ch/record/1300517>.
- [95] R. E. Kalman. “A New Approach to Linear Filtering and Prediction Problems”. In: *Transactions of the ASME – Journal of Basic Engineering* 82 (Series D) (1960), pp. 35–45. URL: <http://www.cs.unc.edu/~{}welch/kalman/media/pdf/Kalman1960.pdf>.
- [96] A. Collaboration. *Universitas Bergensis, Particle Physics Group.* <https://wikihost.uib.no/ift/images/a/ab/ATLASperformance.pdf>. 2015.
- [97] N. Kiryati, Y. Eldar, and A. M. Bruckstein. “A Probabilistic Hough Transform”. In: *Pattern Recogn.* 24.4 (Feb. 1991), pp. 303–316. ISSN: 0031-3203. DOI: [10.1016/0031-3203\(91\)90073-E](https://doi.org/10.1016/0031-3203(91)90073-E). URL: [http://dx.doi.org/10.1016/0031-3203\(91\)90073-E](http://dx.doi.org/10.1016/0031-3203(91)90073-E).
- [98] G. Aad et al. “Electron reconstruction and identification efficiency measurements with the ATLAS detector using the 2011 LHC proton-proton collision data”. In: *Eur. Phys. J.* C74.7 (2014), p. 2941. DOI: [10.1140/epjc/s10052-014-2941-0](https://doi.org/10.1140/epjc/s10052-014-2941-0). arXiv: [1404.2240 \[hep-ex\]](https://arxiv.org/abs/1404.2240).
- [99] W. Lampl et al. “Calorimeter clustering algorithms: Description and performance”. In: (2008).
- [100] *Electron efficiency measurements with the ATLAS detector using the 2012 LHC proton-proton collision data.* Tech. rep. ATLAS-CONF-2014-032. Geneva: CERN, 2014. URL: <https://cds.cern.ch/record/1706245>.
- [101] G. Aad et al. “Electron performance measurements with the ATLAS detector using the 2010 LHC proton-proton collision data”. In: *Eur. Phys. J.* C72 (2012), p. 1909. DOI: [10.1140/epjc/s10052-012-1909-1](https://doi.org/10.1140/epjc/s10052-012-1909-1). arXiv: [1110.3174 \[hep-ex\]](https://arxiv.org/abs/1110.3174).

- [102] G. Aad et al. “Electron and photon energy calibration with the ATLAS detector using LHC Run 1 data”. In: *Eur. Phys. J.* C74.10 (2014), p. 3071. DOI: [10.1140/epjc/s10052-014-3071-4](https://doi.org/10.1140/epjc/s10052-014-3071-4). arXiv: [1407.5063 \[hep-ex\]](https://arxiv.org/abs/1407.5063).
- [103] G. Aad et al. “Measurement of the muon reconstruction performance of the ATLAS detector using 2011 and 2012 LHC proton–proton collision data”. In: *Eur. Phys. J.* C74.11 (2014), p. 3130. DOI: [10.1140/epjc/s10052-014-3130-x](https://doi.org/10.1140/epjc/s10052-014-3130-x). arXiv: [1407.3935 \[hep-ex\]](https://arxiv.org/abs/1407.3935).
- [104] G. Aad et al. “Muon reconstruction performance of the ATLAS detector in proton–proton collision data at $\sqrt{s} = 13$ TeV”. In: *Eur. Phys. J.* C76.5 (2016), p. 292. DOI: [10.1140/epjc/s10052-016-4120-y](https://doi.org/10.1140/epjc/s10052-016-4120-y). arXiv: [1603.05598 \[hep-ex\]](https://arxiv.org/abs/1603.05598).
- [105] D. J. Gross. “Twenty five years of asymptotic freedom”. In: *Nucl. Phys. Proc. Suppl.* 74 (1999), pp. 426–446. DOI: [10.1016/S0920-5632\(99\)00208-X](https://doi.org/10.1016/S0920-5632(99)00208-X). arXiv: [hep-th/9809060 \[hep-th\]](https://arxiv.org/abs/hep-th/9809060).
- [106] E. W. N. Glover and D. A. Kosower. “Recombination methods for jets in p anti-p collisions”. In: *Phys. Lett.* B367 (1996), pp. 369–376. DOI: [10.1016/0370-2693\(95\)01496-9](https://doi.org/10.1016/0370-2693(95)01496-9). arXiv: [hep-ph/9510420 \[hep-ph\]](https://arxiv.org/abs/hep-ph/9510420).
- [107] M. Cacciari, G. P. Salam, and G. Soyez. “The Anti-k(t) jet clustering algorithm”. In: *JHEP* 04 (2008), p. 063. DOI: [10.1088/1126-6708/2008/04/063](https://doi.org/10.1088/1126-6708/2008/04/063). arXiv: [0802.1189 \[hep-ph\]](https://arxiv.org/abs/0802.1189).
- [108] M. Cacciari, G. P. Salam, and G. Soyez. “The Catchment Area of Jets”. In: *JHEP* 04 (2008), p. 005. DOI: [10.1088/1126-6708/2008/04/005](https://doi.org/10.1088/1126-6708/2008/04/005). arXiv: [0802.1188 \[hep-ph\]](https://arxiv.org/abs/0802.1188).
- [109] B. Malaescu et al. *Determination of jet calibration and energy resolution in proton-proton collisions at $\sqrt{s} = 8$ TeV using the ATLAS detector*. Tech. rep. ATL-COM-PHYS-2015-1086. Geneva: CERN, 2015. URL: <https://cds.cern.ch/record/2048678>.
- [110] J. R. Dandoy et al. *Jet energy scale and resolution measurements and their systematic uncertainties in proton-proton collisions at $\sqrt{s} = 13$ TeV with the ATLAS detector*. Tech. rep. ATL-COM-PHYS-2016-213. Geneva: CERN, 2016. URL: <https://cds.cern.ch/record/2136864>.
- [111] T. A. collaboration. “Pile-up subtraction and suppression for jets in ATLAS”. In: (2013).
- [112] G. Aad et al. “Performance of pile-up mitigation techniques for jets in pp collisions at $\sqrt{s} = 8$ TeV using the ATLAS detector”. In: (2015). arXiv: [1510.03823 \[hep-ex\]](https://arxiv.org/abs/1510.03823).

- [113] *A k-Nearest Neighbor Based Algorithm for Multi-label Classification*. Vol. 2. The IEEE Computational Intelligence Society. 2005, 718–721 Vol. 2. URL: http://ieeexplore.ieee.org/xpls/abs_all.jsp?arnumber=1547385.
- [114] G. Aad et al.
“Performance of b -Jet Identification in the ATLAS Experiment”.
In: *JINST* 11.04 (2016), P04008. DOI: [10.1088/1748-0221/11/04/P04008](https://doi.org/10.1088/1748-0221/11/04/P04008). arXiv: [1512.01094 \[hep-ex\]](https://arxiv.org/abs/1512.01094).
- [115] *Optimisation of the ATLAS b -tagging performance for the 2016 LHC Run*. Tech. rep. ATL-PHYS-PUB-2016-012. Geneva: CERN, 2016.
URL: <https://cds.cern.ch/record/2160731>.
- [116] A. Collaboration. *Tau Identification, ATLAS Twiki*. <https://twiki.cern.ch/twiki/bin/view/AtlasProtected/TauIdentification>. 2016.
- [117] T. J. Khoo et al.
Performance of algorithms that reconstruct missing transverse momentum in $\sqrt{s} = 8$ TeV proton-proton collisions in the ATLAS detector. Tech. rep. ATL-COM-PHYS-2015-341. Geneva: CERN, 2015.
URL: <https://cds.cern.ch/record/2012749>.
- [118] B. Brunt et al. *Performance of missing transverse momentum reconstruction with the ATLAS detector using proton-proton collisions at $\sqrt{s} = 13$ TeV*. Tech. rep. ATL-COM-PHYS-2016-407. Geneva: CERN, 2016.
URL: <https://cds.cern.ch/record/2149445>.
- [119] M. Flechl et al. “Improved cross-section predictions for heavy charged Higgs boson production at the LHC”. In: *Phys. Rev.* D91.7 (2015), p. 075015.
DOI: [10.1103/PhysRevD.91.075015](https://doi.org/10.1103/PhysRevD.91.075015). arXiv: [1409.5615 \[hep-ph\]](https://arxiv.org/abs/1409.5615).
- [120] R. D. Ball et al. “Parton distributions with LHC data”.
In: *Nucl. Phys.* B867 (2013), pp. 244–289.
DOI: [10.1016/j.nuclphysb.2012.10.003](https://doi.org/10.1016/j.nuclphysb.2012.10.003). arXiv: [1207.1303 \[hep-ph\]](https://arxiv.org/abs/1207.1303).
- [121] J. Alwall et al.
“The automated computation of tree-level and next-to-leading order differential cross sections, and their matching to parton shower simulations”. In: *JHEP* 07 (2014), p. 079. DOI: [10.1007/JHEP07\(2014\)079](https://doi.org/10.1007/JHEP07(2014)079).
arXiv: [1405.0301 \[hep-ph\]](https://arxiv.org/abs/1405.0301).
- [122] *ATLAS Run 1 Pythia8 tunes*. Tech. rep. ATL-PHYS-PUB-2014-021. Geneva: CERN, 2014. URL: <https://cds.cern.ch/record/1966419>.
- [123] T. Sjostrand et al.
“High-energy physics event generation with PYTHIA 6.1”.
In: *Comput. Phys. Commun.* 135 (2001), pp. 238–259.
DOI: [10.1016/S0010-4655\(00\)00236-8](https://doi.org/10.1016/S0010-4655(00)00236-8). arXiv: [hep-ph/0010017 \[hep-ph\]](https://arxiv.org/abs/hep-ph/0010017).

- [124] G. Aad et al. “Differential top-antitop cross-section measurements as a function of observables constructed from final-state particles using pp collisions at $\sqrt{s} = 7$ TeV in the ATLAS detector”.
In: *JHEP* 06 (2015), p. 100. DOI: [10.1007/JHEP06\(2015\)100](https://doi.org/10.1007/JHEP06(2015)100).
arXiv: [1502.05923 \[hep-ex\]](https://arxiv.org/abs/1502.05923).
- [125] H.-L. Lai et al. “New parton distributions for collider physics”.
In: *Phys. Rev.* D82 (2010), p. 074024. DOI: [10.1103/PhysRevD.82.074024](https://doi.org/10.1103/PhysRevD.82.074024).
arXiv: [1007.2241 \[hep-ph\]](https://arxiv.org/abs/1007.2241).
- [126] J. Gao et al. “CT10 next-to-next-to-leading order global analysis of QCD”.
In: *Phys. Rev.* D89.3 (2014), p. 033009. DOI: [10.1103/PhysRevD.89.033009](https://doi.org/10.1103/PhysRevD.89.033009).
arXiv: [1302.6246 \[hep-ph\]](https://arxiv.org/abs/1302.6246).
- [127] P. M. Nadolsky et al.
“Implications of CTEQ global analysis for collider observables”.
In: *Phys. Rev.* D78 (2008), p. 013004. DOI: [10.1103/PhysRevD.78.013004](https://doi.org/10.1103/PhysRevD.78.013004).
arXiv: [0802.0007 \[hep-ph\]](https://arxiv.org/abs/0802.0007).
- [128] P. Z. Skands. “Tuning Monte Carlo Generators: The Perugia Tunes”.
In: *Phys. Rev.* D82 (2010), p. 074018. DOI: [10.1103/PhysRevD.82.074018](https://doi.org/10.1103/PhysRevD.82.074018).
arXiv: [1005.3457 \[hep-ph\]](https://arxiv.org/abs/1005.3457).
- [129] D. Collaboration. *Useful diagrams of top signals and backgrounds*.
http://www-d0.fnal.gov/Run2Physics/top/top_public_web_pages/top_feynman_diagrams.html; accessed 1-September-2016. 2016.
- [130] N. Davidson, T. Przedzinski, and Z. Was.
“PHOTOS Interface in C++: Technical and Physics Documentation”.
In: *Comput. Phys. Commun.* 199 (2016), pp. 86–101.
DOI: [10.1016/j.cpc.2015.09.013](https://doi.org/10.1016/j.cpc.2015.09.013). arXiv: [1011.0937 \[hep-ph\]](https://arxiv.org/abs/1011.0937).
- [131] D. J. Lange. “The EvtGen particle decay simulation package”.
In: *Nuclear Instruments and Methods in Physics Research Section A: Accelerators, Spectrometers, Detectors and Associated Equipment* 462.1–2 (2001). BEAUTY2000, Proceedings of the 7th Int. Conf. on B-Physics at Hadron Machines, pp. 152 –155. ISSN: 0168-9002.
DOI: [http://dx.doi.org/10.1016/S0168-9002\(01\)00089-4](http://dx.doi.org/10.1016/S0168-9002(01)00089-4). URL: <http://www.sciencedirect.com/science/article/pii/S0168900201000894>.
- [132] A. D. Martin et al. “Uncertainties on alpha(S) in global PDF analyses and implications for predicted hadronic cross sections”.
In: *Eur. Phys. J.* C64 (2009), pp. 653–680.
DOI: [10.1140/epjc/s10052-009-1164-2](https://doi.org/10.1140/epjc/s10052-009-1164-2). arXiv: [0905.3531 \[hep-ph\]](https://arxiv.org/abs/0905.3531).
- [133] A. D. Martin et al. “Heavy-quark mass dependence in global PDF analyses and 3- and 4-flavour parton distributions”.
In: *Eur. Phys. J.* C70 (2010), pp. 51–72.
DOI: [10.1140/epjc/s10052-010-1462-8](https://doi.org/10.1140/epjc/s10052-010-1462-8). arXiv: [1007.2624 \[hep-ph\]](https://arxiv.org/abs/1007.2624).

- [134] A. Buckley et al. “LHAPDF6: parton density access in the LHC precision era”. In: *Eur. Phys. J.* C75 (2015), p. 132. DOI: [10.1140/epjc/s10052-015-3318-8](https://doi.org/10.1140/epjc/s10052-015-3318-8). arXiv: [1412.7420 \[hep-ph\]](https://arxiv.org/abs/1412.7420).
- [135] G. Cowan et al. “Asymptotic formulae for likelihood-based tests of new physics”. In: *Eur. Phys. J.* C71 (2011). [Erratum: *Eur. Phys. J.* C73,2501(2013)], p. 1554. DOI: [10.1140/epjc/s10052-011-1554-0](https://doi.org/10.1140/epjc/s10052-011-1554-0), [10.1140/epjc/s10052-013-2501-z](https://doi.org/10.1140/epjc/s10052-013-2501-z). arXiv: [1007.1727 \[physics.data-an\]](https://arxiv.org/abs/1007.1727).
- [136] A. Aktas et al. “Measurement and QCD analysis of the diffractive deep-inelastic scattering cross-section at HERA”. In: *Eur. Phys. J.* C48 (2006), pp. 715–748. DOI: [10.1140/epjc/s10052-006-0035-3](https://doi.org/10.1140/epjc/s10052-006-0035-3). arXiv: [hep-ex/0606004 \[hep-ex\]](https://arxiv.org/abs/hep-ex/0606004).
- [137] M. Klein and R. Yoshida. “Collider Physics at HERA”. In: *Prog. Part. Nucl. Phys.* 61 (2008), pp. 343–393. DOI: [10.1016/j.ppnp.2008.05.002](https://doi.org/10.1016/j.ppnp.2008.05.002). arXiv: [0805.3334 \[hep-ex\]](https://arxiv.org/abs/0805.3334).
- [138] “Summary of ATLAS Pythia 8 tunes”. In: (2012).
- [139] “New ATLAS event generator tunes to 2010 data”. In: (2011).
- [140] P. Z. Skands. “Tuning Monte Carlo Generators: The Perugia Tunes”. In: *Phys. Rev.* D82 (2010), p. 074018. DOI: [10.1103/PhysRevD.82.074018](https://doi.org/10.1103/PhysRevD.82.074018). arXiv: [1005.3457 \[hep-ph\]](https://arxiv.org/abs/1005.3457).
- [141] J. Pumplin et al. “New generation of parton distributions with uncertainties from global QCD analysis”. In: *JHEP* 07 (2002), p. 012. DOI: [10.1088/1126-6708/2002/07/012](https://doi.org/10.1088/1126-6708/2002/07/012). arXiv: [hep-ph/0201195 \[hep-ph\]](https://arxiv.org/abs/hep-ph/0201195).
- [142] G. Aad et al. “Observation and measurement of Higgs boson decays to WW* with the ATLAS detector”. In: *Phys. Rev.* D92.1 (2015), p. 012006. DOI: [10.1103/PhysRevD.92.012006](https://doi.org/10.1103/PhysRevD.92.012006). arXiv: [1412.2641 \[hep-ex\]](https://arxiv.org/abs/1412.2641).
- [143] M. Dyndal and L. Schoeffel. “The role of finite-size effect on the spectrum of equivalent photons in photon-photon interactions in proton-proton collisions at the LHC”. In: *Phys. Lett.* B 741 (2015).
- [144] L. A. Harland-Lang, V. A. Khoze, and M. G. Ryskin. “Exclusive physics at the LHC with SuperChic 2”. In: *Eur. Phys. J.* C76.1 (2016), p. 9. DOI: [10.1140/epjc/s10052-015-3832-8](https://doi.org/10.1140/epjc/s10052-015-3832-8). arXiv: [1508.02718 \[hep-ph\]](https://arxiv.org/abs/1508.02718).

- [145] G. Aad et al. “Measurement of total and differential W^+W^- production cross sections in proton-proton collisions at $\sqrt{s} = 8$ TeV with the ATLAS detector and limits on anomalous triple-gauge-boson couplings”. In: *JHEP* 09 (2016), p. 029. DOI: [10.1007/JHEP09\(2016\)029](https://doi.org/10.1007/JHEP09(2016)029). arXiv: [1603.01702 \[hep-ex\]](https://arxiv.org/abs/1603.01702).
- [146] M Chelstowska et al. *Background estimation in the $H \rightarrow WW^{(*)} \rightarrow \ell\nu\ell\nu$ analysis with 20.7 fb^{-1} of data collected with the ATLAS detector at $\sqrt{s} = 8$ TeV.* Tech. rep. ATL-COM-PHYS-2013-1630. Geneva: CERN, 2013. URL: <https://cds.cern.ch/record/1636127>.